Title
A WISE Measurement of the 2.4 μm Galaxy Luminosity Function and its Implications for the Extragalactic Background Light at 3.4 μm

Author
Lake, Sean Earl

Publication Date
2017

Peer reviewed|Thesis/dissertation

University of California
Los Angeles

A *WISE* Measurement of the 2.4 μm Galaxy Luminosity Function and its Implications for the Extragalactic Background Light at 3.4 μm

A dissertation submitted in partial satisfaction
of the requirements for the degree
Doctor of Philosophy in Physics

by

Sean Earl Lake

2017

Abstract of the Dissertation

A *WISE* Measurement of the 2.4 μm Galaxy Luminosity Function and its Implications for the Extragalactic Background Light at 3.4 μm

by

Sean Earl Lake

Doctor of Philosophy in Physics

University of California, Los Angeles, 2017

Professor Edward L. Wright, Chair

The measurement of the the Extragalactic Background Light (EBL) has seen some controversy in recent works, with direct and indirect measures conflicting. Specifically, upper limits based on analyzing the plausible opacity obscuring TeV spectra of blazars suggests that the density of radiation with wavelengths near 3.4 μm is one third to one half as intense as direct measures of the same (for example: Aharonian et al., 2006; Levenson et al., 2007; Matsumoto et al., 2005). The dominant contributor of the EBL at 3.4 μm is expected to be ordinary starlight from relatively local, $z < 1$, galaxies, so an estimate of the amount of light emitted by galaxies based on the galaxy Luminosity Function (LF) should provide a useful lower limit to the EBL. While analyses of this sort have been done by others (Domínguez et al., 2011; Helgason et al., 2012), the full sky coverage of the AllWISE database has made it possible for us to improve the measurement of both the LF at 2.4 μm and the EBL using the large public spectroscopic redshift surveys. In order to do so, we had to develop a mathematical model for the measurement of a generalization of the LF, which is the density of galaxies per unit comoving volume per unit luminosity, to the Spectro-Luminosity Functional (SLF), which replaces the density per unit single luminosity, $\mathrm{d}L$, with the density per luminosities at all frequencies, $\mathcal{D}L_\nu$. Our best combined analysis of the data yields present day Shechter Function LF parameters of: $L_\star = 6.4 \pm [0.1_{\mathrm{stat}}, 0.3_{\mathrm{sys}}] \times 10^{10}\, L_{2.4\,\mu\mathrm{m}\,\odot}$ ($M_\star = -21.67 \pm [0.02_{\mathrm{stat}}, 0.05_{\mathrm{sys}}]$ AB mag), $\phi_\star = 5.8 \pm [0.3_{\mathrm{stat}}, 0.3_{\mathrm{sys}}] \times 10^{-3}\,\mathrm{Mpc}^{-3}$, and

$\alpha = -1.050 \pm [0.004_{\mathrm{stat}},\, 0.03_{\mathrm{sys}}]$; this implies a present day density of galaxies of $0.08\,\mathrm{Mpc}^{-3}$ brighter that $10^6\,L_{2.4\,\mu\mathrm{m}\,\odot}$ ($10^{-3}\,\mathrm{Mpc}^{-3}$ brighter than $L_\star$) and a luminosity density equivalent to $3.8 \times 10^8\,L_{2.4\,\mu\mathrm{m}\,\odot}\,\mathrm{Mpc}^{-3}$. The net EBL at $3.4\,\mu$m that our synthesis model produces from galaxies closer than $z = 5$ is $I_\nu = 9.0 \pm 0.5\,\mathrm{kJy\,sr}^{-1}$ ($\nu I_\nu = 8.0 \pm 0.4\,\mathrm{nW\,m}^{-2}\,\mathrm{sr}^{-1}$), largely in agreement with similar LF based estimates of the EBL.

The dissertation of Sean Earl Lake is approved.

Alexander Kusenko

Matthew A. Malkan

Alice E. Shapley

Edward L. Wright, Committee Chair

University of California, Los Angeles

2017

Table of Contents

List of Figures

List of Tables

Acknowledgments

for my Father, Mother, Sisters, Brothers,
and all the other members of my family without whose support
this would not have been possible for me to write.

Vita

2004	B.A. (Physics, Math minor) cum Laude, University of Pennsylvania. Recipient Penn Leadership Scholarship, 2000-2004. On the Dean's List 2000–2001 and 2003-2004.
September 2005 – March 2009	Teaching Assistant, Department of Physics and Astronomy. University of California, Los Angeles, California (UCLA).
2008	M.S. (Physics), UCLA.
March 2009 – present	Research Assistant, Department of Physics and Astronomy, UCLA. Researched the applicability of the Random Sample Consensus (RANSAC) algorithm to the problem of finding asteroids in *WISE* satellite data. Analyzed data from *WISE* using extant data sets to calculate the galaxy luminosity function.

Publications and Presentations

Optical Spectroscopic Survey of High-latitude WISE-selected Sources

Lake, S. E.; Wright, E. L. et al in The Astronomical Journal, Volume 143, Issue 1.

Paper characterizing a small one night optical spectroscopic survey of *WISE*-selected sources.

Modeling Stars to Improve the Faint Flux Calibration of WISE

Lake, S. E.; Wright, E. L. et al.

Poster presented at AAS Meeting #221 on using stellar photosphere models of well isolated stars in the Sloan Digital Sky Survey (SDSS) to correct for the background oversubtraction done on *WISE* data.

The 3.4 μm *Extragalactic Background Light as Measured Using WISE*

Lake, S. E.; Wright, E. L. et al.

Presentation describing advances in luminosity function measurement techniques needed to synthesize multiple data sets into a single measurement.

Explanatory Supplement to the AllWISE Data Release Products

Cutri, R. M.; Wright, E. L. et al.

Primary author of section on catalog completeness. Produced non-*Spitzer* based analysis using data set from the faint flux calibration poster.

K-corrections: an Examination of their Contribution to the Uncertainty of Luminosity Measurements

Lake, S. E.; and Wright, E. L. accepted by The Open Journal of Astrophysics.

Paper describing how to estimate the uncertainty in K-corrected quantities based on the variety of spectral energy distributions.

A Close Examination of the Measurement and Parametrization of Luminosity Functions in an Expanding Universe

Lake, S. E.; Wright, E. L. et al. submitted to the Astrophysical Journal.

Paper introducing the concept of the spectro-luminosity functional, $\Psi[L_\nu]$, and the statistical formulae needed to measure the same.

CHAPTER 1

Introduction

The extragalactic background light (EBL, review: Cooray, 2016) is, from an observational perspective, the direction averaged light observed if all light originating within the Milky Way (foreground) and cosmic microwave background (CMB, background) is subtracted out. From a physical perspective, it is the intergalactic radiation density accumulated over cosmic time as emitted by galaxies and active galactic nuclei (AGN) over their entire history. As such it contains information about the star formation, AGN accretion, and dust accumulation histories of the universe, even for sources that are too faint to detect individually. The primary challenge in measuring the EBL directly is the presence of "foregrounds" like the atmosphere (from ground based measurements), the zodiacal light, moon glow, and light from sources in our own galaxy. Worse, the foregrounds are frequently as large or large than the signal, leading to large large uncertainties inherent in subtracting two positive, and nearly equal, quantities. Because of this there is a need to accurately model what known components contribute to the overall background as accurately as possible in order to tease out potentially interesting signals in the EBL; signals like what fraction is light from the first stars, small nearby galaxies, and the diffuse stellar halos of galaxies. The contribution of galactic halos, for example, was measured in an analysis of near infrared background fluctuations using data from the Spitzer Deep, Wide-Field Survey (SDWFS) in Cooray et al. (2012).

Figure 1.1 comes from Domínguez et al. (2011) and shows a large number of ultraviolet to far infrared measurements of the EBL. The most important part of the plot, from the perspective of this work, is the starlight dominated stretch that covers the optical to near-infrared (near-IR), roughly 0.5–5μm. In that region upper limits based on blazar gamma ray opacity measurements (particularly the orange line based on Aharonian et al., 2006) are in tension with direct measurements (for example: Tsumura et al., 2013; Levenson et al., 2007; Matsumoto et al., 2005), though recent work on gamma ray production by blazar accelerated protons has lessened the strictness of these bounds (Essey & Kusenko, 2010; Essey et al., 2011; Aharonian et al., 2013). Indirect studies of the contribution of all galaxies by extrapolating from the resolved ones to their total contribution to the background around $3.5\,\mu$m have had mixed results, ranging from $5.85\,\mathrm{kJy\,sr^{-1}}$ ($4.86\,\mathrm{nW\,m^{-2}\,sr^{-1}}$) in Helgason et al. (2012) to $10.8^{+2.1}_{-1.1}\,\mathrm{kJy\,sr^{-1}}$ ($9.0^{+1.7}_{-0.9}\,\mathrm{nW\,m^{-2}\,sr^{-1}}$) in Levenson & Wright (2008).

The goal of the work that went into this thesis is to provide an estimate of the contribution to the EBL of galaxies and AGN that has a greater fidelity to the underlying physics of how galaxies' contribution to the EBL was made than is possible with the extrapolation of flux histograms, as was done in Fazio et al. (2004), Levenson & Wright (2008), and Driver et al. (2016), provides. That fidelity comes from using luminosity functions (LFs), which are observed to be well approximated by Schechter functions, as developed in the Press-Schechter formalism of Press & Schechter (1974) and Schechter (1976). A similar approach was taken by Domínguez et al. (2011) and Helgason et al. (2012), which both used previously measured LFs from the literature to calculate the EBL that those luminosity functions imply. This work improves on both of those in terms of both the sophistication of the analysis and the size of the sample.

The improvement that made this work possible is based on measuring a generalization of the luminosity function that is known as the spectro-luminosity functional, denoted $\Psi[L_\nu](z)$. The quantity $\Psi[L_\nu](z)$ is defined by $\Psi[L_\nu](z)[\mathcal{D}L_\nu]\,\mathrm{d}V_c$ being the mean number of galaxies with a spectral energy distribution in the function space volume, $[\mathcal{D}L_\nu]$, around L_ν and in comoving real space volume $\mathrm{d}V_c$ at the redshift z. Ψ can be factored into an ordinary luminosity function, $\Phi(L, z)$, and the conditional likelihood of the normalized SED, $\mathcal{L}_{\mathrm{SED}}[L_\nu](\cdot|L, z)$; ($L$ and z are placed after the vertical bar to emphasize that they are non-random quantities with respect to $\mathcal{L}_{\mathrm{SED}}$). By modeling the density over the function space of SEDs it is possible to simultaneously analyze multiple spectroscopic redshift samples that were selected using different observer frame fluxes, and to do so in a consistent manner with a minimum of auxiliary, nuisance, parameters. Full details of how this is done can be found in Chapter 2.

In order to make the transition from spectro-luminosity functional to luminosity function analytically tractable we chose to approximate $\mathcal{L}_{\rm SED}$ as a Gaussian. This simplified model fails to reproduce well known features from the study of galaxies, like the split between 'red sequence' and 'blue cloud' galaxies in color-magnitude diagrams of optical wavelengths, but is still a useful approximation. Like any Gaussian, the distribution is characterized by a mean normalized SED, $\mu_\nu(\nu)$, and a covariance of normalized SEDs, $\Sigma(\nu, \nu')$. The measurement of these quantities for this thesis are described in Chapter 3, which focuses on how to use $\Sigma(\nu, \nu')$ to calculate the variance added to a luminosity measurement when K-corrections are involved, and how to approximate $\Sigma(\nu, \nu')$ using a finite number of template SEDs. Ideally this measurement would have been done at the same time as the luminosity function measurements, allowing a full characterization of how the uncertainties in all parameters are related. This was not possible due to computational speed limitations. We, therefore, decided to use the zCOSMOS-10k bright catalog (Lilly et al., 2009; Knobel et al., 2012), because of its combination of depth, simple selection criteria, and available auxiliary photometry to most tightly constrain μ_ν and Σ.

One of the jobs Ψ does, from a certain perspective, is to incorporate modeling the selection function into the process of measuring an LF. No selection function model is perfect and, becuase the number of targets is a function that behaves as a power law in flux with negative exponent, systematic uncertainties in the selection of faint targets can easily dominate for many LF related quantities, even for medium sized spectroscopic surveys. Because of this, we conducted a small, sparsely targeted, one night redshift survey using the DEep Imaging Multi-Object Spectrograph (Faber et al., 2003, DEIMOS) on the Keck II telescope of targets in the *WISE* Preliminary Data Release. The resulting data set is named *WISE*/DEIMOS. The selection of targets based on *WISE* W1 flux should minimize the systematic uncertainties in the LF, as long as the luminosity measured is what the W1 filter observes at the median redshift of the sample. The systematic effects should be even smaller in the $3.4\,\mu$m background calculated from the resulting LF. A reanalysis of the redshift catalog originally published in Lake et al. (2012) is in Chapter 4.

With the *WISE*/DEIMOS survey serving as the anchor, we selected a number of publicly available spectroscopic redshift surveys that are targeted on observed flux in a single filter to analyze. The five additional surveys selected (in order of decreasing area/increasing depth) are: 6dFGS data release 3 (Jones et al., 2009), the main galaxy sample from the Sloan Digital Sky Survey (SDSS) data release 10 (Strauss et al., 2002; Ahn et al., 2014a), the GAlaxy and Mass Assembly (GAMA) survey data release 2 (Liske et al., 2015), the AGN and Galaxy Evolution Survey (Kochanek et al., 2001, AGES), and the zCOSMOS survey. Full details of the characteristics of each survey, and the steps taken to make the selection more homogeneous across the different surveys, are in Chapter 5.

The combed data set constructed from multiple redshift surveys in Chapter 5 is complicated, with many potential source of bias. For that reason, and to isolate biases uncovered in the process, the measurements of the LF parameters in Chapter 6 are broken down into multiple subsamples: six survey specific samples (labeled: 6dFGS, SDSS, GAMA, AGES, *WISE*/DEIMOS, and zCOSMOS), and six combined samples (labeled: Low z, High z, High z Prior, Low z Trim, High z Trim, and High z Trim Prior). Of those samples, the one with the greatest depth and largest sample size is the one labeled High z Prior - high redshift data with a prior on the LF's faint end slope, α, from the Low z sample. The results reported in Chapter 6 are, broadly, in line with previous results from the literature, with improved statistical precision on most parameters.

μ_ν from Chapter 3 is combined with the Bayesian posterior Markov Chain Monte Carlo chains of the LF parameters from Chapter 6 to produce posterior chains of the 3.4 μm EBL in Chapter 7. The background estimates from the LF chains, affected by a bias of unknown origin that necessitated the split of the combined samples into High z and Low z subsamples, show the expected overestimate in the EBL from the very fast LF parameter evolution measured — in some cases higher than the highest direct measures. The subsamples not affected by this problem show a trend of increasing background estimate with increasing depth, so we are confident that the sample with the highest statistical precision, labeled High z Prior, will agree most closely with even more precise measures that will be made in the future.

Finally, Chapter 8 contains a summation of this work and where it fits in the ongoing effort to understand the history of the formation of galaxies and the EBL.

The cosmology used in this thesis is based on the WMAP 9 year ΛCDM cosmology (Hinshaw et al., 2013)[1], with flatness imposed, yielding: $\Omega_M = 0.2793$, $\Omega_\Lambda = 1 - \Omega_M$, and $H_0 = 70\,\mathrm{km\,sec^{-1}\,Mpc^{-1}}$ (giving Hubble time $t_H = H_0^{-1} = 13.97\,\mathrm{Gyr}$, and Hubble distance $D_H = ct_H = 4.283\,\mathrm{Gpc}$). All magnitudes quoted are in the AB system, unless otherwise stated. In cases where the source data was in Vega magnitudes and a magnitude zero point was provided in the documentation, they were used for conversion to AB (2MASS[2] and AllWISE[3]). For the surveys without obviously documented zero points (NDWFS[4], SDWFS[5]) we converted Vega magnitudes to AB magnitudes using those provided in Kochanek et al. (2012). When computing bandpass solar luminosities we utilized the 2000 ASTM Standard Extraterrestrial Spectrum Reference E-490-00[6]. For our standard bandpass, W1 at $z = 0.38$, we get a solar absolute magnitude of $M_{2.4\,\mu\mathrm{m}\,\odot} = 5.337\,\mathrm{AB\ mag}$, corresponding to a luminosity of $L_{2.4\,\mu\mathrm{m}\,\odot} = 3.344 \times 10^{-8}\,\mathrm{Jy\,Mpc^2}$. All coordinates are listed in the J2000 reference frame.

[1] http://lambda.gsfc.nasa.gov/product/map/dr5/params/lcdm_wmap9.cfm

[2] http://www.ipac.caltech.edu/2mass/releases/allsky/faq.html#jansky

[3] http://wise2.ipac.caltech.edu/docs/release/allsky/expsup/sec4_4h.html#WISEZMA

[4] http://www.noao.edu/noao/noaodeep/

[5] http://irsa.ipac.caltech.edu/data/SPITZER/SDWFS/

[6] http://rredc.nrel.gov/solar/spectra/am0/

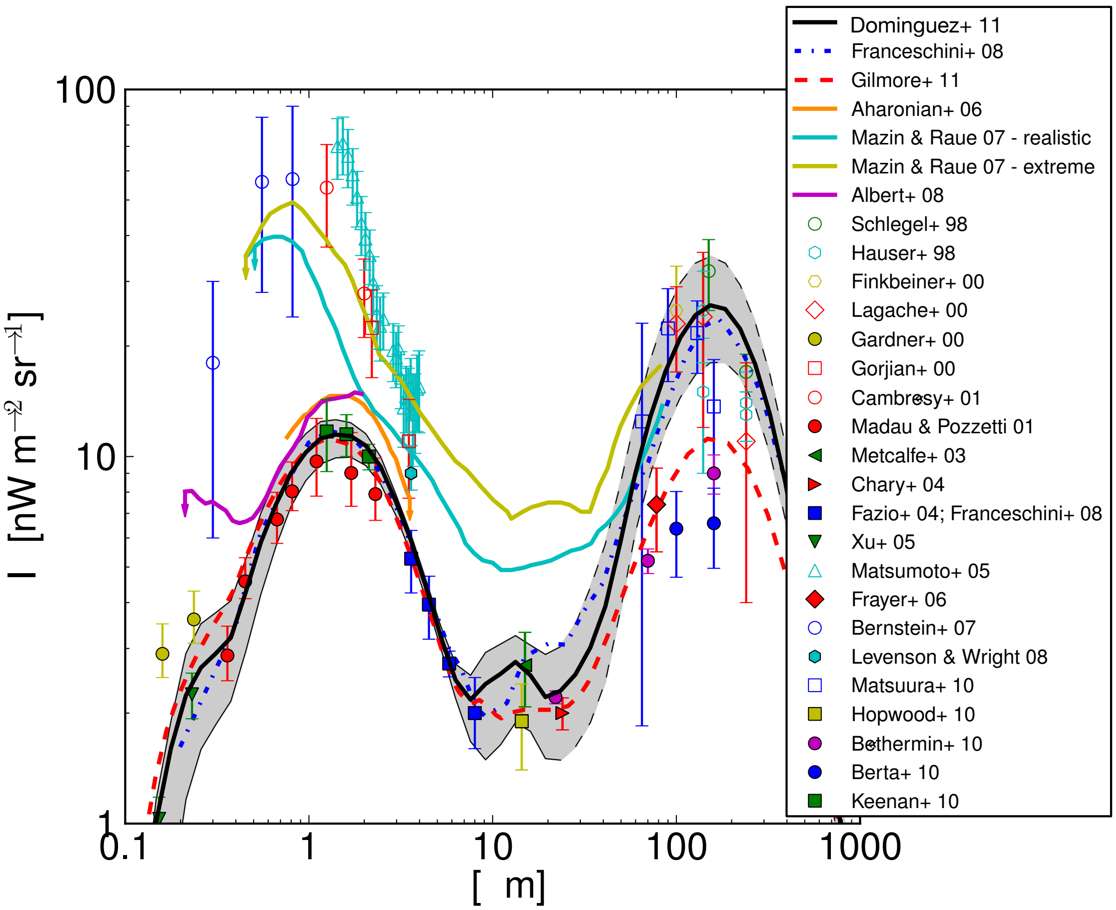

Figure 1.1: Overview of the EBL from ultraviolet to far infrared wavelengths. The bump peaking at around 1.5 μm is believed to be dominated by galaxy starlight, and the one near 110 μm is dust emission from galaxies. This figure comes from Domínguez et al. (2011) and is Figure 2 there. For wavelengths longer than around 400 μm, the CMB (not shown) dominates.

CHAPTER 2

Theoretical Description of the Measurement of Φ

The astronomy community has at its disposal a large back catalog of public spectroscopic galaxy redshift surveys that can be used for the measurement of luminosity functions. Utilizing the back catalog with new photometric surveys to maximum efficiency requires modeling the color selection bias imposed on selection of target galaxies by flux limits at multiple wavelengths. The likelihood derived herein can address, in principle, all possible color selection biases through the use of a generalization of the luminosity function, $\Phi(L)$, over the space of all spectra: the spectro-luminosity functional, $\Psi[L_\nu]$. It is, therefore, the first estimator capable of simultaneously analyzing multiple redshift surveys in a consistent way. We also propose a new way of parametrizing the evolution of the classic Schechter function parameters, $L_\star$ and $\phi_\star$, that improves both the physical realism and statistical performance of the model. The techniques derived in this chapter are used in an Chapter 6 to measure the luminosity function of galaxies at the rest frame wavelength of $2.4\,\mu$m using the *Widefield Infrared Survey Explorer* (*WISE*).

2.1 Introduction

The luminosity function (LF), which describes the demography of objects with respect to their luminosity, is one of the most basic statistical properties that can be measured for objects observed in astronomy. Because it is so basic, and because luminosities cannot be measured directly, the number of ways to estimate the LF for galaxies are numerous

[0]This chapter is based on a paper originally submitted to The Astrophysical Journal in 2016, and currently on hold pending submission of other papers, by the authors: S. E. Lake, E. L. Wright, C.-W. Tsai, and A. Lam.

(see reviews: Johnston, 2011; Willmer, 1997; Binggeli et al., 1988); so numerous, in fact, that it is traditional for papers measuring a luminosity function for galaxies to use multiple estimators, at least one parametric and one non-parametric. The most commonly used non-parametric estimators (refinements of the $1/V_{\text{max}}$ estimator of Schmidt (1968) made by Avni & Bahcall (1980) and step-wise maximum likelihood [SWML] from Efstathiou et al. (1988a)) can be accurately described as a binning of the data with completeness corrections. The most popular parametric estimators are variations on the one from Sandage et al. (1979), commonly called STY.

This chapter seeks to address three weaknesses in how parametric model fitting is currently done for the purpose of applying it to real data in Chapter 6. First, the most common method for addressing incompleteness is not likelihood based and is, therefore, likely to converge more slowly and exhibit higher bias than a more strictly likelihood based one. Second, the existing techniques in the literature can only cope with data sets that are volume limited, flux limited in a single bandpass, or that otherwise have a sharp cutoff in luminosity-redshift space and a constant observation selection probability. Third, the majority also do not address a bias related to spectral energy distribution variety, explored in Ilbert et al. (2004).

This chapter includes the derivation of an estimator that addresses all of these concerns and can, in principle, handle an arbitrary number of flux selection limits. Each flux limit requires an additional dimension in the numerical integration of some probability density function (PDF); for this work that PDF is a multi-dimensional Gaussian. The well known “curse of dimensionality” places limits on the performance of such deterministic numerical integrations, so the estimator is presently useful for analyzing surveys with flux limits in at most two bands. The basis of this new estimator is rooted in a generalization of the luminosity function that uses functional analysis (calculus of variations) to estimate the density of galaxies per unit volume, per unit luminosity, per unit spectral energy distribution (SED) function space volume. This generalization is most naturally called the spectro-luminosity functional.

The derivation is included to also show the way that many of the most popular estimators are related to the one defined in this work. Of the parametric estimators, STY and the estimator from Marshall et al. (1983) are approximations of the one from this work. The following binned LF estimators are also related to the estimator defined in this work: $1/V_{\max}$ of Schmidt (1968), the binned Poisson estimator of Page & Carrera (2000), and corrected Poisson estimator of Miyaji et al. (2001).

It has been observed in multiple measurements of the LF that the density ($\phi_\star$) and luminosity scale ($L_\star$) parameters are evolving with time (Lin et al., 1999; Blanton et al., 2003b; Babbedge et al., 2006; Dai et al., 2009; Loveday et al., 2012; Cool et al., 2012). The most frequently used parametrizations for the evolution of $\phi_\star$ and $L_\star$ are the ones from Lin et al. (1999): $L_\star \propto 10^{0.4Qz}$ and $\phi_\star \propto 10^{0.4Pz}$, with Q and P constants. These parametrizations work well at the empirical level, as long as the evolution is not extrapolated to very high redshifts where, depending on the measured values of the evolution constants P and Q, either or both $\phi_\star$ and $L_\star$ can become un-physically large at high redshifts. To remedy this, we propose a similar modified parametrization based on lookback time, instead of redshift, that also satisfies the boundary condition that at some point in the past $L_\star$ was zero.

There are a number of physical parameters that are derivable from the LF, including: galaxy number density (brighter than some cutoff), the specific rate of change in number density, luminosity density, the specific rate of change in luminosity density, and the normalization of the predicted histogram of extragalactic sources binned by observed flux. This work contains formulae that relate these parameters to the Schechter parameters, with specific application to the form they take when applied to the evolution scheme from Lin et al. (1999) and the one proposed here. There is also a brief discussion of which parameters, from experience, give less correlated errors when used in a Markov Chain Monte Carlo (MCMC) characterization of the Bayesian posterior of the maximum likelihood estimator from this work.

The structure of this chapter is as follows: Section 2.2 contains derivations of multiple ways of measuring LFs based on the likelihood, using both binned and unbinned techniques, Section 2.3 covers different aspects of describing the evolution of Schechter LF parameters, offering improvements motivated on both physical grounds and statistical performance, and Section 2.4 contains a brief discussion on where there is room for improvements going forward.

The performance of the estimators on simulated data sets is not examined, because they are 100% likelihood based, and any simulations that can be done quickly would require the same approximations made in deriving the likelihood. Instead, the tools are applied to real world data in Chapter 6 to measure the luminosity function of galaxies at rest frame 2.4 μm using *WISE* in combination with a number of public spectroscopic redshift surveys.

2.2 Luminosity Function Measurement

The basic definition a luminosity function, $\Phi(L)$, is the number density of sources per unit luminosity per unit volume. This definition often leads to the treatment of Φ as a PDF that is normalized to the density of sources instead of unity. For galaxies this treatment conflicts with the fact that the integral of the reported luminosity functions is frequently divergent (see, for example, the results in Dai et al., 2009). The contents of the section break down, by subsection, as follows: Subsection 2.2.1 resolves this conflict by more precisely defining Φ as a non-normalized density, permitting a rigorous derivation of a corresponding maximum likelihood estimator. Subsection 2.2.2 covers the technique used here to deal with the biases that cosmological redshifting adds to the problem of measuring galaxy luminosity functions over large redshift ranges. The technique used is to expand the definition of luminosity functions to cover their entire spectrum: the spectro-luminosity functional, $\Psi[L_\nu]$. Section 2.2.5 derives the corresponding maximum likelihood estimator for a binned LF estimator, showing how different estimators in the literature correspond to different levels of approximation. Finally, Subsection 2.2.6 gives formulae for estimating the uncertainties in the binned estimators described in the previous subsection.

2.2.1 Luminosity Function Definition

In this work we choose to define Φ rigorously, bordering on pedantically, in order to show where all of the approximations that leave room for future refinements are, and to show how where many existing estimators are approximations of the one derived here. The definition of Φ used here is as follows: given a volume, $\mathrm{d}V_i$, around the point in space at position $\vec{x}_i$, and a luminosity interval, $\mathrm{d}L_i$, around the luminosity L_i, the average number of sources that exist in that bin around that point in luminosity-location space is:

$$\langle m_i \rangle = \Phi(L_i,\, \vec{x}_i)\, \mathrm{d}L_i\, \mathrm{d}V_i, \tag{2.1}$$

where the average is taken over an ensemble of universes with different initial conditions, m_i is the actual number of galaxies around $(L_i,\, \vec{x}_i)$ in a particular universe selected from the ensemble, and i is an index that covers all space-luminosity boxes in a given partition scheme of a particular universe. The homogeneity and isotropy of the universe guarantees that Φ does not actually depend on $\vec{x}$, but it can evolve with time, and, therefore, does depend on redshift, z. What differentiates this definition from others is that it is explicitly an average over a hypothetical ensemble of universes, making it conceptually independent of environment. A similar definition can be arrived at for an environmentally dependent LF, what we would call a conditional luminosity function, the two most common examples of which are the field galaxy LF (low density environment) and the cluster galaxy LF (high density). However, doing so introduces complications to the measurement process related to correctly identifying the environment each galaxy is in, and how to correctly match those classifications across cosmological time, that are beyond the scope of this work.

We can assume that m_i is Poisson distributed, an approximation that is accurate in the limit where the volume of the spatial box is $\langle m_i \rangle \ll 1$, as is done implicitly in Marshall et al. (1983). The random vagaries of whether the or not the galaxies in box i are selected in the observation process can be modeled as a binomial process with probability denoted $S(L_i, \vec{x}_i)$, called the selection function, and a number of trials equal to m_i. When the binomial observation process is combined with the Poisson distribution of m_i, and the number of unobserved galaxies is summed over, the resulting distribution of galaxies observed, n_i, has probability:

$$P(n_i) = \frac{[S_i \Phi_i\, \mathrm{d}L_i\, \mathrm{d}V_i]^{n_i}}{n_i!} \mathrm{e}^{-S_i \Phi_i\, \mathrm{d}L_i\, \mathrm{d}V_i}. \tag{2.2}$$

It is in the next step that the biggest approximation is made. The approximation is to treat all of the $P(n_i)$ as independent, as implied by the cosmological principle (homogeneity and isotropy of the universe). Where this fails is that galaxies have finite size, and overlapping galaxies tend to quickly merge, so no more than one galaxy of any luminosity can occupy a given region of space for long, and the size of that region depends on the luminosity of the galaxy. Outside of that effectively excluded volume, however, galaxies tend to be positively correlated (that is, the presence of a galaxy at one point increases the probability of finding another galaxy nearby), as measured in works on galaxy clustering (for example: Zehavi et al., 2005). A full treatment of the impact these factors would have on the true likelihood of galaxy catalogs is beyond the scope of this work. The cosmological principle approximation applied to Equation 2.2 implies that:

$$\begin{aligned}\ln(P_{\text{catalog}}) = \sum_i \Big[& n_i \ln\left(S_i \Phi_i \, \mathrm{d}L_i \, \mathrm{d}V_i\right) - \ln(n_i!) \\ & - S_i \Phi_i \, \mathrm{d}L_i \, \mathrm{d}V_i \Big] , \end{aligned} \tag{2.3}$$

where P_{catalog} is the probability of observing the catalog of galaxies in the bins being summed over.

Taking the limit that the space-luminosity boxes are small enough that all n_i are either 0 or 1 reduces the first term of the sum to be only over those boxes where a galaxy was observed, the second term vanishes, and the third term becomes an integral. Also trading the probability, P_{catalog}, for a likelihood, $\mathcal{L}_{\text{catalog}}$, gives the penultimate form of the maximum likelihood estimator:

$$\begin{aligned}\ln(\mathcal{L}_{\text{catalog}}) = & \sum_i \ln\left(S(L_i, \vec{x}_i) \, \Phi(L_i,\, z_i)\right) \\ & - \int S(L, \vec{x}) \, \Phi(L,\, z) \, \mathrm{d}L \, \mathrm{d}V. \end{aligned} \tag{2.4}$$

In the sharply cutoff step function completeness limit, that is $S(L, \vec{x})$ takes on one of two constant values, 0 and s, Equation 2.4 becomes identical to the estimator from Marshall et al. (1983).

The next refinement to the estimator is to isolate the normalization of Φ. That is, if $\Phi = \phi_\star \Phi_0(L, z)$, then the likelihood splits into a maximum likelihood estimate for $\phi_\star$ and a likelihood for Φ_0:

$$\phi_\star = \frac{N}{\int S(L, \vec{x})\, \Phi_0(L,\, z)\, \mathrm{d}L\, \mathrm{d}V}, \text{ and} \tag{2.5}$$

$$\ln(\mathcal{L}_{\text{catalog}}) = \sum_i \ln\left(\frac{S(L_i, \vec{x}_i)\, \Phi_0(L_i,\, z_i)}{\int S(L, \vec{x})\, \Phi_0(L,\, z)\, \mathrm{d}L\, \mathrm{d}V}\right), \tag{2.6}$$

where N is the total number of galaxies in the catalog, and terms that in the sum that do not depend on the parameters in Φ are dropped as irrelevant. If the selection function, $S(L_i, \vec{x}_i)$, depends only on the observed flux and the differing effect of cosmological redshifting on galaxies with different SEDs is not significant, then Equation 2.6 becomes identical to the estimator in Sandage et al. (1979), called the STY estimator for the authors of the paper.

The original definition of the estimator given in Sandage et al. (1979) handled incompleteness in a similar way to what we do here, with a more simplified model for it. Some time between the review by Binggeli et al. (1988) and the work of Efstathiou et al. (1988b) the handling of incompleteness changed to weighting the terms of the log-likelihood sum by the inverse of the selection function, as described in Equation 27 of the review of Johnston (2011). Weighting terms in a likelihood estimator with real valued scalars is identical to placing those same scalars into the exponents of the product of the likelihoods. This can make a certain amount of intuitive sense, if the weighting is viewed as correcting the number of observations at each point to be what would have been observed were the data set complete.

The problem with viewing the use of weights in the sum of log-likelihoods as correcting the data is that it does not model the statistical behavior of the completeness corrected data, making estimates based on the weighted sum not likelihoods. While a general demonstration for any binned data set of independent and identically distributed data is possible, the steps are fundamentally the same as if we consider a single Poisson distributed quantity, n, with mean $s\lambda$. In this case, the completeness corrected data, n/s, will have mean λ and variance λ/s. Just dividing the log-likelihood by s, as described, treats n/s as though it were Poisson distributed with mean and variance λ. Figure 2.1 shows a comparison between the distribution of a Poisson distributed quantity, n, with $\lambda = 4.5$ and $s = 0.75$ in comparison with how the weighted log-likelihood behaves with n and a Gaussian with matching mean and variance. A detailed analysis of how getting the variance, and all higher order moments, wrong affects the performance of the estimator is beyond the scope of this work, however it is not a stretch to say that using a distribution that gets the mean right but the variance wrong is an approximation that is not even Gaussian level, which gets the mean and variance right, and therefore likely to exhibit a greater bias than a correct likelihood treatment is. It is worth noting that we are not claiming that working with completeness corrected data is not possible, just that doing so should be limited to cases where the number of objects pre-correction in each bin is large enough that the bin's distribution can be approximated with a Gaussian (the limit where χ^2 statistics are a good approximation), permitting correct treatment of both the bin's mean and variance.

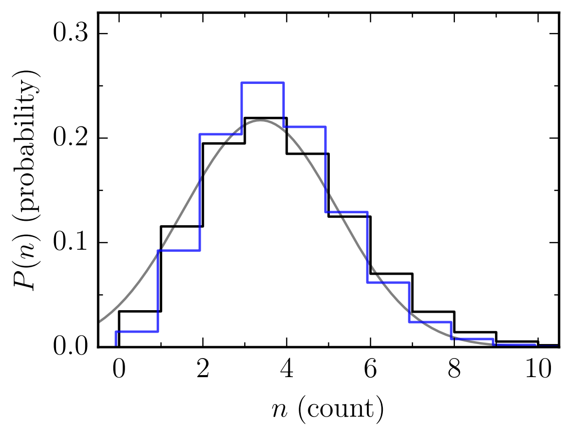

Figure 2.1: Comparison of the distribution of a true Poisson variable (black histogram) to a "completeness corrected" version that has the same mean (blue histogram, offset left) and a Gaussian distribution with matching mean and variance (grey line). The black line has mean $\lambda = 4.5$ and completeness $s = 0.75$, for a combined mean of 3.375. The blue line is the result of taking the formula for a Poisson distributed variable, $P(n) = \lambda^n \mathrm{e}^{-\lambda}/n!$, completeness correcting it with $n \to n/s$, and normalizing the distribution to sum to unity. The blue distribution, which is what current completeness correction techniques implicitly use, is narrower than the black, underestimating the variance of the distribution. The Gaussian distribution with mean and variance 3.375 is provided to show that it more closely matches the black histogram than the blue one does.

The integral in Equations 2.4–2.6 is often only evaluable numerically. As long as the numerical integration only has to be performed once per calculation of $\mathcal{L}_{\mathrm{catalog}}$, and not for every term in the sum, then the computation is usually not too computationally expensive. With both of Equations 2.4 and 2.6, though, the selection function for a flux-limited sample will be different for each source because each source has a unique SED, thus requiring the numerical integral to be evaluated for each source in the catalog. It is the ability to avoid this burdensome calculation that makes the more advanced estimator derived in Section 2.2.2 useful.

2.2.2 The Spectro-Luminosity Functional, Ψ

The phenomenon of cosmological redshifting combined with the variety of galaxy SEDs complicates the process of translating flux selection limits into luminosity selection limits, even for a single band selected survey. In the absence of redshifting, a sharp cut along a straight line in a flux-distance graph translates into a curved line in a luminosity-distance graph, but the sharpness of the cut boundary is unaffected. If all galaxies had the same SED, then the statement in the previous sentence would be unmodified because it would just mean that the boundary curve would have a different shape. For any real collection of galaxies, though, each galaxy has a different SED, making the relationship between flux and luminosity for galaxies overall effectively statistical. Figure 2.2 illustrates a simplified situation in which the fundamental mechanisms are the same: a cut in one variable imposes a smoothly varying completeness in a correlated variable. It is, therefore, necessary to model the distribution of the variety of galaxy SEDs to accurately reproduce the selection function needed by the maximum likelihood estimator.

The straightforward approach to modeling the distribution of SEDs is to generalize the concept of the luminosity function beyond a density of galaxies per unit luminosity, as measured by a single detector, to the density of galaxies per unit volume in the space of possible SEDs, that we are calling Ψ. One advantage of this approach is that it provides a universal intermediate form between models that predict the distribution of galaxy SEDs and all of the different histograms astronomers construct from galaxy luminosities and fluxes (especially: luminosity functions and color-magnitude diagrams). Most importantly, because those predicted histograms are all constructed from the same intermediate, data from disparate surveys with different selection criteria can feed information back into the theory's parameters in a consistent way.

This section takes the following approach: define Ψ and its relation to the standard LF, construct the part of Ψ that extends beyond Φ using a Gaussian approximation, and define an approximation for the Gaussian's parameters using SED templates to reduce the parameters from full functions to matrices.

The full details of how probability densities of functions are handled can be found in some texts on functional analysis, or any text on quantum mechanics or quantum field theory that covers the path integral approach (for example: Peskin & Schroeder, 2007). In a broad sense, the calculus of functions is the same as ordinary vector calculus because a function is as an element of a vector space; the only distinguishing feature is that a limit as the number of dimensions approaches infinity is implicitly taken.

The definition of Ψ begins similarly to the definition of Φ given in the previous section. The mean number of galaxies within a function space volume, $[\mathcal{D}L_\nu]_i$, of the SED $L_\nu(\nu)$, and within a real space volume $\mathrm{d}V_i$ of $\vec{x}_i$ is given by:

$$\langle n \rangle = \Psi[L_\nu](z_i) \cdot \mathrm{d}V_i \cdot [\mathcal{D}L_\nu]_i, \tag{2.7}$$

where the square braces denote that Ψ is a functional of L_ν and the parentheses denote that it is an ordinary function of z_i. A non-rigorous illustration of a density over function space, the concept embodied in Equation 2.7, can be found in Figure 2.3. The lack of specificity in defining what is meant by a "function space volume" is actually reflective of the current state of the field of functional integration (see, for example: Cartier & DeWitt-Morette, 2000; Nakahara, 2003; Zinn-Justin, 2009; Albeverio & Mazzucchi, 2011, and references therein).

The relationship between $\Psi[L_\nu](z)$ and $\Phi(L, z)$ is a marginalization (that is, summing over irrelevant degrees of freedom):

$$\Phi(L, z) = \int [\mathcal{D}L_\nu]\, \delta\left(L - \int L_\nu(\nu) w(\nu, z)\, \mathrm{d}\nu\right) \Psi[L_\nu](z), \tag{2.8}$$

where $w(\nu, z)$ is a weighting function that, through its units and form, defines what the symbol L means, and $\delta(x)$ is the Dirac delta function. For example, if the weighting function depends on redshift in the following way then L is an observer frame flux ready for conversion to a magnitude:

$$w(\nu, z) = \frac{(1+z)\,\nu^{-1}\,R(\nu/[1+z])}{4\pi D_L(z)^2 \int R(\nu)\,F_{\nu,\mathrm{std}}(\nu)\,\nu^{-1}\,\mathrm{d}\nu}, \tag{2.9}$$

where $F_{\nu,\mathrm{std}}(\nu)$ is a flux SED of some standard source, $D_L(z)$ is the luminosity distance, and $R(\nu)$ is the relative detector response to a photon with observer frame frequency ν. As the example equation suggests, the weight functions are meant as a generalization of detector responses, regardless of whether the response is: narrow, as it is for a pixel in a spectrograph; broad, as for an imaging filter; or fully bolometric. Performing similar marginalizations with multiple different weighting functions can produce any color-magnitude diagram, up to a change of variables and application of a selection function, in observer frame or rest frame quantities.

2.2.3 Ψ in Gaussian Approximation

The use of the calculus of functions makes Ψ extremely general and powerful conceptually, however concrete predictions require a projection down from a density over infinite-dimensional function space to one over a finite number of dimensions (a process called marginalization in statistics). The algorithms for doing this numerically for the general case are computationally intensive (see, for example, the field of study known as lattice quantum chromodynamics), so it is important to find a form for Ψ that can be marginalized analytically. To begin with, in order to make the form of Ψ consistent with what is already known about Φ, it is useful to use the ratio of Ψ and Φ to define the conditional likelihood functional of the SED ($\mathcal{L}_{SED}$):

$$\Psi[L_\nu](z) = \mathcal{L}_{\mathrm{SED}}\left[\hat{\Pi}_\perp L_\nu\right](.|L, z) \times \Phi(L, z), \tag{2.10}$$

where $\mathcal{L}_{\mathrm{SED}}\left[\hat{\Pi}_\perp L_\nu\right](.|L, z)$ symbolizes that $\mathcal{L}_{\mathrm{SED}}$ is a functional of the random function $\hat{\Pi}_\perp L_\nu$ and a function of the non-random variables L and z, with the dot there as a placeholder because there are no random scalars on which $\mathcal{L}_{\mathrm{SED}}$ depends. $\hat{\Pi}_\perp$ is an operator that adjusts the SED, L_ν, to satisfy one or more constraints equations of the form:

$$\int \left[\hat{\Pi}_\perp L_\nu\right](\nu) \times w(\nu, z)\,\mathrm{d}\nu = L. \tag{2.11}$$

When there is a single constraint, $\hat{\Pi}_\perp$ can be constructed as a normalization of the SED:

$$\hat{\Pi}_\perp L_\nu \equiv L \frac{L_\nu}{\int L_\nu(\nu)\,w(\nu)\,\mathrm{d}\nu}. \tag{2.12}$$

This is not the only way to define $\hat{\Pi}_\perp$. Factors that affect the form of $\hat{\Pi}_\perp$ include: the number of constraints, whether the weight functions overlap, and whether it is important to maintain the non-negativity of the allowed SEDs. If the form of $\mathcal{L}_{\mathrm{SED}}$ assigns sufficiently low likelihood to un-physically negative SEDs, and all of the weight functions are linearly independent, for example, it is possible to treat L_ν as a vector and construct $\hat{\Pi}_\perp$ as a linear projection operator by performing Gramm-Schmidt orthogonalization on the weight functions.

A more accurate form of $\mathcal{L}_{\mathrm{SED}}$ is derivable using the star formation history of the universe, stellar population synthesis models, dust models, active galactic nuclei (AGN) accretion history models, and some description of the density fluctuations in the universe. The last is important because galaxies with red SEDs, indicating "quiescent" star formation, are typically found in higher density environments than galaxies with the optically blue SEDs that indicate active star formation, so density fluctuations will affect the spread of possible SEDs and balance of red and blue types. This work avoids those complications by just approximating $\mathcal{L}_{\mathrm{SED}}$ as a single Gaussian functional, with the understanding that the approximation can be improved by either combining multiple Gaussians in $\mathcal{L}_{\mathrm{SED}}$ or summing over different luminosity functionals for different types of galaxy (for example, $\Psi_{\mathrm{overall}} = \Psi_{\mathrm{AGN}} + \Psi_{\mathrm{red}} + \Psi_{\mathrm{blue}}$). Explicitly, let $w_0(\nu)$ be the weight function that defines the rest frame luminosity that is the argument of Φ, and $\ell_\nu \equiv L_\nu / \int L_\nu w_0\,\mathrm{d}\nu$, then:

$$\begin{aligned}\mathcal{L}_{\mathrm{SED}}[\ell_\nu] = &\frac{\mathcal{N}}{\sqrt{\mathrm{Det}[\Sigma]}}\\ &\cdot \exp\left(-\frac{1}{2}\int \mathrm{d}\nu\,\mathrm{d}\nu'\,[\ell_\nu(\nu) - \mu_\nu(\nu)]\,\Sigma^{[-1]}(\nu,\nu')\,[\ell_\nu(\nu') - \mu_\nu(\nu')]\right).\end{aligned} \tag{2.13}$$

$\mu_\nu(\nu)$ is the mean of the normalized SEDs, $\Sigma(\nu, \nu')$ is the covariance of normalized SEDs, and $\mathcal{N}$ is a normalization factor with a form that depends on the details of how the function space is parametrized. If the functions are approximated with M boxcars, for example, $\mathcal{N} = (2\pi)^{-M/2}$. $\Sigma^{[-1]}(\nu, \nu')$ is the functional inverse of $\Sigma(\nu, \nu')$, that is it satisfies: $\int \Sigma(x, y)\Sigma^{[-1]}(y, z)\, \mathrm{d}y = \delta(x - z)$. Perhaps the most familiar example of a functional inverse in physics is that of the negative Laplacian operator $(-\nabla^2)$, called its Green's function, given by: $G(\vec{r}, \vec{r}') = 1/(4\pi|\vec{r} - \vec{r}'|)$. Another example specifically from astronomy is implicitly used in the process of image deconvolution; it is formally the same as treating the image's point spread function as the kernel of a linear operator and finding, approximately, that operator's inverse.

It may seem like using a single Gaussian for $\mathcal{L}_{\rm SED}$ is too great an approximation because it cannot produce the most prominent structures seen in color-magnitude diagrams of galaxies: the "red sequence" and "blue cloud". Doing so is equivalent to a standard practice of performing a single LF fit to all of the data to produce an overall LF (for example: Efstathiou et al., 1988b; Loveday, 2000; Cole et al., 2001; Kochanek et al., 2001; Blanton et al., 2003b; Bell et al., 2003; Jones et al., 2006; Babbedge et al., 2006; Cirasuolo et al., 2007; Dai et al., 2009; Smith et al., 2009; Montero-Dorta & Prada, 2009; Loveday et al., 2012; Cool et al., 2012). A further level of refinement is usually, but not always, included where the galaxies are broken down by type (most frequently: early/red "quiescent" galaxies, late/blue "star forming" galaxies, and AGN). This would be equivalent to treating Ψ as the sum of three spectro-luminosity functionals that each have one Gaussian in $\mathcal{L}_{\rm SED}$.

The mean of the normalized SEDs, μ_ν, is required to compute the spectral comoving luminosity density (CLD) of the cosmos, ρ_{L_ν}; it is

$$\begin{aligned} \rho_{L_\nu}(\nu) &= \int [\mathcal{D}L_\nu]\, L_\nu\, \Psi[L_\nu](z) \\ &= \mu_\nu(\nu) \int L\, \Phi(L, z)\, \mathrm{d}L. \end{aligned} \tag{2.14}$$

If μ_ν depends on luminosity, as is allowed, then it will be inside the integral.

Returning to the derivation of an LF estimator from Equation 2.13, the Gaussian form of $\mathcal{L}_{\rm SED}$ and the linearity of detectors makes the transition from function space to a finite number of bandpass fluxes and luminosities an exercise in linear algebra that introduces no new approximations. If there are K luminosities/fluxes of interest, defined by weighting functions $w_k(\nu, z)$ with $k = 1 \ldots K$, then:

$$\mathcal{L}_{\mathrm{SED}}(\{\ell_k\}) = \frac{1}{\sqrt{(2\pi)^K \det(\Sigma)}} \cdot \exp\left(-\frac{1}{2}\sum_{i,j=1}^{K}[\ell_i - \mu_i][\Sigma^{-1}]_{ij}[\ell_j - \mu_j]\right), \tag{2.15}$$

where $\ell_k \equiv \int \ell_\nu(\nu) w_k(\nu, z)\,\mathrm{d}\nu$, $\mu_k \equiv \int \mu_\nu(\nu) w_k(\nu, z)\,\mathrm{d}\nu$, $\Sigma_{ij} \equiv \int \Sigma(\nu, \nu') w_i(\nu, z) w_j(\nu', z)\,\mathrm{d}\nu\,\mathrm{d}\nu'$, and projecting down from function space to this K-dimensional space has transformed the functional determinant and inverse into ordinary matrix ones. Equation 2.15 works as long as all of the weighting functions, $w_k(\nu, z)$, are linearly independent functions.

Equation 2.13 is an approximation because physical SEDs are all non-negative, and the Gaussian form in the equation does not exclude un-physically negative ones. That constraint could have been satisfied by choosing a log-Normal form for the distribution instead of Gaussian, but then the projection into a subspace using a set of weighting functions becomes only possible in terms of spectral quantities, that is $w_k \propto \delta(\nu - \nu_k)$. As long as the value of the mean exceeds the standard deviation by enough, for example $\mu_\nu(\nu) > 2\sqrt{\Sigma(\nu, \nu)}$, for all relevant frequencies the approximation should be accurate enough. Finding a more correct form for $\mathcal{L}_{\mathrm{SED}}$ that satisfies this constraint without approximation is left for future work.

2.2.4 Approximating the Mean and Variance of SEDs Using Templates

In principle, μ_ν and Σ can be measured directly using the population mean and covariance of directly observed, normalized, spectra:

$$\mu_\nu(\nu) \approx \frac{1}{N}\sum_{i=1}^{N} \ell_{\nu,i}(\nu) \equiv \overline{\ell_\nu}(\nu), \text{ and}$$
$$\Sigma(\nu, \nu') \approx \frac{1}{N-1}\sum_{i=1}^{N}(\ell_{\nu,i}(\nu) - \overline{\ell_\nu}(\nu))(\ell_{\nu,i}(\nu') - \overline{\ell_\nu}(\nu')). \tag{2.16}$$

If sufficient high resolution spectroscopic data were available to actually measure μ_ν and Σ as functions, then it would not be necessary to construct Ψ to measure Φ, as Φ could be measured directly. It is, therefore, necessary to further approximate the galaxy SEDs as a sum over a set of templates, for example the four templates of Assef et al. (2010). If there are N_{T} templates in the set with SEDs $\tilde{\ell}_{\nu,a}$, then under the template approximation for each galaxy $\ell_{\nu,i}(\nu) \approx \sum_{a=1}^{N_{\mathrm{T}}} f_{ai}\, \tilde{\ell}_{\nu,a}(\nu)$. Applying the template approximation to Equations 2.16 yields:

$$\begin{aligned} \mu_\nu(\nu) &\approx \sum_{a=1}^{N_{\mathrm{T}}} \overline{f_a}\, \tilde{\ell}_{\nu,a}(\nu), \text{ and} \\ \Sigma(\nu,\nu') &\approx \sum_{a,b=1}^{N_{\mathrm{T}}} \mathrm{cov}(f_a, f_b)\, \tilde{\ell}_{\nu,a}(\nu)\, \tilde{\ell}_{\nu,b}(\nu'), \end{aligned} \tag{2.17}$$

where $\overline{f_a}$ and $\mathrm{cov}(f_a, f_b)$ are a vector and matrix of parameters, respectively. It is worth reiterating that $\tilde{\ell}_{\nu,a}$ are the normalized template spectra, and f_{ai} is the fraction of luminosity contributed by template a to the w_0 band pass for the galaxy identified by index i.

It is possible to include the parameters in Equations 2.17, $\overline{f_a}$ and $\mathrm{cov}(f_a, f_b)$, with the others when fitting the LF to data. Doing so greatly increases the number of free parameters in the fit, however, with $N_T - 1$ degrees of freedom in $\overline{f_a}$ and $(N_T - 1)(N_T - 2)/2$ degrees of freedom in $\mathrm{cov}(f_a, f_b)$, consistent with the normalization condition on the luminosity fractions. It is, therefore, worth it to fix these parameters separately from the measurement of the luminosity function, if possible.

The final form of the LF likelihood to be used in Chapter 6 can now be written down by combining Equations 2.4, 2.10, and 2.15:

$$\begin{aligned} \ln(\mathcal{L}) = &\sum_{\text{galaxies}} \ln\left(S(F_{\mathrm{sel}}, F_0, \vec{x})\mathcal{L}_{\mathrm{SED}}(F_{\mathrm{sel}}, F_0|L_0)\Phi(L_0, z)\right) \\ &- \int S(F_{\mathrm{sel}}, F_0, \vec{x})\mathcal{L}_{\mathrm{SED}}(F_{\mathrm{sel}}, F_0|L_0)\Phi(L_0, z)\, \mathrm{d}F_{\mathrm{sel}}\, \mathrm{d}F_0\, \mathrm{d}L_0\, \mathrm{d}V_c, \end{aligned} \tag{2.18}$$

where F_0 is the observer frame flux K-corrected to L_0, L_0 is the luminosity corresponding to w_0, $\vec{x}$ is the position in space of the galaxies, and F_{sel} is the flux which was used to select redshift survey targets, assuming it is not the same as F_0. While the selection function, $S(F_{\mathrm{sel}}, F_0, \vec{x})$, can be smooth, it is useful to approximate it as flat where it is non-zero, uniform on the sky within the boundary of the survey, and confined to any appropriate redshift limits.

The explicit form of $\mathcal{L}_{\text{SED}}$ can be derived from Equation 2.15:

$$\begin{aligned} \mathcal{L}_{\text{SED}}(F_{\text{sel}}, F_0|L_0) &= \frac{\mathrm{e}^{\tau_1+\tau_2}}{\sqrt{(2\pi)^2 \det(\sigma)}} \cdot \left(\frac{4\pi D_L(z)^2}{(1+z)L_0}\right)^2 \\ &\quad \cdot \exp\left(-\frac{1}{2}\sum_{i,j=1}^{2} [\ell_i - \mu_i]\,[\sigma^{-1}]_{ij} \cdot [\ell_j - \mu_j]\right), \text{ and} \\ \ell_i &= \frac{F_i 4\pi D_L(z)^2 \mathrm{e}^{\tau_i}}{(1+z)L_0}, \end{aligned} \tag{2.19}$$

where τ_i is the optical depth of foreground dust and gas extinction toward the target galaxy. When numerically computing $\mathcal{L}_{\text{SED}}$ it is important that the matrix σ in Equation 2.19 is invertable. A simple model for the noise to signal ratio in the observed fluxes, F_i, added to the diagonal entries of Σ_{ij} suffices for this purpose (no Einstein summation is assumed):

$$\sigma_{ij} = \Sigma_{ij} + \left(\delta_{ij} A_i F_i^{B_i} + \sigma_{\tau\,i}\sigma_{\tau\,j}\right)\mu_i\mu_j, \tag{2.20}$$

where A and B are noise model parameters derived from an ordinary least squares fit of $\ln(\sigma_F^2 F^{-2})$ to $\ln(F)$, that is a log-space fit of the squared noise-to-signal ratio to the log of the observed flux. While more realistic models incorporate multiple sources of noise, like the background or positional jitter, a single power law is often sufficient since the color covariance, Σ_{ij}, is the dominant contribution to σ_{ij} at most redshifts. $\sigma_{\tau\,i}$ is a way of including the impact of differences in foreground dust and gas obscuration over the survey field, if the survey was targeted on fluxes that were not extinction corrected; specifically, it is the standard deviation of the dust optical depth of the Milky Way for targets in the survey if selection was based on pre-extinction corrected fluxes. The form of the $\sigma_{\tau\,i}$ contribution to the matrix is set by the fact that each direction has a single $\mathrm{E}(B-V)$ that each τ_i is proportional to in the extinction model of Cardelli et al. (1989), so the uncertainties at different wavelengths are correlated.

The effective selection function in redshift-luminosity space, the $S(L, z)$ from Section 2.2.1, is directly derivable from $\mathcal{L}_{\text{SED}}$ as:

$$S(L, z) = \int S(F_{\text{sel}}, F_0, \vec{x})\ \mathcal{L}_{\text{SED}}(F_{\text{sel}}, F_0|L)\,\mathrm{d}F_{\text{sel}}\,\mathrm{d}F_0. \tag{2.21}$$

It is to avoid evaluating the integrals in Equation 2.21 numerically for every different galaxy in a survey that Equation 2.4 is not recommended as the best LF likelihood estimator.

It is also arguable that rest frame luminosities, L_0, are not actually directly observable outside of a narrow range of redshifts. In that light, the expression of the LF likelihood is:

$$\ln(\mathcal{L}) = \sum_i \ln(\rho_n(\vec{F}_i, z_i)) - \int \rho_n(\vec{F}, z)\,\mathrm{d}^M F\,\mathrm{d}V$$
$$\rho_n(\vec{F}, z) \equiv S(\vec{F}, z) \int \mathcal{L}_{\mathrm{SED}}(\vec{F}|L, z)\ \Phi(L, z)\,\mathrm{d}L. \tag{2.22}$$

This has all of the computational load drawbacks of Equation 2.21. It also has the problem that the normalizing integral, the integral over $\mathrm{d}^M F$, is an integral in a high dimensional space over a finite box, and that further slows numerical performance, even for a Gaussian function.

2.2.5 Binned Luminosity Function Estimators

The three most popular binned estimators for the LF are: $1/V_{\max}$ (Schmidt, 1968), step-wise maximum likelihood (SWML) (Efstathiou et al., 1988a), and C^- (Lynden-Bell, 1971). C^- is built around estimating the cumulative luminosity function, $\int_L^\infty \Phi(s, z)\,\mathrm{d}s / \int_{L_0}^\infty \Phi(s, z)\,\mathrm{d}s$, and does not recover the normalization. SWML is based on the STY version of the likelihood, and ends up with correlated errors between the bins from the technique used to recover Φ's normalization. The $1/V_{\max}$ estimator has very well explored drawbacks, sensitivity to clustering (Takeuchi et al., 2000), and trouble near the luminosity limits (Page & Carrera, 2000).

Miyaji et al. (2001) proposed an estimator they named $N^{\mathrm{obs}}/N^{\mathrm{mdl}}$:

$$\Phi(L_i, z_i) = \Phi^{\mathrm{mdl}}(L_i, z_i) \cdot \frac{N_i^{\mathrm{obs}}}{N_i^{\mathrm{mdl}}}, \tag{2.23}$$

where $\Phi(L_i, z_i)$ is the value of the LF in L-z bin i, "mdl" is short for "model," Φ^{mdl} is an approximate LF model, N_i^{mdl} is the expected number of observations in bin i according to approximate model LF Φ^{mdl}, and N_i^{obs} is the number of objects observed to be in bin i. Miyaji et al. (2001) did not include a derivation of this estimator, so one follows here, including some refinements.

The definition of the luminosity function implies that the mean number of galaxies in a bin is:

$$\langle N_i \rangle = \int_{\text{bin}} S(L,z)\Phi(L,z)\,\mathrm{d}L\,\mathrm{d}V. \tag{2.24}$$

The weighted mean value theorem implies that:

$$\Phi(L',z') = \frac{\langle N_i \rangle}{\int_{\text{bin}} S(L,z)\,\mathrm{d}L\,\mathrm{d}V}, \tag{2.25}$$

for some (L',z') in the L-z bin where the selection function, S, is non-zero. The maximum likelihood estimator for $\langle N_i \rangle$ is the observed number, N_i (if the N_i are Poisson distributed), thus:

$$\Phi(L',z') = \frac{N_i}{\int_{\text{bin}} S(L,z)\,\mathrm{d}L\,\mathrm{d}V}. \tag{2.26}$$

In the approximation that (L',z') is at the center of the box and S is a step function, Equation 2.26 is the estimator from Page & Carrera (2000), which corrects for the near luminosity limits problems of the $1/V_{\text{max}}$ estimator. Recovering the $1/V_{\text{max}}$ estimator requires (in order): making the step function S approximation, making the bins infinitesimally thin in the luminosity direction, and finally binning infinitesimal luminosity bins back down into the coarse bins desired, yielding (for log-space binning):

$$\Phi(L_i,z_i) = \frac{1}{S(L_i,z_i)L_i\Delta\ln L_i}\sum_j \frac{1}{\Delta V_j}, \tag{2.27}$$

where j runs over objects in bin i, $\Delta V_j \equiv V(z_{\text{hi}}) - V(z_{\text{lo}})$, z_{hi} is the smaller of the upper redshift of the bin and z_{max}, the maximum redshift at which the galaxy is observable, and similar in the opposite sense for z_{lo}. ΔV_j is called V_a, for volume available, in Avni & Bahcall (1980).

The $N^{\text{obs}}/N^{\text{mdl}}$ estimator of Miyaji et al. (2001) comes from using an approximate model for the LF, Φ^{mdl}, to correct the estimate from Equation 2.26 from being accurate at some unknown point in the bin to being an estimate of Φ at the center of the bin. This process is formally identical to how flux corrections for different SED shapes in astronomy are done:

$$\begin{aligned}\Phi(L_i,z_i) &= \frac{\Phi^{\text{mdl}}(L_i,z_i)}{\Phi^{\text{mdl}}(L',z')}\cdot\frac{N_i}{\int_{\text{bin}} S(L,z)\,\mathrm{d}L\,\mathrm{d}V},\\ &= \Phi^{\text{mdl}}(L_i,z_i)\cdot\frac{N_i}{\langle N_i^{\text{mdl}}\rangle},\end{aligned} \tag{2.28}$$

where the second line undoes the weighted mean value theorem.

The downside of the $N^{\mathrm{obs}}/N^{\mathrm{mdl}}$ estimator, which can also be described as a corrected Poisson estimate, is that there is some dependence on the model LF introduced by the correction. A detailed exploration of this sensitivity is beyond the scope of this work, but any model closer to the true LF than $\Phi^{\mathrm{mdl}} = \text{constant}$, the model implicitly assumed when approximating L' and z' as being at the center of the bin in Equation 2.26, will give improved results.

2.2.6 Error Analysis

The uncertainties in the binned estimators can be estimated using propagation of errors and the assumption that Poisson/shot noise describes all the variance:

$$\begin{aligned} \sigma^2_{1/V_{\max},\, i} &= \left(\frac{1}{L_i \Delta \ln L_i}\right)^2 \sum_j \frac{1}{(S_j \Delta V_j)^2}, \text{ and} \\ \sigma^2_{N^{\mathrm{obs}}/N^{\mathrm{mdl}},\, i} &= \left(\frac{\Phi_i^{\mathrm{mdl}}}{\langle N_i^{\mathrm{mdl}}\rangle}\right)^2 N_i. \end{aligned} \tag{2.29}$$

The formula for $\sigma^2_{1/V_{\mathrm{max,i}}}$ comes from doing propagation of errors in the process of binning down the estimate in the luminosity direction. Equations 2.29 underestimate the error because they do not account for a number of factors, including: cosmic variance, redshift uncertainties, or luminosity uncertainties (including the contribution from the variety of SED colors discussed in Chapter 3). How to handle these factors in the presence of smoothly varying selection functions is beyond the scope of this work.

2.3 Luminosity Function Parametrizations

For galaxies, the standard practice is to model the LF as a Schechter function:

$$\Phi(L, z) = \frac{\phi_\star(z)}{L_\star(z)} \left(\frac{L}{L_\star(z)}\right)^{\alpha} \mathrm{e}^{-L/L_\star(z)}. \tag{2.30}$$

This form for the LF was derived in Schechter (1976) under the assumption that galaxies build up in luminosity through a process of merging. While mergers are not the only way for galaxies to build up in luminosity, the function still works well empirically. Figure 2.4 contains an illustration of the shape the Schechter function takes, in log-log space, including labels for $L_\star$ and $\phi_\star$, and illustrations of how the shape changes when each of the parameters changes, as they would for evolution in time.

In principle all three of the parameters in Φ could evolve with z, but measuring the evolution in α requires data that is deep over a broad range of redshifts, so most works assume it is constant. For $L_\star$ and $\phi_\star$ the most frequently used parameterizations are those of Lin et al. (1999) ($L_\star \propto 10^{0.4Qz}$ and $\phi_\star \propto 10^{0.4Pz}$, with P and Q constants). While these parameterizations work fine in a small range of redshifts, they allow for unphysically unbounded evolution at high z. This work, therefore, introduces the following similar parameterizations in terms of $t_L(z)$, the lookback time at redshift z:

$$\begin{aligned} \phi_\star &= \phi_0 \mathrm{e}^{-R_\phi t_L(z)}, \text{ and} \\ L_\star &= L_0 \mathrm{e}^{-R_L t_L(z)} \left(1 - \frac{t_L(z)}{t_0}\right)^{n_0}, \end{aligned} \tag{2.31}$$

where R_ϕ is the density evolution rate, R_L is the luminosity evolution rate, n_0 is the initial luminosity index, and t_0 is the lookback time at which galaxies first lit up (some redshift between reionization and recombination). Given the definitions of the parameters, $L_\star(t_L = t_0) = 0$ is a boundary condition, requiring that $n_0 > 0$. Parametrizing $\phi_\star$ evolution in terms of lookback time also guarantees that it will remain finite for all redshifts regardless of whether R_ϕ is positive or negative. The addition of a power law to the evolution of $L_\star$ is inspired by the model of star formation rate (SFR) in individual galaxies used in Lee et al. (2010) and tested against simulations in Simha et al. (2014): $\mathrm{SFR}(t) \propto t \exp(-t/\tau)$, where t is measured from the onset of star formation.

One advantage of the form for $L_\star$ in Equation 2.31 is that the model now contains an estimate of where the big galaxies hit their peak luminosity, the redshift at which $L_\star$ has a maximum, $z_\star$:

$$t_L(z_\star) = t_0 + \frac{n_0}{R_L}. \tag{2.32}$$

Note that $L_\star$ only has a maximum at finite time if $R_L < 0$; when this condition is not met $L_\star$ increases without bound for all future time, putting the maximum at $z = -1$.

A graph of how our simple model for $L_\star(z)$ evolves with cosmological time can be found in Figure 2.5.

2.3.1 Derived LF Parameters

A number of physical quantities are derivable from the luminosity function. The first pair of such quantities are the density of galaxies brighter than some cutoff, the zeroth moment of the Luminosity function, and its specific rate of change:

$$n_g(L > L_{\min}) = \int_{L_{\min}}^{\infty} \Phi(L, z)\, \mathrm{d}\, L, \text{ and} \tag{2.33}$$

$$R_n \equiv -\frac{\partial \ln(n_g)}{\partial t_L}, \tag{2.34}$$

respectively. But for the low luminosity cutoff, necessary to make n_g finite, both quantities would be universal; that is, independent of the bandpass they are measured in. Because R_n depends only weakly on the parameter $L_{\min}/L_\star$ (small for most redshifts), it is approximately universal, making it extremely useful to compare measurements of LF evolution regardless of which luminosity was used in the measurement.

For a general Schechter function n_g and R_n are:

$$n_g = \phi_\star \Gamma\left(\alpha + 1, \frac{L_{\min}}{L_\star}\right), \text{ and} \tag{2.35}$$

$$\begin{aligned} R_n = &-\phi_\star^{-1}\frac{\partial \phi_\star}{\partial t_L} - \left(\frac{\left[\frac{L_{\min}}{L_\star}\right]^{\alpha+1} \mathrm{e}^{-L_{\min}/L_\star}}{\Gamma\left(\alpha+1,\, \frac{L_{\min}}{L_\star}\right)}\right) L_\star^{-1}\frac{\partial L_\star}{\partial t_L} \\ &- \left(\frac{\int_{L_{\min}/L_\star}^{\infty} x^\alpha \ln(x)\, \mathrm{e}^{-x}\, \mathrm{d}x}{\Gamma\left(\alpha+1,\, \frac{L_{\min}}{L_\star}\right)}\right)\frac{\partial \alpha}{\partial t_L} \\ \approx &-\phi_\star^{-1}\frac{\partial \phi_\star}{\partial t_L} + \min\left(\alpha+1,\, 0\right) L_\star^{-1}\frac{\partial L_\star}{\partial t_L} \\ &- \left(\left[\ln\left(\frac{L_{\min}}{L_\star}\right) - \frac{1}{\alpha+1}\right]\Theta(-\alpha-1) \right. \\ &\left. + \psi^{(0)}(\alpha+1)\Theta(\alpha+1)\right)\frac{\partial \alpha}{\partial t_L}, \end{aligned} \tag{2.36}$$

where $\Gamma(a, z)$ is the (upper) incomplete gamma function, $\psi^{(0)}(x)$ is the digamma function, and $\Theta(x)$ is the unit step function (Heaviside). As long as α is (nearly) constant, and

$L_{\min} \ll L_\star$, the band dependence of R_n is vanishingly small, making R_n universal at most times. The time when the universality of R_n fails is at early times (high redshifts near reionization) when $L_\star$ is near $L_{\min}$. For the parametrization defined here, and the one defined in Lin et al. (1999), respectively:

$$R_n = R_\phi - \min(1+\alpha, 0)\left[R_L + \frac{n_0}{t_0 - t_L}\right], \text{ and} \tag{2.37}$$

$$R_n = -\frac{2}{5}\ln(10)\left(P - \min(1+\alpha, 0)Q\right)\frac{\mathrm{d}\,z}{\mathrm{d}\,t_L}. \tag{2.38}$$

For the purposes of fitting a LF to data in a Bayesian framework, it can be useful to make the substitution $R_n(0) = R_\phi - (1+\alpha)(R_L + n_0 t_0^{-1})$ to replace R_ϕ. This substitution is profitable because we have observed $R_n(0)$ to be less correlated with α and $L_\star$ than R_ϕ with real data sets.

The CLD, ρ_L, and its specific rate of change are defined as:

$$\rho_L = \int_0^\infty L\Phi(L, z)\,\mathrm{d}\,L, \text{ and} \tag{2.39}$$

$$R_\rho = -\frac{\partial \ln(\rho_L)}{\partial t_L}. \tag{2.40}$$

Applying the definitions to the Schechter function parametrization of Φ yields:

$$\rho_L = \phi_\star L_\star \Gamma(\alpha + 2), \text{ and} \tag{2.41}$$

$$R_\rho = -\phi_\star^{-1}\frac{\partial \phi_\star}{\partial t_L} - L_\star^{-1}\frac{\partial L_\star}{\partial t_L} - \psi^{(0)}(\alpha+2)\frac{\partial \alpha}{\partial t_L}, \tag{2.42}$$

where $\psi^{(0)}(x)$ is the digamma function. When further specialized to the parametrization defined here and the one from Lin et al. (1999), Equation 2.42 gives:

$$R_\rho = R_\phi + R_L + \frac{n_0}{t_0 - t_L}, \text{ and} \tag{2.43}$$

$$R_\rho = -\frac{2}{5}\ln(10)(P + Q)\frac{\mathrm{d}\,z}{\mathrm{d}\,t_L}, \tag{2.44}$$

respectively. The redshift at which the CLD hits a maximum, z_ρ, can also be found for the parametrization defined here by solving for z_ρ in the equation:

$$t_L(z_\rho) = t_0 + \frac{n_0}{R_\phi + R_L}. \tag{2.45}$$

Like with the Equation 2.32, existence of a solution at finite time to Equation 2.45 requires the assumption that the present CLD is decreasing, $R_\phi + R_L < 0$, with a maximum at $z = -1$ otherwise.

The third quantity of interest is closely related to to the flux counts density on the sky, $\mathrm{d}\,N/(\mathrm{d}\,F\,\mathrm{d}\,\Omega)$. It is a well known result that for an infinite Euclidean universe with a static LF that $\mathrm{d}\,N/(\mathrm{d}\,F\,\mathrm{d}\,\Omega) \propto F^{-5/2}$. It is possible to show that the constant of proportionality, here called $\kappa_\star$, can be calculated from the Schechter LF parameters:

$$\kappa_\star = \frac{\phi_\star L_\star^{3/2}}{\Omega_{\mathrm{sky}} 4\pi^{1/2}} \Gamma\left(\alpha + \frac{5}{2}\right), \tag{2.46}$$

as long as $L_\star$, α, and $\phi_\star$ are assumed constant.

The utility of parametrizing the LF in terms of $\kappa_\star$ is that, as the LF measurements in Chapter6 shows, real data constrains it more than $\phi_\star$, making it less correlated to the other parameters in the Schechter function. Further, when performing a Markov Chain Monte Carlo analysis of a model, it is important to have reasonable bounds for the parameters in the data to constrain the search space. For $\kappa_\star$, it is possible to produce a histogram of fluxes in log-log axes, weighted to remove the Euclidean power law slope $(-5/2)$ and the effects of redshift, and read off a reasonable range of values that $\kappa_\star$ can take. To remove the non-evolution effects of redshift it is sufficient to histogram the flux the source would have if the universe were static and Euclidean, $\tilde{F} \equiv L/(4\pi D_{\mathrm{cT}}^2(z))$, where $D_{\mathrm{cT}}(z)$ is the comoving distance transverse to the line of sight (also called D_M). $L_\star$ can be similarly constrained by visual inspection of luminosity histograms. The fundamental definition of $\phi_\star$, $\Phi(L_\star) \propto \phi_\star L_\star^{-1}$, means that the value of $\phi_\star$ is contingent on the value of other observables, and therefore less straightforward to read off a reasonable range from inspection of a graph.

The models produced here for the evolution of $L_\star$ and $\phi_\star$ have the advantage that they are computationally simple. While their form is based on improving the early cosmic time behavior of the models compared to the models of Lin et al. (1999), there is much room for improvement yet. The models in this chapter imply, for instance, that the long time CLD will exponentially decay to zero. This behavior conflicts with a lower bound on the rate at which the CLD can decrease implied by at least two stellar population synthesis models. Assuming that the CLD is already dominated by stars and not AGN, the fastest the CLD can decay is the rate it would drop if all star formation were to cease abruptly. Thus the CLD decay rate is bounded from below by the luminosity decay rate of a simple stellar population (SSP). Figure 2.6 shows the evolution of an SSP's absolute magnitude in two infrared bands that bracket $\lambda = 2.4\,\mu$m (2MASS K_s and *WISE* W1) with two different initial mass functions (Salpeter and Chabrier) from two different population synthesis models (Bruzual & Charlot, 2003; Maraston, 2005) as implemented by the EzGal software package (described in: Mancone & Gonzalez, 2012). The different combinations are not labeled because the details are not important here, only the overall trend that they all decay in luminosity like a power law (approximately $\propto t^{-1/2}$), which is much slower than an exponential decay.

2.4 Discussion

We summarize the commonly adopted luminosity function estimate processes, including the estimators from: Schmidt (1968), Sandage et al. (1979), Marshall et al. (1983), Page & Carrera (2000), and Miyaji et al. (2001). This work also introduces improvements to the luminosity function measuring process from the point of view of mathematical rigor, compatibility with the physical constraints implied by the current understanding of cosmology, and raw statistical performance (statistical orthogonality of parameters). While that last property is not demonstrated here, it will be apparent when the techniques defined here are applied to the real world data sets of Chapter 5 in Chapter 6. In particular, we will show that the cuts to the data sets necessary to render the selection functions approximately flat remove 27–81% of the data in the set, depending on how flat the selection function is required to be. Making such a cut is not sufficient to relieve the computational burden required to address the selection biases addressed in this work, however, because determining the shape of the flat region requires roughly the same effort on the part of the scientist analyzing the data.

We hope that the decision to present not just the final form of the estimator, but also its derivation, will make it easier for future users of these techniques to adapt them to their specific needs, and even to make improvements as computational techniques and hardware improve. Areas where there is significant room for improvement in the model include:

- the model does not yet make any allowance for the effect of clustering/cosmic variance,
- the model does not make allowance for the effects of finite galaxy size in relation to mergers,
- the model does not account for line of sight overlap, coincidental or otherwise (confusion and collision),
- the long time evolution of $L_\star$ and $\phi_\star$ defined here conflicts with the behavior of population synthesis models, and
- the Gaussian approximation for $\mathcal{L}_{\rm SED}$ restricts its applicability to a limited range of wavelengths where the standard deviation of the SED is less than its mean.

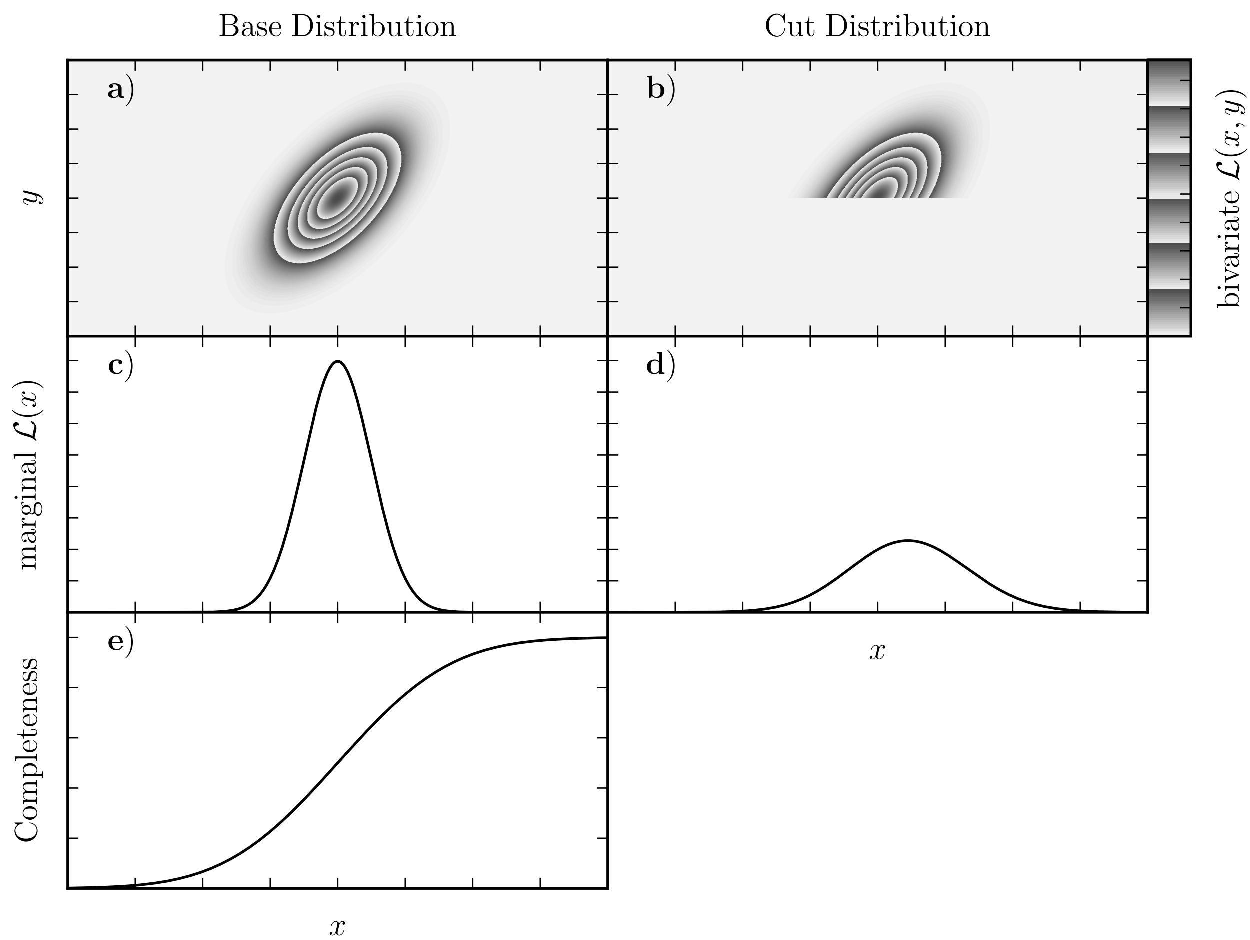

Figure 2.2: Illustration how a sharp cut on one variable imposes a blurred cut on a correlated variable. The relationships are simplified, but the concept is the same for the relationship between flux and luminosity with SED variability thrown in. Panel **a** contains the base, uncut, bivariate distribution in x and y. Panel **b** shows the same distribution as **a** with a cut imposed based on y with the same color scale. Panel **c** shows the projected (marginal) distribution in x obtained from integrating Panel **a** over all y. Panel **d** shows the projected (marginal) distribution in x obtained from integrating Panel **b** over all y on the same scale as Panel **c**. Panel **e** shows the completeness of the distribution in **d** with respect to the uncut distribution in **c** (the ratio of **d** over **c**).

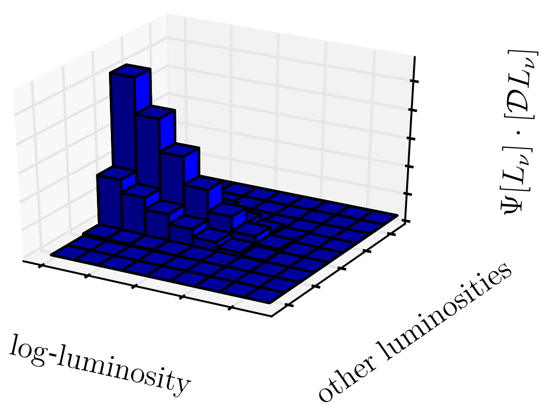

Figure 2.3: Cartoon illustrations of a function space density with the functions approximated by a sequence of N step functions. The x and y axes represent some measure of a galaxy's luminosity and all the other degrees of freedom in the SED, respectively. The value of $\Phi(L)\,\mathrm{d}\,L$ can be found by summing over the uncountably infinite number of axes hidden in the "other luminosities" axis.

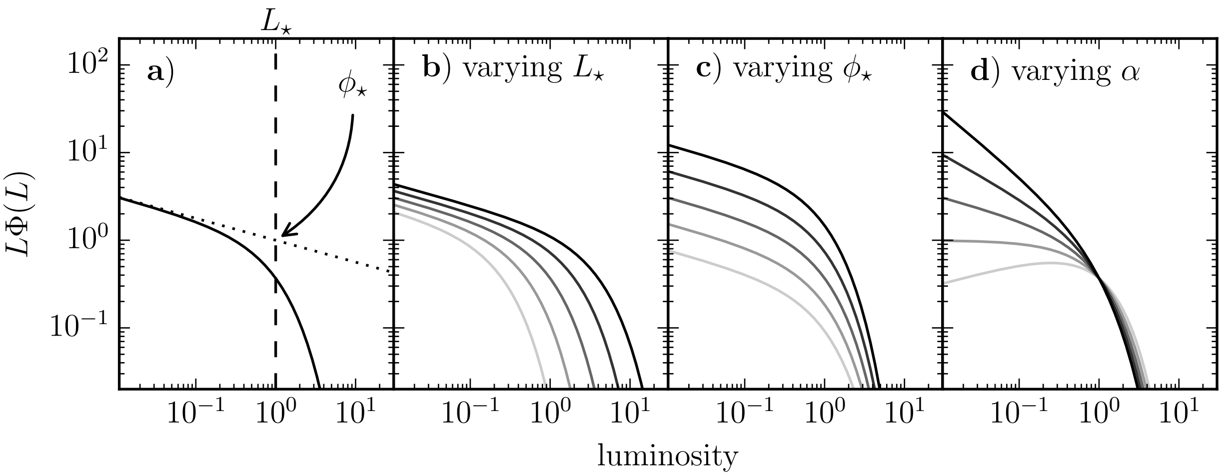

Figure 2.4: Illustrations of the shape of the Schechter function (times L) in log-log space, and how that shape changes as the parameters, $L_\star$, $\phi_\star$, and α, vary. Panel **a** is a labeled illustration with $L_\star = 1$, $\phi_\star = 1$, and $\alpha = -1.25$. The vertical dashed line shows $L_\star$, and the dotted line shows the faint end slope (asymptotic power law for faint luminosity, log-log slope in this graph is $\alpha + 1$) and how $\phi_\star$ is the y value of where the dashed and dotted lines intersect. Panels **b**–**d** show how the Schechter function changes with $L_\star$, $\phi_\star$, and α, respectively. The lines are increasingly dark with increasing magnitude of the parameter being varied.

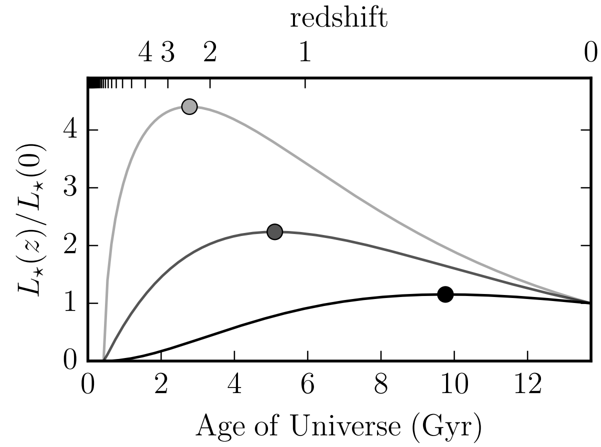

Figure 2.5: Illustration of how $L_\star$ evolves over cosmic time in the model introduced in this chapter. The value of R_L used is $-3t_H^{-1}$, the value of t_0 is the lookback time of the redshift of recombination ($z = 1088.16$), and the values of n_0 are 0.5, 1, and 2, in increasing darkness. The circular dots are placed at the time of peak $L_\star$ for each curve. The cosmology assumed is based on the WMAP 9 year ΛCDM cosmology (Hinshaw et al., 2013).

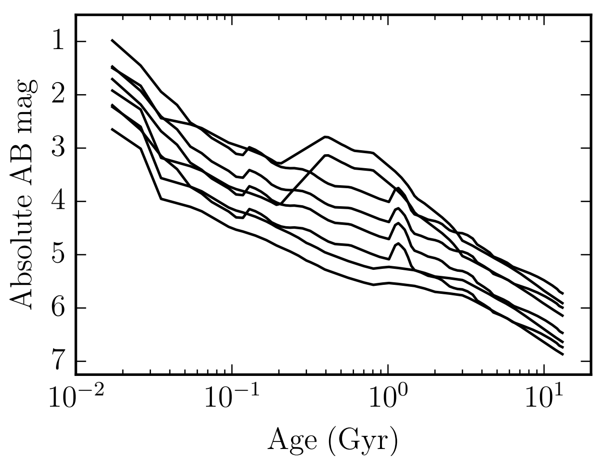

Figure 2.6: Absolute magnitude evolution tracks of simple stellar populations using the models from Bruzual & Charlot (2003) and Maraston (2005), in K_s and W1 bands, and with Salpeter and Chabrier IMFs. The different combinations are unlabeled because what is important is that the luminosity decays in a power law like fashion (approximately $\propto t^{-1/2}$), and not an exponential one.

CHAPTER 3

K-corrections: an Examination of their Contribution to the Uncertainty of Luminosity Measurements

In this chapter we provide formulae that can be used to determine the uncertainty contributed to a measurement by a K-correction and, thus, valuable information about which flux measurement will provide the most accurate K-corrected luminosity. All of this is done at the level of a Gaussian approximation of the statistics involved, that is, where the galaxies in question can be characterized by a mean spectral energy distribution (SED) and a covariance function (spectral 2-point function). This chapter also includes approximations of the SED mean and covariance for galaxies, and the three common subclasses thereof, based on applying the templates from Assef et al. (2010) to the objects in zCOSMOS bright 10k (Lilly et al., 2009) and photometry of the same field from Capak et al. (2007), Sanders et al. (2007), and the AllWISE source catalog.

3.1 Introduction

The K-correction was originally defined in the work of Humason et al. (1956). As initially defined, it was limited to filter transforms from an observer frame photometric filter to the same filter in the galaxy's rest frame. Later work generalized this concept to include transforms to other rest frame observations (for example, Blanton et al., 2003a). There is a thorough summary of the state of the art of K-corrections in Hogg et al. (2002). K-corrections are primarily useful when a large number of objects need to be characterized and

[0]This chapter is based on a paper originally published in The Open Journal of Astrophysics in 2016 under DOI: 10.21105/astro.1603.07299 by the authors: S. E. Lake and E. L. Wright.

there is not sufficient data about all of them to fully specify the spectral energy distribution (SED) of each object, or when theoretical knowledge of the objects' SEDs are deficient. Put in other words, K-corrections are the correct approach to take when the uncertainty in the predictions of the theoretical model exceeds the uncertainty of performing a filter transformation on a small number of observations. What has been missing in the literature, thus far, is an objective specification of which observation frame filter to choose to perform this transformation when multiple close filters are available, or, even better, how to combine two or more filters to increase the signal to noise ratio (SNR) of the resulting measurement.

The answer to both of the questions above, how to combine and which filters to choose, must be informed by an approximation of the contribution of the K-correction process to the uncertainty of the corrected measurement. It is also important to consider how systematic differences between fluxes measured using different filters can add differing biases. In particular, the biases in photometric measurements taken at different wavelengths will usually vary because of wavelength dependent background and resolution effects. It is also important to consider whether the post K-correction measurements need to be statistically independent (for example, for the construction of color-magnitude diagrams). Assuming systematic consistency is desirable beyond maximizing the SNR of every individual measurement, the answer to the question of which filters to K-correct and combine using an inverse variance weighted average is whichever filters produce K-corrected quantities with sufficiently high combined SNR for the data set as a whole. Examples of this sort of consideration include: Sloan Digital Sky Survey (SDSS) i band measurements have significantly higher SNR than z band ones, so it may yield more precise results for the data set as a whole to K-correct from observer frame i to rest frame z than from z to z, even though the z to z correction can be smaller for a large number of galaxies.

Including information about the uncertainty added by the K-correction offers an improvement on the present state in the literature where filters are often chosen for K-correction based only on nearness of filters, regardless of whether the K-correction would move the flux across a spectral break with a wide range of strengths in galaxies' SEDs (for example, the 4,000 Å break).

The structure of this chapter is as follows: Section 3.2 contains a short derivation of the propagation of errors level (Gaussian statistics) uncertainty in the K-correction, Section 3.3 describes the data used to measure the SED covariance function on galaxies (overall, red, blue, and Active Galactic Nuclei [AGN]), and Section 3.4 summarizes the results of the measurement.

3.2 Theory

The general form of the K-correction, adapted from Equation 9 of Hogg et al. (2002) by inverting a fraction and changing variables in an integral, used here is shown in Equation 3.1:

$$K_{\mathrm{ratio}} = \frac{1}{1+z}\left(\frac{\int \frac{\mathrm{d}\nu}{\nu} L_\nu(\nu) Q(\nu)}{\int \frac{\mathrm{d}\nu}{\nu} g_\nu^Q(\nu) Q(\nu)}\right) \times \left(\frac{\int \frac{\mathrm{d}\nu}{\nu} g_\nu^R(\nu) R(\nu)}{\int \frac{\mathrm{d}\nu}{\nu} L_\nu(\nu) R\left(\frac{\nu}{1+z}\right)}\right), \tag{3.1}$$

where $R(\nu)$ is the observer frame detector's relative response to a photon of frequency ν (the Relative Photon Response [RPR]), $g_\nu^R(\nu)$ is the spectral energy distribution (SED) of the standard/zero point source of the observer's instrument, $L_\nu(\nu)$ is the rest frame luminosity SED of the source, and $Q(\nu)$ is the RPR of the instrument being K-corrected to (often Q = R). The usual definition of the K-correction is in terms of magnitudes, and in that case $K = 2.5 \log_{10}(K_{\mathrm{ratio}})$. The content of Equation 3.1 can be summarized, in the notation of functional calculus, as:

$$K_{\mathrm{ratio}} = \frac{1}{1+z}\left(\frac{L_{Qe}[L_\nu]}{L_{Ro}[L_\nu]}\right), \tag{3.2}$$

where e and o are added to the subscripts to emphasize that they are calculated in emitted frame and observer frame, respectively.

Both $L_{Qe}[L_\nu]$ and $L_{Ro}[L_\nu]$ are what are known as 'functionals' of L_ν - functions that map an entire function to the real numbers. In particular, they fit into the class of linear functionals that have the general form:

$$f[L_\nu] = \int w(\nu)\, L_\nu(\nu)\, \mathrm{d}\nu. \tag{3.3}$$

As long as the function w is non-negative, and therefore falls into the class of weighting functions, then the form and units that w has dictates the interpretation of the functional f.

If $w = 1$, then f is the bolometric luminosity. If $w(\nu) \propto \delta(\nu - \nu')$, then f is proportional to a spectral luminosity. Most commonly in astronomy the weighting function is a detector's response to a photon, $w(\nu) \propto R(\nu)/\nu$. The weight function can also be proportional to r^{-2}, the inverse square of the distance, in which case all of the aforementioned quantities are fluxes instead of luminosities.

The important part of the previous paragraph, establishing notation aside, is that the linearity of L_{Qe} and L_{Re} combines with the form of Equation 3.2 to make K_{ratio} completely independent of the normalization of the SED. For concreteness, we define the normalization luminosity and the normalized SED, respectively, in terms of $w_N(\nu)$ to be:

$$\begin{aligned} L_N &\equiv \int w_N(\nu)\, L_\nu(\nu)\, \mathrm{d}\nu, \text{ and} \\ \ell_\nu(\nu) &\equiv \frac{L_\nu(\nu)}{L_N}. \end{aligned} \tag{3.4}$$

Because the K-correction in Equation 3.2 is also a functional of the SED, it is necessary to adapt standard multi-dimensional propagation of errors to functional calculus to calculate the uncertainty in K_{ratio}. In multiple dimensions the propagation of errors formula that relates the covariance of some quantities, $\vec{x}$, to a vector valued function of those quantities, $\vec{f}(\vec{x})$, is:

$$\mathrm{cov}(f_i, f_j) = \sum_{m,n} \frac{\partial f_i(\vec{x})}{\partial x_m} \frac{\partial f_j(\vec{x})}{\partial x_n} \mathrm{cov}(x_m, x_n). \tag{3.5}$$

Equation 3.5 generalizes immediately to functional calculus in an obvious way:

$$\mathrm{cov}(f_i, f_j) = \int \frac{\delta f_i[\ell_\nu]}{\delta \ell_\nu(\nu)} \frac{\delta f_j[\ell_\nu]}{\delta \ell_\nu(\nu')} \Sigma(\nu, \nu')\, \mathrm{d}\nu\, \mathrm{d}\nu', \tag{3.6}$$

where $\Sigma(\nu, \nu')$ is the two point function of normalized SEDs in the class of galaxies being K-corrected; symbolically,

$$\begin{aligned} \mu_\nu(\nu) &\equiv \langle \ell_\nu(\nu) \rangle\,, \text{ and} \\ \Sigma(\nu, \nu') &= \langle (\ell_\nu(\nu) - \mu_\nu(\nu))\, (\ell_\nu(\nu') - \mu_\nu(\nu)) \rangle\,, \end{aligned} \tag{3.7}$$

where $\mu_\nu(\nu)$ is the mean SED.

The formula in Equation 3.6 is more general than is actually required because all fluxes and luminosities are linear functions of the SED, not general ones. So, if a set of luminosities is defined by positive semi-definite weight functions, $L_i = \int w_i(\nu)\, L_\nu(\nu)\, \mathrm{d}\nu$, then:

$$\mathrm{cov}(L_i, L_j) = L_N^2 \int w_i(\nu) w_j(\nu') \Sigma(\nu, \nu')\, \mathrm{d}\nu\, \mathrm{d}\nu'. \tag{3.8}$$

All of the tools are in place to produce the covariance of multiple K-corrections using the propagation of errors formalism. First, the variance of a single K-correction is:

$$\mathrm{var}(K_{\mathrm{ratio}}) = K_{\mathrm{ratio}}^2 \left(\frac{\mathrm{var}(L_Q)}{L_Q^2} + \frac{\mathrm{var}(L_R)}{L_R^2} - 2\frac{\mathrm{cov}(L_Q,\, L_R)}{L_Q\, L_R} \right), \tag{3.9}$$

where the variances and covariance are calculated by applying Equation 3.8. If multiple quantities are being K-corrected, then covariance matrix among the K-corrections takes the form:

$$\begin{aligned} \mathrm{cov}(K_i,\, K_j) = K_i K_j \Bigg(& \frac{\mathrm{cov}(L_{Qi},\, L_{Qj})}{L_{Qi}\, L_{Qj}} - \frac{\mathrm{cov}(L_{Qi},\, L_{Rj})}{L_{Qi}\, L_{Rj}} \\ & - \frac{\mathrm{cov}(L_{Ri},\, L_{Qj})}{L_{Ri}\, L_{Qj}} + \frac{\mathrm{cov}(L_{Ri},\, L_{Rj})}{L_{Ri}\, L_{Rj}} \Bigg). \end{aligned} \tag{3.10}$$

The spectral versions of Equations 3.9 and 3.10 are:

$$\mathrm{var}(K_{\mathrm{ratio}}) = K_{\mathrm{ratio}}^2 \left(\frac{\Sigma(\nu_Q,\, \nu_Q)}{\ell_\nu(\nu_Q)^2} + \frac{\Sigma(\nu_R,\, \nu_R)}{\ell_\nu(\nu_R)^2} - 2\frac{\Sigma(\nu_Q,\, \nu_R)}{\ell_\nu(\nu_Q)\, \ell_\nu(\nu_R)} \right), \text{ and} \tag{3.11}$$

$$\begin{aligned} \mathrm{cov}(K_i,\, K_j) = K_i K_j \Bigg(& \frac{\Sigma(\nu_{Qi},\, \nu_{Qj})}{\ell_\nu(\nu_{Qi})\, \ell_\nu(\nu_{Qj})} - \frac{\Sigma(\nu_{Qi},\, \nu_{Rj})}{\ell_\nu(\nu_{Qi})\, \ell_\nu(\nu_{Rj})} \\ & - \frac{\Sigma(\nu_{Ri},\, \nu_{Qj})}{\ell_\nu(\nu_{Ri})\, \ell_\nu(\nu_{Qj})} + \frac{\Sigma(\nu_{Ri},\, \nu_{Rj})}{\ell_\nu(\nu_{Ri})\, \ell_\nu(\nu_{Rj})} \Bigg), \end{aligned} \tag{3.12}$$

respectively. It is worth reinforcing that the luminosity used for normalization, L_N, must be the same for calculating $\ell_\nu(\nu)$ and $\Sigma(\nu,\, \nu')$, as is required for the covariance of K-corrections to be as independent of normalization as the K-correction itself is.

If either Q or the observer frame R are proportional to the function that defines the SED normalization luminosity, then the form of Equation 3.9 simplifies greatly:

$$\mathrm{var}(K_{\mathrm{ratio}}) = K_{\mathrm{ratio}}^2 \frac{\mathrm{var}(L)}{L_N^2}, \tag{3.13}$$

with a further simplification when the luminosity L is a spectral luminosity at the frequency ν:

$$\mathrm{var}(K_{\mathrm{ratio}}) = K_{\mathrm{ratio}}^2 \Sigma(\nu, \nu). \tag{3.14}$$

The units in Equation 3.14 look a little odd because it is being evaluated in the special case where $K_{\mathrm{ratio}} \propto L_\nu / L_N = \ell_\nu(\nu)$, or its multiplicative inverse, and therefore $\ell_\nu(\nu)$ is unitless by construction, making $\Sigma(\nu,\ \nu')$ unitless also.

The reason for exploring the simplified versions of the variance of K_{ratio} is that it highlights the centrality of $\Sigma(\nu, \nu')$ to the considerations here. Because of this its properties and the process of measuring it merit closer examination. Σ has the property, clear by inspection of its definition, that it is symmetric under interchange of frequencies $\Sigma(\nu, \nu') = \Sigma(\nu', \nu)$. Less obvious is that Σ has nodal lines that originate from the fact that all of the SEDs have to satisfy the normalization condition defined for $\ell_\nu(\nu)$. If the normalization luminosity is defined by the function $w_N(\nu)$, then the conditions imposed on the SEDs and Σ, respectively, are:

$$\begin{aligned} 1 &= \int \ell_\nu(\nu)\, w_N(\nu)\, \mathrm{d}\nu, \text{ and} \\ 0 &= \int \Sigma(\nu, \nu')\, w_N(\nu')\, \mathrm{d}\nu'. \end{aligned} \tag{3.15}$$

If the normalization luminosity is even approximately spectral compared to the standard deviation of galaxy SEDs around frequency ν_N, this condition will produce sharp sign flips on the $\nu = \nu_N$ and $\nu' = \nu_N$ axes in graphs of the correlation coefficient, $\rho(\nu, \nu') = \Sigma(\nu, \nu') / \sqrt{\Sigma(\nu, \nu)\, \Sigma(\nu', \nu')}$.

As with any covariance, $\Sigma(\nu, \nu')$ can be measured by replacing the expectation brackets in the definition, Equation 3.7, with bias corrected sample averages:

$$\Sigma(\nu, \nu') \approx \frac{1}{N-1} \left(\sum_{i=1}^{N} \ell_{\nu,i}(\nu)\, \ell_{\nu,i}(\nu') - \frac{1}{N} \left[\sum_{i=1}^{N} \ell_\nu(\nu) \right] \cdot \left[\sum_{i=1}^{N} \ell_\nu(\nu') \right] \right). \tag{3.16}$$

It is usually not practical, however, to measure Σ using full spectra. In this common case, it is possible to approximate Equation 3.16 by writing each SED as a linear combination of n_T template spectra, $\ell_{\nu,i}(\nu) = \sum_{j=1}^{n_T} f_{ij} \ell_{\nu,j}(\nu)$, as were produced in, for example, Assef et al. (2010) and Rieke et al. (2009). Note that the templates have to be scaled to match the normalization condition, and when this is done the coefficients will satisfy $\sum_{j=1}^{n_T} f_{ij} = 1$. In terms of the template approximation, Equation 3.16 becomes:

$$\begin{aligned}
\mu_j &\equiv \frac{1}{N}\sum_{i=1}^{N} f_{ij}, \\
\sigma_{jk}^2 &\equiv \frac{1}{N-1}\sum_{i=1}^{N} f_{ij}f_{ik} - \frac{N}{N-1}\mu_j\mu_k, \text{ and} \\
\Sigma(\nu,\nu') &\approx \sum_{j,k=1}^{n_T} \sigma_{jk}^2\, \ell_{\nu,k}(\nu)\, \ell_{\nu,j}(\nu);
\end{aligned} \tag{3.17}$$

that is, the templates reduce the infinite dimensional covariance function to an $n_T \times n_T$ covariance matrix of the template fractions.

3.3 Data and Observations

The measurement of the galaxy SED covariance in this chapter is based on the template spectra approximation outlined at the end of Section 3.2. The template set used is the one defined in Assef et al. (2010). The set consists of four templates that correspond, roughly, to galaxies that are: red (named Elliptical), moderately star forming blue (Sbc), starburst blue (Irregular), and active galactic nuclei (AGN). The AGN template, additionally, has a dust obscuration model parametrized by E$(B-V)$, the extinction excess. Graphs of the templates, normalized to the *WISE* W1 filter at a redshift of $z = 0.38$ (effective wavelength $\lambda \approx 2.4\,\mu$m), can be found in Figure 3.1.

The presence of AGN dust obscuration as a non-linear parameter throws off the mathematics behind Equations 3.17. There are multiple ways of getting around this problem, including replacing the AGN SED with multiple AGN SEDs that have different fixed extinction values. In order to make the results as simple as possible to produce, we only use one extinction value: the median E$(B-V)$ for galaxies which had a sufficient AGN contribution to make the measured E$(B-V)$ meaningful (see below). This means that the covariance measurement presented here will be an underestimate of the true spread among SEDs, particularly on the blue side of the spectrum. Estimating how much of an underestimate it is

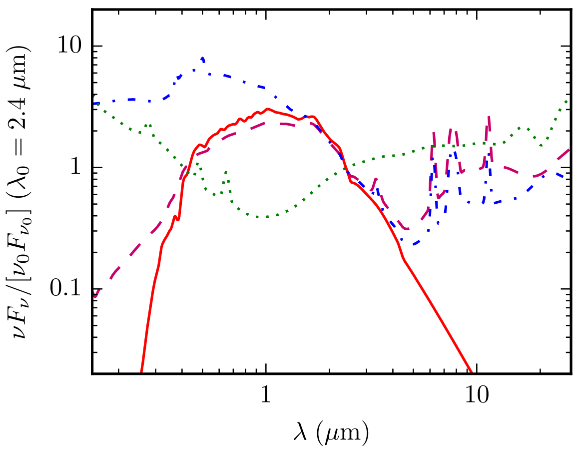

Figure 3.1: The template spectra used from Assef et al. (2010). The red solid line is the template called "Elliptical." The purple dashed line is "Sbc." The blue dash-dotted line is "Irregular." And the green dotted line is "AGN," unobscured.

by looking at the distribution of E$(B-V)$ values will prove inexact, because the effect of the parameter on individual SEDs is non-linear and the distribution of values observed is highly asymmetric. With those caveats in mind, we examined the distribution excess extinctions qualitatively and found it to have a width around 1 magnitude.

The scatter in observed AGN extinctions will be greater than what is imposed by dust near the black hole alone because galaxy inclination will change the amount of interstellar medium that the AGN's light has to travel through. Inclination will not just affect the measured AGN extinction, though, because the amount of dust the stellar light must travel through is also inclination dependent. The model we use in this work does not make any allowance for extinction within the target galaxy of anything but the AGN, though, so inclination effects will similarly modify the template fractions assigned to the galaxies in the fitting process. All of this has the effect of increasing the scatter of observed SEDs compared to the scatter that would be exhibited by a measure of the underlying physical properties of the galaxies. Despite these limitations, the work presented here should be sufficiently accurate for measuring a luminosity function in the near to mid-IR because of reduced dust absorption in those wavelengths.

Table 3.1. zCOSMOS Photometry Used

Survey	Bands	Citation
COSMOS	FUV, NUV, u^*, B_j, g^+, V_j, …	
	… r^+, F814W, i^+, i^*, z^+, J, K_s	Capak et al. (2007)
SDSS-DR10	u, g, r, i, z	Ahn et al. (2014b)
S-COSMOS-DR3	c1, c2, c3, c4	Sanders et al. (2007)
AllWISE	W1, W2, W3, W4	Wright et al. (2010)

Note. — Photometric surveys used for fitting zCOSMOS sources.

Measuring the f_{ij} of Equations 3.17 using the Assef et al. (2010) templates requires fitting the templates to observed photometry of a collection of galaxies, preferably with spectroscopic redshifts and a rich collection of filters. The zCOSMOS Bright 10k sample, described in Lilly et al. (2009) and Knobel et al. (2012), is in the COSMOS field and, therefore, has a very rich set of publicly available photometry. The photometry we used is summarized in Table 3.1. The targeting for the survey is based on photometry from Hubble Advanced Camera for Surveys (ACS) Wide Field Camera (WFC) imaging with the F814W filter, which is approximately I-band. The version of the data used for this analysis is Data Release 2.

The photometric surveys were cross-matched to the zCOSMOS data set based on a spatial cross-match that uniquely assigns a detection to its closest companion in zCOSMOS up to a maximum search radius that depended on the resolution of the external survey. For most surveys, the search radius was $1''$, but for AllWISE it was $3''$ (half the full width at half maximum of point sources for the *WISE* W1 beam).

Selecting high quality redshifts from zCOSMOS is somewhat involved because of the detailed 'confidence class' (`cc`) system used. The recommendation in Lilly et al. (2009) is to accept all sources with `cc` equal to: any 3.X, 4.X, 1.5, 2.4, 2.5, 9.3, and 9.5. Based on the description of those classes, the analysis here accepted sources that fit in the recommended classes, but also those with a leading 1 (10 was added to show broad line AGN), 18.3, 18.5 (both broad line AGN consistent with the photometric redshift), and rejected all secondary targets (2 in the tens or hundreds digit). This can be done by accepting sources for which the text string version of `cc` matches the regular expression “`([34]\..*)|([1289]\.5)|(2\.4)|([89]\.3)`” and doesn't match “`^2\d+\.`”. Finally, the targets fell into three selection classes, column named `i`, and ‘unintended’ sources are rejected by requiring $\mathtt{i} > 0$.

In addition to good redshifts, the sources needed to have a minimum amount quality of photometry available to make the template fitting reliable. To that end, we limited the analysis to sources that meet all the following conditions: redshifts satisfy $0.05 < z \leq 1.0$, the sources have at least five high quality photometric measurements (the number of free parameters in the SED fit when unconstrained, description follows), and were measured in S-COSMOS to have a have $F_{\mathrm{c1}} \geq 5\,\mu$Jy (corresponds to an empirical SNR limit of about 30, about 22.15 mag) using a $3''$ aperture in *Spitzer*'s IRAC channel 1 ($\lambda_{\mathrm{eff}} \approx 3.6\,\mu$m). The external photometric measurements were deemed to be of sufficient quality if the photometry was not flagged as contaminated in the survey, or otherwise marked as obviously invalid by being less than or equal to zero.

The templates were constructed to be fit to fluxes using χ^2 applied to a linear combination of the template fluxes with non-negative coefficients, and a search in the 1-dimensional parameter space for the best AGN extinction excess, $\mathrm{E}(B-V) = (2.5/\ln(10)) \cdot (\tau_B - \tau_V)$. That is, the model has the form:

$$\begin{aligned} F_\nu(\nu, z) = {} & a_{\mathrm{E}} F_{\mathrm{E}}(\nu, z) + a_{\mathrm{S}} F_{\mathrm{S}}(\nu, z) \\ & + a_{\mathrm{I}} F_{\mathrm{I}}(\nu, z) + a_{\mathrm{A}} F_{\mathrm{A}}(\nu, z, \tau_B - \tau_V), \end{aligned} \tag{3.18}$$

$$\chi^2 = \sum_{i \in \{\mathrm{filters}\}} \left(\frac{F_{\mathrm{obs}\,i} - F_{\mathrm{mod}\,i}}{\sigma_i} \right), \tag{3.19}$$

with all $a_i \geq 0$, and $12 > \tau_B - \tau_V \geq 0$. The a_i were fit using the SciPy `optimize` package's routine `nnls` (quadratic programming for non-negative least squares), and $\tau_B - \tau_V$ were fit with the routine `brent` with fallback to `fmin` (Nelder-Meade simplex).

There is one modification to that procedure for the fits done for this chapter. The templates do not include the ability to tune dust obscuration of the galaxy's stars, so a dusty starburst that has a detection in *WISE*'s $12\,\mu$m filter, W3, will often be best fit with a galaxy that is dominated by its Elliptical component (to satisfy optical redness) and a super-obscured AGN ($\tau_B - \tau_V > 12$) masquerading as the emission from the stellar dust component. The problem this creates is that it makes the SED fit the data more poorly in the most important range for the subsequent uses to which we intend to put this data, where K-corrections from observer frame W1 to $2.4\,\mu$m rest wavelength are performed. We used two techniques to work around this problem. First, we limited the excess in optical depth as $\tau_B - \tau_V \leq 12$ (equivalently, $\mathrm{E}(B-V) \leq 13.03$). Second, when the SED was badly modeled ($\chi^2 > \max(N_{\mathrm{df}}, 1) \times 100$) and unlikely to be an AGN ($W1 - W2 > 0.5$ Vega mag with uncertainty, $\sigma_{W1-W2} < 0.2$ Vega mag), we used the best model with $\mathrm{E}(B-V) = 0$. The reduced χ^2 criterion was determined by subjective empirical examination, and the color based selection was found in Assef et al. (2013) to select low redshift AGN with 90% completeness. Overall, $2,604$ galaxies were fit using the 'alternate' fitting mode where the AGN template was set at $\mathrm{E}(B-V) = 0$ and $4,621$ were fit in the 'main' fitting mode where the AGN extinction was allowed to vary. For the subsets the breakdown is: none of the 268 AGN, $1,139$ of the $1,903$ Red, and $1,465$ of the $5,054$ Blue galaxies were fit in the alternate mode.

Limiting the excess optical depth, $\tau_B - \tau_V$, to be non-negative introduces a bias to the parameter estimation of the individual galaxies. It is even physically possible for a source to appear bluer than expected if the line of sight is unobscured and dust clouds are reflecting excess blue light into it (that is, the line of sight contains significant contribution from reflection nebulae in the target). Even so, applying a negative optical depth excess to dust obscuration models is not likely to produce an accurate spectrum for reflection, and the magnitude of the negative excess doesn't have to be large to cause the estimate of the maximum redshift at which the galaxy could be observed to diverge.

There is a final detail involved in dealing with AGN obscuration measurements. The impact of changes in $\tau_B - \tau_V$ on the shape of the overall SED depends on what fraction of the luminosity the AGN contributes. If a minuscule fraction of the luminosity is contributed by the AGN, then the shape of the SED is insensitive to how obscured the AGN template is, rendering the value that the fitting process assigns to $\tau_B - \tau_V$ meaningless. It is, therefore, necessary when computing statistics involving $\tau_B - \tau_V$ to limit the sample to those galaxies for which the AGN's contribution to the shape of the SED is non-negligible. The cutoff used in this work, set arbitrarily, is that the fraction of $2.4\,\mu$m luminosity contributed must be greater than 0.1%. The cutoff is set low for two reasons: first, the shapes of the template spectra mean that the ability to measure extinction in the AGN template depends on both what other templates are present and which wavelengths were observed; and second, we prefer to make less aggressive cuts to the data when making them without making a rigorous exploration of their impact on the data.

The resulting data set contains $7,225$ galaxies. The template fit parameters of the data set are included in this work (at figshare.com[1] with a digital object identifier[2]) in gzipped[3] IPAC Table format[4], an excerpt from which is in Table 3.2. The normalization condition chosen for the templates is the luminosity *WISE*'s W1 filter would observe directly in a galaxy at redshift $z = 0.38$ ($\lambda_{\text{eff}} \approx 2.4\,\mu$m), after the effect of AGN obscuration has been applied to the AGN template. The latter choice ensures that the template fractions sum to 1, and that each f represents the fraction of $2.4\,\mu$m luminosity contributed by the corresponding component of the galaxy.

We also performed a classification of galaxies into three possible subsets for which SED means and covariances were measured: AGN, red galaxies, and blue galaxies. The scheme for how this classification was done is outlined in the flowchart in Figure 3.2. The dividing line for whether a galaxy is considered an AGN is if more than 50% of its $2.4\,\mu$m luminosity comes

[1] `https://figshare.com/articles/zCOSMOS_Template_Fractions_tbl_gz/3804210`

[2] `https://doi.org/10.6084/m9.figshare.3804210`

[3] `https://www.gnu.org/software/gzip/`

[4] `http://irsa.ipac.caltech.edu/applications/DDGEN/Doc/ipac_tbl.html`

from the obscured AGN component. The dividing line for whether a galaxy is "red" was determined empirically by examining the smoothed $M_u - M_r$ versus M_g, that is a standard rest frame color versus absolute magnitude diagram, shown in Figure 3.3. The rest frame Sloan filter M_u, M_r, and M_g were calculated by K-correcting observer frame Subaru g^+, r^+, and i^+ fluxes, respectively, from the Capak et al. (2007) data. We experimented with a photometric classification scheme for AGN, specifically the Stern wedge from Stern et al. (2005), but the reduced sensitivity of the longer wavelength IRAC data meant that the blue and AGN mean SEDs were nearly the same. The final classification process shown in Figure 3.2 resulted in: 266 AGN (3.7% of the sample), 1,906 red sequence galaxies (26.4% of the sample), and 5,053 blue cloud galaxies (69.9% of the sample).

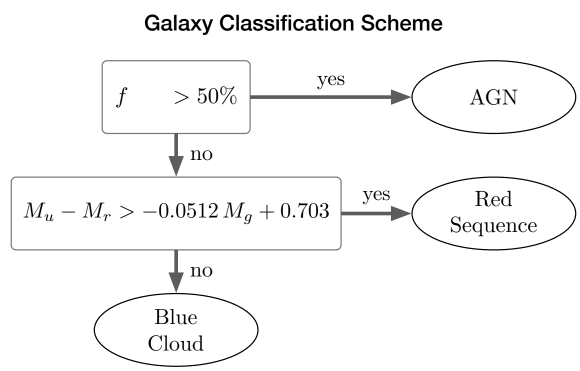

Figure 3.2: Simple flowchart showing how galaxies were classified into AGN, red or blue galaxies in this work.

3.4 Results

The template parameters for the mean SEDs, μ_j in Equations 3.17 and the median $\tau_B - \tau_V$, of the different subsamples can be found in Table 3.3. The template covariance matrices, σ_{jk} in Equations 3.17, are in split up into Tables 3.4–3.7 for the overall sample of, AGN, red, and blue galaxies, respectively. Using the numbers in these tables with the normalized templates and obscuration models of Assef et al. (2010) is sufficient to calculate the covariance associated with any set of K-corrections. It is useful to examine

Table 3.2. Excerpt of Fit Data

ID	ra	dec	f_Ell	f_Sbc	f_Irr	f_AGN	EBmV	ChiSqr	Ndf	FitMode	class
	°	°					mag				
700178	150.305008	1.876265	0.2611	0.0000	0.4446	0.2943	0.0000	1.27E+02	11	main	B
700189	150.308258	1.916484	1.0000	0.0000	0.0000	0.0000	0.0000	8.30E+03	16	alt	B
700274	149.926743	1.869646	0.6927	0.0000	0.1911	0.1162	0.0000	1.98E+01	7	main	B
700291	149.890167	1.859292	0.9394	0.0000	0.0000	0.0606	0.0921	3.50E+02	13	main	R
700298	149.816711	1.916690	0.0803	0.6652	0.1738	0.0807	0.0000	1.02E+02	10	main	B
700447	150.425690	2.123886	0.1311	0.5809	0.1246	0.1633	0.0450	9.10E+01	12	main	B

Note. — Excerpt from the data set included with this work in IPAC Table format. The ID column is the unique identification number given to the target in the zCOSMOS survey. `ra` and `dec` are the J2000 right ascension and declination in the zCOSMOS targets, in decimal degrees. `f_Ell`, `f_Sbc`, `f_Irr`, and `f_AGN` are the fraction of 2.4 μm luminosity contributed by the Elliptical, Sbc, Irregular, and obscured AGN templates, respectively. `EBmV`$= (2.5/\ln(10)) \cdot (\tau_B - \tau_V)$ is the excess extinction in the AGN obscuration model. `ChiSqr` is the raw χ^2 from the fitting process. `Ndf` is the net number of degrees of freedom in the fitting process (number of filters used minus 5), ignoring the way the effective dimensionality is altered by the constraints on the fitting process. `FitMode` is a character string that takes on one of two values: "main" if $\tau_B - \tau_V$ was allowed to vary in the fitting process, "alt" if it was set to 0 as described in the text. `class` denotes the class assigned to the galaxy, and is one of 'A', 'R', or 'B' for 'AGN', 'Red', and 'Blue', respectively. The full table is available at: `https://figshare.com/articles/zCOSMOS_Template_Fractions_tbl_gz/3804210` with doi: with doi:10.6084/m9.figshare.3804210.

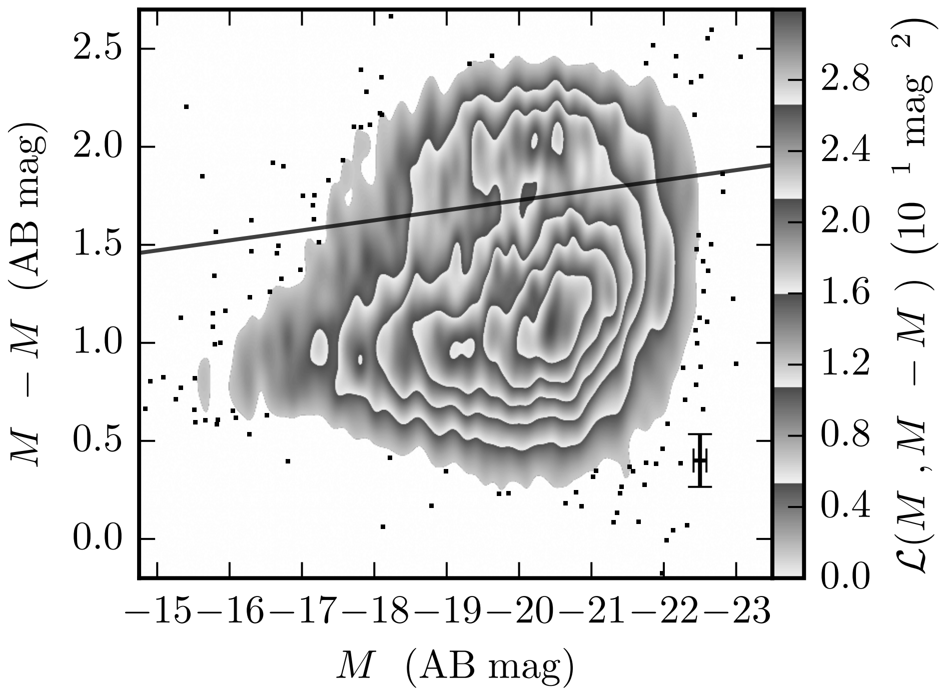

Figure 3.3: Color-magnitude diagram showing the dividing line between the red sequence (above the line) and the blue cloud (below). The point with error bars shows the standard deviation of the smoothing kernel applied to the data in the dense region of the plot.

graphs of the diagonal elements of the covariance, $\sqrt{\Sigma(\nu,\, \nu)}$, and the correlation function, $\rho(\nu,\, \nu') = \Sigma(\nu,\, \nu')/\sqrt{\Sigma(\nu,\, \nu)\, \Sigma(\nu',\, \nu')}$, to get a feel for how they behave, and to have as a reference for quick spectral calculations of K-correction covariances.

Graphs of $\sqrt{\Sigma(\nu,\, \nu)}$ for the $2.4\,\mu$m normalized SEDs can be found in Figure 3.4. The standard deviation increases with wavelength distance from $2.4\,\mu$m, but there are dips and jumps around spectral features with a wide variety of strengths, specifically spectral breaks and lines. Further, the increase in the spread is steeper on the short wavelength side than the long one, supporting the assertion that simple wavelength distance is not sufficient to determine which observer frame bands are the best to K-correct from. The scaling on the graph is linear in y and logarithmic in x, so the large nearly linear stretches in the graphs represent growth that is logarithmic in wavelength ratio in the standard deviation of galaxy SEDs. The final notable feature is that the spread of red galaxy SEDs, in panel **c**, is low, as to be expected from the comparative narrowness of the red sequence in color-magnitude diagrams like Figure 3.3. The comparatively large spread in AGN SEDs, panel **b**, is surprising because the AGN selection criterion is that most of the galaxy's light at $2.4\,\mu$m, close to the minimum of the AGN SED, comes from the AGN. This criterion explicitly limits the range of possible values for the f_{AGN}, and implicitly limits the other fractions because they must sum to 1. The selection criterion does affect the template covariance matrix as expected (compare the σ column in Table 3.5 to the ones in Tables 3.6 and 3.7). The most likely culprit for the variability is how the AGN template is so different from the other three (see Figure 3.1). The blue cloud galaxies, in panel **d**, have a higher spread than any of the other types of galaxies, especially in the spectral lines, other than panel **a**, which summarizes the standard deviation for all galaxies.

The non-monotinicity of $\sqrt{\Sigma(\nu,\,\nu)}$ is actually suppressed in Figure 3.4 because the normalization luminosity lies in a range of frequencies where most galaxy SEDs don't show much variety. A clearer example of the SED variance exhibiting a broad maximum can be found in Figure 3.5, where $\sqrt{\Sigma(\nu,\,\nu)}$ is plotted for all galaxies with a normalization luminosity in the rest frame B filter instead of $2.4\,\mu$m. The standard deviation is pinched off by the normalization near 445 nm and the spread among the SED templates in the 2–5 μm range is intrinsically low, producing a marked peak in the standard deviation in most of the optical and near-IR. Because the uncertainty in the K-correction requires input from a B normalized SED and a redshift, it is not possible to say, for sure, that the variance involved in correcting from B to, say, $4\,\mu$m is smaller than correcting from I to $4\,\mu$m. Even so, real correlations, like the far IR radio correlation, should show a pattern like this in plots of $\sqrt{\Sigma(\nu,\,\nu)}$ that cover the relevant frequency range.

Very few astronomers are interested in K-correcting only to $2.4\,\mu$m, and that's where the utility of the correlation function, shown in Figure 3.6, comes in. As Equations 3.9 and 3.10 show, by combining the full $\Sigma(\nu,\,\nu')$ with the SED used in generating the K-correction (normalized to $2.4\,\mu$m) and the filter curves, any covariance of K-corrections can be calculated.

The most prominent features in the correlation coefficient graphs related to physics,

Table 3.3. Mean SED Parameters

Subsample	$\langle f_{\rm Ell}\rangle$	$\langle f_{\rm Sbc}\rangle$	$\langle f_{\rm Irr}\rangle$	$\langle f_{\rm AGN}\rangle$	$\overline{\tau_B - \tau_V}$[a]
all	0.490	0.269	0.114	0.127	0.023
AGN	0.180	0.076	0.078	0.666	0.207
Red	0.823	0.131	0.011	0.035	0.303
Blue	0.380	0.331	0.155	0.134	0.015

Note. — Mean of the 2.4 μm luminosity template fractions, alongside the median excess extinction on the AGN. Numbers are given to three decimal places regardless of experimental uncertainty.

[a] $\overline{\tau_B - \tau_V}$ here means the median of $\tau_B - \tau_V$.

as opposed to mathematical artifacts that comes purely from the choice of normalization wavelength, in the graphs are the thick white lines. For points on those lines, the SED colors $L_\nu(\lambda_1)/L_\nu(2.4\,\mu\text{m})$ and $L_\nu(\lambda_2)/L_\nu(2.4\,\mu\text{m})$ are uncorrelated, meaning that they contain no mutual information and, therefore, provide maximally independent information about the shape of the SED. The location of those white lines is determined by where the template SEDs that dominate the sample diverge from each other. In the case of the red galaxies (Panel **c**) this happens roughly at the $4,000\,\text{Å}$ break. For the other galaxies, the diversity of SEDs is more broad and the divergence of the templates is more gradual so the main uncorrelated band is more broad and more difficult to pin down to a single phenomenon.

The other prominent features present as horizontal and vertical striping. Those are caused by the presence of absorption and emission lines in some templates and not others. The most prominent emission lines present in the templates are: MgII (279.8 nm), OII (doublet, 372.6 and 372.9 nm), OIII (merged 495.9 and 500.7 nm), Hα, and PAH lines at $\lambda > 3\,\mu$m. The absorption lines are primarily a feature of the Elliptical template and that is responsible for the less prominent striping in the optical.

Table 3.4. Covariance Matrix of All SED Templates

Parameter	σ	δf_{Ell}	δf_{Sbc}	δf_{Irr}	δf_{AGN}
δf_{Ell}	0.353	1.000	−0.727	−0.366	−0.373
δf_{Sbc}	0.325	−0.727	1.000	−0.209	−0.224
δf_{Irr}	0.153	−0.366	−0.209	1.000	0.268
δf_{AGN}	0.163	−0.373	−0.224	0.268	1.000

Note. — The σ column contains the standard deviations of the parameters, and the rest of the columns are the correlation matrix among the template fractions. Numbers are given to three decimal places regardless of experimental uncertainty.

Table 3.5. Covariance Matrix of AGN SED Templates

Parameter	σ	δf_{Ell}	δf_{Sbc}	δf_{Irr}	δf_{AGN}
δf_{Ell}	0.162	1.000	−0.459	−0.388	−0.417
δf_{Sbc}	0.118	−0.459	1.000	−0.212	−0.112
δf_{Irr}	0.136	−0.388	−0.212	1.000	−0.370
δf_{AGN}	0.131	−0.417	−0.112	−0.370	1.000

Note. — The σ column contains the standard deviations of the parameters, and the rest of the columns are the correlation matrix among the template fractions. Numbers are given to three decimal places regardless of experimental uncertainty.

Table 3.6. Covariance Matrix of Red SED Templates

Parameter	σ	δf_{Ell}	δf_{Sbc}	δf_{Irr}	δf_{AGN}
δf_{Ell}	0.260	1.000	−0.941	−0.111	−0.229
δf_{Sbc}	0.252	−0.941	1.000	−0.041	−0.070
δf_{Irr}	0.043	−0.111	−0.041	1.000	−0.046
δf_{AGN}	0.079	−0.229	−0.070	−0.046	1.000

Note. — The σ column contains the standard deviations of the parameters, and the rest of the columns are the correlation matrix among the template fractions. Numbers are given to three decimal places regardless of experimental uncertainty.

Table 3.7. Covariance Matrix of Blue SED Templates

Parameter	σ	δf_{Ell}	δf_{Sbc}	δf_{Irr}	δf_{AGN}
δf_{Ell}	0.304	1.000	−0.728	−0.215	−0.189
δf_{Sbc}	0.337	−0.728	1.000	−0.418	−0.375
δf_{Irr}	0.162	−0.215	−0.418	1.000	0.346
δf_{AGN}	0.128	−0.189	−0.375	0.346	1.000

Note. — The σ column contains the standard deviations of the parameters, and the rest of the columns are the correlation matrix among the template fractions. Numbers are given to three decimal places regardless of experimental uncertainty.

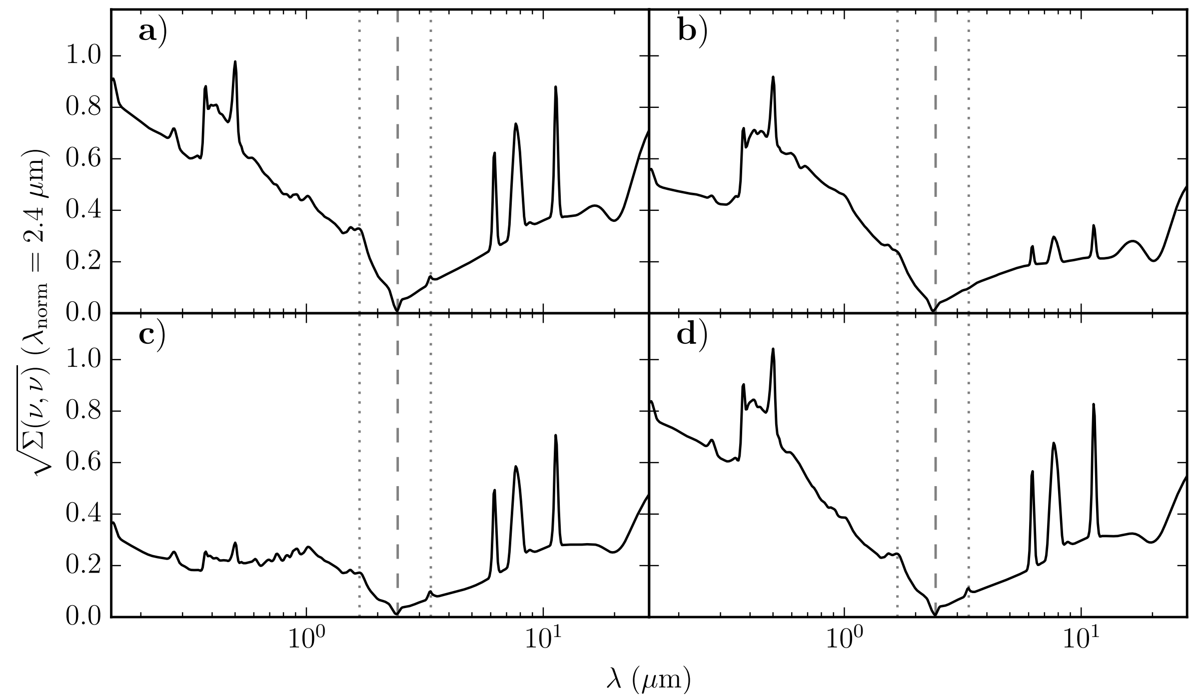

Figure 3.4: Panel **a** shows the SED standard deviation ($\sqrt{\Sigma(\nu,\nu)}$) for all galaxies in the sample, and Panels **b**, **c**, and **d** show the same data for AGN, red, and blue galaxies, respectively. The vertical dashed line highlights the effective wavelength of the normalization luminosity, and the dotted lines show the effective rest frame wavelength of *WISE*'s W1 channel for galaxies at the redshifts $z = 0$ and 1. Note the there are no units given for $\Sigma(\nu, \nu')$ because the normalization luminosity used, L_N, fits the standard practice in astronomy of its weighting function, $w_N(\nu)$, having the units needed to make L_N a weighted mean of L_ν, that is $w_N(\nu)$ has units [Hz^{-1}].

3.5 Conclusion

In this work we derived formulae for computing the uncertainty added to an observed flux when it is K-corrected. We also showed, by approximating the SED covariance function using template fitting data, that the choice of which observations to K-correct to the rest frame quantities desired should be informed by information about the variety of the SEDs of the objects in question. While the discussion in the body of this chapter focused on K-corrections, they are just a specific type of filter transformation, and the adaptation of the formulae here to all filter transforms is trivial: just drop the factors of $(1 + z)$.

An example of a filter transformation that the covariance of observer frame SEDs can inform is the transformation from broad band filter to a spectral quantity (for example: W1 to $3.4\,\mu$m). Note how the SED standard deviation plots in Figure 3.4 have a minimum near $2.4\,\mu$m. If the normalization luminosity were actually the spectral luminosity at $2.4\,\mu$m that minimum would be a zero of the function. Because the normalization is actually $^{0.38}$W1, in the notation of Blanton et al. (2003b) and subsequent works, the function only achieves a minimum that is close to zero at a wavelength very near $2.4\,\mu$m. A similar plot of observer frame SED standard deviation for stars would show a similar minimum at the spectral wavelength most correlated with the broad band measurement, making that wavelength a good candidate for labeling as the filter's effective wavelength.

This study of the galaxy SED correlation function, and the mean normalized SED of galaxies, is also useful in that it feeds in to a generalization of the luminosity function that we call the spectroluminosity functional, $\Psi[L_\nu]$. We explored the usefulness and mechanics of measuring $\Psi[L_\nu]$ in Chapter 2, and using the data from this chapter and $\Psi[L_\nu]$ to measure the ordinary luminosity function, $\Phi(L)$, in Chapter 6.

Finally, there are definitely improvements that can be made to the techniques used here. The templates used are static, and the mean SEDs are not allowed to depend on luminosity. The latter is somewhat justified by the weak index in the power law relating g-band luminosity to $M_u - M_r$ color in the cut (-0.0512, see Figure 3.2), but it would still be an improvement to allow for a luminosity dependence in the SED mean.

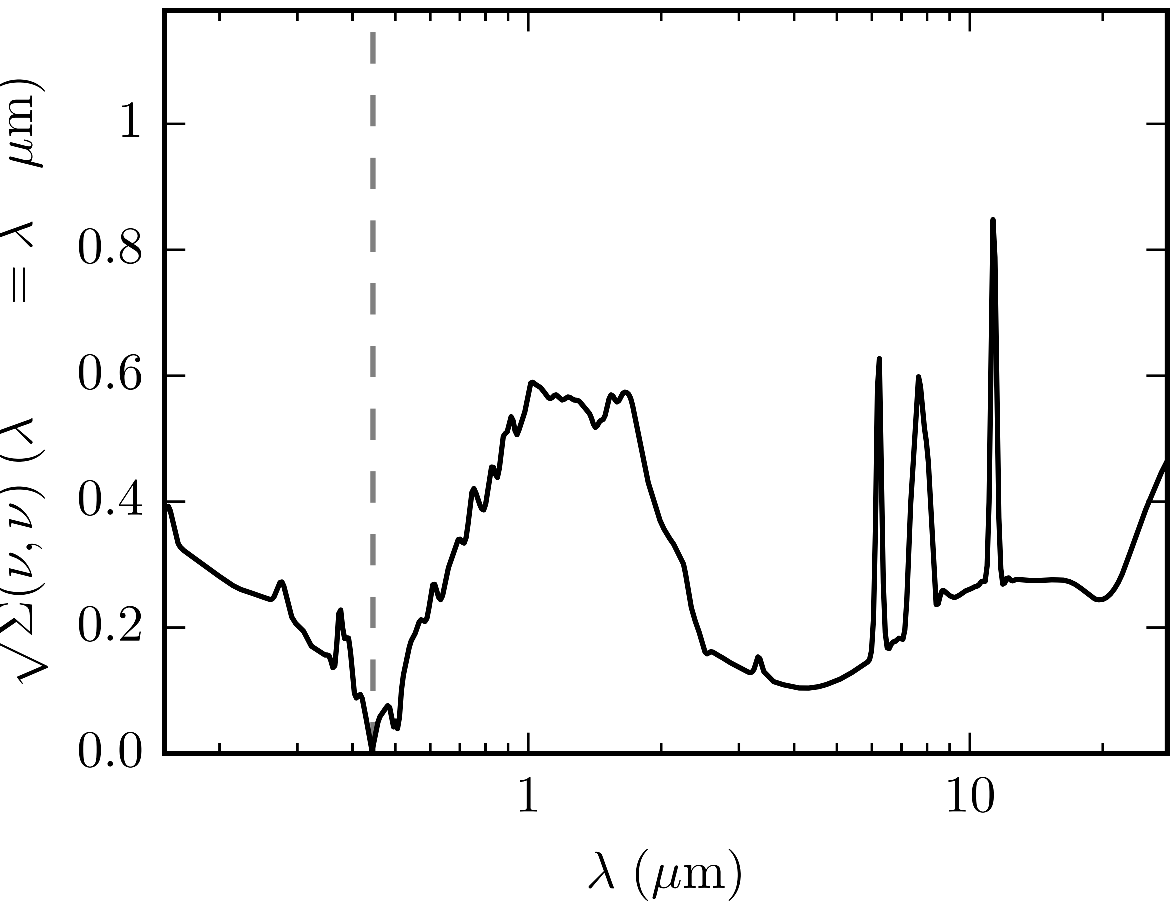

Figure 3.5: The SED standard deviation ($\sqrt{\Sigma(\nu,\nu)}$) for all galaxies in the sample. The vertical dashed line highlights the effective wavelength of the normalization luminosity, which is the Johnson-Cousins B filter for this plot only. Note the there are no units given for $\Sigma(\nu,\nu')$ because the normalization luminosity used, L_N, fits the standard practice in astronomy of its weighting function, $w_N(\nu)$, having the units needed to make L_N a weighted mean of L_ν, that is $w_N(\nu)$ has units [Hz^{-1}].

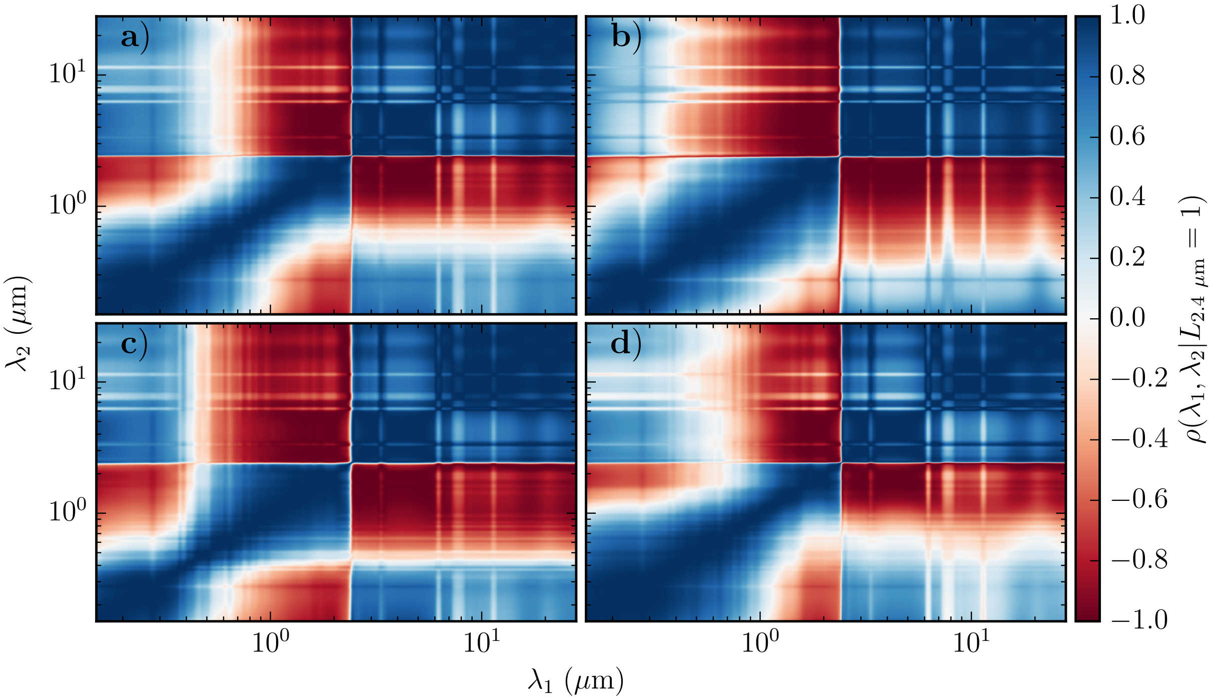

Figure 3.6: SED correlation functions, $\rho(\nu,\,\nu') = \Sigma(\nu,\,\nu')/\sqrt{\Sigma(\nu,\,\nu)\,\Sigma(\nu',\,\nu')}$. Panel **a** shows ρ for all galaxies, while **b**, **c**, and **d** show ρ for AGN, red, and blue galaxies, respectively. The dominant feature in the graphs, the sign flips across the $\lambda_{\{1,2\}} = 2.4\,\mu$m axes, is due to the choice of normalizing the SEDs to that wavelength. The impact of spectral features, emission and absorption lines, in the templates also stand out as horizontal and vertical striping. The final feature worth noting is the sign flip that corresponds, roughly, to when the wavelengths are on opposite sides of the point where the template SEDs that dominate the population diverge, generating the thick white lines where the sign of ρ flips.

CHAPTER 4

Description of the *WISE*/DEIMOS Survey

We report on the results of an optical spectroscopic survey at high Galactic latitude ($|b| \geq 30°$) of a sample of *WISE*-selected targets, grouped by *WISE* W1 ($\lambda_{\text{eff}} = 3.4\,\mu$m) flux, which we use to characterize the sources *WISE* detected. We observed 762 targets in 10 disjoint fields centered on ultra-luminous infrared galaxy (ULIRG) candidates using the DEIMOS spectrograph on Keck II. We find 0.30 ± 0.02 galaxies arcmin^{-2} with a median redshift of $z = 0.32 \pm 0.01$ for the sample with W1 $\geq 120\,\mu$Jy. The foreground stellar densities in our survey range from $0.25 \pm 0.07\,\text{arcmin}^{-2}$ to $1.1 \pm 0.1\,\text{arcmin}^{-2}$ for the same sample. We obtained spectra that produced science grade redshifts for $\geq 90\%$ of our targets for sources with W1 flux $\geq 120\,\mu$Jy that also had i-band flux $\gtrsim 18\,\mu$Jy. We used for targeting very preliminary data reductions available to the team in August of 2010. Our results therefore present a conservative estimate of what is possible to achieve using *WISE*'s Preliminary Data Release for the study of field galaxies.

4.1 Introduction

The *Wide-field Infrared Survey Explorer* (*WISE*) is an all-sky mid-infrared survey satellite that NASA launched on December 14, 2009. Operating simultaneously in four bands, centered at 3.4, 4.6, 12 and 22 μm (W1-W4, hereafter), *WISE* completed its first full coverage of the sky in late July 2010, its cryogenic mission ended in early October 2010, and the satellite was put into safe mode in February 2011. *WISE* will provide an IR atlas of the full

[0]This chapter is based on a paper originally published to The Astronomical Journal in 2012 under the DOI: 10.1088/0004-6256/143/1/7 by the authors: S. E. Lake, E. L. Wright, S. Petty, R. J. Assef, T. H. Jarrett, S. A. Stanford, D. Stern, and C.-W. Tsai.

sky hundreds of times deeper than IRAS containing hundreds of millions of targets (5σ point source sensitivity is equal to or better than 0.08, 0.11, 1 and 6 mJy in the four passbands). A Preliminary Data Release covering 57% of the sky took place on April 14, 2011. Prior to this release, the *WISE* team undertook several programs to characterize the survey, including a comparison of *WISE* and *Spitzer* sources at the ecliptic poles by Jarrett et al. (2011).

We expect that *WISE* has detected cluster $L_\star$ galaxies out to a redshift of $z \sim 1$. This expectation is based on using a passive evolution model from Bruzual & Charlot (2003) that fits cluster luminosity functions to predict the $L_\star$ flux density in W1 as a function of redshift. This puts *WISE* in an interesting position with respect to the publicly available spectroscopic surveys. The surveys with coverage comparable to *WISE* are not nearly as deep, and the deep surveys were not nearly as wide, as shown in Table 4.1. Furthermore, the targeting for most other surveys rely on mixes of limiting magnitudes in primarily optical bands, morphologies, and colors, increasing the problem of selection effects in any attempt to use them to characterize the *WISE* sources. While using existing spectroscopic databases is useful for determining the redshifts of numerous *WISE* sources, it is not possible to construct flux-limited samples in the *WISE* bands with complete spectroscopic coverage. The importance of having such data available is that it greatly simplifies the statistical analysis of quantities that rely on flux-limited galaxy samples, such as luminosity functions or correlation functions. In order to characterize the sources selected by the W1 bandpass, we have carried out a spectroscopic survey of *WISE*-selected objects blind to all considerations but W1 flux. Here we present the design and results from the survey we carried out using the DEep Imaging Multi-Object Spectrograph (Faber et al., 2003, DEIMOS) on the Keck II telescope on UT 2010 September 14 selected by a W1 flux-classified catalog.

All magnitudes from the Sloan Digital Sky Survey (SDSS) are model fluxes converted to standard AB magnitudes, and all other magnitudes are given in the Johnson Vega system used in the *WISE* database. We made no attempt to adjust our photometry to account for source morphology or extent. Thus, colors based on combining *WISE* and SDSS magnitudes in this chapter will have significant systematic offsets from the actual physical colors, but are useful nevertheless. We have also not corrected fluxes for extinction.

Table 4.1. Spectroscopic Survey Characteristics

Survey	median(z)	Coverage (Ω) (sr)	Ref
6dFGS	0.053	5.2	Jones et al. (2009)
SDSS-DR8	0.1	2.43	Aihara et al. (2011)
2dFGRS	0.11	0.5	Colless et al. (2003)
WiggleZ	0.6	0.3	Drinkwater et al. (2010)
GAMA	0.2	4.4×10^{-2}	Baldry et al. (2010)
AGES	0.31	2.3×10^{-3}	Kochanek et al. (2012)
zCOSMOS	0.61	5.2×10^{-4}	Lilly et al. (2009)
This Work	0.33	6.78×10^{-6}	

Note. — A sample of redshift surveys showing their area and depth. A more comprehensive comparison can be found in Figure 1 of Baldry et al. (2010). Note that while the areal coverage of our survey is small the 10 fields are widely dispersed, minimizing cosmic variance.

4.2 DEIMOS Survey Design

To select our targets, we used the *WISE* Level 3 operations (L3o) preliminary database[1]. The Infrared Processing and Analysis Center (IPAC) constructed the L3o database by coadding *WISE* frames in a stripe of ecliptic longitude from a single day. Each stripe had a depth near the center of approximately 12 frames of coverage; roughly equivalent to the depth of the Preliminary Data Release on the ecliptic. IPAC then extracted the source detections in the coadded images as described in section IV of the *WISE* Preliminary Release Explanatory Supplement, but with earlier versions of all software. The source extractions had a minimum signal to noise ratio (SNR) of 3.5 in one of *WISE*'s channels – half that used for the Preliminary Data Release – because reliability of the internal database was less of a concern than for the Preliminary Data Release.

The main selection criterion for objects in our survey was that the source was in the L3o database. We sorted these objects into three samples based on fluxes from *WISE*'s most

[1] `http://wise2.ipac.caltech.edu/docs/release/prelim/expsup/`

sensitive band, W1: 1) the design required *WISE* sensitivity of 120 μJy (5-σ, Liu et al., 2008), and 2) the initial estimate of the in-orbit sensitivity of 80 μJy (5-σ, Wright et al., 2010). We will refer to these samples by the following names, inspired by their flux ranges in μJy, from here on: $\{\geq 120\}$, $\{80\text{–}120\}$, and $\{< 80\}$ (includes sources not detected in W1). The classification based on W1 flux determined the priority in resolving conflicts when assigning slits on the mask, maximizing our ability to construct complete W1 flux limited samples. We adopted the profile fit photometry (`w1mpro`) for our flux measurements because we expect the majority of our targets, stars and field galaxies, to be point-like in the *WISE* beam (6.1$''$ full width at half maximum [FWHM]).

The only other selection criterion we imposed was that $R \geq 15.0$ mag, as suggested by the DEIMOS documentation, to avoid saturation of the detector. Out of a desire to maintain as wide a pool of targets as possible, we used the Naval Observatory Merged Astrometric Dataset (Zacharias et al., 2004, NOMAD) to perform this cut. The imprecision of photographic magnitudes is acceptable here due to the rarity of such bright sources and the fact that they are already well characterized by extant surveys.

The survey fields all had near their center a *WISE*-selected high-z ultra-luminous infrared galaxy (ULIRG) candidate from selection criteria addressed below. Since we expect that the rest of the field will be filled with objects at much lower redshift, this should not have significantly biased the survey. The presence of lower redshift contaminants, such as merging galaxies and AGN, in the color regions used to select these candidates does introduce a potential source of bias to our survey. We therefore include the ULIRG candidate selection criteria we used here even though we have found no evidence of such bias.

The *WISE* Extragalactic Team produced several different selection techniques for selecting ULIRGs and Hyper-Luminous Infrared Galaxies (HyLIRGS). One example of which can be found in the color-space plot in Figure 4.1. In this figure we used templates from the Spitzer Wide-area InfraRed Extragalactic survey (SWIRE Polletta et al., 2007) augmented by GRASIL models (Silva et al., 1998) to model the expected structure of the *WISE* W1$-$W2 versus W2 $-$ W3 color space.

We selected ULIRG candidates based on the results of a previous spectroscopy study done using the Low Resolution Imaging Spectrometer (LRIS, Oke et al., 1995) at Keck I that followed up *WISE*-selected ULIRG candidates (e.g. Eisenhardt et al., 2012). Of the 64 targets in the *WISE* team's LRIS observations as of August 2010, 18 were confirmed $z > 1.5$ ULIRGs. We used the *WISE* colors and magnitudes of these objects to define a region of color-magnitude space to select the 10 ULIRG candidates for our DEIMOS run. We used the *WISE* colors and magnitudes of the previously confirmed ULIRGs to produce the following limits: $0.3 < \mathrm{W1} - \mathrm{W2} < 2$, $\mathrm{W2} - \mathrm{W3} > 1.5$, $\mathrm{W3} - \mathrm{W4} > 2$, $\mathrm{W1} > 10$, $\mathrm{W2} > 10$, $\mathrm{W3} > 8$, and $\mathrm{W4} > 5.5$ mag. The magnitude limits were imposed to bias the selection towards very red (i.e., 12 and 22 μm bright) $z > 1.5$ ULIRGs. The details of the LRIS observations are described in Eisenhardt et al. (2012).[2]

Each DEIMOS mask consists of a rectangular $16.7' \times 5'$ field from which two corners and a circular arc along the long side are lost to vignetting, leaving a total area of 68.3 arcmin^2. Each target had a minimum slit length of $5''$ with $2''$ between the slits, allowing 70–80 targets per mask given the source densities in *WISE*'s L3o database. We designed the masks to have $2.0''$ wide slits in order to accommodate the astrometric uncertainties of the large number of fainter sources. As of September 2010, our understanding of the L3o database's astrometric accuracy could be found in Wright et al. (2010). They measured an astrometric uncertainty of $0.15''$ for *WISE* sources with SNR ≥ 20.0. Extrapolating downward in quadrature as a means of estimation, this implies a 1-σ 1-axis uncertainty of $0.62''$ for sources with SNR ~ 5. With a $1''$ slit that implies a loss rate of 42%, whilst a $2''$ slit gives 11%.

After positioning each field to contain the ULIRG candidate and 6 bright sources for alignment ($15 \leq R \leq 17$ mag), we assigned slits to objects in each of the categories using the dsimulator mask design software. Due to the high sampling rate of targets in the $\{\geq 120\}$ category we were able to include the good spectra for the alignment box targets without significantly biasing our results. All targets in a given W1 flux category had the same priority and thus the program assigned slits to them in such a way as to maximize the

[2]Much of this paragraph, and its technical content, was contributed by S. Petty

number of slits. We then added targets to the mask in order of decreasing category flux, resulting in the sampling rates given in Table 4.2.

We experienced a higher loss rate than anticipated due to the then-unknown pipeline error that led to quasi-random errors in declination in excess of the quoted positional uncertainty. Positions of objects in the *WISE* Preliminary Data Release may be offset from their true positions by many times the quoted positional uncertainty. Approximately 20% of the sources fainter than 491 μJy suffer from a pipeline coding error that biases the reported position by ~ 0.2–$1.0''$ in the declination direction. This error can affect sources as bright as W1 $\sim$ 2mJy. The effect of this error on slit losses can be mitigated by aligning slits away from an East-West PA. The Cautionary Notes section of the *WISE* Preliminary Release Explanatory Supplement describes the origin and nature of this effect in detail.

In principle a $1''$ error combined with a $2''$ wide slit should not present a problem for sources brighter than $i \sim 23$ mag with 45 minutes of integration on Keck. When combined with the astrometric uncertainty inherent in targeting sources with low SNR, though, it can result in the outright loss of a source. Some of our low SNR sources were as much as $4''$ away from the closest SDSS source. There are problems inherent in comparing surveys conducted at different wavelengths, so we did not perform a detailed analysis of all source offsets from SDSS counterparts. We were able to better quantify how many sources were lost due to this problem after the final pass processing is complete. The aforementioned error will be corrected and the images will have greater coverage depth than the frames used to make the L3o database. The number of sources without positional matches within $6''$ to non-artifact sources in the AllWISE data release is 13 - 10 in $\{< 80\}$ and 3 in $\{\geq 120\}$.

The primary focus of our survey was to obtain redshifts for the sources brighter than 80 μJy in W1. We therefore decided to integrate for a total of 45 minutes on each field, splitting the time into 5-minute and 40-minute exposures to maximize our dynamic range. This strategy also allowed us to expose the maximum of 10 fields possible with DEIMOS in the course of a single night. The instrument documentation suggested that this exposure time would yield an SNR in the range of 3–7 per pixel for a galaxy with $R_{\mathrm{AB}} = 21.0$ mag. We selected the lowest dispersion grating available in DEIMOS, 600 lines mm^{-1}, set for a

Table 4.2. Field Characteristics

Field Number	α (°)	δ (°)	PA (°)	b (°)	⟨Coverage⟩ (Frames)	$\{\geq 120\}$ ($f_{Q\geq3}/f_{\rm targ}/N_{\rm tot}$)	$\{80\text{–}120\}$ ($f_{Q\geq3}/f_{\rm targ}/N_{\rm tot}$)	$\{< 80\}$ ($f_{Q\geq3}/f_{\rm targ}/N_{\rm tot}$)	SDSS DR8
1	310.28533	−14.49725	120	−30.73209	12.9	0.97/0.70/84	1.00/0.29/34	0.78/0.22/41	Y
2	312.36350	−11.68394	107	−31.43735	12.3	1.00/0.59/99	0.90/0.30/33	0.71/0.18/40	N
3	313.93537	−12.49886	73	−33.17407	11.5	0.98/0.77/74	0.93/0.37/38	0.83/0.29/21	P
4	338.96217	16.07672	86	−35.70137	12.8	1.00/0.72/68	0.55/0.42/26	0.81/0.27/59	Y
5	345.77133	4.09244	90	−49.27066	13.1	1.00/0.69/55	0.89/0.36/25	0.56/0.34/95	Y
6	25.06929	−12.15469	37	−71.14944	8.9	0.91/0.81/54	0.85/0.38/34	0.58/0.30/88	N
7	27.71867	−18.08917	161	−73.59517	7.0	1.00/0.77/44	1.00/0.52/29	0.60/0.24/103	P
8	38.37908	23.55133	−169	−33.64597	11.8	1.00/0.80/45	0.91/0.46/24	0.62/0.51/57	Y
9	47.65929	12.24742	−109	−38.13031	10.9	1.00/0.76/46	0.75/0.51/39	0.56/0.24/75	P
10	50.92692	4.58761	50	−41.44942	10.9	0.98/0.74/58	0.72/0.49/37	0.65/0.35/57	Y
Combined	—	—	—	—	11.0	0.98/0.72/627	0.84/0.41/319	0.63/0.30/636	—

Note. — The mask coordinates (J2000 equatorial coordinates), position angle, Galactic latitude, median coverage in W1 as of the Preliminary Data Release, whether the field overlaps with SDSS DR8, and fraction of slits that produced high quality spectra / fraction of targets assigned slits / total available targets, broken down by W1 flux sample (limits in μJy). Per the recommendation made in the DEEP2 pipeline, the slits were set for 5° greater than the mask PA. The letters in the SDSS DR8 column denote whether the field overlaps with SDSS DR8, and stand for 'Yes,' 'No,' and 'Partial.'

750.0 nm central wavelength with the order blocking filter GG495. This produced a wavelength range of 495–1015 nm for targets near the center line of the mask, and a moderate resolution. For objects filling the $2''$ slit we achieved a resolving power of $R = \lambda/\Delta\lambda = 861$ at $\lambda = 736.9$ nm. Exploring the resolving power across the wavelength range revealed that we were slit width limited, as shown by a strongly linear trend of the form $R = \lambda/\lambda_0$.

The artifact identification system was not used in the production of the L3o database we used for target selection, and we deliberately did not pre-reject sources based on visual identification on the chance that they may have been real sources that were contaminated. There was, therefore, definitely some contamination of the sample — we later confirmed 9 targets as artifacts by examining the *WISE* images for targets that showed no optical emission and eliminated them from consideration in all metrics of the survey. To minimize the impact of this without introducing any non-flux cuts to the survey we positioned the fields to avoid very bright stars (W1 $\gtrsim$ 11.0 mag) that produce large diffraction spikes.

We performed the data reduction using the DEEP2 pipeline, and the analysis using the SpecPro software package described in Masters & Capak (2011). SpecPro calculates redshifts based on a cross correlation of templates to the 1-dimensional spectra, but we required clear identification of matching emission or absorption features to consider the redshift reliable. We calculated K-corrections using a weighted geometric mean of the low resolution spectral energy distribution (SED) templates of Assef et al. (2010) as a crude approximation made for the sake of simplicity. Specifically, we used templates for Elliptical, Sbc and Im galaxies and assigned them weights 0.5, 0.25, and 0.25, respectively. This approximation was made because nearly half of our sample did not have enough multi-wavelength broad-band photometry to perform proper SED fits to estimate K-corrections.

4.3 Results and Discussion

We were able to successfully measure high quality redshifts based on visually identifiable emission or absorption features for 640 of the 762 targets in the 10 masks not lost to vignetting. Five of our fields fall within, and three of them partially overlap with, the Sloan

Digital Sky Survey data release 8 (Aihara et al., 2011, SDSS DR8), as seen in Table 4.2. We therefore classified the fraction of targeted sources for which we obtained high quality spectra by flux density using both W1 and SDSS i band model magnitudes in Figure 4.2. This allows us to characterize the performance of our spectroscopic survey relative to the rest of the *WISE* survey for W1 and the sources contained in both *WISE* and SDSS for i. Our survey successfully classified $> 90\%$ of the target list for sources with W1 $\lesssim 16\,\mathrm{mag}$ and $i \lesssim 20.75\,\mathrm{mag}$, and $> 50\%$ for W1 $\lesssim 18\,\mathrm{mag}$ and $i \lesssim 23\,\mathrm{mag}$.

In the following sub-sections we will discuss the properties of targets we were able to characterize using spectra such as those shown in Figure 4.3 and attempt to estimate the composition of those that we could not. If the spectrum produced a science grade classification and redshift we assigned quality class, Q, of three or four. If the spectrum was inconclusive but confirmed the presence of a source then Q is zero, one or two. If there was no evidence of emission in excess of the sky background anywhere, then $Q = -1$.

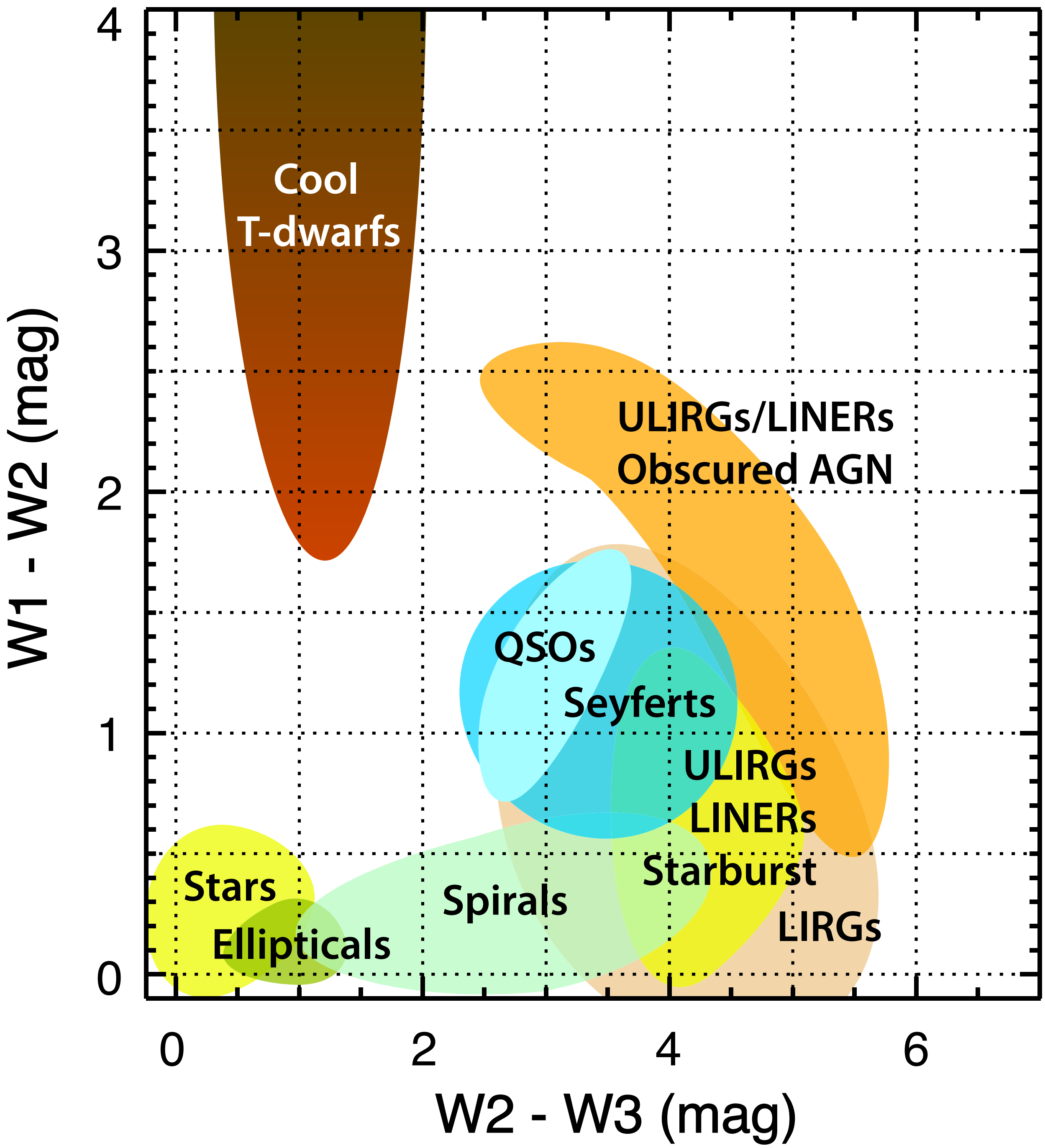

Figure 4.1: Color space regions where different classes of *WISE* detected sources, both Galactic and extragalactic, would fall based on SWIRE templates augmented by GRASIL models. Adapted by its original author, C.-W. Tsai, from the graph published in Wright et al. (2010).

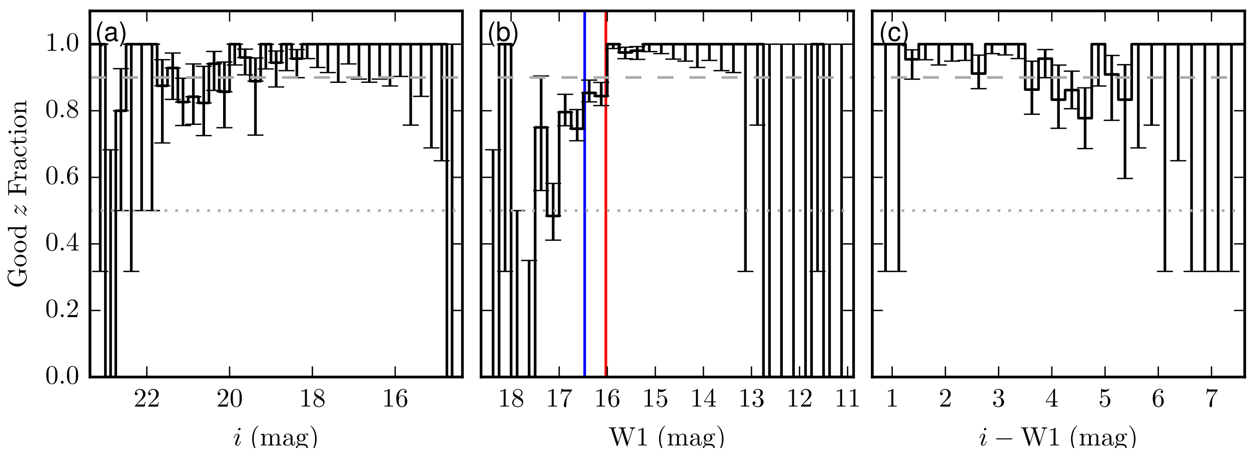

Figure 4.2: The fraction of sources with magnitude uncertainty less than 1.0 in each magnitude bin that had $Q \geq 3$ spectra. Panel a) shows the fraction of sources with good redshifts as a function of i band AB model magnitudes using SDSS photometry. Panel b) shows the good redshift fraction as a function of W1, with the sample boundaries highlighted using the solid vertical dark grey and light grey lines (colored blue and red for 80 and 120 μJy, respectively, in the online version). Panel c) shows the same quantity as a function of W1 $- i$ color. Error bars assume that obtaining a good spectrum was a binomial random process, with confidence intervals constructed according to the technique in Feldman & Cousins (1998).

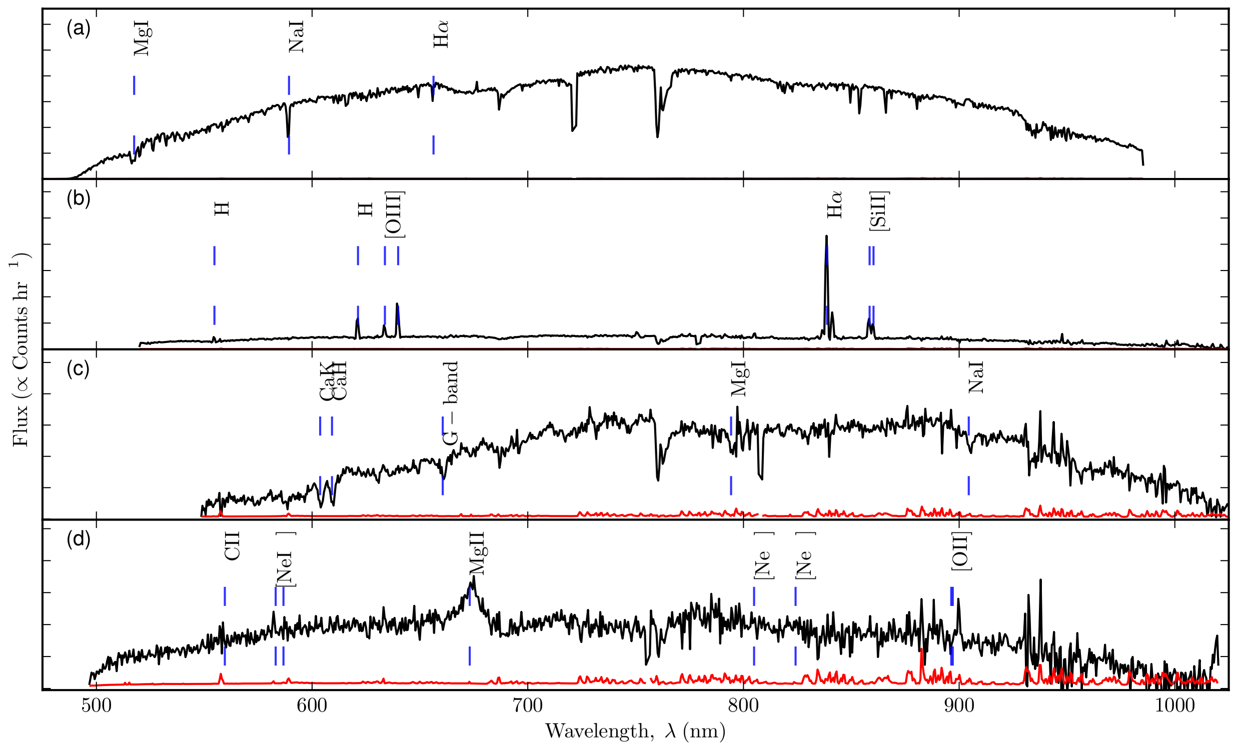

Figure 4.3: Typical spectra we obtained for different classes of objects. All the spectra are uncalibrated and binned down eight to one for clarity. All plots are in observed frame wavelengths with typical spectral lines we used to identify such objects labeled with vertical broken lines (colored blue in the online version), even if the feature is not evident in the example spectrum. The line near the bottom of each graph is the standard deviation of the flux at the given wavelength (colored red in the online version). Panel (**a**) is a spectrum for a K-type star, (**b**) is an emission line galaxy at $z = 0.27802 \pm 0.00003$, (**c**) is an absorption line galaxy at $z = 0.535 \pm 0.001$, and (**d**) is a broad-lined AGN at $z = 1.406 \pm 0.001$. All of the spectra shown are in the quality class $Q = 4$.

4.3.1 Stellar Results

Figure 4.4 shows the stellar density for sources with W1 fluxes $\geq 80\,\mu$Jy on a field by field basis, compared with the expected stellar contribution based on the Galactic star count model of Jarrett et al. (1994). The results are in good agreement with the model both overall and on a field by field basis. The breakdown of our target stars by spectral class is in Figure 4.5. We also checked our stellar population for the occurrence of statistically significant color excesses in the longer wavelength channels of *WISE*. Of the 338 stars we spectrally identified, none of them presented a color $W1 - Wx \geq 1.0$ with the restriction that SNR ≥ 7.0 in both of the channels used to calculate the color.

4.3.2 Extragalactic Results

One simple measure of a photometric survey is the median redshift of the galaxies detected. We estimate that *WISE* detects field galaxies back to the median redshift of at least 0.48 ± 0.02 by linearly interpolating the cumulative distribution that corresponds to Figure 4.6. The reason for referring to this value as a lower limit is due to the fact that we did not correct for the median lowering bias caused by reduced success rates in measuring redshifts of galaxies from the fainter samples. A more detailed breakdown of the median redshift by flux depth and galaxy spectral type can be found in Table 4.3. In principle, our results could also have been biased by the different spectral features present on the detector as a function of galaxy spectral type and redshift. For example, an absorption line galaxy with $z \lesssim 0.2$ would not have presented visible Ca II H and K lines, leaving us to rely on the less prominent Na I doublet at 580.3 nm and the Mg I line at 517.5 nm for measuring the redshift. The lesser prominence of these lines, however, means that we are more likely to be able to classify a faint source at higher redshift rather than at than lower, as evidenced by the absence of $\{< 80\}$ sources in the three lowest bins of Figure 4.6.

A more important measure of the depth achieved, however, is the redshift to which $L_\star$ galaxies are detected in abundance, because this sets the depth to which the survey can provide constraints on the faint-end slope of the luminosity function. In Figure 4.7 we have plotted the luminosity of our sources versus their redshift alongside the simple evolving model for $L_\star(z)$ from Dai et al. (2009) ($L_\star(z) = L_{\star 0}10^{0.4Qz}$, $Q = 1.2 \pm 0.4$), making the approximation that the *Spitzer* InfraRed Array Camera (IRAC) channel 1, with effective wavelength $3.6\,\mu$m, is the same as W1. From this function for $L_\star(z)$ we find that at a W1 flux limit of $80\,\mu$Jy *WISE* detects $L_\star$ galaxies back to $z = 0.7^{+0.3}_{-0.2}$.

Our estimate of the redshift to which *WISE* detects $L_\star$ galaxies has a caveat to its accuracy. The evidence that a caveat is needed comes from the mismatch between the predicted galaxy densities and the observed densities, seen in Figures 4.4 and 4.6. In total *WISE* detects at least $(1.9 \pm 0.1) \times 10^3$ counts deg^{-2} field galaxies with observed W1 flux $\geq 80\,\mu$Jy while the prediction from the model is $(5 \pm 2) \times 10^3$ counts deg^{-2}, a discrepancy of 1.3σ. Although the mismatch is not statistically significant, it is unlikely to be due to incompleteness in our survey, but possibly due to the extrapolation of their results to a flux limit of $80\,\mu$Jy. The sample used by Dai et al. (2009) was limited to $[3.6] > 143\,\mu$Jy (< 15.7 mag) and their analysis was restricted to $z < 0.6$. As discussed by Dai et al. (2009), the $M_\star$ evolution they find is faster than that found by other surveys (although at different wavelengths) and seems to overestimate that of other studies at higher redshifts (see their Figure 10). Coupled with their assumption of a non-evolving faint-end slope (determined primarily from their $z < 0.2$ sample), this could tentatively explain the differences we find. A detailed study of the WISE-selected mid-infrared galaxy luminosity function is the subject of Chapter 6.[3]

Figures 4.4 and 4.6 also provide evidence that our ULIRG candidate targeting did not introduce a significant bias toward over-dense fields. Both the radial and angular densities show little evidence for the presence of large clusters. Indeed, the one significant single field over-density in redshift we found at $\langle z \rangle = 0.2127 \pm 0.0006$ was in field 6 ($b \approx -71°$) and the ULIRG candidate was at $z \approx 1$.

We have found that the $1.6\,\mu$m bump in the typical galaxy SED produces a straightforward correlation between many of the *WISE*/SDSS colors and redshift for galaxies without

[3]Much of this paragraph was originally written by R. J. Assef and D. Stern.

observed broad-line emission. The correlation is strongest using the g, r, or i filter with W1, but is apparent when matching any SDSS filter with W1 or W2. We plot an example in Figure 4.8, using i because it is the SDSS band nearest to the center of our spectra. We fit $\ln(F_{\mathrm{W1}}/F_i)$ to $\ln(1+z)$ using a function of the form $y = m(x - x_0) + b$ and a badness of fit/likelihood:

$$- \ln(\mathcal{L}) = \frac{1}{2}\sum_{i=1}^{N}\left[\frac{(y_i - m[x_i - x_0] - b)^2}{\sigma_{y,i}^2 + [m\sigma_{x,i}]^2 + \sigma_{\mathrm{ext}}^2} + \frac{1}{2}\ln\left(\sigma_{y,i}^2 + [m\sigma_{x,i}]^2 + \sigma_{\mathrm{ext}}^2\right)\right], \qquad (4.1)$$

where σ_{ext} is the extrinsic scatter in excess of the statistical uncertainty of the measurements and it, alongside m and b, is a fit parameter on which we optimize $\mathcal{L}$. We set x_0 as a free parameter to reduce the off-diagonal terms of the covariance matrix of the main fit parameters. Specifically, we set $x_0 = \langle x_i \rangle$ with weights $w_i = \left(\sigma_{y,i}^2 + [m\sigma_{x,i}]^2 + \sigma_{\mathrm{ext}}^2\right)^{-1}$. The resulting parameters can be found in Table 4.4. The implication of this correlation is that Figure 4.2c) gives us a rough estimate of our completeness relative to *WISE* as a function of redshift. Specifically, we are 90% complete to $z \sim 0.5$ and 50% complete to $z \sim 0.9$.

We present in Tables 4.5 and 4.6 an excerpt of the redshift catalog, which will be made available as an electronic table with the paper that will be based on Chapter 5 and at at `https://dx.doi.org/10.6084/m9.figshare.3860016`.

4.3.3 The Spectroscopically Unclassifiable Population

The breakdown of the spectral qualities by sample can be found in Table 4.7. Table 4.8 presents classifications rates as a function of spectrum type and bandpass for sources with magnitude uncertainties ≤ 1 mag. It is clear from the detection rates in Table 4.8 that the most complete choice, overall, for analyzing the sample for which we could not get $Q > 2$ spectra is to match W1 with SDSS r, i, or z. Given the wavelength coverage of our spectra, we choose to use r and i.

We also provide Figure 4.9 for comparison with Figure 4.1. While there are several stars outside of the boundary outlined for main sequence stars in Figure 4.9, and this could be considered indicative of the presence of debris disks (Wolf & Hillenbrand, 2003), these sources should be approached with caution. All of them have a W3 SNR in the range $(1.7, 3.5)$ and

Table 4.3. Extragalactic Summary

Galaxy Spectral Type	W1 Flux (μJy)	Density (count arcmin^{-2})	median z[a]	Source count
Absorption[b]	≥ 120	0.16 ± 0.02	0.32 ± 0.03	82
	≥ 80	0.26 ± 0.03	0.37 ± 0.01	109
	≥ 0	0.32 ± 0.03	$0.40^{+0.03}_{-0.02}$	121
Emission[c]	≥ 120	0.14 ± 0.03	0.32 ± 0.02	69
	≥ 80	0.28 ± 0.03	$0.42^{+0.02}_{-0.03}$	111
	≥ 0	0.69 ± 0.05	0.52 ± 0.02	191
All Field[d]	≥ 120	0.30 ± 0.02	0.32 ± 0.01	151
	≥ 80	0.54 ± 0.04	0.38 ± 0.02	221
	≥ 0	1.01 ± 0.06	0.49 ± 0.02	313
Broad-lined AGN	≥ 120	0.022 ± 0.007	$0.53^{+0.30}_{-0.05}$	11
	≥ 80	0.028 ± 0.008	$0.83^{+0.04}_{-0.30}$	13
	≥ 0	0.05 ± 0.01	$0.94^{+0.16}_{-0.06}$	17

[a]Calculated by linearly interpolating the cumulative counts histogram using the same bins as in Figure 4.6.

[b]Galaxies without detected emission lines.

[c]Galaxies with detected emission lines that are not obviously broadened.

[d]Union of Absorption and Emission galaxies.

Note. — Extragalactic population density and median redshift as a function of galaxy type and W1 flux cutoff. The densities cannot be obtained by dividing the target count column by the survey area because of the sampling rate corrections needed.

Table 4.4. $i - \mathrm{W1}$ vs. $\ln(1+z)$ Fit Parameters

y-variable	slope (m)	y-intercept (b)	Scatter (σ_{ext})	x-offset (x_0)
$\ln(F_{\mathrm{W1}}/F_i)$	4.2 ± 0.2	1.05 ± 0.03	0.33 ± 0.02	0.364
$i - \mathrm{W1}$	4.6 ± 0.2 mag	3.81 ± 0.03 mag	0.36 ± 0.02 mag	0.364

Table 4.5. *WISE*/DEIMOS Redshift Catalog (Excerpt, Column Set 1)

Designation	ID	Ra	Dec	W1targ	TG	mask	SlitNum	z	z_err	q_z
		(°)	(°)	Vega mag						
WISEPC J204135.21-143417.4	1	310.3967285	-14.5715008	14.67	2	1	1	0.0	nan	4
WISEPC J204119.59-143134.0	2	310.3316345	-14.5261354	14.641	2	1	2	0.0	nan	4
WISEPC J204137.83-143121.4	3	310.4076538	-14.5226231	15.516	2	1	3	0.0	nan	4
WISEPC J204049.57-142749.0	4	310.2065735	-14.463625	15.541	2	1	4	nan	nan	0
NA	5	310.2065736	-14.463626	nan	5	1	4	0.0	nan	2
WISEPC J204105.33-142605.4	6	310.2722473	-14.4348354	14.018	2	1	5	0.0	nan	4
WISEPC J204046.91-142428.3	7	310.1954651	-14.4078646	15.265	2	1	6	0.0	nan	4
WISEPC J204136.37-143333.8	8	310.4015503	-14.5594082	15.682	2	1	7	0.0	nan	4
WISEPC J204124.66-143326.9	9	310.3527832	-14.5574875	15.351	2	1	8	0.0	nan	3
NA	10	310.3527833	-14.5574876	nan	5	1	8	0.0	nan	4

Note. — First set of columns of example lines from the catalog of redshifts we will be making available based on data gathered with DEIMOS. The first set of columns are shown in Table 4.6. Note that the selection magnitudes came from the L3o database used for internal verification and are thus extremely preliminary. `Designation` is the official designation in the *WISE* Preliminary Catalog, with `NA` if the source was serendipitously on the slit. `ID` is a unique integer assigned to the source in the catalog. `Ra` and `Dec` are the right ascension and declination in J2000 decimal degrees. `W1targ` is the Vega relative W1 magnitude used to classify sources into target groups. `TG` is the target group the source falls into: 2 is in $\{\geq 120\}$, 3 is in $\{80\text{–}120\}$, 4 is in $\{< 80\}$, and 5 is a serendipitous source. `mask` is the slit mask/field the source is in. `SlitNum` is the number of the slit the source fell on. `z` is the geocentric redshift observed for the source on the single night survey. `z_err` is the uncertainty in the redshift SpecPro calculates based on cross correlation of the template. `q_z` is the subjective redshift quality (≥ 3 is science quality).

Table 4.6. *WISE*/DEIMOS Redshift Catalog (Excerpt, Column Set 2)

`ID`	`class`	`SpecProTemplate`	`R`	`cont`	`SpecFeatures`
1	Star	G Star	1	1	NaI Ha
2	Star	M Star	1	1	NaI BaI
3	Star	G Star	1	1	NaI Ha
4	Indet	NA	1	0	
5	Star	K Star	1	1	
6	Star	G Star	1	1	NaI Ha
7	Star	M Star	1	1	NaI TiO BaI Ha TiO
8	Star	K Star	1	1	NaI BaI Ha
9	Star	A Star	1	1	Ha
10	Star	M Star	1	1	NaI TiO BaI TiO

Note. — Second set of columns of example lines from the catalog of redshifts we will be making available based on data gathered with DEIMOS. The first set of columns are shown in Table 4.5.`ID` is repeated here for clarity, but not in the electronic table. `class` is the spectroscopic classification of the target, one of: Star, Gal (galaxy), QSO (broad-line AGN), Indet (spectrum seen, indeterminate), and Unseen (nothing detected at the right position on the slit). `SpecProTemplate` is the template in SpecPro that was subjectively closest to the observed spectrum. `R` is an integer that is 1 if the source is 'real' (within $6''$ of an AllWISE source that is not flagged as an artifact in W1), 0 otherwise. `cont` is 1 if continuum flux was visible in the spectrum, 0 otherwise. `SpecFeatures` is a list of identified spectroscopic features, in order of increasing wavelength, by the name given to them in SpecPro.

the size of the color excess varies nearly monotonically with the decrease in the W2 SNR. In short, these detections are near the noise floor of W3 and therefore the criterion that $\sigma_{W3} \leq 1.0$ is really a lower limit on the uncertainty in the flux in the direction of zero. Such Gaussian error estimates do not include the asymmetry required by a more rigorous treatment of the statistics. We also cannot rule out chance alignments with background objects that are dominating the *WISE* colors coinciding with a star that dominated the DEIMOS spectra.

Of the 759 not yet identified as spurious targets in our survey, 461 (60%) are in the coverage of SDSS DR8. Of those covered, only 56 (12%) did not have a clear counterpart in the SDSS DR8 database. From those 56 without a clear counterpart, we were able to get 20 (36%) good spectra. Of the 405 targets with SDSS counterparts we failed to get good spectra for 20 (5%). This has also given us the opportunity to characterize the sources that were in Sloan and not characterized by our survey, as shown in the color-color plot in Figure 4.10. There is an obvious bias toward missing targets that are in the predominantly extragalactic region of the color-color plot. This is consistent with the fact that the missed sources were overwhelmingly from the faintest sample, $\{< 80\}$, and the findings in Jarrett et al. (2011) that galaxies outnumber stars at the North Ecliptic Pole ($b \sim 30°$) for W1 $\gtrsim 15.0\,$mag (W1 flux $\lesssim 300\,\mu$Jy). Also of note is that the undetected galaxies are almost entirely from the region with $r - \mathrm{W1} \geq 4.2\,$mag, reinforcing the probability that our survey has a bias against high redshift sources.

We have listed in Table 4.9 all of the targets which had an SNR ≥ 7.0 in one of the *WISE* bands and for which there is no corresponding detection in the SDSS database, no Two Micron All Sky Survey (2MASS) detection, and no evidence of optical flux in the spectra we obtained. The purpose of Table 4.9 is to enable potential further followup of what are, at present, uniquely *WISE* sources.

Table 4.7. Spectroscopic Quality by Sample

Q	$\{\geq 120\}$ ($N_{\rm tot} = 449$)	$\{80$–$120\}$ ($N_{\rm tot} = 130$)	$\{< 80\}$ ($N_{\rm tot} = 183$)
3–4	98.9%	84.0%	66.9%
0–2	1.1%	11.5%	16.9%
-1	0.0%	4.6%	16.3%

Note. — The fraction of targets in each spectral quality class broken down into the W1 flux ranges that defined each sample, in μJy.

Table 4.8. Spectroscopically Classified Target Detection Rate by Channel

Filter Name	Emission Galaxies ($f_{Q>2}$ [$N_{\rm tot}$])	Absorption Galaxies ($f_{Q>2}$ [$N_{\rm tot}$])	Broad-lined AGN ($f_{Q>2}$ [$N_{\rm tot}$])	Stars ($f_{Q>2}$ [$N_{\rm tot}$])
u	54.4% [114]	30.3% [66]	91.7% [12]	76.4% [212]
g	76.3% [114]	83.3% [66]	100.0% [12]	98.1% [212]
r	83.3% [114]	93.9% [66]	100.0% [12]	99.1% [212]
i	84.2% [114]	95.5% [66]	100.0% [12]	99.1% [212]
z	82.5% [114]	93.9% [66]	100.0% [12]	97.6% [212]
J	5.2% [191]	19.0% [121]	17.6% [17]	80.2% [343]
H	5.2% [191]	19.0% [121]	11.8% [17]	78.7% [343]
K_s	5.2% [191]	18.2% [121]	17.6% [17]	65.6% [343]
W1	99.0% [191]	99.2% [121]	94.1% [17]	100.0% [343]
W2	99.0% [191]	98.3% [121]	94.1% [17]	99.7% [343]
W3	72.8% [191]	59.5% [121]	82.4% [17]	56.0% [343]
W4	51.8% [191]	61.2% [121]	70.6% [17]	60.3% [343]

Note. — The fraction of targets with high quality ($Q > 2$) spectra detected ($\sigma \leq 1.0$ mag) by each photometric band, with the number of total available targets in brackets next to the fraction in percent. The photometry used to construct this table came from SDSS DR8, 2MASS, and *WISE*.

Table 4.9. Well Detected Targets Without External Confirmation, Part 1

Designation	α ($^\circ$)	δ ($^\circ$)	W1 (mag)	W2 (mag)	W3 (mag)	W4 (mag)	SDSS DR8
WISEPC J223522.72+160246.4	338.844696	16.0462303	16.55 ± 0.08	15.92 ± 0.14	(12.5)	(10.6)	Y
WISEPC J223520.69+160256.2	338.8362122	16.0489521	16.26 ± 0.06	16.06 ± 0.17	(11.9)	(8.8)	Y
WISEPC J223612.04+160410.9	339.0502014	16.0696964	16.80 ± 0.10	15.77 ± 0.13	(13.0)	(8.9)	Y
WISEPC J223549.62+160325.9	338.9567566	16.0572128	17.30 ± 0.15	16.07 ± 0.19	(12.8)	(8.8)	Y
WISEPC J230244.12+040424.8	345.6838684	4.0735693	16.94 ± 0.11	16.22 ± 0.20	(13.7)	(8.9)	Y
WISEPC J230232.49+040640.5	345.6354065	4.1112514	16.86 ± 0.10	16.45 ± 0.25	(12.4)	(8.9)	Y
WISEPC J230337.04+040652.5	345.9043579	4.1145945	16.67 ± 0.09	16.24 ± 0.20	(12.3)	(8.4)	Y
WISEPC J014002.89−121449.2	25.0120697	−12.2470074	16.48 ± 0.07	15.95 ± 0.16	12.71 ± 0.47	(8.9)	N
WISEPC J014015.47−120412.0	25.0644922	−12.070013	17.11 ± 0.12	16.31 ± 0.20	(12.1)	(9.0)	N

Note. — The positions and *WISE* photometry for sources that lack confirming detections in SDSS DR8, 2MASS, or this survey. All sources on this list must have SNR ≥ 7.0 in at least one *WISE* channel in the AllWISE catalog and have $\mathtt{R} = 1$ in the catalog described in this work are included. Magnitudes in parentheses are 2-σ upper limits on the flux. The right ascension (α) and declination (δ) are in J2000 decimal degrees. The magnitudes are all Vega relative and come from the AllWISE survey. The SDSS DR8 column is 'Y' if the source falls within the footprint of the SDSS DR8 photometric catalog, 'N' if not.

Table 4.10. Well Detected Targets Without External Confirmation, Part 2

Designation	α (°)	δ (°)	W1 (mag)	W2 (mag)	W3 (mag)	W4 (mag)	SDSS DR8
WISEPC J015105.38−181240.8	27.77243235	−18.2113495	16.96 ± 0.10	16.26 ± 0.21	(13.3)	(8.8)	N
WISEPC J023332.24+233608.5	38.3843384	23.6023865	16.75 ± 0.10	16.13 ± 0.20	(13.1)	(8.9)	Y
WISEPC J023331.58+233632.1	38.3816109	23.6089439	17.17 ± 0.12	16.03 ± 0.17	12.4 ± 0.5	(8.9)	Y
WISEPC J023330.90+233924.9	38.378788	23.6569328	16.44 ± 0.07	15.98 ± 0.16	(13.1)	(9.1)	Y
WISEPC J031012.81+121232.6	47.5534058	12.2090826	16.76 ± 0.10	(16.3)	12.4 ± 0.5	(8.4)	N
WISEPC J031044.10+121309.5	47.683773	12.2193298	16.84 ± 0.11	15.91 ± 0.16	(12.2)	(8.9)	Y
WISEPC J031108.75+121544.4	47.7864838	12.2623577	17.01 ± 0.13	15.77 ± 0.16	(12.2)	(9.5)	N
WISEPC J032345.02+043501.2	50.9376183	4.5836883	16.12 ± 0.06	15.39 ± 0.10	(12.4)	(9.0)	Y
WISEPC J032342.02+043503.6	50.9251213	4.5843415	16.22 ± 0.06	15.74 ± 0.14	(13.6)	(9.1)	Y
WISEPC J032321.13+043126.1	50.8380814	4.5239253	16.59 ± 0.08	16.44 ± 0.26	(11.6)	(8.9)	Y

Note. — See Table 4.9 for a description of the contents of this table. This one is merely a continuation of the contents therein.

4.4 Conclusion

With its ability to detect $L_\star$ galaxies out to $z \sim 0.7$ in the areas with fewest repeat observations and its nearly 4π sr coverage, *WISE* is able to play an important role in studies of galaxy populations and cosmic structures at moderate redshifts. Chapter 6 reports on the $3.4\,\mu$m luminosity function to redshift $z \leq 1$, derived using this data in conjunction with public spectroscopic data sets. In Chapter 7 we trace the contribution to extragalactic background light in the mid-IR from galaxies and constrain the stellar mass of galaxies.

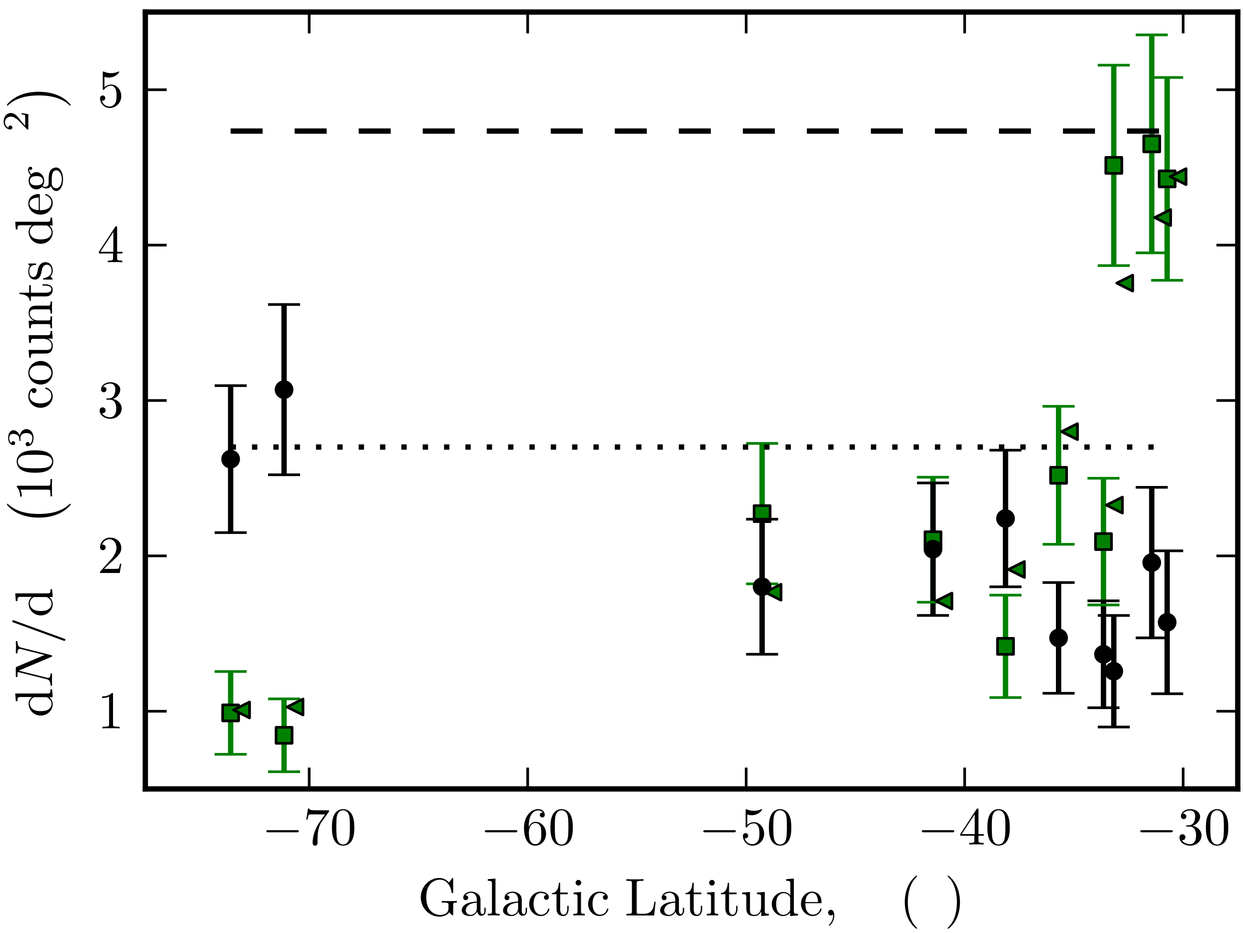

Figure 4.4: Observed versus predicted source densities for sources with W1 flux $\geq 80\,\mu$Jy. The black circles are the observed galaxy densities, while the prediction is the horizontal dashed line and the 1-σ uncertainty in that prediction is the dotted line. The squares are the observed star densities, and the triangles shifted to the right are the prediction (colored green in the online version). The predicted star counts are based on a model adapted from Jarrett et al. (1994). The predicted galaxy counts come from integrating a Schechter luminosity function using the parameters measured in Dai et al. (2009) using the *Spitzer*/IRAC 3.6 μm channel out to a redshift of 1.25.

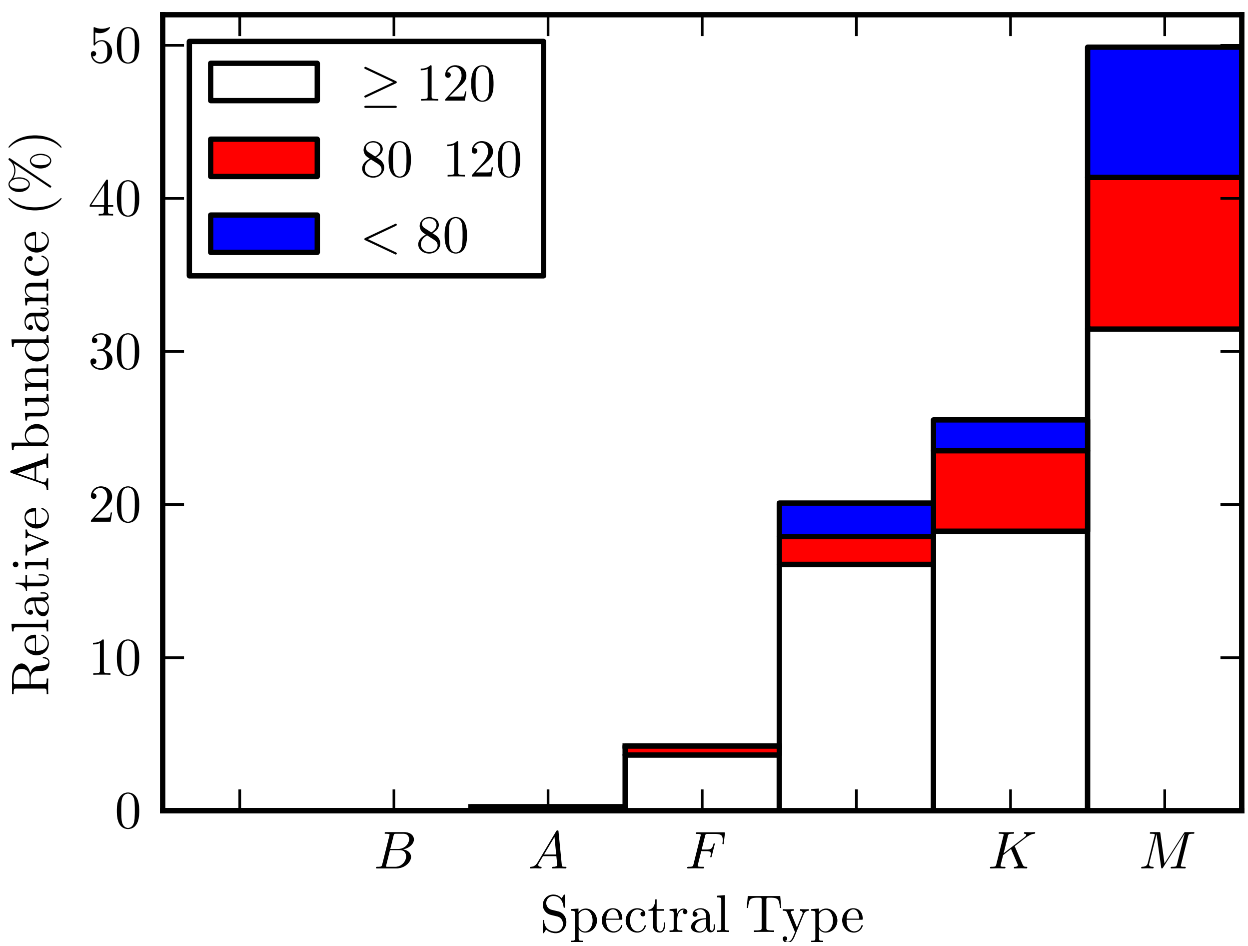

Figure 4.5: Relative abundances of the different stellar spectral types. All quantities are attempt rate corrected. The accuracy of the spectral classification of an individual star is accurate to at least ± half a spectral class. The accuracy is better in the case of M-type stars and stars that have good optical photometry from SDSS DR8.

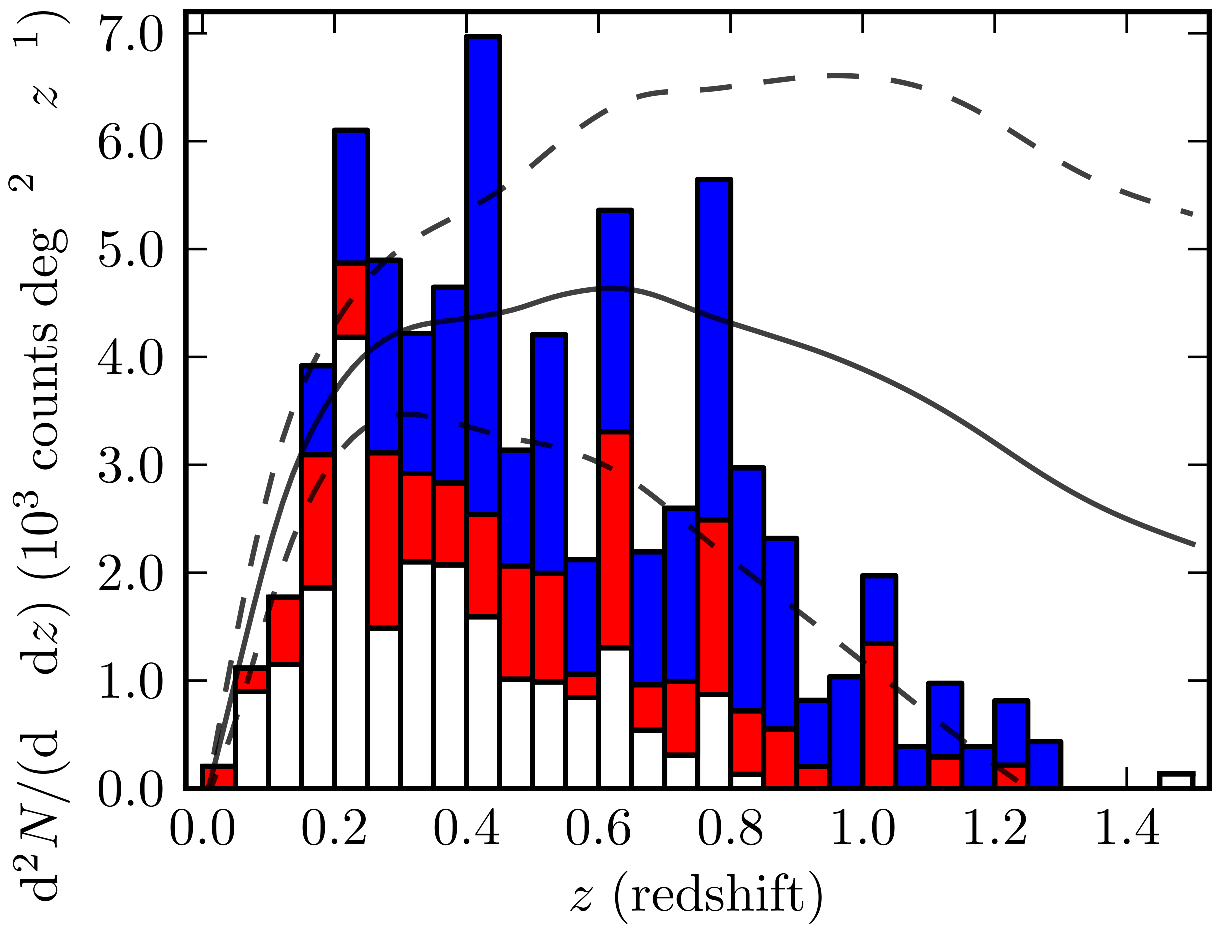

Figure 4.6: Stacked bar histogram of the robust spectroscopic redshifts from our survey. The white bars are the $\{> 120\}$ sample, the light grey (red in the online version) bars are the $\{80–120\}$ sample, and the dark grey (blue in the online version) bars are the $\{< 80\}$ sample. The height of each bar was sampling rate corrected on a field by field basis by dividing by the values in Table 4.2. The solid line represents the predicted source density based on integrating a Schechter function with the parameters from Dai et al. (2009) down to an observable flux limit of 80 μJy. The dashed lines are the 1-σ confidence band for the prediction.

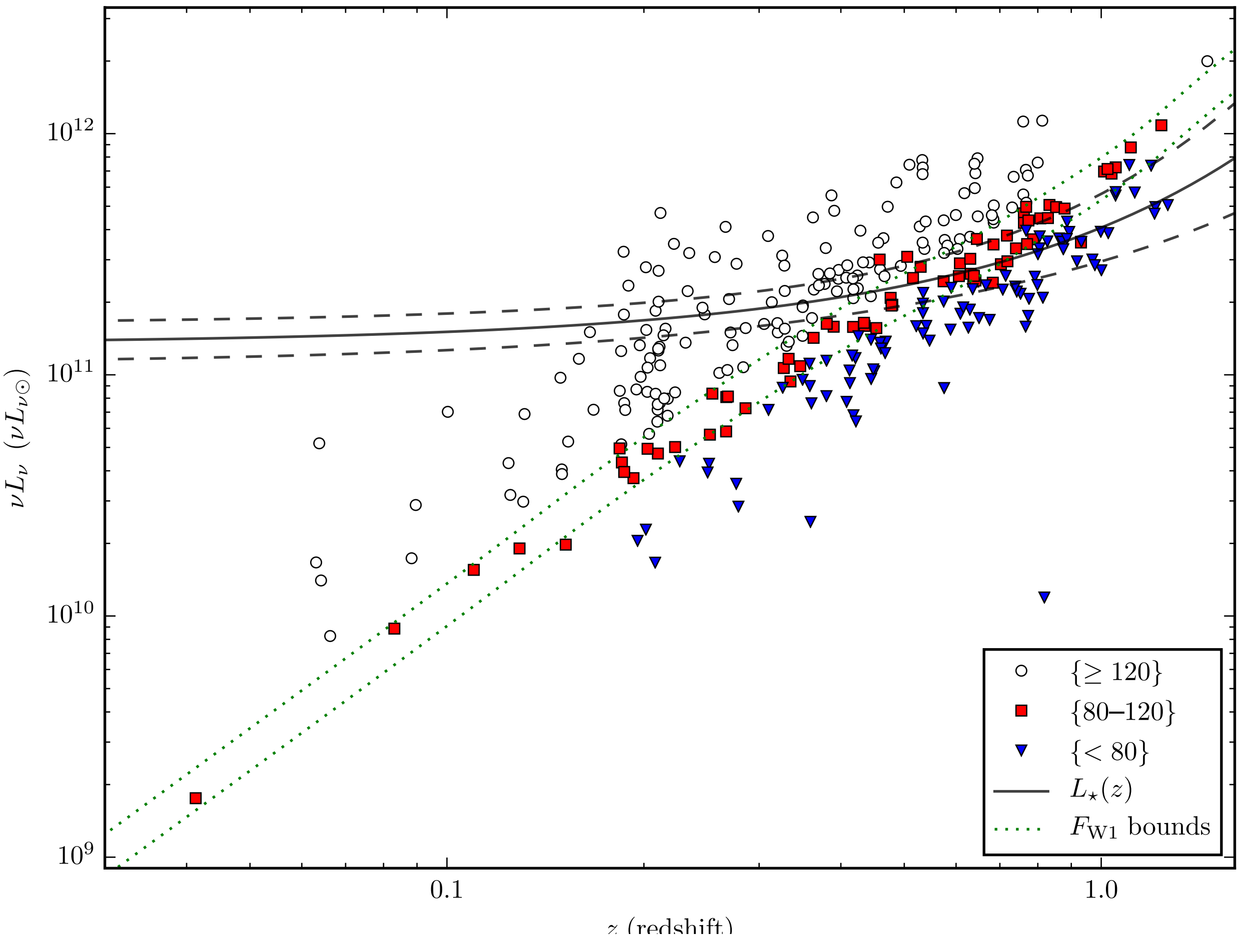

Figure 4.7: W1 luminosity, approximated as νL_ν in units where νL_ν for Sol is 1, against observed redshift. The solid line represents the expected $\nu L_\nu(z)$ for $L_\star$ galaxies based on the linearly evolving $M_\star$ measurement from Dai et al. (2009) using the *Spitzer*/IRAC 3.6 μm channel. The dashed lines are the 1-σ confidence bands from straightforward error propagation of the uncertainties in the luminosity function parameters. The dotted lines are $\nu L_\nu(z)$ for an 120 μJy and 80 μJy source. The sources that cross into other regions are due to higher SNR photometry that became available after target selection.

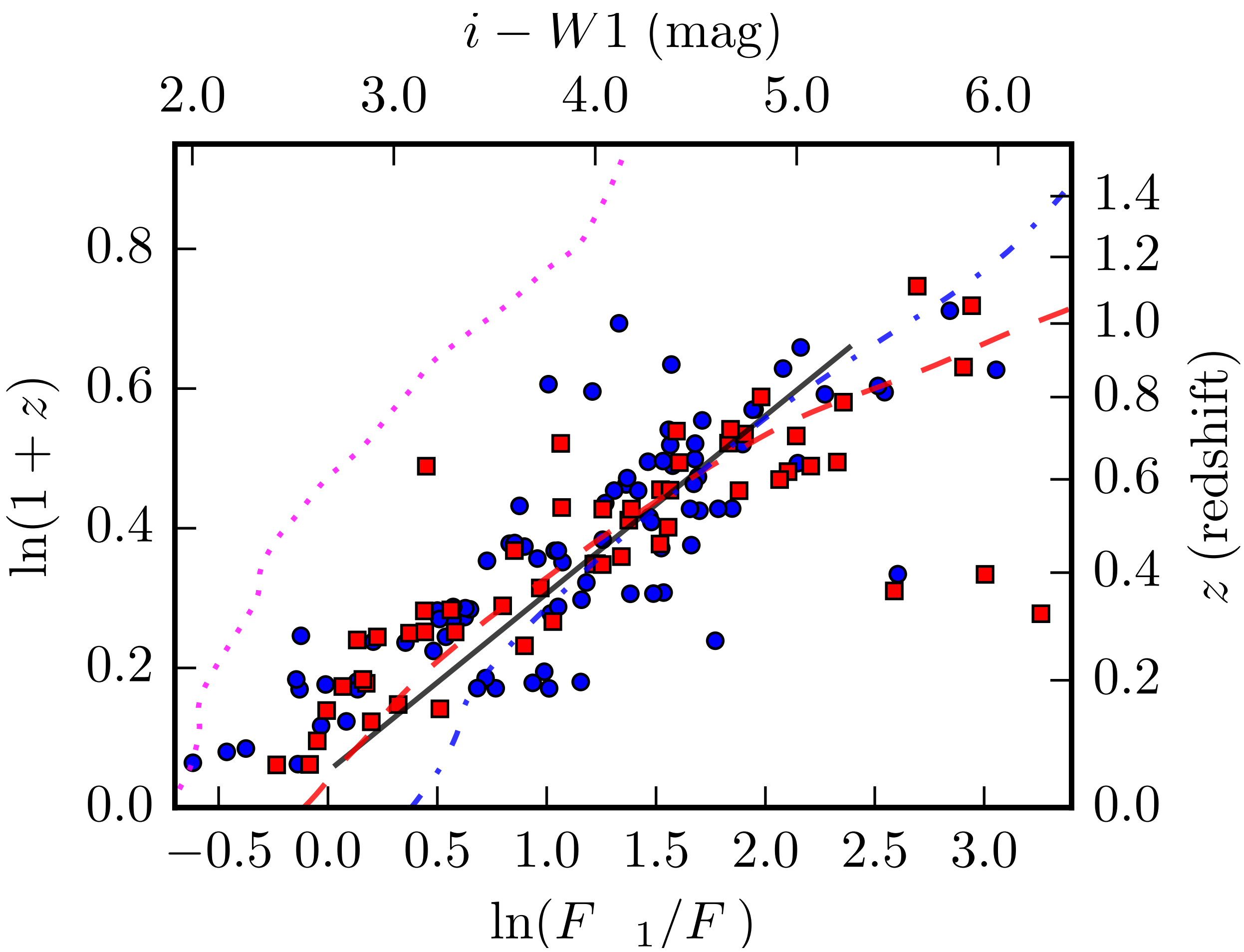

Figure 4.8: $\ln(1+z)$ versus $\ln(F_{\mathrm{W1}}/F_i)$ (both fluxes in Jy) color for non-broad-lined sources in our survey that have high quality ($Q > 2$) spectra, unique source correlation between SDSS and *WISE*, and both σ_i, $\sigma_{\mathrm{W1}} \leq 1.0\,\mathrm{mag}$. The circles are galaxies for which we detected emission lines (blue in the online version) and the squares had only absorption lines (red in the online version). The solid line is the result of a maximum likelihood fit of color to a linear function of $\ln(1+z)$ with extrinsic scatter for points with $z \leq 1$. The dashed, dash-dotted, and dotted lines are the tracks formed by the Elliptical (red online), Sbc (blue online), and Im (magenta online) templates from Assef et al. (2010), respectively.

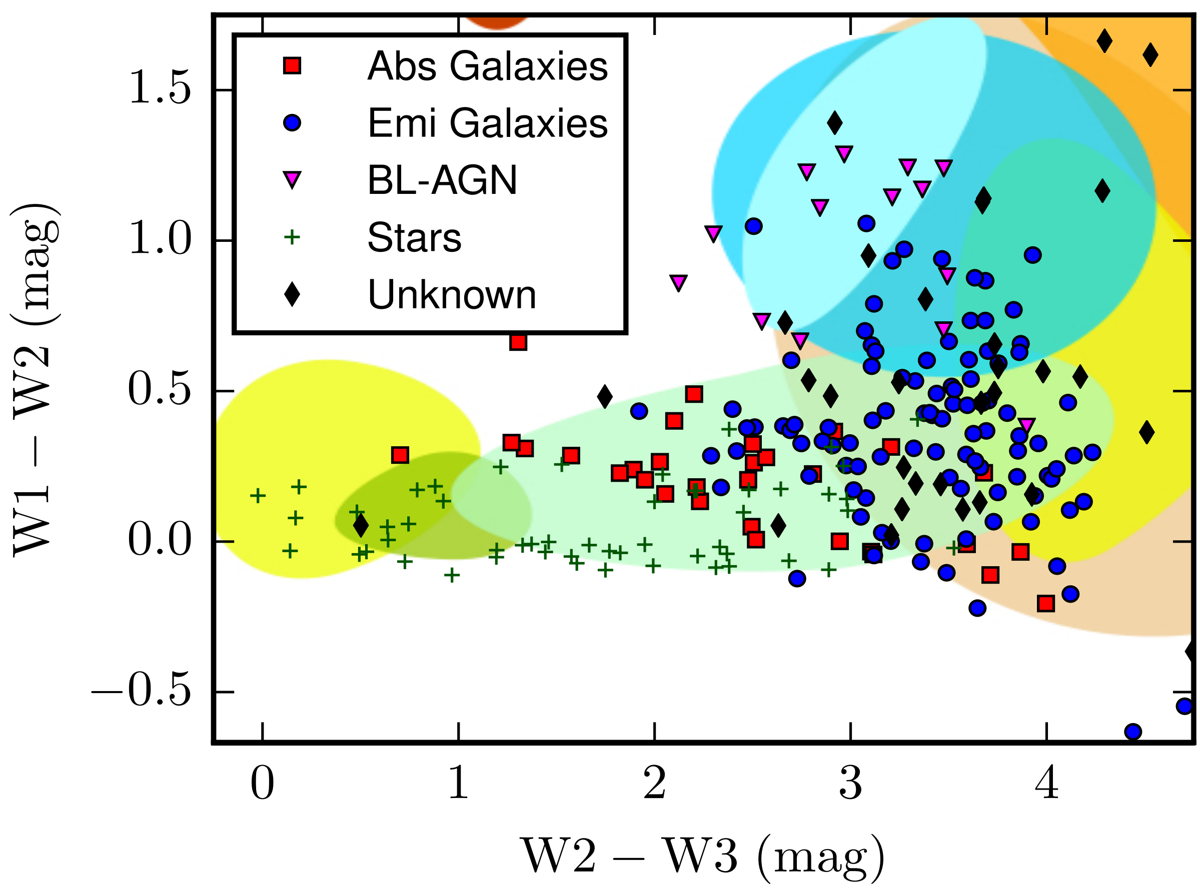

Figure 4.9: Our DEIMOS targets with minimally acceptable photometric uncertainty (σ_{W1}, σ_{W2}, and $\sigma_{\mathrm{W3}} \leq 1.0\,$mag). Sources marked with an light grey circle (blue in the online version) are emission line galaxies with measurable redshifts, dark grey squares are absorption line galaxies (red in the online version), triangles pointing down (magenta in the online version) are broad-lined AGN, plus marks are stars (green in the online version), and black diamonds are sources we could not classify to a high degree of certainty based on the spectra we obtained. Regions from Figure 4.1 are reproduced, in color, in the online version.

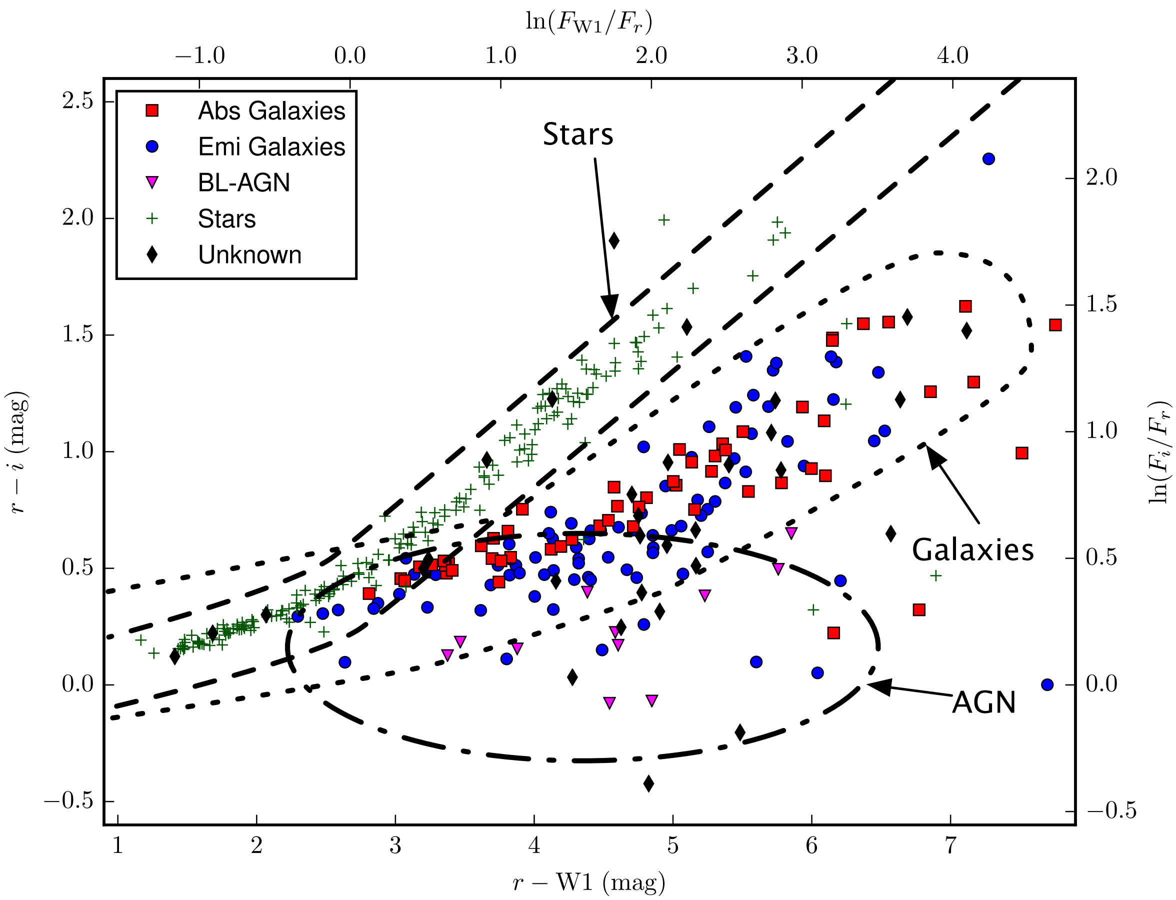

Figure 4.10: Our DEIMOS targets associated with a single target in SDSS DR8 and having minimally acceptable photometric uncertainty (σ_i, σ_r, and $\sigma_{W1} \leq 1.0$ mag). Sources marked with an open circle are galaxies with measurable redshifts, triangles pointing down are broad-lined AGN, plus marks are stars, and diamonds are sources we could not classify to a high degree of certainty based on the spectra we obtained. We placed the regions qualitatively based on a combination of the data from this survey and a pseudo-random selection of spectroscopically classified sources from SDSS DR8 (not shown).

CHAPTER 5

Description of All Data Used

The *WISE* satellite surveyed the entire sky multiple times in four infrared (IR) wavelengths (3.4, 4.6, 12, and 22 μm; Wright et al., 2010). This all-sky IR photometric survey makes it possible to leverage many of the large publicly available spectroscopic redshift surveys to measure galaxy properties in the IR. While characterizing the cross-matching of *WISE* data to a single survey is a straightforward process, doing it with six different redshift surveys takes a fair amount of space to characterize adequately, because each survey has unique caveats and characteristics that need addressing. This work describes a data set that results from matching five public redshift surveys with the AllWISE data release. The combined data set has an additional flux limit of 80 μJy (19.14 AB mag) in *WISE*'s W1 filter imposed in order to limit it to targets with high completeness and reliable photometry in the AllWISE data set. Consistent analysis of all of the data is only possible if the color bias discussed in Ilbert et al. (2004) is addressed (for example: the techniques explored in Chapter 2). The sample defined herein is used in Chapter 6, to measure the luminosity function of galaxies at 2.4 μm rest frame wavelength, and the selection process of the sample is optimized for this purpose.

5.1 Introduction

The astronomy community has an embarrassment of riches when it comes to the depth and breadth of its publicly available catalog of data, both photometric (Sloan Digital Sky

[0]This chapter is based on a paper in preparation for submission to The Astrophysical Journal in 2017, one of those on which Chapter 2's paper waits, by the authors: S. E. Lake, E. L. Wright, R. J. Assef, T. H. Jarrett, S. Petty, S. A. Stanford, D. Stern, and C.-W Tsai.

Survey [SDSS], Two Micron All Sky Survey [2MASS], Galaxy Evolution Explorer [GALEX], Widefield Infrared Survey Explorer [WISE], to name a few), and spectroscopic (for example, 6dF Galaxy Survey [6dFGS], SDSS, Galaxy and Mass Assembly [GAMA]). As tempting as it is to combine all of the available data into a unified measurement of the luminosity function (LF) of galaxies, there is no single standard for how targets are selected for measurement of spectroscopic redshifts or how the resulting data is characterized. So any effort to analyze a data set that is a synthesis of many data sets requires a careful consideration of whether the target selection processes are sufficiently similar to be modeled in a unified way, and characterization of the resulting data set after all quality cuts are made.

This chapter contains a description of the sample selection process, and a characterization of the same, for spectroscopically measured redshift catalogs of galaxies pulled from six different surveys and crossmatched, wherever possible, to additional photometric information from SDSS data release 10 (SDSS-DR10), the 2-Micron All Sky Survey (2MASS), and the AllWISE Source and Reject Catalogs. The spectroscopic galaxy surveys tapped are: the 6dFGS Data Release 3 K_s selected sample (Jones et al., 2009), SDSS Main Galaxy Sample (Strauss et al., 2002; Ahn et al., 2014a), GAMA data release 2 (Liske et al., 2015), the AGN and Galaxy Evolution Survey (AGES) (Kochanek et al., 2012), the zCOSMOS 10k-Bright Spectroscopic Sample (Lilly et al., 2009), and a reanalysis of the *WISE*/DEIMOS survey (originally presented in: Lake et al., 2012). What all of these surveys have in common is that their target selection processes are driven, primarily, by observed flux in one channel: 2MASS K_s, SDSS r, SDSS r, Hubble F814W (approximately I), NOAO Deep Wide Field Survey (NDWFS) I, and *WISE* W1, respectively. The simple selection process leaves room, computationally, for the imposition of a further flux cut in W1 for the combined catalog without significantly increasing the complexity of the selection process.

A measurement of the LF using the data described herein takes place in Chapter 6. The technique needed to account for the biases in such a diverse group of redshift surveys simultaneously is to broaden the concept of the LF to be a density over the galaxies' entire spectral energy distribution (SED), as described in Chapter 2. Two necessary components of that process are the mean and spectral covariance of galaxy spectra. This chapter makes use of the mean and covariance of galaxy SEDs as measured in Chapter 3. The techniques developed allow us to address the SED dependent completeness concerns raised in Ilbert et al. (2004), and make the minimum cuts to the data needed in the process. In this work, the mean SED is used to cut galaxies that are likely low luminosity outliers in luminosity-redshift space, caused by contamination, as well as to compute curves bounding the regions in luminosity-redshift space where SED variety completeness is nearly constant.

The layout of this chapter is as follows: Section 5.2 describes the data sets chosen and all cuts made to the sets. Each data set has its own subsection where details peculiar to it are described. The effects of the primary cuts on the data are demonstrated in graphs that are not completeness corrected in order to show what physical parameters, primarily redshift and luminosity, measurements based on the data set will be most sensitive to. Section 5.3 contains excerpts from the machine readable tables of the selected data published with this work. Finally, Section 5.4 contains concluding remarks.

All magnitudes in this chapter are in the AB magnitude system, unless otherwise specified. In cases where the source data was in Vega magnitudes and a magnitude zero point was provided in the documentation, they were used for conversion to AB (2MASS[1] and AllWISE[2]). For the surveys without obviously documented zero points (NDWFS[3], SDWFS[4]) we converted Vega magnitudes to AB magnitudes using those provided in Kochanek et al. (2012).

5.2 Data Selection and Characterization

The defining data set of this chapter is the *WISE* W1 selected survey originally described in Lake et al. (2012) and here in Chapter 4, hereafter *WISE*/DEIMOS. The biggest advantage of *WISE*/DEIMOS is that the target selection function is extremely simple, driven at the

[1] `http://www.ipac.caltech.edu/2mass/releases/allsky/faq.html#jansky`

[2] `http://wise2.ipac.caltech.edu/docs/release/allsky/expsup/sec4_4h.html#WISEZMA`

[3] `http://www.noao.edu/noao/noaodeep/`

[4] `http://irsa.ipac.caltech.edu/data/SPITZER/SDWFS/`

faint end entirely by the target's flux at $3.4\,\mu$m, W1 filter. The disadvantage is that the sample size is relatively small ($N \sim 200$). The smallness of the *WISE*/DEIMOS sample, and AllWISE's sky coverage, is what drove the decision to leverage the existing catalog of redshift surveys. We imposed a W1 flux limit of $80\,\mu$Jy (19.14 AB mag) on all surveys to make the results from the disparate surveys as comparable to the *WISE*/DEIMOS data set as possible. The complete list of surveys used is found in Table 5.1.

We cross matched the surveys to the AllWISE catalog (Cutri et al., 2013) and reject table using a spatial match with a $6''$ radius, the full width at half maximum (FWHM) of the *WISE* beam, keeping only the nearest matching source. We then traversed the list again to ensure that each source from AllWISE was associated with only one target from the redshift survey, assigning the AllWISE source to the closest target in cases where multiple targets matched a single source. The reason for this choice is that the target closest to the photo-center of the AllWISE source is likely the one providing the dominant contribution to the detected flux. While an ad-hoc deblending procedure could have been developed, the issue was infrequent enough to make addressing it in this fashion not worthwhile; less than 3% of sources in zCOSMOS-10k, the deepest, and narrowest, survey in this work.

Performing the initial search out to $6''$ allowed us to examine how the match radius affected both the completeness and purity of the sample. In that analysis we decided that keeping only sources with a match within half of the *WISE* beam's FWHM ($3''$) was, subjectively, an adequate compromise among all of the sample completeness and purity factors, since the target likely contributes the majority of the flux in the *WISE* measurement. Sources with matches between $6''$ and $3''$ that pass all other tests are regarded as lost to contamination, and are treated as a reduction in completeness for the survey. The same is done for sources which are flagged as having contaminated photometry in W1 in the AllWISE database (`w1cc_map` $\neq 0$). The fraction of points lost to contamination by these criteria are: 9.2% for 6dFGS, 4.1% for SDSS, 3.8% for GAMA, 3.0% for AGES, 11.8% for zCOSMOS, and 1.4% for *WISE*/DEIMOS.

The large *WISE* beam means that the vast majority of galaxies detected in the AllWISE data release are unresolved and well characterized by the point-spread function (PSF)

Table 5.1. Summary of Spectroscopic Surveys Used

Survey	Release version	Redshifts min/median/max	Coverage (Ω) (sr)	Band	$m_{\rm lim}$ AB mag	Reference
6dFGS	3	0.01 / 0.05 / 0.20	4.17[a]	K_s	11.25/14.49	Jones et al. (2009)
SDSS-DR7	7	0.01 / 0.10 / 0.33	2.40[b]	r	13.0/17.77	Abazajian et al. (2009)
GAMA	2	0.01 / 0.18 / 0.43	4.39×10^{-2}	r	14.0/19.0	Baldry et al. (2010)
AGES	1	0.05 / 0.31 / 1.00	2.36×10^{-3}	I	15.5/18.9/20.4	Kochanek et al. (2012)
zCOSMOS-10k	2	0.05 / 0.61 / 1.00	5.2×10^{-4}	I^*	15.0/22.5	Lilly et al. (2009)
WISE/DEIMOS	2	0.05 / 0.38 / 1.00	5.78×10^{-5}	W1	15.0/18.70/19.14[c]	Lake et al. (2012)

Note. — Redshift surveys used in the data analysis here. The selection for zCOSMOS was done using the Hubble Space Telescope's Advanced Camera for Surveys (ACS) filter F814W, which is approximately I-band. The selections for AGES and *WISE*/DEIMOSare split into a complete bright and sparse faint samples. The Redshifts column contains the median redshift of the survey, and the minimum and maximum redshifts likely to be useful. The smaller surveys, for example, have a bias against selecting galaxies that are local, large, and resolved because they would obstruct the field of higher redshift galaxies, so they require a higher minimum redshift cutoff. The larger surveys, contrastingly, when they contain high redshift sources they are more likely to be redshift blunders, and so they require a lower maximum redshift.

[a] Inital 6dFGS area is 5.2 sr, but all data with $\delta \geq -11.5°$ was removed to eliminate overlap with other surveys.

[b] Initial SDSS area is 2.45 sr, but the footprint of the smaller, deeper, surveys also used here are removed to eliminate overlap.

[c] The upper limit is in R-band magnitudes, as required in the Keck/DEIMOS documentation, and measured in the USNO's NOMAD catalog (Zacharias et al., 2004).

Table 5.2. Photometric Surveys Used by Spectroscopic Survey

Spectroscopic Survey	Photometric Survey	Bands	Citation
WISE/DEIMOS[a]	GALEX gr7	FUV, NUV	Martin et al. (2005)
	2MASS	J, H, K_s	Skrutskie et al. (2006)
	SDSS-DR10	u, g, r, i, z	Ahn et al. (2014a)
	AllWISE	W1, W2, W3, W4	Wright et al. (2010)
6dFGS	GALEX gr7	FUV, NUV	Martin et al. (2005)
	2MASS	J, H, K_s	Skrutskie et al. (2006)
	AllWISE	W1, W2, W3, W4	Wright et al. (2010)
SDSS	SDSS-DR10	u, g, r, i, z	Ahn et al. (2014b)
	2MASS	J, H, K_s	Skrutskie et al. (2006)
	AllWISE	W1, W2, W3, W4	Wright et al. (2010)
GAMA	GAMA	FUV, NUV	Liske et al. (2015)
	SDSS-DR7	u, g, r, i, z	Abazajian et al. (2009)
	UKIDSS LAS	Y, J, H, K	Lawrence et al. (2007)
	AllWISE	W1, W2, W3, W4	Wright et al. (2010)
AGES	SDSS-DR10	u, g, r, i, z	Ahn et al. (2014b)
	NDWFS-DR3	B_w, R, I, K	Jannuzi & Dey (1999)
	SDWFS-DR1.1	c1, c2, c3, c4	Ashby et al. (2009)
	AllWISE	W1, W2, W3, W4	Wright et al. (2010)
zCOSMOS	COSMOS	FUV, NUV, u^*, B_j, g^+, V_j,	
		r^+, F814W, i^+, i^*, z^+, J, K_s	Capak et al. (2007)
	SDSS-DR10	u, g, r, i, z	Ahn et al. (2014b)
	S-COSMOS-DR3	c1, c2, c3, c4	Sanders et al. (2007)
	AllWISE	W1, W2, W3, W4	Wright et al. (2010)

Note. — Photometric surveys used for fitting SEDs to sources, in order of increasing wavelength.

[a] Not all sources have all data available, whether it was a question of coverage or depth, so roughly half of the sources were only characterized by *WISE* data.

photometry stored in the `w?flux` columns of the database. While there were not enough resources to perform a full and independent extended source analysis of the *WISE* survey, the team was able to place elliptical apertures on sources that are already identified in the 2MASS Extended Source Catalog (XSC). Figure 5.1 shows the trend in $L_\nu(2.4\,\mu\mathrm{m})$ computed by K-correcting SDSS r model fluxes (profile fit flux measurements) versus using *WISE* W1 fluxes as a function of the reduced χ^2 of the W1 PSF fit on sources from the SDSS survey. Panel **a** shows the trend when using W1 PSF photometry, and panel **b** shows the trend when using the W1 elliptical apertures. While both sets of data have a trend, the elliptical aperture has a smaller trend at large χ^2.

The hazard of using only PSF fluxes for resolved sources (even for only marginally resolved ones) is twofold: first, $L_\star$ will be underestimated for low redshift galaxies; leading to the second, that the evolution in $L_\star$ will be overestimated. This bias will have further effects on the values observed in other LF parameters. $\kappa_\star$, the normalization of flux counts, should be slightly decreased because the bias is a blunting of the flux counts histogram at the bright end. Because the definition of $\phi_\star$ makes its value dependent on $L_\star$, both its value and the evolution of that value will be strongly affected. We therefore attempt to minimize this bias by using the elliptical aperture flux when `w?rchi2` ≥ 3, if it is not an upper limit and if the source is within $5''$ of the XSC source (`xscprox` ≤ 5). As the measurements in Chapter 6 show, this effort was not entirely successful.

In the future, the ideal solution would be to generalize the photometry software used in producing the AllWISE catalog, WPHOT[5], to process the images used to generate each survey's target list at the same time as the *WISE* images using a profile model for the galaxies; similar to what was done in Lang et al. (2014).

Model fitting techniques that correct for model completeness using a smoothly varying selection function, as we applied to this data set in Chapter 6, tend to make the model parameters particularly sensitive to outliers that are in low completeness regions. The most prominent example of this outlier effect in this work are objects which pass all of the selection

[5] `http://wise2.ipac.caltech.edu/docs/release/allsky/expsup/sec4_4c.html`

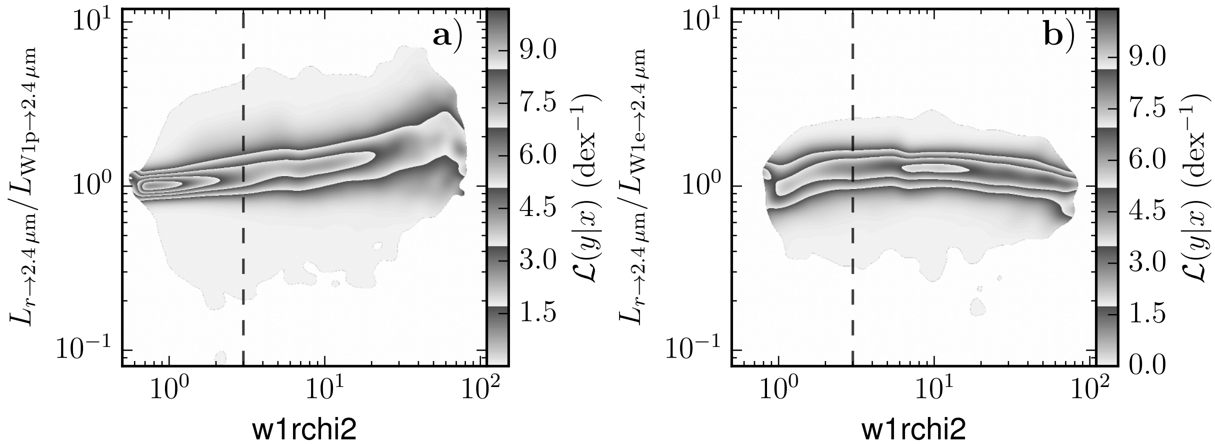

Figure 5.1: Plots of $L_{r\to 2.4\,\mu\mathrm{m}}/L_{\mathrm{W1}\to 2.4\,\mu\mathrm{m}}$ versus the reduced χ^2 of the W1 PSF photometry fit. Panel **a** uses the PSF photometry for W1, and Panel **b** uses the elliptical aperture fluxes. The data used is described in Section 5.2.3, with the additional restriction that points have non-upper limit elliptical aperture fluxes. The vertical line at reduced $\chi^2 = 3$ shows the separation we adopted between data for which the PSF flux was preferable and that for which the elliptical flux was preferable.

flux cuts, but are in a position in the luminosity-redshift plane that has an extremely low selection probability assigned to it by the model. The two most common reasons for this are: sources with contaminated optical photometry; and sources that are marginally resolved by *WISE*, but which do not have elliptical aperture photometry available. We calculated $L_\nu(2.4\,\mu\mathrm{m})$ from the *WISE* photometry and, if it isn't contaminated to the same extent as the optical selection photometry, then the source can be an outlier on the low side in a luminosity-redshift graph. Low luminosity outliers are in a region that the completeness model assigns a low probability of having been selected. This causes a large swing in the estimate of the LF model parameters in order to get a finite density at the position of the outlier. An example of a source with contaminated targeting photometry can be found in Figure 5.2, and one that lacks an elliptical aperture in AllWISE but the psf flux is improper is in Figure 5.3. Because the apparent radius of a galaxy is correlated to both its luminosity and redshift, and the probability of significant contamination varies inversely with flux and with the area subtended on the sky by the source, these lead to selection effects and biases. In principle these effects can be modeled if a radius-luminosity relationship is added onto the overall model, but that would require a set of radius measurements that is consistent across surveys, and that also has an accurate determination of the effect of seeing.

The factors discussed in the previous paragraph make it necessary to cut data with low selection probability and low luminosity as outliers. For that reason, a reduced maximum redshift was applied to 6dFGRS, SDSS, and GAMA, as shown in Table 5.1. Further, the minimum selection fluxes were extrapolated into luminosity cuts using the mean SED for all galaxies measured using the data from Chapter 3. The fractions of $2.4\,\mu$m luminosity contributed by each of the templates from Assef et al. (2010), with the median AGN obscuration, can be found in Table 3.3 and a graph of the mean SED, with a 1-σ type variance band around it, is in Figure 5.4. For AGES and *WISE*/DEIMOS, surveys with a tiered target selection strategy, each survey was treated though it were comprised of two fully independent surveys for this cut, with the division line set by the intermediate magnitude limit in Table 5.1. Finally, if the survey documentation did not explicitly cite a maximum flux limit, then one was imposed that cut the brightest few sources in order to ensure an accurate upper flux limit for the survey.

The *WISE* All-Sky data release had a known and documented[6] overestimation of the background, leading to an underestimation of the flux for faint sources. The AllWISE release remedied most, but not all, of the problem[7]. We, therefore, added a small flux to correct for the over-subtraction in the PSF photometry, on average, in W1 and W2. The values added are $1.5\,\mu$Jy and $7\,\mu$Jy in W1 and W2, respectively, as shown in Table 6 of the catalog completeness section of the AllWISE Explanatory Supplement[8]. The aperture photometry was not affected by this issue, so when elliptical aperture photometry was used in this work it was unaltered.

Targets from each survey were also matched to other photometric surveys using a $1''$ spatial match in order to obtain more photometric points to use in modeling the spectral energy

[6] http://wise2.ipac.caltech.edu/docs/release/allsky/expsup/sec6_3c.html#flux_under

[7] http://wise2.ipac.caltech.edu/docs/release/allwise/expsup/sec2_2.html

[8] http://wise2.ipac.caltech.edu/docs/release/allwise/expsup/sec2_4a.html

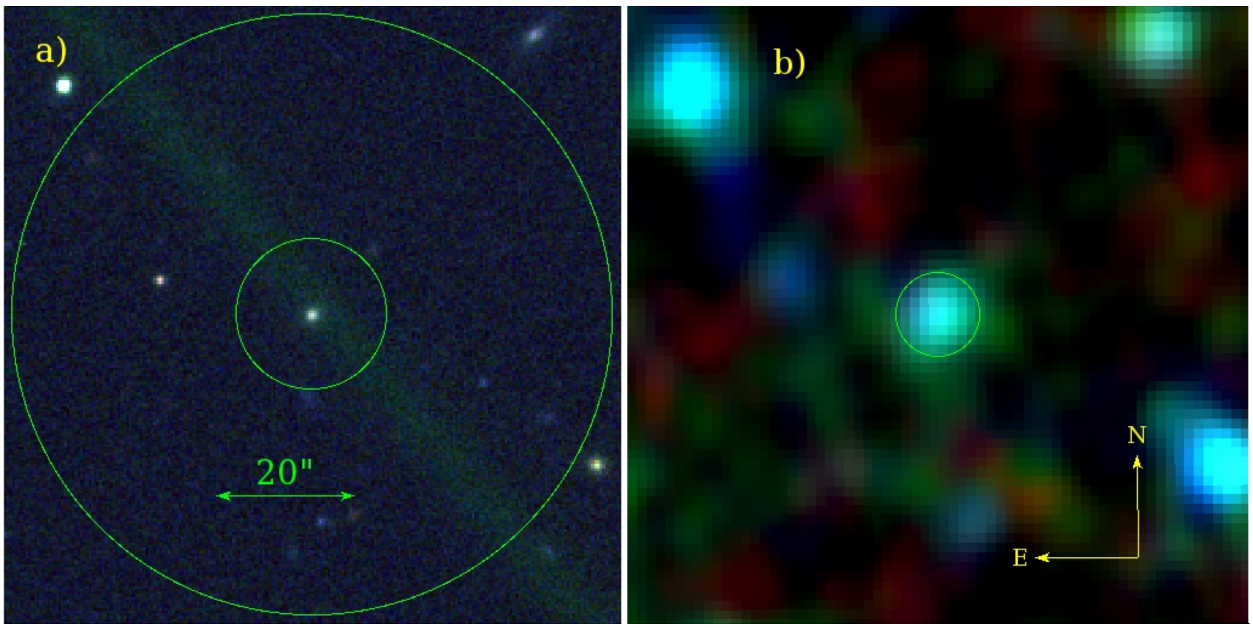

Figure 5.2: Panels show a source with contaminated optical photometry that causes a source that should not have been selected for the redshift sample to be included. Panel **a** is centered on the target source with SDSS *gri* mapped to blue, red, and green, respectively, in a linear scale with the scale of each channel set to fit the source. The green streak is a likely cosmic ray hit. The outer circle is the Petrosian photometry aperture, used to measure the flux in determining targeting, and the inner circle is the aperture that contains half of the flux of the outer one. Panel **b** shows the same field, as imaged by *WISE*, with W1 mapped to yellow, and W2 to red. The green circle on this panel shows the twice the FWHM of the native *WISE* W1 beam. The coordinates of this source are: 138.33114°, 19.70335° in J2000 right ascension and declination.

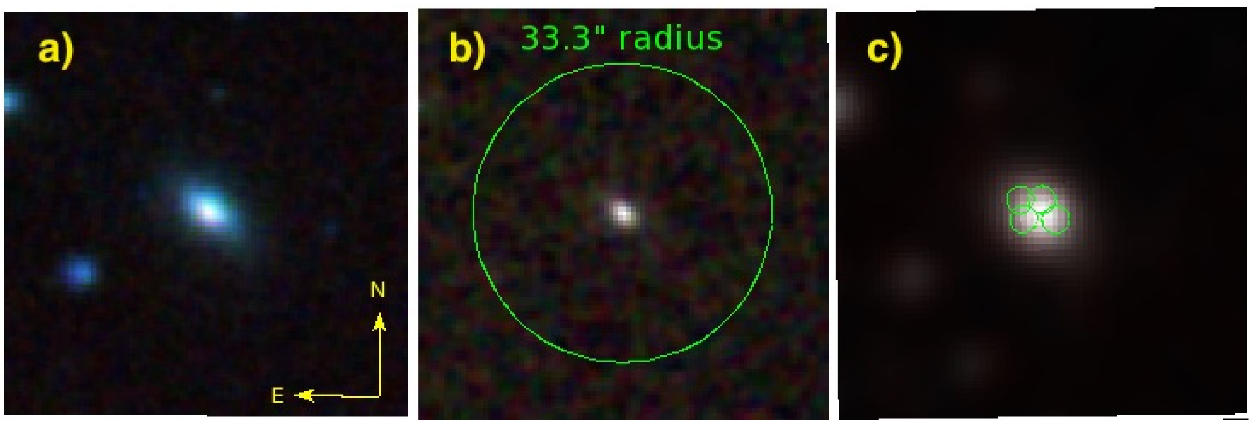

Figure 5.3: Panels show different views of a source that is large enough for *WISE* psf flux measurements to miss a significant portion of its flux. This particular example happens to have been divided into four different sources by the WPHOT pipeline. Panel **a** shows the galaxy as seen in the Digital Sky Survey 2, with B, R, and I mapped to blue, green, and red. Panel **b** shows the 2MASS view, with J, H, and K_s mapped to blue, green, and red. The $33.3''$ circle shows the radius out to which the radial profile was integrated to calculate the flux used in selection. Panel **c** shows the same galaxy as shown in the AllWISE coadd atlas, with W1 mapped to yellow, and W2 to red. The green circles have $3.1''$ radii, and show the sources into which the galaxy is divided in the AllWISE database. The coordinates of this source are: $24.48083°$, $-50.36086°$ in J2000 right ascension and declination.

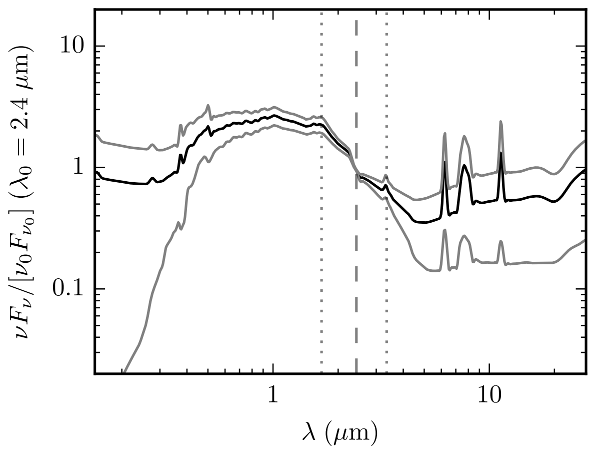

Figure 5.4: The mean SED of galaxies in the redshift range $0.05 < z \leq 1$, as measured using the data and SED fits from Chapter 3. The solid grey lines show the 1-σ type variance band around the mean SED, the dashed vertical line is at $2.4\,\mu$m and the vertical dotted lines show the effective wavelengths of the *WISE* W1 filter for galaxies at the extreme redshifts of the sample, $z = 0,\ 1$.

distributions (SEDs) of the galaxies. The SED models were made using the four templates from Assef et al. (2010). The set of templates contained four basis galaxies, identified as Elliptical, Sbc, Irregular, and Active Galactic Nucleus (AGN). All of the models are normalized to be $10^{10}\,\mathrm{L}_\odot$ in the wavelength range 0.03–30 μm. The AGN template, additionally, has a dust obscuration model parametrized by $\mathrm{E}(B-V)$. The models, normalized to unit luminosity at $2.4\,\mu$m with the AGN unobscured, can be found in Figure 5.5.

The templates were constructed to be fit to fluxes by minimizing χ^2 with respect to to a linear combination of the template fluxes with non-negative coefficients, and a search in the 1-dimensional parameter space for the best AGN extinction, $\mathrm{E}(B-V) = (2.5/\ln(10))\cdot(\tau_B - \tau_V)$. That is, the model has the form:

$$\begin{aligned} F_\nu(\nu, z) = {} & a_\mathrm{E} F_\mathrm{E}(\nu, z) + a_\mathrm{S} F_\mathrm{S}(\nu, z) \\ & + a_\mathrm{I} F_\mathrm{I}(\nu, z) + a_\mathrm{A} F_\mathrm{A}(\nu, z, \tau_B - \tau_V), \end{aligned} \tag{5.1}$$

$$\chi^2 = \sum_{i \in \{\text{filters}\}} \left(\frac{F_{\mathrm{obs}\,i} - F_{\mathrm{mod}\,i}}{\sigma_i} \right), \tag{5.2}$$

with all $a_i \geq 0$, and $12 > \tau_B - \tau_V \geq 0$. The a_i were fit using the SciPy `optimize` package's routine `nnls` (quadratic programming for non-negative least squares), and $\tau_B - \tau_V$ were fit

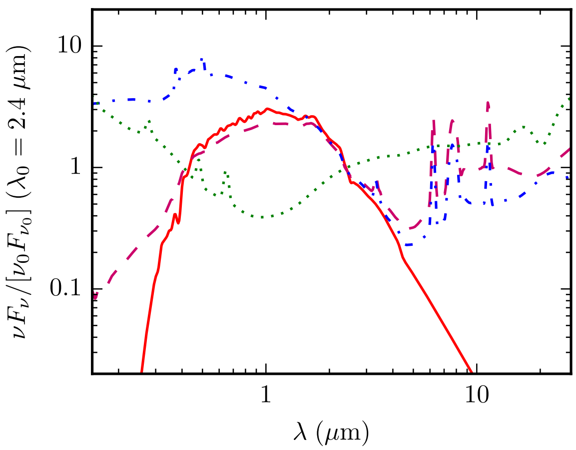

Figure 5.5: The template spectra used from Assef et al. (2010). The red solid line is the template called "Elliptical." The purple dashed line is "Sbc." The blue dash-dotted line is "Irregular." And the green dotted line is "AGN," unobscured.

with the routine `brent` (Brent's algorithm) with fallback to `fmin` (Nelder-Meade simplex).

There is one modification to that procedure for the fits done for this work. The templates do not include the possibility of adjustable dust obscuration of the stellar population, so a dusty starburst that has a detection in *WISE*'s 12 μm filter, W3, will often be best fit with a galaxy that is dominated by its Elliptical component (to satisfy optical redness) and a super-obscured AGN ($\tau_B - \tau_V > 12$) masquerading as the emission from the stellar dust component. The problem this creates is that it makes the SED fit the data more poorly in the most important range for work on the 2.4 μm luminosity function, where K-corrections from W1 to 2.4 μm are performed. We used two techniques to work around this problem. First, we limited the excess in optical depth as $\tau_B - \tau_V \leq 12$ (equivalently, $\mathrm{E}(B-V) \leq 13.03$). Second, when the SED was badly modeled ($\chi^2 > \max(N_{\mathrm{df}}, 1) \times 100$) and unlikely to be an AGN ($W1 - W2 > 0.5$ Vega mag), we used the best model with an unobscured AGN, $\mathrm{E}(B-V) = 0$. The reduced χ^2 criterion was determined by subjective empirical examination, and the AGN selection was found in Assef et al. (2013) to select low redshift AGN with 90% completeness.

Limiting the excess optical depth, $\tau_B - \tau_V$, to be non-negative introduces a bias to the parameter estimation of the individual galaxies. It is even physically possible for a source to appear bluer than expected if the line of sight is unobscured and dust clouds are reflecting excess blue light into it (that is, the line of sight contains a significant contribution from reflection nebulae in the target galaxy). Even so, applying a negative optical depth excess to dust obscuration models is not likely to produce an accurate spectrum for reflection (since obscuration models both reflection and absorption), and the magnitude of the negative excess doesn't have to be large to cause the estimate of the maximum redshift at which the galaxy would be included in the sample to diverge.

The AllWISE data release also has an issue where the flux uncertainties in W1 could be overestimated, or even missing, in the ecliptic longitudes covered by the "3-band cryo" portion of the survey[9]. The flux uncertainties are needed to model SEDs using Equation 5.2, so we substitute an uncertainty calculated from `w1sigp2`, the uncertainty in the mean flux measured from individual calibrated frames by the *WISE* photometry system, in magnitudes. This quantity differs from, and is usually less reliable than, the standard flux and uncertainty columns. This is because the standard uncertainty is calculated by simultaneously fitting all of the frames at the same time, and `w1sigp2` is calculated measuring the flux on each frame individually. Therefore the standard columns are to be favored if there isn't strong evidence that the standard flux uncertainty is overestimated. Empirically, the substitution was justified when the following equation is satisfied:

$$\sigma_{\mathrm{W1}} > 2\sqrt{\left(0.02F_{\mathrm{W1}}\right)^2 + \sigma^2_{\mathrm{W1p2}}}, \tag{5.3}$$

with $\sigma_{\mathrm{W1p2}} \equiv 0.4\ln(10)[\texttt{w1sigp2}]F_{0\,\mathrm{W1}}10^{-0.4[\texttt{w1magp}]}$. The relationship between `w1magp`, the mean flux (in magnitudes) for which `w1sigp2` is the uncertainty, and `w1sigp2` is more tightly correlated in the same way that the standard W1 flux and uncertainty columns are, making the use of `w1magp` in the conversion from magnitude to flux uncertainties preferable.

The template models were used to generate K-corrections from W1 flux to $2.4\,\mu$m rest frame luminosities using the equations from Hogg et al. (2002) and Blanton et al. (2003a). We corrected to $2.4\,\mu$m rest frame luminosity in order to minimize the errors associated with

[9] `http://wise2.ipac.caltech.edu/docs/release/allwise/expsup/sec2_2.html#w1sat`

K-correction for the overall sample in the same fashion as was done in Blanton et al. (2003b). In other words, W1 fluxes were K-corrected to the wavelength W1 samples at the median redshift of sources with $F_{\mathrm{W1}} \geq 80\,\mu\mathrm{Jy}$ from *WISE*/DEIMOS, $z = 0.38$.

Details of how each survey was processed that are peculiar to each survey, and what auxiliary photometric data was used, can be found in the following subsections, starting with this work's defining survey, *WISE*/DEIMOS, and then in decreasing order in survey area on the sky.

5.2.1 ***WISE*/DEIMOS Details**

WISE/DEIMOS consisted of a one night survey performed on the Keck II telescope using the DEIMOS instrument (Faber et al., 2003), with resulting data reduced using the DEEP2 spec2d pipeline (Newman et al., 2013; Cooper et al., 2012), and analyzed using SpecPro (Masters & Capak, 2011). *WISE*/DEIMOS included observations of 10 different slit masks at disparate positions with high galactic latitude ($b > 30°$). So, while the net area covered by those 10 masks is small, $5.78 \times 10^{-5}\,\mathrm{sr} = 0.190\,\mathrm{deg}^2$, the sample is less affected by cosmic variance than one might naively expect because the fields are non-contiguous. Because the source density varies with galactic latitude, the targeting completeness varies from field to field, necessitating the use of a selection function that varies by field.

A small number of sources, about 5, in Lake et al. (2012) had incorrectly measured redshifts, or lack thereof. This is based on a closer reanalysis of the data with more consistent standards for when a redshift is to be assigned, as will be explained below in the discussion of quality codes. An excerpt from the machine readable table can be found in Tables 4.5 and 4.6.

The reanalyzed data contains four main columns relevant for selecting subsamples. The column `TG`, short for 'Target Group,' contains an integer encoding which group of targets the source was in. The values `TG` takes are: 1 for the central source of the DEIMOS slit mask, 2 for W1 bright sources ($F_{\mathrm{W1}} \geq 120\,\mu\mathrm{Jy}$, in the *WISE* Preliminary Release), 3 for W1 intermediate sources ($120\,\mu\mathrm{Jy} > F_{\mathrm{W1}} \geq 80\,\mu\mathrm{Jy}$), 4 for W1 faint or non-detected sources

($80\,\mu$Jy $> F_{\mathrm{W1}}$), and 5 for targets that serendipitously fell on the slit of a target. For analysis of pseudo-randomly selected galaxies with well known selection completeness, targets with $1 < \mathtt{TG} < 5$ should be used. In order to have good completeness of the initial detections we recommend further limiting the sample to $\mathtt{TG} < 4$, as is done in Chapter 6.

The quality of the redshift is encoded in a column of integers named `q_z`, and takes on the values: -1 for sources with no detected flux in the spectrum, 0 for sources that have a spectrum but for which it was not possible to even estimate a redshift, 1 for targets where a redshift measurement was possible but no spectral features could be identified (blunders could not be ruled out, confidence $< 50\%$), 2 for targets where the redshift is better but still uncertain (confidence $< 95\%$), 3 for targets that have a secure redshift with at least one clearly identifiable spectral feature or more of lesser quality (absorption or emission lines), and 4 for targets with multiple clearly identifiable spectral features.

The analysis of the spectra allowed the targets to be broken up by classification, `class`. `class` takes on four possible values: “Gal” for ordinary galaxies, “QSO” for broad-line AGN, “Star” for stellar spectra, “Indet” for spectra of indeterminate type, “Unseen” for sources without any detectable flux in the spectrum, and “Lost” for sources lost to instrument constraints. Naturally, an analysis of extragalactic targets must be limited to “Gal” and “QSO” targets.

The last selection relevant column is `R`. `R` stands for “Real” and takes the value 1 if the source produced a spectrum or can be associated with a non-artifact source in the AllWISE database, and 0 otherwise. Only targets with $\mathtt{R} = 1$ are relevant.

The completeness of the W1 faint sample is much lower and more poorly defined compared to the brighter two, as can be seen by comparing the spectroscopy completenesses ($f_{Q\geq3}$) in Table 4.2, so the combined sample defined in this work is limited to only targets with $F_{\mathrm{W1}} \geq 80\,\mu$Jy for all surveys. This was done in order to make the results from all the surveys as comparable as possible. The following subsections contain plots showing the distribution of primary selection flux of the survey versus F_{W1}. They show that the effect of both cuts must be accounted for when analyzing all surveys deeper than SDSS.

Figure 5.6 is a scatter plot of redshifts versus luminosity, alongside the marginal histograms in redshift and log-luminosity for the sources used in the analysis herein. The plots are meant to show the raw quantity of data available at each redshift and luminosity, and thus contain no completeness corrections, and are normalized to the total number of data points. Of particular note, *WISE*/DEIMOS contains few redshifts $z > 1$, and only one with $z \leq 0.05$. Given that the slit mask targeting avoided large resolved galaxies, the survey has a selection bias against redshifts lower than this, so we have limited the sources included from all surveys to be both low redshift ($z \leq 1$), and have $z > 0.05$ for small area surveys or $z > 0.01$ for large area ones (6dFGS, SDSS, and GAMA).

Figure 5.6, panel **a**, also contains blue curves bounding regions where the color variety completeness is approximately constant (to within 2% for the light blue curve, and 5% for the dark blue curve). Color variety completeness is defined by:

$$S_{\mathrm{color}}(L, z) \equiv \frac{\langle S(F_{\mathrm{sel}}, F_0, \vec{x})\rangle_{\mathcal{L}_{\mathrm{SED}}}}{\max(S(F_{\mathrm{sel}}, F_0, \vec{x}))}, \tag{5.4}$$

where $S(F_{\mathrm{sel}}, F_0, \vec{x})$ is the selection probability (completeness) for a galaxy at real space position $\vec{x}$ (for example, α, δ, and z) with two observer frame fluxes at different wavelengths, F_{sel} and F_0. The average in the numerator is weighted by the likelihood that a galaxy at redshift, z and with (spectral) luminosity L will be observed to have fluxes F_{sel} and F_0 (called $\mathcal{L}_{\mathrm{SED}}$, see Equations 2.19), including both color variety and a model for measurement noise. The denominator is the maximum value that $S(F_{\mathrm{sel}}, F_0, \vec{x})$ takes, removing factors like intentionally sparse sampling from $S_{\mathrm{color}}(L, z)$. The faint sample is automatically excluded from these regions because it is too narrow to provide a flat selection region.

The reason for including the blue curves in the plot is that they show the regions where the likelihood model defined in Chapter 2 can be neglected. In the case of *WISE*/DEIMOS, the 95% curve leaves 91 sources (43.8% of the pre-cut data), and the 98% curve leaves 40 (19.2% of pre-cut).

The photometry from outside sources available for *WISE*/DEIMOS was non-uniform, as mentioned in Table 5.2. In total, roughly half of the sources have some photometry outside of AllWISE available, but that leaves only W1 and W2 photometry for the majority of the other half. This is not a problem for the accuracy of the K-corrections used in this work, shown in Figure 5.7, because non-AGN galaxy SEDs are remarkably uniform in the wavelength range of interest (1.7–3.4 μm, see the 1-σ varience band around the mean in Figure 5.4). This is why Assef et al. (2013) were able to show that this one color is remarkably good at picking out low redshift AGN, and therefore sufficient for narrowing the SED model in the wavelength range of interest. This fact also makes it extremely difficult to photometrically split the galaxies into red and blue types, as is done for most works on the galaxy luminosity functions. This is a problem because red cluster member galaxies typically have a different LF than bluer field galaxies, not to mention AGN. For that reason, most studies of the LF will remove AGN entirely, and perform two analyses on the ordinary galaxy data: one analysis with a single luminosity function, and one where the red and blue galaxies are modeled separately. The *WISE*/DEIMOS data could be split by spectroscopic characteristics, but only broadly (for example, by the presence of emission lines), and performing a comparable analysis on the other surveys would have been prohibitively time consuming.

5.2.2 6dFGS Details

The 6dF Galaxy Survey (6dFGS) was originally defined in Jones et al. (2004), and the final data release used in this chapter is described in Jones et al. (2009). 6dFGS contains several sub-samples selected using different techniques, but the sample of primary interest to this chapter is the one selected from the 2 Micron All Sky Survey (2MASS) extended source catalog using the K_s-band flux. This subset is designated as having `PROGID` = 1, and satisfies $K_s < 14.49$ AB mag. The reason the K_s selected sample is the most relevant to this work is because K_s is adjacent to W1 in wavelength, and so subject to less potential selection bias than surveys that were selected optically, as the flux-flux graph in Figure 5.8 shows.

Selecting the subset of redshifts with high confidence is relatively straightforward with 6dFGS. Those targets with $3 \leq$ `quality` < 6, where '`quality`' is the name of the column of integers classifying redshifts by the quality, selects for targets with science quality redshifts

($\texttt{quality} \geq 3$) and removes those that are Milky Way sources (they have $\texttt{quality} = 6$).

The 6dFGS survey is relatively shallow, as can be seen by the luminosity-redshift graph in Figure 5.9, and its marginalized histograms therein, but the coverage is enormous, 4.17 sr after imposing a $\delta < -11.5$ cut to eliminate overlap with SDSS, so the sample size after all limits are imposed is $27,091$. Because of this wide coverage, the analysis here covers galaxies as low as $z = 0.01$, but the shallow depth requires an upper limit on the redshifts at $z = 0.2$. The bright limit imposed on this survey is $K_s > 11.25$ AB mag.

The blue curves in Figure 5.9 are defined by constant values of the color variety selection function, $S_{\mathrm{color}}(L, z)$ (see Equation 5.4), and bound regions where it is greater than 98% (light blue) and 95% (dark blue). They demarcate the regions where the selection function is close enough to constant that the likelihood model defined in Chapter 2 can be neglected. For 6dFGS, 95% 17,571 sources (64.9% of the pre-cut data), and the 98% curve leaves 15,652 (57.8% of pre-cut).

The photometric data used to model galaxy SEDs and define K-corrections, shown in Figure 5.10, is summarized in Table 5.2. The shape of the data distribution in Figure 5.10 is consistent with Figure 4 from Dai et al. (2009), which used the same set of templates for SED fitting, and Figure 4 from Blanton et al. (2003b). The characteristics of the distribution can be explained as the majority of galaxies being fit primarily by the elliptical, Sbc, and irregular templates from Figure 5.5, that all have nearly the same shape in the region between 1.7–3.4 μm, with a long tail of outliers that are dominated by the AGN template.

5.2.3 SDSS Details

The Sloan Digital Sky Survey (SDSS) data release 7, as described in Abazajian et al. (2009), contained three main extragalactic spectroscopic samples: the main galaxy sample defined in Strauss et al. (2002), the red luminous galaxy sample defined in Eisenstein et al. (2001), and the quasar sample defined in Richards et al. (2002). While it would have been nice to be able to use all three samples, the latter two samples are defined using both flux and color cuts, which the model described in Chapter 2 cannot yet accommodate in a timely fashion. Only the main galaxy sample is defined in terms of flux ($r \leq 17.77\,\mathrm{mag}$, Petrosian) and surface brightness ($\mu_{50} \leq 24.5\,\mathrm{mag\,arcsec^{-2}}$) in one channel, after extinction correction based on the dust maps from Schlegel et al. (1998). The analysis in this work is therefore limited to the main galaxy sample, with 476,744 sources after all limits are imposed. These limits included cutting out around the survey footprints of the three surveys with significant overlap that were deeper than SDSS, as listed in Table 5.3. There was no overlap with *WISE*/DEIMOS.

Explicitly, in terms of the columns of the SDSS dr10 CasJobs[10] database, the selected galaxies had to have: `class` set as either "GALAXY" or "QSO," `zwarning` = 1, (`legacy_target1 & 0x40`) $\neq 0$ (that is, the Main Galaxy Sample flag is set), `sdssPrimary` = 1, and `legacyPrimary` = 1.

The flux-flux plot is in Figure 5.11, and it shows that the optical flux limit is the relevant limit for the vast majority of the sources, but not 100% of them. Like 6dFGS, SDSS has a large area on the sky (2.40 sr, after de-overlapping) and so it, too, has a lower redshift limit in this work of 0.01. Likewise, SDSS's shallow depth required upper redshift limit at $z = 0.33$, and a bright magnitude limit at $r = 13.0\,\mathrm{mag}$. Also in Figure 5.11 is a density plot that shows the relationship of the data to the surface brightness limit, defined as the mean surface brightness within a circle that contains half of the source's Petrosian flux. Ideally any analysis would include the surface brightness limit in the selection function model. Practically, the surface brightness limit is far from the main body of the data and incorporating it would require an additional measurement of a luminosity-radius relationship that is beyond the scope of the model described in Chapter 2.

The luminosity-redshift graph is in Figure 5.12, along with its marginalizations into histograms. The K-corrections applied to calculate those luminosities are shown in Figure 5.13, and the auxiliary photometric information used to fit the SED models and calculate K-corrections is outlined in Table 5.2. The shape of the data distribution in Figure 5.13 is consistent with Figure 4 from Dai et al. (2009), which used the same set of templates for SED fitting, and Figure 4 from Blanton et al. (2003b). The characteristics of the distribu-

[10] `http://skyserver.sdss3.org/casjobs/`

Table 5.3. SDSS Cutouts for Deeper Surveys

Survey	$\alpha >$ °	$\alpha <$ °	$\delta >$ °	$\delta <$ °
GAMA	129.00	141.00	-1.00	$+3.00$
GAMA	174.00	186.00	-2.00	$+2.00$
GAMA	211.50	223.50	-2.00	$+2.00$
AGES	216.11	219.77	$+32.80$	$+35.89$
zCOSMOS	149.45	150.78	$+1.60$	$+2.86$

Note. — J2000 right ascension (α) and declination (δ) limits for data removed from SDSS for the data described in this work in order to prevent double counting of any sources.

tion can be explained as the majority of galaxies being fit primarily by the elliptical, Sbc, and irregular templates from Figure 5.5, that all have nearly the same shape in the region between 1.7–3.4 μm, with a long tail of outliers that are dominated by the AGN template.

The blue curves in Figure 5.12 are defined by constant values of the color variety selection function, $S_{\rm color}(L, z)$ (see Equation 5.4), and bound regions where it is greater than 98% (light blue) and 95% (dark blue). They demarcate the regions where the selection function is close enough to constant that the likelihood model defined in Chapter 2 can be neglected. For SDSS, 95% 162,916 sources (34.2% of the pre-cut data), and the 98% curve leaves 105,835 (22.2% of pre-cut).

5.2.4 GAMA Details

The Galaxy And Mass Assembly (GAMA) survey was originally defined over three fields for the first data release, described in Baldry et al. (2010), and later expanded to 5 fields, as described in the second data release paper, Liske et al. (2015). After the final data release the depth at which the data is complete will vary depending on the field. For the second data release, all of the fields are complete down to at least $r = 19$ mag, extinction corrected

Petrosian, and so that is the limit used for the selection in this work. Selecting science quality redshifts from GAMA is relatively straightforward, as the GAMA team supplies a 'normalized quality' integer, `NQ`. The high quality redshifts satisfy: `NQ` > 2.

As can be seen in Figure 5.14, the optical limit is the controlling one for the vast majority of sources, but the W1 flux limit is relevant for a sizable fraction of the galaxies in GAMA. Like SDSS, GAMA imposes surface brightness limits, both high and low. Their relationship to the data can be found in Figure 5.14, and just like in the analysis of SDSS, it is beyond the scope of the model described in Chapter 2 to account for these limits. After all limits are imposed, this survey contributes 44,495 sources to the analysis.

The luminosity versus redshift density plot, found in Figure 5.15 with its marginalizations, shows that GAMA is the shallowest survey to significantly sample galaxies from the median redshift of the *WISE*/DEIMOS survey. It is also the narrowest survey for which the selection defined in this work covers redshifts down to $z = 0.01$, and for which a low maximum redshift was imposed at $z = 0.43$. The bright limit imposed here was at $r = 14\,\mathrm{mag}$.

The blue curves in Figure 5.15 are defined by constant values of the color variety selection function, $S_{\mathrm{color}}(L, z)$ (see Equation 5.4), and bound regions where it is greater than 98% (light blue) and 95% (dark blue). They demarcate the regions where the selection function is close enough to constant that the likelihood model defined in Chapter 2 can be neglected. For GAMA, 95% 15,659 sources (35.2% of the pre-cut data), and the 98% curve leaves 9,641 (21.7% of pre-cut).

The K-corrections applied to calculate the luminosities are shown in Figure 5.16, and the photometry used to fit the SEDs used to calculate the K-corrections are summarized in Table 5.2. The shape of the data distribution in Figure 5.16 is consistent with Figure 4 from Dai et al. (2009), which used the same set of templates for SED fitting, and Figure 4 from Blanton et al. (2003b). The characteristics of the distribution can be explained as the majority of galaxies being fit primarily by the elliptical, Sbc, and irregular templates from Figure 5.5, that all have nearly the same shape in the region between 1.7–3.4 μm, with a long tail of outliers that are dominated by the AGN template.

5.2.5 AGES Details

The AGN and Galaxy Evolution Survey (AGES), described in Kochanek et al. (2012), is a spectroscopic redshift survey targeted using photometry from the NOAO Deep, Wide-Field, Survey (NDWFS) and the *Spitzer* Deep, Wide-Field, Survey (SDWFS). Kochanek et al. (2012) defines a lot of subsamples with different flux-limits. The analysis in this work uses the main I-band selected sample, defined with (`code06 & 0x80000`) $\neq 0$ (`&` is the 'bitwise and' operator, and `0x80000` is a hexadecimal integer equal to 2^{20} in base 10) in Kochanek et al. (2012), which is defined by I-band flux limits to be complete brighter than $I = 18.9\,\mathrm{mag}$, and 20% complete below that down to $I = 20.4\,\mathrm{mag}$. The AGES data with well analyzed completeness is limited to a set of 15 overlapping circular fields, but the released redshifts cover a larger area. Limiting the analysis to just those redshifts in the canonical fields requires selecting sources with `field` > 0.

The relationship of the data to the flux limits are shown in Figure 5.17. This is the survey for which taking into account both the optical and W1 flux limits is most important because the locus on which most galaxies are found goes into the corner defined by the flux limits. AGES is narrow enough that the analysis in this work only includes data with redshifts $z > 0.05$ and deep enough for redshifts out to $z = 1$. The bright limit we imposed is at $I = 15.5\,\mathrm{mag}$. After all limits are imposed, AGES contributes 6,588 galaxies to the analysis in this work.

The NDWFS astrometry has a known astrometric offset relative to other major surveys. So before performing the final $3''$ distance match cut, we calculated the mean offset of nearest neighbors and used that offset to correct the distance between the AllWISE source and the NDWFS sources. The offsets we found were:$-0.29''$ in right ascension, and $-0.14''$ in declination.

The density plot showing the luminosities versus redshift is in Figure 5.18, alongside its marginalizations. The blue curves in Figure 5.18 are defined by constant values of the color variety selection function, $S_{\mathrm{color}}(L, z)$ (see Equation 5.4), and bound regions where it is greater than 98% (light blue) and 95% (dark blue). The faint sample is automatically excluded from these regions because it is too narrow to provide a flat selection region. They demarcate the regions where the selection function is close enough to constant that the likelihood model defined in Chapter 2 can be neglected. For AGES, 95% 2,096 sources (36.5% of the pre-cut data), and the 98% curve leaves 1,664 (29.0% of pre-cut).

The K-corrections used to calculate luminosities for AGES galaxies are shown in Figure 5.19, and the photometric data used to fit the SEDs for calculating the K-corrections is summarized in Table 5.2. The shape of the data distribution in Figure 5.19 is consistent with Figure 4 from Dai et al. (2009), which used the same set of templates for SED fitting, and Figure 4 from Blanton et al. (2003b). The characteristics of the distribution can be explained as the majority of galaxies being fit primarily by the elliptical, Sbc, and irregular templates from Figure 5.5, that all have nearly the same shape in the region between 1.7–3.4 μm, with a long tail of outliers that are dominated by the AGN template.

The photometry published with the main AGES paper, Kochanek et al. (2012), did not include uncertainties, so we performed a cross-match against NDWFS and SDWFS (the combined epoch IRAC c1 driven extraction stack only). The AGES sources didn't always have a counterpart in the NDWFS and SDWFS catalogs. In the case of SDWFS, that is because the data release used here is newer than the one used for AGES and this work only used the c1 stack catalog. Noise models were, therefore, also fit to the data to produce model uncertainties when a catalog uncertainty was unavailable. The noise model takes the form of a smoothly broken power law:

$$\sigma(F) = \sigma_{\mathrm{knee}} \left(\frac{F}{F_{\mathrm{knee}}}\right)^{\alpha} \left(\frac{1}{2} + \frac{1}{2} \cdot \left[\frac{F}{F_{\mathrm{knee}}}\right]^{|\beta| s}\right)^{\mathrm{sign}(\beta)/s}, \tag{5.5}$$

where F_{knee} is the location of the break, or knee, in the power law, $\sigma_{\mathrm{knee}} \equiv \sigma(F_{\mathrm{knee}})$, α is the faint end slope, β is the change in slope at F_{knee}, and s is a positive parameter setting the sharpness of the break. For $s \to 0$ the break becomes infinitely wide, and for $s \to \infty$ it becomes infinitely sharp (that is, a corner). The noise model parameters found from fitting individual bands, after trimming outliers, are listed in Table 5.4.

Table 5.4. AGES Error Models

Band	F_{knee} μJy	σ_{knee} μJy	α	β	s
B_w	0.13	0.017	0.51	-0.39	6.5
R	0.76	0.010	0.58	-0.47	8.3
I	1.3	0.15	0.49	-0.38	14
K	48	8.3	0.80	-0.56	5.9
c1	5.3	0.99	0.67	-0.59	6.7
c2[a]	1	1.3	0.10	0	0
c3[a]	1	7.3	0.042	0	0
c4[a]	1	7.8	0.025	0	0

Note. — Noise model parameters used to compute flux uncertainties in the absence of uncertainties from NDWFS or SDWFS, as defined in Equation 5.5.

[a]The data for this channel did not exhibit a knee, so a power law fit was used instead.

5.2.6 zCOSMOS Details

The analysis in this work uses the subset of the zCOSMOS survey known as the "10k-Bright Spectroscopic Sample," is described in Lilly et al. (2009) and Knobel et al. (2012). The COSMOS field has been the subject of an intensive campaign of imaging by many groups, as described in Scoville et al. (2007). zCOSMOS based its targeting on photometry from Hubble Advanced Camera for Surveys (ACS) Wide Field Camera (WFC) imaging with the F814W filter, which is approximately I-band. The 10k, data release 2, subset of the survey is 62% complete for compulsory targets, and 30% complete for the rest. Selecting high quality redshifts from zCOSMOS is the most involved of the surveys used here because of the detailed 'confidence class' (`cc`) system used. The recommendation in Lilly et al. (2009) is to accept all sources with `cc` equal to: any 3.X, 4.X, 1.5, 2.4, 2.5, 9.3, and 9.5. Based on the description of those classes, the analysis here accepts sources that fit in the recommended classes, but also those with a leading 1 (10 was added to show broad line AGN), 18.3, 18.5, and to reject all secondary targets (2 in the tens or hundreds digit). This can be done by accepting sources for which the text string version of `cc` matches the regular expression "`([34]\..*)|([1289]\.5)|(2\.4)|([89]\.3)`" and doesn't match "`^2\d+\.`". Finally, the targets fell into three selection classes, column named `i`, and 'unintended' sources are rejected by requiring `i` > 0.

As Figure 5.20 shows, even zCOSMOS is affected by the need to use both W1 and I-band limits in the analysis of the data. Like AGES, the narrowness of zCOSMOS means that the analysis herein is limited to redshifts $z > 0.05$. After all limits are imposed, this survey contributes 1,267 galaxies to the analysis.

The density plot showing the data in luminosity-redshift space is in Figure 5.21, alongside its marginalizations. The blue curves in Figure 5.21 are defined by constant values of the color variety selection function, $S_{\text{color}}(L, z)$ (see Equation 5.4), and bound regions where it is greater than 98% (light blue) and 95% (dark blue). They demarcate the regions where the selection function is close enough to constant that the likelihood model defined in Chapter 2 can be neglected. For zCOSMOS, 95% 890 sources (72.7% of the pre-cut data), and the 98% curve leaves 763 (62.3% of pre-cut).

The K-corrections used to calculate those luminosities are shown in Figure 5.22, and the photometric information used to fit the SEDs used to calculate the K-corrections are summarized in Table 5.2. The shape of the data distribution in Figure 5.22 is consistent with Figure 4 from Dai et al. (2009), which used the same set of templates for SED fitting, and Figure 4 from Blanton et al. (2003b). The characteristics of the distribution can be explained as the majority of galaxies being fit primarily by the elliptical, Sbc, and irregular templates from Figure 5.5, that all have nearly the same shape in the region between 1.7–3.4 μm, with a long tail of outliers that are dominated by the AGN template.

5.3 Post Selection Data Tables

Each cross-matched survey has its own layout, but the general layout is as follows: target coordinates in decimal degrees (J2000 right ascension and declination), the unique object identifier from the redshift survey (if provided), the identifiers from the photometric surveys to which the object successfully matched, the parameters from the template fits (including the χ^2 of the fit and the formal number of degrees of freedom; ignoring the impact that the constraints on the parameters have on that number), and the boundary redshifts for inclusion in this data set (including an intermediate redshift, `z_mid`, for sources in *WISE*/DEIMOS or AGES to account for the intermediate flux cuts of those surveys). In order to keep file size down, that is the extent of the information published with this work. The rest of the information, like the redshift and photometric properties, is available from the various original sources referenced in the tables of Section 5.2. The tables will be published with the paper based on this chapter and under the digital object identifier (DOI) `10.6084/m9.figshare.4003680` in gzipped IPAC table format when the paper based on this chapter is published. Excerpts from the machine readable tables can be found in: Tables 5.5 and 5.6 for *WISE*/DEIMOS, Tables 5.7 and 5.8 for 6dFGS, Tables 5.9 and 5.10 for SDSS, Tables 5.11 and 5.12 for GAMA, Tables 5.13 and 5.14 for AGES, and Tables 5.15 and 5.16 for zCOSMOS.

5.4 Discussion

The data gathered and characterized here was collected primarily to use in measuring the $2.4\,\mu$m luminosity function of all galaxies back to a redshift of $z = 1$, as is done in Chapter 6. The main purpose of this work is to describe, in detail, the cuts made to the data and the characteristics of the resulting set. This process is an essential component in evaluating the sensitivity of the measurements carried out in Chapter 6 and in making the data presented here both auditable and extendable. The multi-wavelength data sets available for most of the surveys covered here are extensive, and a more sophisticated spectro-luminosity functional analysis than what is in Chapter 6 should be possible if a fast and deterministic high dimension Gaussian integrator can be developed.

Table 5.5. Excerpt from *WISE*/DEIMOS Extended Data, Column Set 1

Ra	Dec	WDID	GALEX_ID	SDSS_ID	AllWISE_ID
°	°				
310.319670	−14.525610	19	null	1237668758314746796	3099m152_ac51-053725
310.367640	−14.514580	23	null	1237668758314746981	3099m152_ac51-053735
310.315280	−14.509710	27	null	1237668758314747310	3099m152_ac51-053770
310.217560	−14.419560	59	null	1237668758314681889	3099m152_ac51-053534
312.385500	−11.708410	102	6379641521644244188	null	3121m122_ac51-047591
312.394260	−11.672530	153	null	null	3121m122_ac51-048520
312.344700	−11.667790	155	null	null	3121m122_ac51-047825

Note. — First set of *WISE*/DEIMOS extended data columns. The first two columns are the right ascension and declination, in J2000 decimal degrees. The `WDID` column is an integer index uniquely assigned to targets in the *WISE*/DEIMOS survey. `GALEX_ID` is a uniquely identifying integer assigned in GALEX gr7 to the source (`null` if not matched). `SDSS_ID` is an integer assigned to the matched source in SDSS data release 10 (`null` if not matched). `AllWISE_ID` is the `source_id` assigned to the source in the AllWISE survey.

Table 5.6. Excerpt from *WISE*/DEIMOS Extended Data, Column Set 2

`WDID`	`Ell`	`Sbc`	`Irr`	`AGN`	`AGN_EBmV`	`chisqr`	`Ndf`	`z_min`	`z_mid`	`z_max`
	$10^{10}\,L_\odot$	$10^{10}\,L_\odot$	$10^{10}\,L_\odot$	$10^{10}\,L_\odot$	mag					
19	3.7020e−02	0.0000e+00	9.9700e−01	1.1220e−03	0.5440	6.170e−28	−2	0.029	0.114	0.138
23	7.6680e+00	0.0000e+00	9.7900e−01	7.9500e−01	0.0000	1.530e+01	3	0.060	0.472	0.579
27	0.0000e+00	4.2510e+01	3.5730e+00	0.0000e+00	0.0000	7.000e+01	1	0.090	0.653	0.820
29	0.0000e+00	4.4060e+00	6.8300e+00	4.3520e−02	1.9000	1.040e−28	−2	0.076	0.353	0.444
34	0.0000e+00	0.0000e+00	1.0010e+01	3.4300e−01	10.0000	0.000e+00	−3	0.088	0.383	0.469
39	1.7650e+00	1.6330e+01	1.4730e+01	6.7500e−01	10.5500	2.070e−27	−1	0.115	0.534	0.670

Note. — Second set of *WISE*/DEIMOS extended data columns. The first column, `WDID`, is not actually repeated in the table but is repeated here for clarity. The columns `Ell`, `Sbc`, `Irr`, and `AGN` are the template scales, $a_{\rm E}$, $a_{\rm S}$, $a_{\rm I}$, and $a_{\rm A}$ in Equation 5.1. The units quoted are the overall normalization given for the templates in Assef et al. (2010). `AGN_EBmV` is the excess extinction, $E(B-V)$, applied to the AGN template. `chisqr` is the χ^2 of the model from Equation 5.2, and `Ndf` is the formal number of degrees of freedom in the model (number of filters minus five). `z_min` is the closest redshift at which the galaxy satisfies upper flux cuts, `z_mid` is the redshift at which it satisfies the middle flux cut, and `z_max` is the farthest redshift at which the galaxy satisfies the lower flux cuts.

Table 5.7. Excerpt from 6dFGS Extended Data, Column Set 1

Ra °	Dec °	6dFGS_ID	GALEX_ID	AllWISE_ID
359.499210	−28.958080	7	6380767410811569507	0000m288_ac51-016147
359.369120	−29.047580	11	6380767411885310513	0000m288_ac51-013523
358.042580	−29.079060	19	6380767412959052516	3582m288_ac51-016561
358.872330	−27.883440	37	6380767402221635495	3583m273_ac51-000009
359.041330	−27.466580	39	6380767391484215299	3583m273_ac51-024746
0.059370	−26.730940	52	6380767390412573430	0000m273_ac51-059368

Note. — First set of 6dFGS extended data columns. The first two columns are the right ascension and declination, in J2000 decimal degrees. The `6dFGS_ID` column is an integer index uniquely assigned to targets in the 6dFGS survey. `GALEX_ID` is a uniquely identifying integer assigned in GALEX gr7 to the source (`null` if not matched). `AllWISE_ID` is the `source_id` assigned to the source in the AllWISE survey.

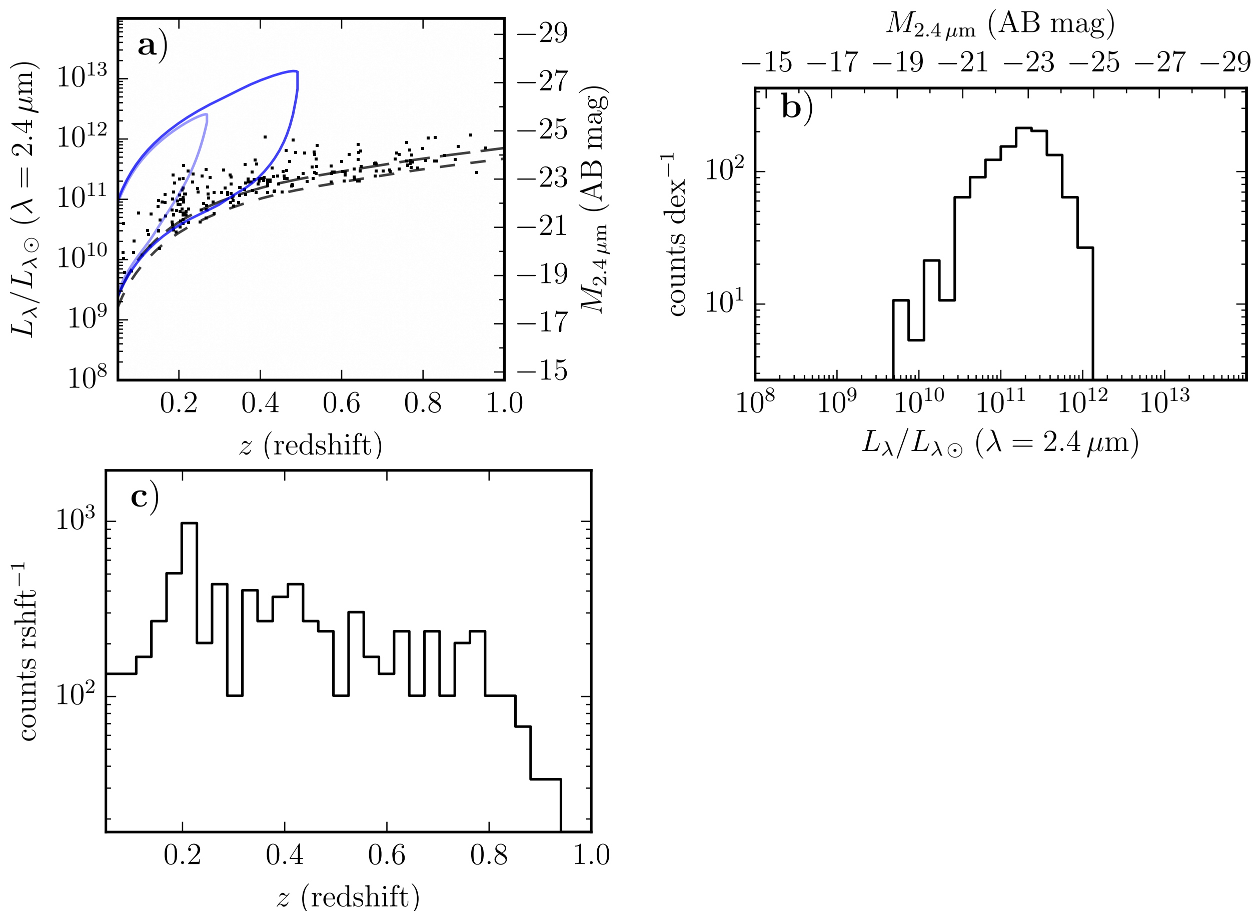

Figure 5.6: Panel **a** contains a scatter plot showing the range of luminosities and redshifts sampled by the *WISE*/DEIMOS survey. The dashed lines show luminosity cuts based on the mean SED from Chapter 3: any source in the bright sample that falls below the long dashed line is cut, and any source in the faint sample that falls below the dashed line is cut. The blue translucent lines show where the SED variety completeness is 95% and 98%, in order of increasing lightness. Panels **b** and **c** contain histograms of the data in redshift and luminosity, respectively, after the cuts in panel **a** are applied. No completeness corrections are applied, and the distributions are normalized to the number of data points the set contributes, $N = 222$ in **a** and 208 in all other panels.

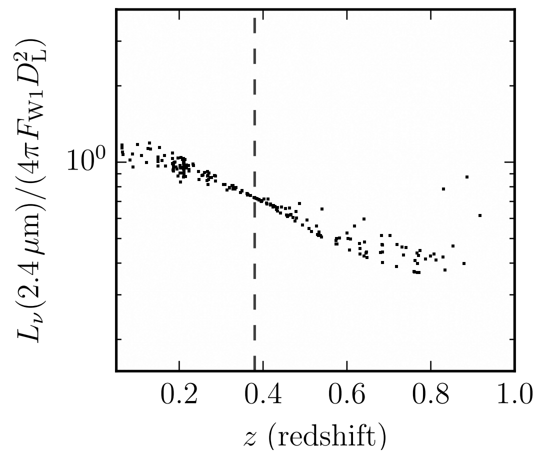

Figure 5.7: Scatter plot of K-corrections from W1 to rest frame 2.4 μm applied to *WISE*/DEIMOS data. The vertical dashed line at $z = 0.38$ marks the fiducial redshift used in this work, where the K-correction is only the bandwidth scaling by $1 + z$.

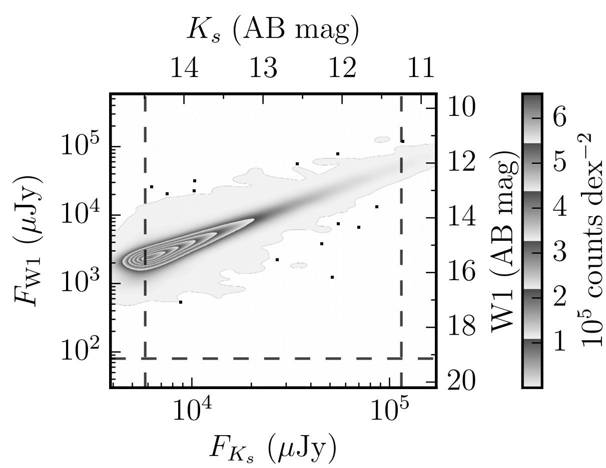

Figure 5.8: Density plot showing the measured fluxes in relationship to the selection limits imposed by the 6dFGS survey ($14.49 \geq K_s > 11.25$) and our analysis ($F_{\mathrm{W1}} \geq 80\,\mu$Jy). Note how the additional *WISE* limit eliminates no data.

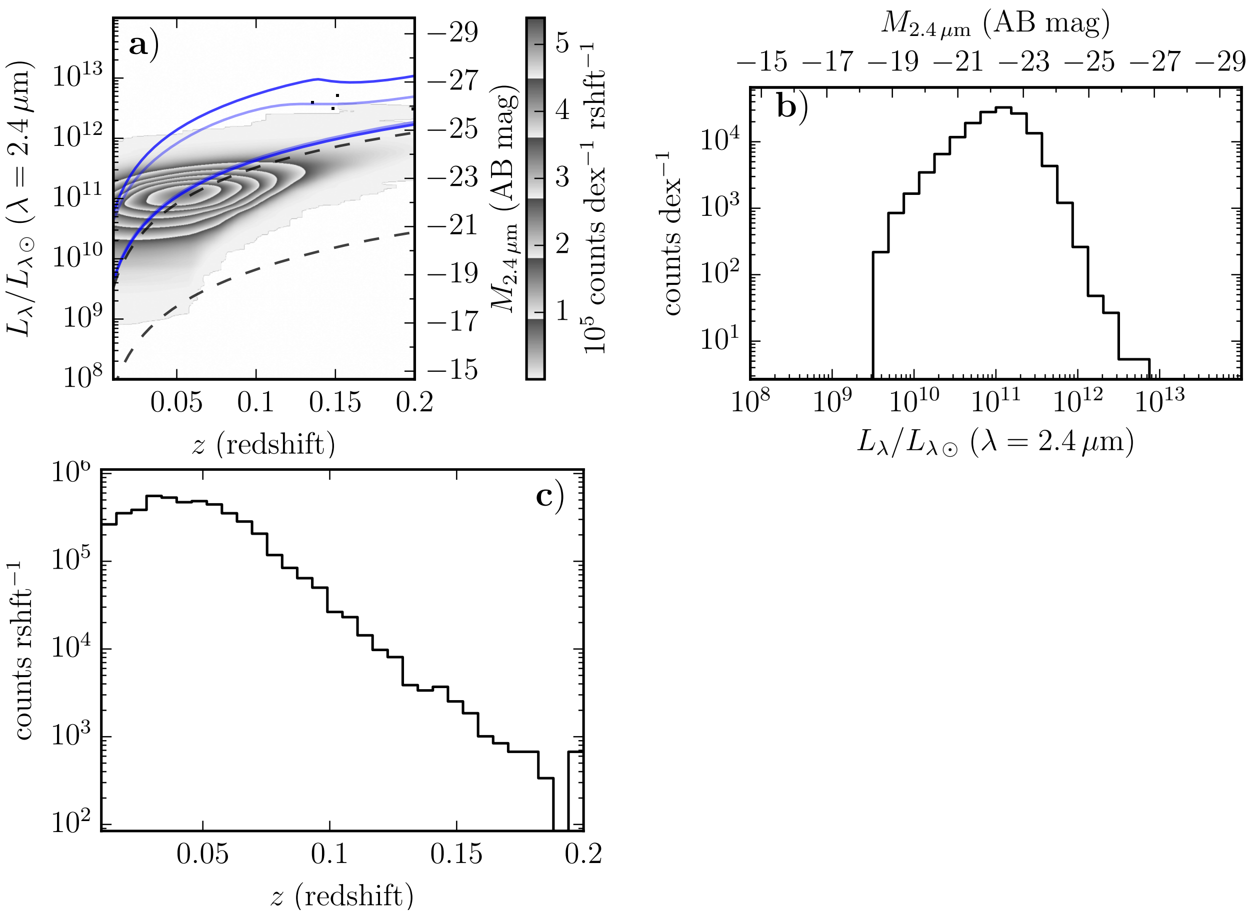

Figure 5.9: Panel **a** contains a density plot showing the range of luminosities and redshifts sampled by the 6dFGS survey. The dashed lines show luminosity cuts based on the mean SED from Chapter 3: any source lower than either line is cut. The blue translucent lines show where the SED variety completeness is 95% and 98%, in order of increasing lightness. Panels **b** and **c** contain histograms of the data in redshift and luminosity, respectively, after the cut in panel **a** is applied. No completeness corrections are applied, and the distributions are normalized to the number of data points the set contributes, $N = 47,335$ in panel **a**, and $28,232$ in all other panels.

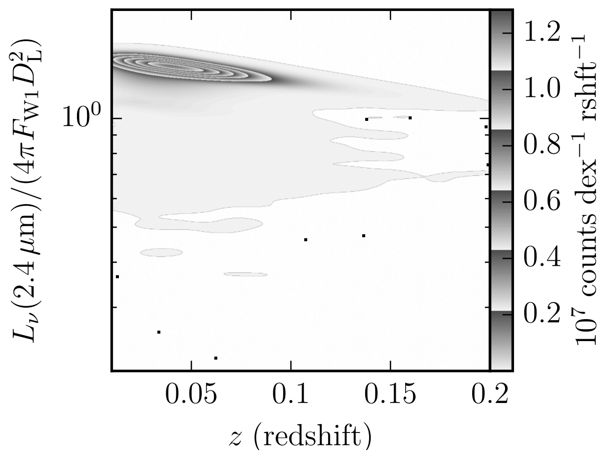

Figure 5.10: Density plot of K-corrections from W1 to rest frame $2.4\,\mu$m applied to 6dFGS data.

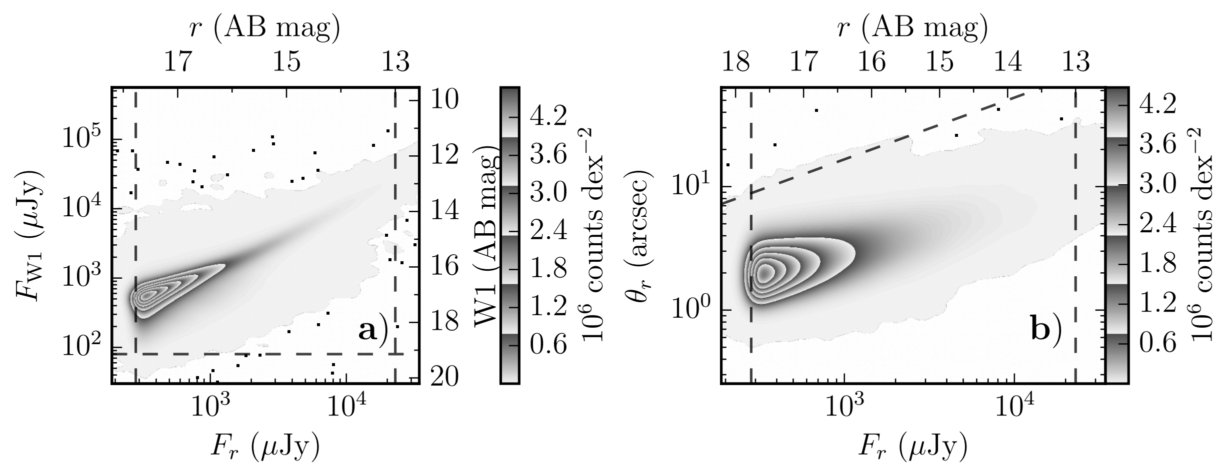

Figure 5.11: Panel **a** contains a density plot showing the measured fluxes in relationship to the selection limits imposed by the SDSS survey ($17.77 \geq r > 13.0$) and our analysis ($F_{\mathrm{W1}} \geq 80\,\mu$Jy). Note how the additional *WISE* limit eliminates a small fraction of data. Panel **b** contains a density plot showing the measured fluxes in relationship to the selection limits imposed by the SDSS survey ($17.77 \geq r > 10.5$) as the vertical dashed lines and surface brightness within the radius containing half of the Petrosian flux ($0.5F_r \geq \Sigma_{\min}\pi\theta_r^2$, $-2.5\log_{10}[\Sigma_{\min}/3631\,\mathrm{Jy}] = 24.5\,\mathrm{mag\,arcsec^{-2}}$) as the diagonal line in the upper left hand corner of the plot.

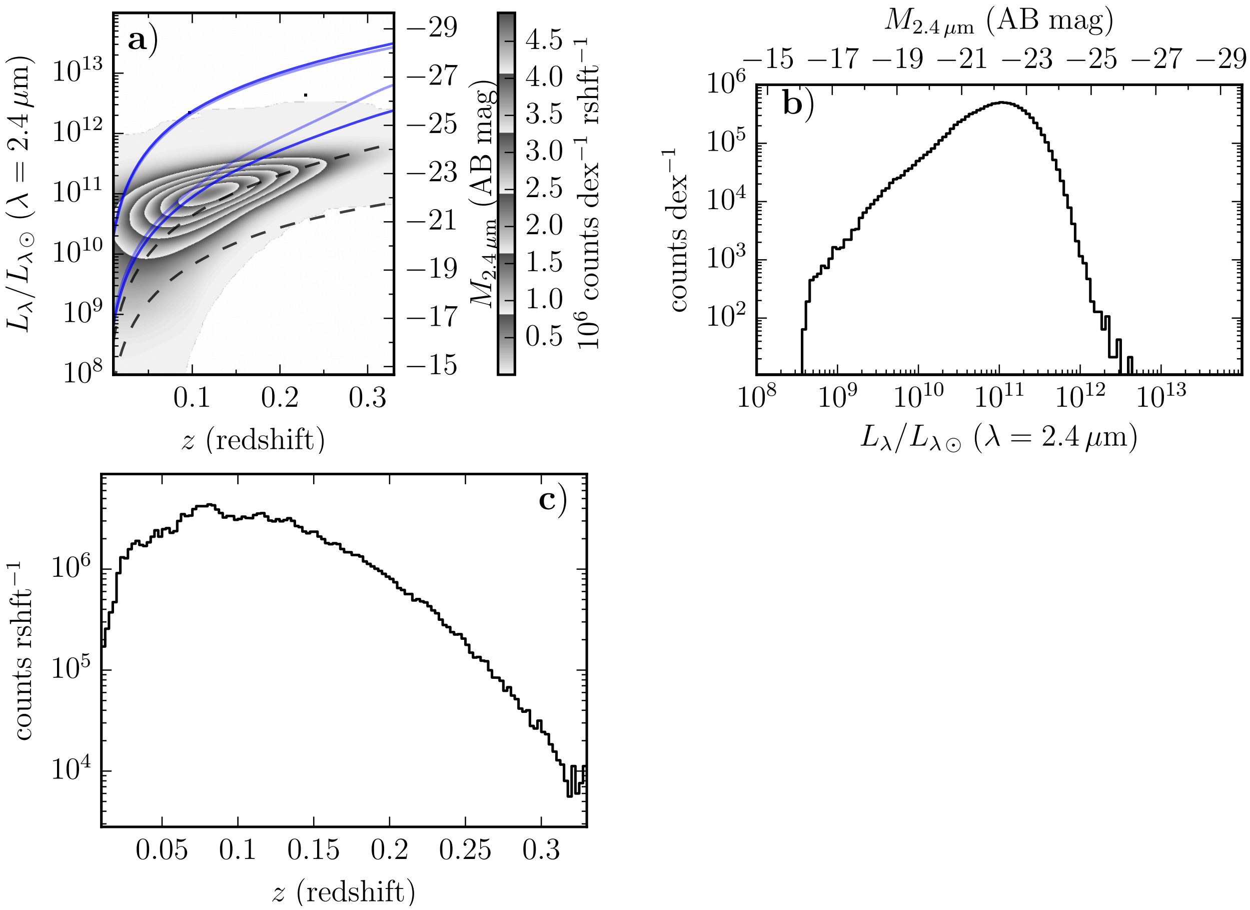

Figure 5.12: Panel **a** contains a density plot showing the range of luminosities and redshifts sampled by the SDSS survey. The dashed lines show luminosity cuts based on the mean SED from Chapter 3: any source lower than either line is cut. The blue translucent lines show where the SED variety completeness is 95% and 98%, in order of increasing lightness. Panels **b** and **c** contain histograms of the data in redshift and luminosity, respectively, after the cut in panel **a** is applied. No completeness corrections are applied, and the distributions are normalized to the number of data points the set contributes, $N = 626,007$ in panel **a**, and $476,868$ in all other panels.

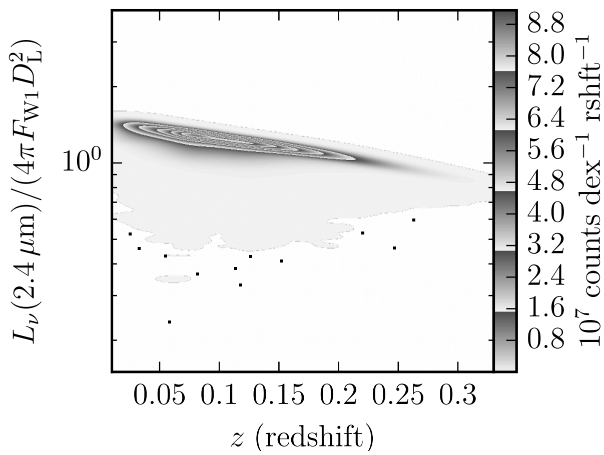

Figure 5.13: Density plot of K-corrections from W1 to rest frame 2.4 μm applied to SDSS data.

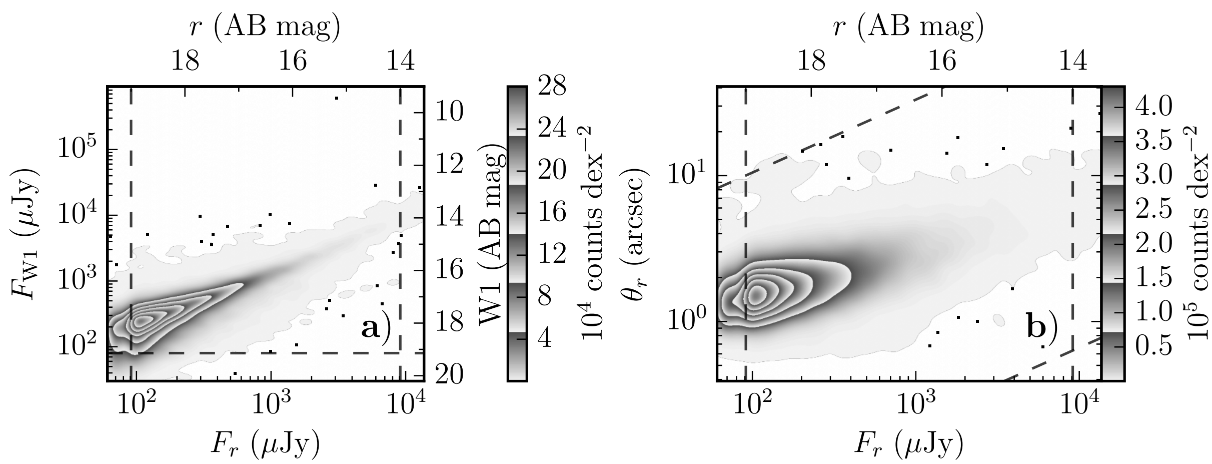

Figure 5.14: Panel **a** contains a density plot showing the measured fluxes in relationship to the selection limits imposed by the GAMA survey ($19 \geq r > 10$) and our analysis ($F_{\mathrm{W1}} \geq 80\,\mu$Jy). Note how the additional *WISE* limit eliminates a noticeable fraction of the data. Panel **b** contains a density plot showing the measured fluxes in relationship to the selection limits imposed by the GAMA survey ($19 \geq r > 14$) as the vertical dashed lines and surface brightness within the radius containing half of the Petrosian flux ($\Sigma_{\max}\pi\theta_r^2 \geq 0.5F_r \geq \Sigma_{\min}\pi\theta_r^2$, $-2.5\log_{10}[\Sigma_{\min}/3631\,\mathrm{Jy}] = 24.5\,\mathrm{mag\,arcsec^{-2}}$, $-2.5\log_{10}[\Sigma_{\max}/3631\,\mathrm{Jy}] = 15\,\mathrm{mag\,arcsec^{-2}}$) as the diagonal line in the upper left hand corner of the plot.

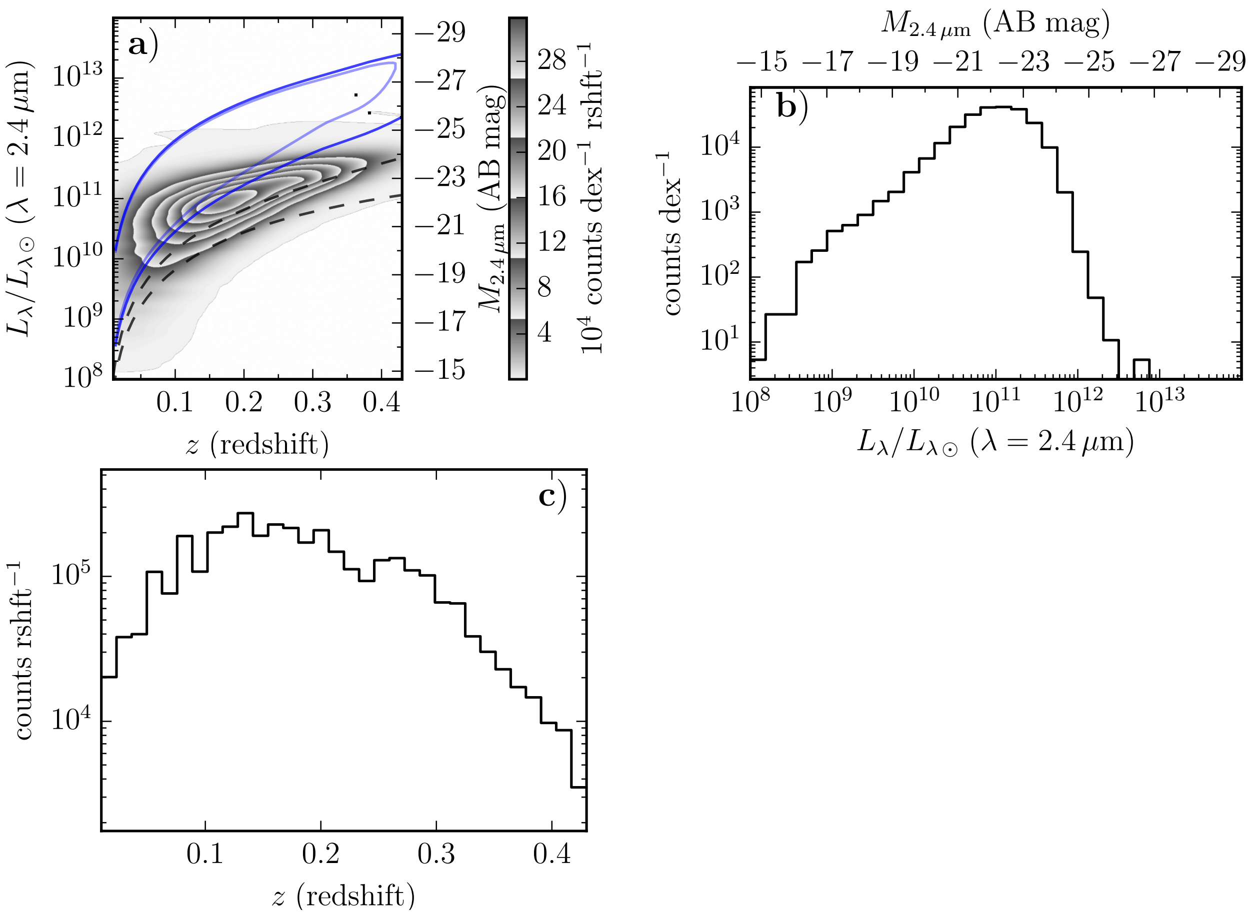

Figure 5.15: Panel **a** contains a density plot showing the range of luminosities and redshifts sampled by the GAMA survey. The dashed lines show luminosity cuts based on the mean SED from Chapter 3: any source lower than either line is cut. Panels **b** and **c** contain histograms of the data in redshift and luminosity, respectively, after the cut in panel **a** is applied. The blue translucent lines show where the SED variety completeness is 95% and 98%, in order of increasing lightness. No completeness corrections are applied, and the distributions are normalized to the number of data points the set contributes, $N = 52,773$ in panel **a**, and $44,604$ in all other panels.

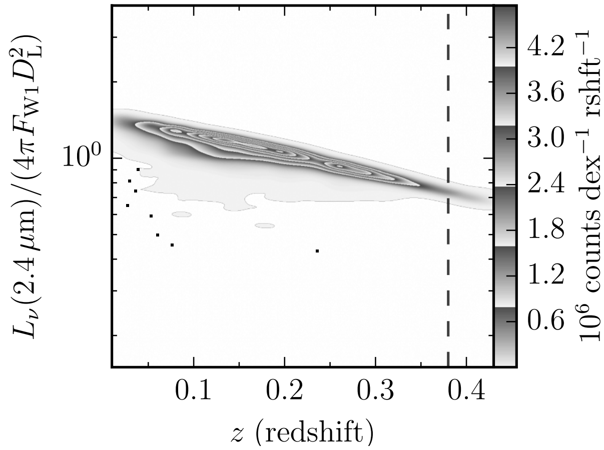

Figure 5.16: Density plot of K-corrections from W1 to rest frame $2.4\,\mu$m applied to GAMA data. The vertical dashed line at $z = 0.38$ marks the fiducial redshift used in this work, where the K-correction is only the bandwidth scaling by $1 + z$.

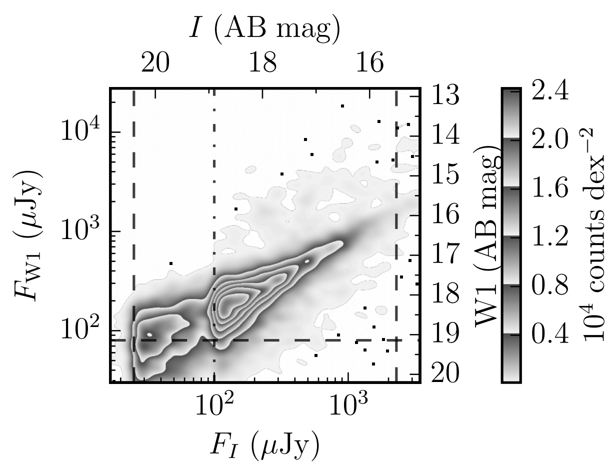

Figure 5.17: Density plot showing the measured fluxes in relationship to the selection limits imposed by the AGES survey ($20.4 \geq I > 15.5$ with 20% completeness setting in fainter than $I = 18.9$) and the analysis here ($F_{\mathrm{W1}} \geq 80\,\mu$Jy). Note how this is the first survey for which the main locus on which galaxies lie intersects the *WISE* limit imposed here.

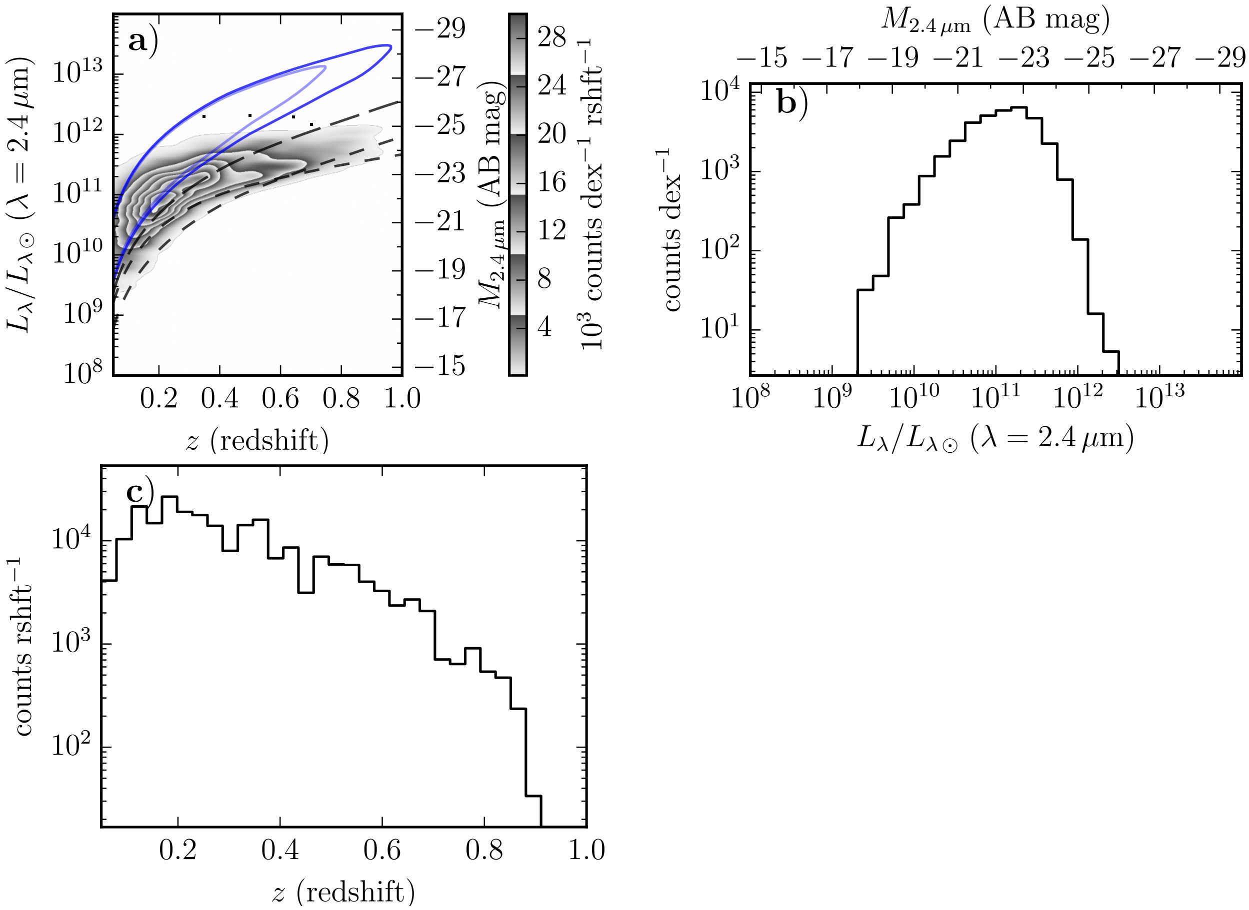

Figure 5.18: Panel **a** contains a density plot showing the range of luminosities and redshifts sampled by the AGES survey. The short dashed lines show luminosity cuts based on the mean SED from Chapter 3: any source lower than either short dashed line is cut, and any source brighter than $I = 18.9$ AB mag and below the long dashed line is cut. The blue translucent lines show where the SED variety completeness is 95% and 98%, in order of increasing lightness. Panels **b** and **c** contain histograms of the data in redshift and luminosity, respectively, after the cut in panel **a** is applied. No completeness corrections are applied, and the distributions are normalized to the number of data points the set contributes, $N = 6,603$ in panel **a**, and $6,553$ in all other panels.

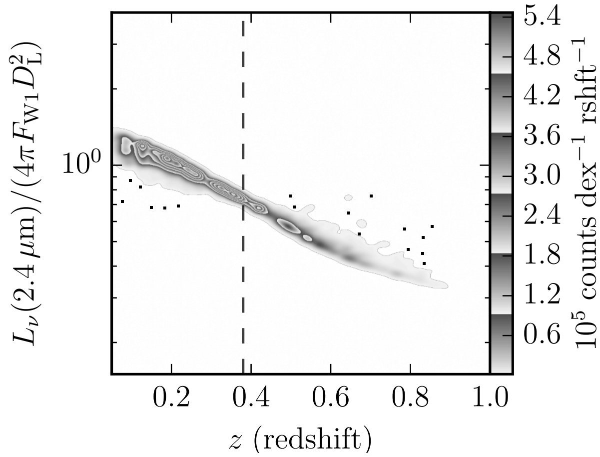

Figure 5.19: Density plot of K-corrections from W1 to rest frame $2.4\,\mu$m applied to AGES data. The vertical dashed line at $z = 0.38$ marks the fiducial redshift used in this work, where the K-correction is only the bandwidth scaling by $1 + z$.

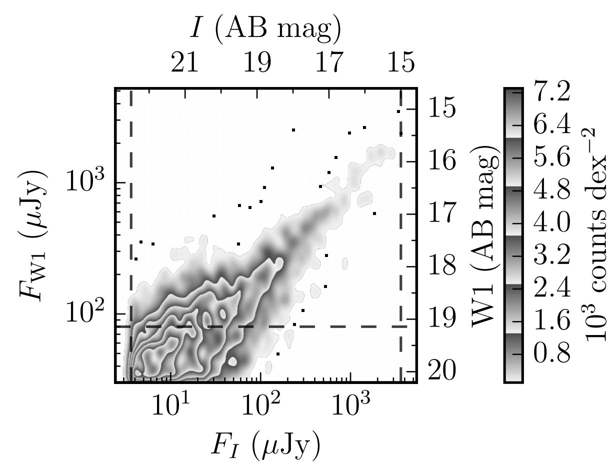

Figure 5.20: Density plot showing the measured fluxes in relationship to the selection limits imposed by the zCOSMOS survey ($22.5 \geq I > 15.0$) and here ($F_{\mathrm{W1}} \geq 80\,\mu$Jy). Note how the majority of the data is eliminated by the *WISE* limit we imposed, though the data is still near the intersection of the limits.

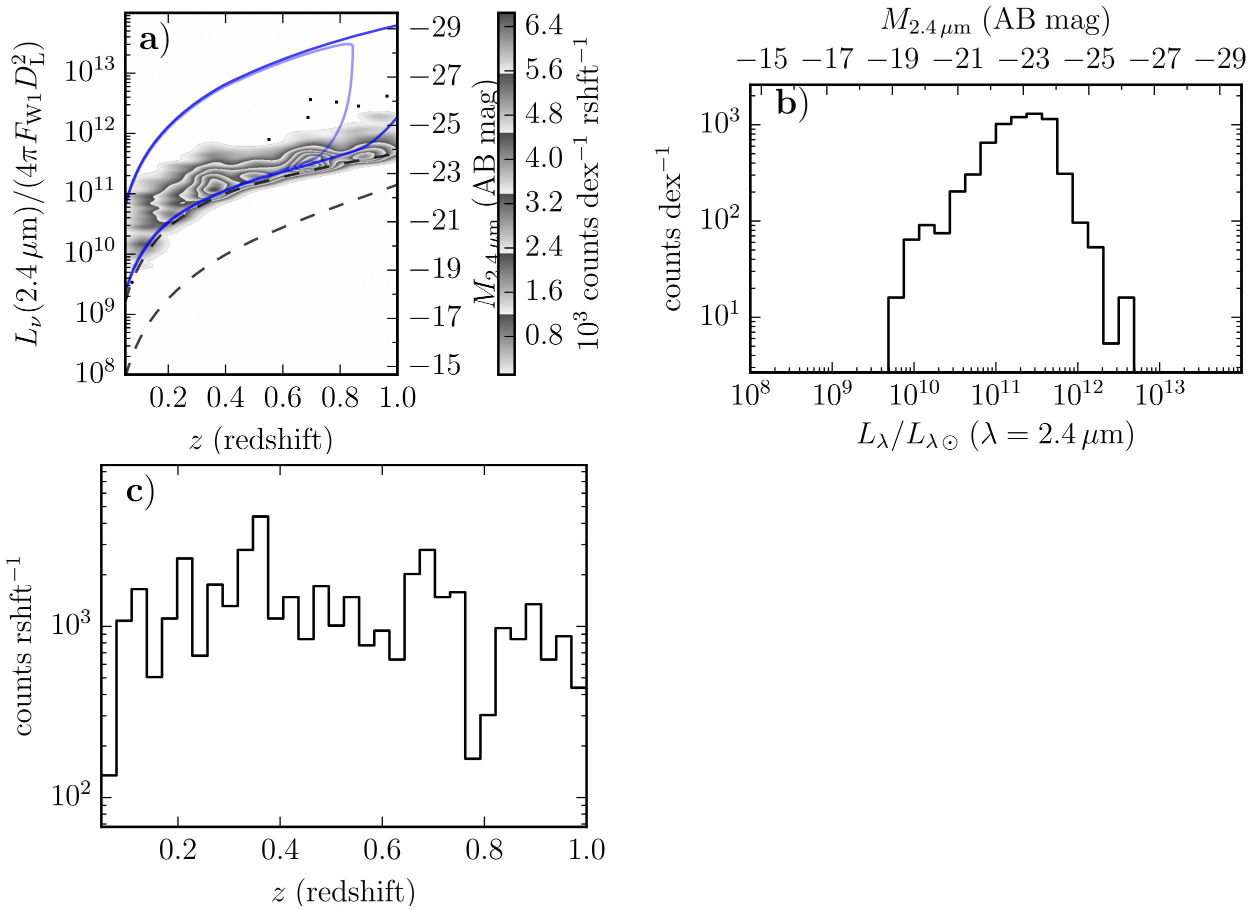

Figure 5.21: Panel **a** contains a density plot showing the range of luminosities and redshifts sampled by the zCOSMOS survey. The dashed lines show luminosity cuts based on the mean SED from Chapter 3: any source lower than either line is cut. The blue translucent lines show where the SED variety completeness is 95% and 98%, in order of increasing lightness. Panels **b** and **c** contain histograms of the data in redshift and luminosity, respectively, after the cut in panel **a** is applied. No completeness corrections are applied, and the distributions are normalized to the number of data points the set contributes, $N = 1,301$ in panel **a**, and $1,231$ in all other panels.

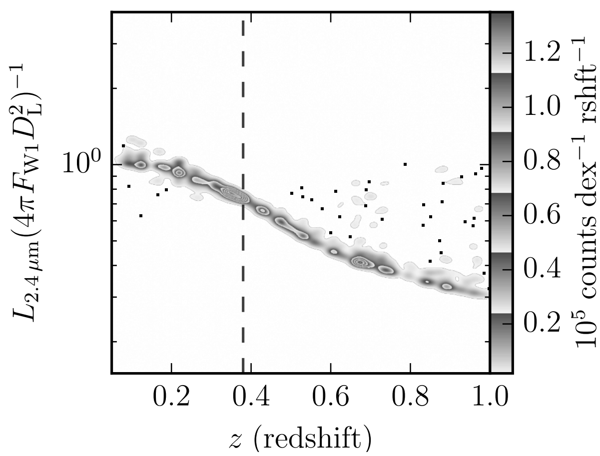

Figure 5.22: Density plot of K-corrections applied from W1 to rest frame $2.4\,\mu$m to zCOSMOS data. The vertical dashed line at $z = 0.38$ marks the fiducial redshift used in this work, where the K-correction is only the bandwidth scaling by $1 + z$.

Table 5.8. Excerpt from 6dFGS Extended Data, Column Set 2

6dFGS_ID	Ell	Sbc	Irr	AGN	AGN_EBmV	chisqr	Ndf	z_min	z_max
	$10^{10}\,L_\odot$	$10^{10}\,L_\odot$	$10^{10}\,L_\odot$	$10^{10}\,L_\odot$	mag				
7	2.5270e+01	0.0000e+00	3.5290e−01	0.0000e+00	0.0000	2.420e+02	1	0.053	0.102
11	2.5640e+01	0.0000e+00	0.0000e+00	1.7940e−02	13.0300	9.700e+01	2	0.056	0.106
19	8.4300e−01	0.0000e+00	0.0000e+00	0.0000e+00	0.0000	5.420e+04	3	0.044	0.085
37	7.0300e−01	0.0000e+00	0.0000e+00	0.0000e+00	0.0000	2.750e+03	2	0.044	0.085
39	3.8890e−01	0.0000e+00	1.3050e−02	4.2480e−03	13.0300	2.630e+01	2	0.007	0.014
52	1.8140e+00	0.0000e+00	0.0000e+00	0.0000e+00	0.0000	1.720e+04	3	0.042	0.080

Note. — Second set of 6dFGS extended data columns. The first column, 6dFGS_ID, is not actually repeated in the table but is repeated here for clarity. The columns Ell, Sbc, Irr, and AGN are the template scales, $a_{\rm E}$, $a_{\rm S}$, $a_{\rm I}$, and $a_{\rm A}$ in Equation 5.1. The units quoted are the overall normalization given for the templates in Assef et al. (2010). AGN_EBmV is the excess extinction, $E(B-V)$, applied to the AGN template. chisqr is the χ^2 of the model from Equation 5.2, and Ndf is the formal number of degrees of freedom in the model (number of filters minus five). z_min is the closest redshift at which the galaxy satisfies upper flux cuts, and z_max is the farthest redshift at which the galaxy satisfies the lower flux cuts.

Table 5.9. Excerpt from SDSS Extended Data, Column Set 1

`Ra` °	`Dec` °	`SDSS_ID`	`AllWISE_ID`
54.936790	0.216800	468504134002173952	0544p000_ac51-047826
57.025340	0.208850	1398488404370417664	0574p000_ac51-036206
57.296590	0.185310	1398496375829719040	0574p000_ac51-036226
57.442290	0.158840	1398494451684370432	0574p000_ac51-038743
57.452670	0.044340	1398499399486695424	0574p000_ac51-027223
57.490400	0.074350	1398501598509950976	0574p000_ac51-027204

Note. — First set of SDSS extended data columns. The first two columns are the right ascension and declination, in J2000 decimal degrees. The `SDSS_ID` column is an integer index uniquely assigned to targets in the SDSS survey (comes from `specObjID` column of the `SpecObj` table in the SDSS data release 10 context of CasJobs). `AllWISE_ID` is the `source_id` assigned to the source in the AllWISE survey.

Table 5.10. Excerpt from SDSS Extended Data, Column Set 2

SDSS_ID	Ell	Sbc	Irr	AGN	AGN_EBmV	chisqr	Ndf	z_min	z_max
	$10^{10}\,L_\odot$	$10^{10}\,L_\odot$	$10^{10}\,L_\odot$	$10^{10}\,L_\odot$	mag				
468504134002173952	3.3080e+01	0.0000e+00	3.3620e−01	0.0000e+00	0.0000	6.000e+02	5	0.001	0.231
1398488404370417664	1.2430e+00	0.0000e+00	5.3500e−01	0.0000e+00	0.0000	1.370e+03	7	0.001	0.085
1398496375829719040	3.2860e+01	0.0000e+00	4.5820e+00	0.0000e+00	0.0000	1.430e+03	7	0.001	0.244
1398494451684370432	4.4810e+01	0.0000e+00	2.9780e+00	0.0000e+00	0.0000	1.440e+03	5	0.001	0.291
1398499399486695424	1.1560e+01	0.0000e+00	7.6900e−01	8.2500e−01	13.0300	7.200e+01	7	0.001	0.154
1398501598509950976	3.2190e+01	0.0000e+00	1.2100e+00	0.0000e+00	0.0000	4.410e+02	5	0.001	0.239

Note. — Second set of SDSS extended data columns. The first column, `SDSS_ID`, is not actually repeated in the table but is repeated here for clarity. The columns `Ell`, `Sbc`, `Irr`, and `AGN` are the template scales, $a_{\rm E}$, $a_{\rm S}$, $a_{\rm I}$, and $a_{\rm A}$ in Equation 5.1. The units quoted are the overall normalization given for the templates in Assef et al. (2010). `AGN_EBmV` is the excess extinction, $E(B-V)$, applied to the AGN template. `chisqr` is the χ^2 of the model from Equation 5.2, and `Ndf` is the formal number of degrees of freedom in the model (number of filters minus five). `z_min` is the closest redshift at which the galaxy satisfies upper flux cuts, and `z_max` is the farthest redshift at which the galaxy satisfies the lower flux cuts.

Table 5.11. Excerpt from GAMA Extended Data, Column Set 1

Ra °	Dec °	GAMA_ID	AllWISE_ID
174.022810	0.705940	6806	1739p000_ac51-051576
174.100730	0.658910	6808	1739p000_ac51-051657
174.184930	0.709040	6826	1739p000_ac51-049388
174.302790	0.789990	6837	1739p015_ac51-002444
174.346900	0.696450	6840	1739p000_ac51-049335
174.396030	0.820770	6844	1739p015_ac51-002401

Note. — First set of GAMA extended data columns. The first two columns are the right ascension and declination, in J2000 decimal degrees. The `GAMA_ID` column is an integer index uniquely assigned to targets in the GAMA survey. `AllWISE_ID` is the `source_id` assigned to the source in the AllWISE survey.

Table 5.12. Excerpt from GAMA Extended Data, Column Set 2

GAMA_ID	Ell	Sbc	Irr	AGN	AGN_EBmV	chisqr	Ndf	z_min	z_max
	$10^{10}\,L_\odot$	$10^{10}\,L_\odot$	$10^{10}\,L_\odot$	$10^{10}\,L_\odot$	mag				
6806	1.1200e+01	2.6850e+01	2.7800e+00	5.2950e−02	0.1897	1.850e+02	8	0.052	0.383
6808	1.0400e+01	0.0000e+00	5.2300e−01	3.2660e−03	0.0000	2.280e+02	6	0.031	0.246
6826	2.7550e+00	0.0000e+00	3.2140e−01	0.0000e+00	0.0000	3.590e+03	7	0.015	0.130
6837	1.2690e+00	0.0000e+00	3.7570e−01	0.0000e+00	0.0000	1.070e+03	7	0.014	0.122
6840	1.1440e+01	0.0000e+00	3.8140e−01	3.0720e−02	0.2743	5.300e+02	7	0.032	0.248
6844	6.3390e+00	0.0000e+00	1.1100e−01	0.0000e+00	0.0000	1.070e+03	7	0.024	0.192

Note. — Second set of GAMA extended data columns. The first column, GAMA_ID, is not actually repeated in the table but is repeated here for clarity. The columns Ell, Sbc, Irr, and AGN are the template scales, $a_{\rm E}$, $a_{\rm S}$, $a_{\rm I}$, and $a_{\rm A}$ in Equation 5.1. The units quoted are the overall normalization given for the templates in Assef et al. (2010). AGN_EBmV is the excess extinction, $E(B-V)$, applied to the AGN template. chisqr is the χ^2 of the model from Equation 5.2, and Ndf is the formal number of degrees of freedom in the model (number of filters minus five). z_min is the closest redshift at which the galaxy satisfies upper flux cuts, and z_max is the farthest redshift at which the galaxy satisfies the lower flux cuts.

Table 5.13. Excerpt from AGES Extended Data, Column Set 1

Ra °	Dec °	AGES_ROW	NDWFS_ID	SDSS_ID	AllWISE_ID
216.393850	32.806960	6	346042	1237662684146041043	2159p333_ac51-002610
216.548230	32.807660	11	346533	1237662684146106652	2159p333_ac51-002915
216.818990	32.809900	26	348131	null	2159p333_ac51-000046
216.245250	32.812800	53	350281	1237664852570800769	2159p333_ac51-002806
217.374410	32.814140	64	351325	1237664853108064555	2177p333_ac51-008367
216.179020	32.814450	68	351568	1237664852570800403	2159p333_ac51-005461

Note. — First set of AGES extended data columns. The first two columns are the right ascension and declination, in J2000 decimal degrees. AGES does not have an identifier for its sources, but the plain text tables in Kochanek et al. (2012) have corresponding rows. `AGES_ROW` column contains the identity of the row the galaxy was published in, starting from 0. `NDWFS_ID` is a uniquely identifying integer assigned in NDWFS to the source (`null` if not matched). `SDSS_ID` is a uniquely identifying integer assigned in SDSS to the matching source (`null` if not matched). `AllWISE_ID` is the `source_id` assigned to the source in the AllWISE survey.

Table 5.14. Excerpt from AGES Extended Data, Column Set 2

AGES_ROW	Ell	Sbc	Irr	AGN	AGN_EBmV	chisqr	Ndf	z_min	z_mid	z_max
	$10^{10}\,L_\odot$	$10^{10}\,L_\odot$	$10^{10}\,L_\odot$	$10^{10}\,L_\odot$	mag					
6	1.6020e+00	5.7740e+00	0.0000e+00	0.0000e+00	0.0000	4.670e+03	4	0.006	0.200	0.243
11	3.7850e+00	0.0000e+00	0.0000e+00	9.4300e−02	0.2111	1.990e+02	4	0.006	0.190	0.276
26	7.4000e+01	0.0000e+00	0.0000e+00	0.0000e+00	0.0000	4.930e+03	4	0.026	0.580	0.865
53	2.5890e+01	0.0000e+00	2.8970e+00	0.0000e+00	0.0000	4.350e+01	4	0.017	0.453	0.745
64	1.0030e+01	2.6980e+00	0.0000e+00	9.0800e−02	0.1290	2.910e+02	4	0.010	0.293	0.477
68	1.5140e+01	1.1810e+00	1.1090e−01	0.0000e+00	0.0000	4.210e+02	1	0.012	0.333	0.482

Note. — Second set of AGES extended data columns. The first column, AGES_ROW, is not actually repeated in the table but is repeated here for clarity. The columns Ell, Sbc, Irr, and AGN are the template scales, $a_{\rm E}$, $a_{\rm S}$, $a_{\rm I}$, and $a_{\rm A}$ in Equation 5.1. The units quoted are the overall normalization given for the templates in Assef et al. (2010). AGN_EBmV is the excess extinction, $E(B-V)$, applied to the AGN template. chisqr is the χ^2 of the model from Equation 5.2, and Ndf is the formal number of degrees of freedom in the model (number of filters minus five). z_min is the closest redshift at which the galaxy satisfies upper flux cuts, z_mid is the redshift at which it satisfies the middle flux cut, and z_max is the farthest redshift at which the galaxy satisfies the lower flux cuts.

Table 5.15. Excerpt from zCOSMOS Extended Data, Column Set 1

Ra °	Dec °	zCOS_ID	COS_ID	SCOS_ID	SDSS_ID	AllWISE_ID
150.502790	1.877650	700137	507130	null	null	1497p015_ac51-048699
150.280590	2.021280	700529	null	null	1237653664722125224	1497p015_ac51-051213
150.122600	2.108540	700585	768236	null	null	1497p015_ac51-054126
150.183040	2.028990	700587	null	128673	null	1497p015_ac51-053799
150.393000	2.342770	701269	1213568	199260	null	1497p030_ac51-000271
150.653290	1.625360	800270	67120	41381	1237653664185385269	1512p015_ac51-036648

Note. — First set of zCOSMOS extended data columns. The first two columns are the right ascension and declination, in J2000 decimal degrees. The `zCOS_ID` column is an integer index uniquely assigned to targets in the zCOSMOS survey. `COS_ID` is a uniquely identifying integer assigned in Capak et al. (2007) to the matching source (`null` if not matched). `SCOS_ID` is a uniquely identifying integer assigned in SCOSMOS to the matching source (`null` if not matched). `AllWISE_ID` is the `source_id` assigned to the source in the AllWISE survey.

Table 5.16. Excerpt from zCOSMOS Extended Data, Column Set 2

zCOS_ID	Ell	Sbc	Irr	AGN	AGN_EBmV	chisqr	Ndf	z_min	z_max
	$10^{10}\,L_\odot$	$10^{10}\,L_\odot$	$10^{10}\,L_\odot$	$10^{10}\,L_\odot$	mag				
700137	1.1040e+01	6.2540e+00	0.0000e+00	3.7750e+00	1.0530	4.840e+02	8	0.069	0.885
700529	0.0000e+00	5.2540e+00	1.0580e+00	1.5040e−01	4.5620	5.030e−30	−2	0.015	0.291
700585	5.1830e+00	0.0000e+00	0.0000e+00	3.3260e+00	0.6960	1.430e+03	11	0.043	0.733
700587	1.2620e+01	0.0000e+00	1.6640e+00	0.0000e+00	0.0000	1.630e+03	2	0.021	0.471
701269	1.4070e+01	5.1540e+00	3.5440e−01	1.2210e+01	1.0640	3.920e+02	8	0.078	0.986
800270	0.0000e+00	2.8730e+01	7.7600e−01	0.0000e+00	0.0000	9.300e+03	17	0.088	0.574

Note. — Second set of zCOSMOS extended data columns. The first column, `zCOS_ID`, is not actually repeated in the table but is repeated here for clarity. The columns `Ell`, `Sbc`, `Irr`, and `AGN` are the template scales, $a_{\rm E}$, $a_{\rm S}$, $a_{\rm I}$, and $a_{\rm A}$ in Equation 5.1. The units quoted are the overall normalization given for the templates in Assef et al. (2010). `AGN_EBmV` is the excess extinction, $E(B-V)$, applied to the AGN template. `chisqr` is the χ^2 of the model from Equation 5.2, and `Ndf` is the formal number of degrees of freedom in the model (number of filters minus five). `z_min` is the closest redshift at which the galaxy satisfies upper flux cuts, and `z_max` is the farthest redshift at which the galaxy satisfies the lower flux cuts.

CHAPTER 6

Measured Values of Luminosity Function Parameters

The *WISE* satellite surveyed the entire sky multiple times in four infrared wavelengths (3.4, 4.6, 12, and 22 μm; Wright et al., 2010). The unprecedented combination of coverage area and depth gives us the opportunity to measure the luminosity function of galaxies, one of the fundamental quantities in the study of them, at 2.4 μm to an unparalleled level of formal statistical accuracy in the near infrared. The big advantage of measuring luminosity functions at wavelengths in the window ≈ 2 to $3.5\,\mu$m is that it correlates more closely to the total stellar mass in galaxies than others. In this chapter we report on the parameters for the 2.4 μm luminosity function of galaxies obtained from applying the spectroluminosity functional based methods defined in Chapter 2 to the data sets described in Chapter 5 using the mean and covariance of 2.4 μm normalized SEDs from Chapter 3. In terms of single Schechter function parameters evaluated at the present epoch, the combined result is: $\phi_\star = 5.8 \pm [0.3_{\rm stat},\, 0.3_{\rm sys}] \times 10^{-3}\,{\rm Mpc}^{-3}$, $L_\star = 6.4 \pm [0.1_{\rm stat},\, 0.3_{\rm sys}] \times 10^{10}\,L_{2.4\,\mu{\rm m}\,\odot}$ ($M_\star = -21.67 \pm [0.02_{\rm stat},\, 0.05_{\rm sys}]\,{\rm AB\ mag}$), and $\alpha = -1.050 \pm [0.004_{\rm stat},\, 0.03_{\rm sys}]$, corresponding to a galaxy number density of $0.08\,{\rm Mpc}^{-3}$ brighter than $10^6\,L_{2.4\,\mu{\rm m}\,\odot}$ ($10^{-3}\,{\rm Mpc}^{-3}$ brighter than $L_\star$) and a 2.4 μm luminosity density equivalent to $3.8 \times 10^8\,L_{2.4\,\mu{\rm m}\,\odot}\,{\rm Mpc}^{-3}$. The high statistical accuracy is achieved by combining many large public redshift surveys with the wide coverage from *WISE*, and the unevenness in statistical accuracy is a result of our efforts to work around biases of uncertain origin that affect resolved and marginally resolved galaxies. With further refinements, the techniques applied in this chapter promise to advance the study of the spectral energy distribution of the universe as a whole.

---

[0]This chapter is based on a paper in preparation for submission to The Astrophysical Journal in 2017, one of those on which Chapter 2's paper waits, by the authors: S. E. Lake, E. L. Wright, R. J. Assef, T. H. Jarrett, S. Petty, S. A. Stanford, D. Stern, and C.-W Tsai.

6.1 Introduction

The luminosity function (LF) is one of the most basic statistical properties measured for any class of objects in astronomy. The fundamental nature of the LF means that it has been measured for galaxies many times, in many different bandpasses (a small sample: Bell et al., 2003; Blanton et al., 2003b; Cool et al., 2012; Dai et al., 2009; Jones et al., 2006; Kelvin et al., 2014; Kochanek et al., 2001; Lin et al., 1999; Loveday et al., 2012; Loveday, 2000; Montero-Dorta & Prada, 2009; Smith et al., 2009).

The release of the AllWISE catalog generated from the data gathered by the *WISE* satellite, described in Wright et al. (2010) and Cutri et al. (2013), marks the availability of $3.4\,\mu$m (W1) and $4.6\,\mu$m (W2) photometric data that is better than 95% complete over the vast majority of the sky down to 44 and $88\,\mu$Jy, respectively. This new data set presents the opportunity to utilize the large number of public redshift surveys, in tandem with a small *WISE*-selected survey of our own, to measure the near-IR luminosity function of galaxies at $2.4\,\mu$m to unprecedented accuracy. The advantage of measuring the luminosity function in this range of wavelengths is that fluxes suffer from minimal dust extinction in both the target galaxy and the Milky Way, according to dust extinction models like the one from Cardelli et al. (1989). Further, near infrared light traces the target galaxy's stellar mass in evolved stars more faithfully than optical wavelengths (Loveday, 2000), as long as the contribution of thermally pulsing asymptotic giant branch (TP-AGB) stars can be correctly accounted for in the population synthesis models (for example: Bruzual & Charlot, 2003; Maraston, 2005). We measure the luminosity function at $2.4\,\mu$m, in particular, because it is the wavelength directly observed by W1 for galaxies at the median redshift, $z = 0.38$, of galaxies with $F_{\rm W1} > 80\,\mu$Jy in Lake et al. (2012).

The new opportunity presented also presented new challenges. First, even limiting the redshift surveys to those that are publicly available and that are, primarily, selected by flux at a single wavelength meant that there were a lot of details that needed to be addressed in the characterization and selection process for the six surveys used here. Because of this, the primary characterization is done separately in Chapter 5. Second, we limited the surveys to be well above the sensitivity limits of the AllWISE data set, a minimum flux of 80 μJy in W1 (19.14 AB mag), in order to minimize the additional incompleteness from the cross-match and to match the properties of Lake et al. (2012) as closely as possible. This means that the surveys have flux limits at two wavelengths. The two flux limits, combined with the wide range of redshifts included in the analysis, $0.01 < z \leq 1.0$, meant that the existing luminosity function measurement tools were not adequate to the challenge of analyzing the collected data set. For this reason, a new estimator based on analyzing the likelihood of a galaxy's entire spectral energy distribution (SED) is derived in Chapter 2. The likelihood estimate used in this work is based on the mean and covariance of SEDs as measured in Chapter 3.

The structure of this chapter is as follows: Section 6.2 summarizes properties of the data used to measure the 2.4 μm luminosity function described in Chapter 5, Section 6.3 summarizes the estimators used in this paper to perform the measurements, Section 6.4 goes over the results of the analysis, and Section 6.6 contains the conclusions drawn from the analysis.

6.2 Data Summary

The full description of the data sets used in this work can be found in Chapter 5. For convenience, the table summarizing the properties of the spectroscopic surveys used from that chapter is reproduced here in Table 6.1.

As described in Section 2.2.4, the parametric model used here requires models for the relationship between noise and flux. Because the flux selection cuts are all relatively bright a single power law of the form

$$\left(\frac{\sigma_F}{F}\right)^2 = \left(\frac{F}{A}\right)^B \tag{6.1}$$

was adequate. The model also requires an estimate of the mean, $\langle\tau\rangle$, and standard deviation, σ_τ, of the dust obscuration for each selection filter in the field of the redshift survey. Table 6.2 contains the parameters measured for each survey, with separate values for the

Table 6.1. Summary of Spectroscopic Surveys Used (copy)

Survey	Release version	Redshifts min/median/max	Coverage (Ω) (sr)	Band	m_{lim} AB mag	Reference
6dFGS	3	0.01 / 0.05 / 0.20	4.17[a]	K_s	11.25/14.49	Jones et al. (2009)
SDSS-DR7	7	0.01 / 0.10 / 0.33	2.40[b]	r	13.0/17.77	Abazajian et al. (2009)
GAMA	2	0.01 / 0.18 / 0.43	4.39×10^{-2}	r	14.0/19.0	Baldry et al. (2010)
AGES	1	0.05 / 0.31 / 1.00	2.36×10^{-3}	I	15.5/18.9/20.4	Kochanek et al. (2012)
zCOSMOS-10k	2	0.05 / 0.61 / 1.00	5.2×10^{-4}	I^*	15.0/22.5	Lilly et al. (2009)
WISE/DEIMOS	2	0.05 / 0.38 / 1.00	5.78×10^{-5}	W1	15.0/18.70/19.14[c]	Lake et al. (2012)

Note. — Redshift surveys used in the data analysis here. The selection for zCOSMOS was done using the Hubble Space Telescope's Advanced Camera for Surveys (ACS) filter F814W, which is approximately I-band. The selections for AGES and *WISE*/DEIMOSare split into a complete bright and sparse faint samples. The Redshifts column contains the median redshift of the survey, and the minimum and maximum redshifts likely to be useful. The smaller surveys, for example, have a bias against selecting galaxies that are local, large, and resolved because they would obstruct the field of higher redshift galaxies, so they require a higher minimum redshift cutoff. The larger surveys, contrastingly, when they contain high redshift sources they are more likely to be redshift blunders, and so they require a lower maximum redshift.

[a] Inital 6dFGS area is 5.2 sr, but all data with $\delta \geq -11.5°$ was removed to eliminate overlap with other surveys.

[b] Initial SDSS area is 2.45 sr, but the footprint of the smaller, deeper, surveys also used here are removed to eliminate overlap.

[c] The upper limit is in R-band magnitudes, as required in the Keck/DEIMOS documentation, and measured in the USNO's NOMAD catalog (Zacharias et al., 2004).

optical selection filter and W1. The calculation of the incompleteness due to flux variety also use the parameters in the table to calculate the selection function in redshift-luminosity space, $S(L, z)$.

There is one additional plot set not in Chapter 5 that are necessary for understanding the choices made about how to analyze the data, found in Figure 6.1. It shows that `w1rchi2` behaves about as one would expect for galaxies with $z < 1$ where, even if galaxies in the past were the same size as today, the increasing angular diameter distance gives them, overall, a smaller radius on the sky. The vertical line at $z = 0.2$ is placed there after trial and error as a dividing line between samples that are significantly contaminated by resolved and marginally resolved objects ($z \leq 0.2$), and those that are sufficiently point-like to render resolution concerns moot ($z > 0.2$). In this work we describe the set of all galaxies that come from below $z = 0.2$ as the low z sample, and those from above the line as the high z sample.

As a check on the impact the new analysis techniques from Chapter 2, we have also analyzed high and low redshift subsamples that had completeness above 98% of the maximum value for the survey, as defined by Equation 2.21, and as shown by the light blue contours on the luminosity-redshift plots in Chapter 5. These samples, called the 'trim' simples, have significantly lower numbers of galaxies with the accompanying increase in statistical uncertainty, but also reduced systematic uncertainty from the constancy of the selection function.

The number of sources each survey makes to the combined samples, as well as their overall sizes, can be found in Table 6.3.

6.3 Analysis Methods and Models Summary

The analyses in this work are centered around maximum likelihood estimates of the quantities related to the LF. As is customary in most works on the LF, we analyze the data using both binned and parametric estimators. The full description and derivation of the estimators used here is in Chapter 2. Two standard binned estimators were adapted for this work: $1/V_{\max}$

Table 6.2. Noise Models Used for Parametric Fits and Completeness

Survey	$A_{\rm opt}$	$B_{\rm opt}$	$A_{\rm W1}$	$B_{\rm W1}$	$\langle\tau_{\rm opt}\rangle$	$\sigma_{\tau\,\rm opt}$	$\langle\tau_{\rm W1}\rangle$	$\sigma_{\tau\,\rm W1}$
	nJy		nJy		10^2	10^2	10^3	10^3
6dFGS	43410	−0.9068	5.469×10^{-6}	−0.2774	2.559	3.142	12.69	15.58
SDSS	203.7	−1.174	0.9552	−0.5334	0	0	6.173	6.107
GAMA	66.15	−1.419	6.793	−0.6317	0	0	5.914	1.801
AGES	37.12	−1.472	1.570	−0.5651	2.002	0.4561	2.015	0.4591
WISE/DEIMOS	89.52	−0.457	675.6	−1.016	23.91	23.89	15.8	15.79
zCOSMOS	102.1	−1.379	139.1	−0.8576	3.134	0.2279	3.141	0.2283

Note. — Noise model parameters fit to each survey, separately. The 'opt' parameters pertain to the optical filter used for selection in the survey (see Table 6.1), and the 'W1' parameters are the parameters for the W1 filter. The A and B parameters relate to a power law fit of signal-to-noise ratio to flux (see Equation 6.1), and $\langle\tau\rangle$ and σ_τ are the mean and standard deviation of the optical depth from foreground dust obscuration, averaged over targets in the survey. When the dust obscuration parameters are zero, target selection was performed on fluxes after extinction correction instead of before. All quantities given to four significant figures, regardless of the statistical or systematic uncertainties in the quantities.

Table 6.3. Combined Samples Sizes

Sample	N_{6dFGS}	N_{SDSS}	N_{GAMA}	N_{AGES}	N_{WD}[a]	N_{zC}[b]	N_{tot}
Low z	27,071	450,731	28,619	2,000	36	133	508,590
High z	0	26,556	15,872	3,741	171	1,091	47,431
Low z Trim	15,891	106,003	9,513	1,212	25	116	132,760
High z Trim	0	21	125	452	17	647	1,262

Note. — Number of sources contributed by each survey to the combined samples named in the first column. The last column contains the total number of sources in each combined sample.

[a] *WISE*/DEIMOS

[b] zCOSMOS

from Schmidt (1968) as modified by Avni & Bahcall (1980); and $N_{\mathrm{obs}}/N_{\mathrm{mdl}}$ from Miyaji et al. (2001). The adaptation was to handle situations where the selection function varies significantly over the bin in luminosity-redshift space. For the $1/V_{\max}$ estimator, the varying completeness corrected version of the estimator, with log-spaced bins in luminosity, is given by:

$$\Phi(L_i, z_i) = \frac{1}{S(L_i, z_i) L_i \Delta \ln L_i} \sum_j \frac{1}{\Delta V_j}, \tag{6.2}$$

where the redshift-luminosity bin is labeled by the index i, $\Phi(L_i, z_i)$ is the constant estimate of the luminosity function for that bin, the sum is over sources that fall into the bin, and ΔV_j is the volume available to the source to still be in both the bin and the selection criteria of the survey.

The varying completeness corrected version of $N_{\mathrm{obs}}/N_{\mathrm{mdl}}$ is, formally, much closer to the form of the original estimator from Miyaji et al. (2001):

$$\begin{aligned}\Phi(L_i, z_i) &= \Phi^{\mathrm{mdl}}(L_i, z_i) \cdot \frac{N_i}{\langle N_i^{\mathrm{mdl}} \rangle} \\ &= \frac{\Phi^{\mathrm{mdl}}(L_i, z_i)}{\int_{\mathrm{bin}} \Phi^{\mathrm{mdl}}(L, z)\, S(L, z)\, \mathrm{d}L\, \mathrm{d}V} \cdot N_i, \end{aligned} \tag{6.3}$$

where $\Phi^{\mathrm{mdl}}(L, z)$ is an approximate ('model') luminosity function that brings the estimator closer to evaluating the luminosity function at the center of the bin, (z_i, L_i), as long as

$\Phi^{\mathrm{mdl}}(L,z)$ is closer to the true luminosity function than the implicitly assumed $\Phi^{\mathrm{mdl}}(L,z) =$ constant of an uncorrected estimator. For these purposes, this work assumes $\Phi^{\mathrm{mdl}}(L,z)$ is a Schechter function that has a faint end slope $\alpha = -1$ and $M_\star = -22\,\mathrm{mag}$ (near the peak of the luminosity histograms in Chapter 5).

The parametric estimator used in this work is based on the spectro-luminosity functional, Ψ. The final estimator of the likelihood of the data is a little complicated, requiring a few nested equations to express. The outermost equation is given by:

$$\begin{aligned}\ln(\mathcal{L}) = \sum_{\text{galaxies}} & \ln(S(F_{\mathrm{sel}}, F_0, \vec{x})\mathcal{L}_{\mathrm{SED}}(F_{\mathrm{sel}}, F_0|L_0)\Phi(L_0,z)) \\ & - \int S(F_{\mathrm{sel}}, F_0, \vec{x})\mathcal{L}_{\mathrm{SED}}(F_{\mathrm{sel}}, F_0|L_0)\Phi(L_0,z)\,\mathrm{d}F_{\mathrm{sel}}\,\mathrm{d}F_0\,\mathrm{d}L_0\,\mathrm{d}V_c,\end{aligned} \tag{6.4}$$

where the selection function, S, calculates the probability that a source with given observed fluxes, F_{sel} and F_0, and at spatial position $\vec{x}$ is selected for inclusion in the survey. This flux selection function is assumed to take only two values: 0 for excluded regions, and $0 < s < 1$ for sources in selected regions (s is the overall completeness). Basically, its primary purpose is to set the limits of the integration.

$\mathcal{L}_{\mathrm{SED}}$ is the likelihood for a galaxy to have a particular SED given it has $2.4\,\mu\mathrm{m}$ luminosity L_0, projected down from the full function space to the fluxes F_{sel} and F_0. In this work we approximate the full $\mathcal{L}_{\mathrm{SED}}$ as a Gaussian and incorporate an uncertainty model for the fluxes and dust extinction to get:

$$\begin{aligned}\mathcal{L}_{\mathrm{SED}}(F_{\mathrm{sel}}, F_0|L_0) &= \frac{\mathrm{e}^{\tau_1+\tau_2}}{\sqrt{(2\pi)^2\det(\sigma)}} \cdot \left(\frac{4\pi D_L(z)^2}{(1+z)L_0}\right)^2 \\ &\quad \cdot \exp\left(-\frac{1}{2}\sum_{i,j=2}^{2}[\ell_i-\mu_i][\sigma^{-1}]_{ij}\cdot[\ell_j-\mu_j]\right), \text{ and} \\ \ell_i &= \frac{F_i 4\pi D_L(z)^2\mathrm{e}^{\tau_i}}{(1+z)L_0}.\end{aligned} \tag{6.5}$$

τ_i is the optical depth due to dust in the Milky Way present for flux in filter i, when the selection fluxes weren't extinction corrected, 0 when they were. $D_L(z)$ is the luminosity distance to the source. The F_i are one of F_{sel} or F_0 and are the measured fluxes. μ_i is the mean value ℓ_i takes, as predicted from the mean SED. σ is a covariance matrix that takes the following form (no summation):

$$\sigma_{ij} = \Sigma_{ij} + \left(\delta_{ij} A_i F_i^{B_i} + \sigma_{\tau\, i}\sigma_{\tau\, j}\right) \mu_i \mu_j, \tag{6.6}$$

where A and B are model parameters fit using ordinary least squares in log-space of $\sigma_F^2 F^{-2}$ to F, $\sigma_{\tau\, i}$ is the standard deviation of the optical depth present for fluxes in channel i over the survey targets, and Σ_{ij} is the covariance of SEDs projected down to apply to the space spanned by F_{sel} and F_0, similar to the calculations described in Chapter 3. The optical depths are calculated from the dust extinction model of Cardelli et al. (1989) using the E$(B - V)$ dust maps from Schlegel et al. (1998).

$\Phi(L_0, z)$ is a Schechter luminosity function, originally defined in Schechter (1976),

$$\Phi(L, z) = \frac{\phi_\star}{L_\star} \left(\frac{L}{L_\star}\right)^{\alpha} \mathrm{e}^{-L/L_\star}. \tag{6.7}$$

The parameterization for evolution in $\phi_\star$ and $L_\star$ are:

$$\begin{aligned} \phi_\star &= \phi_0 \mathrm{e}^{-R_\phi t_L(z)}, \text{ and} \\ L_\star &= L_0 \mathrm{e}^{-R_L t_L(z)} \left(1 - \frac{t_L(z)}{t_0}\right)^{n_0}, \end{aligned} \tag{6.8}$$

where $t_L(z)$ is the lookback time of a source at redshift z, R_ϕ is the specific evolution rate in ϕ and is assumed to be constant, R_L is the luminosity evolution rate, t_0 is the time of first light (set here to $t_0 = t_L(z_{\mathrm{recom}})$ since our data cannot meaningfully constrain it), and n_0 is the power law index for the early time increase in $L_\star$.

As explained in Chapter 2, the actual fitting was done using derived parameters that proved to be more statistically orthogonal than the ones given above. In terms of the parameters from Equation 6.8, they are:

$$R_n = R_\phi - \min(1 + \alpha, 0) \left[R_L + \frac{n_0}{t_0}\right], \text{ and} \tag{6.9}$$

$$\kappa_\star = \frac{\phi_0 L_0^{3/2}}{\Omega_{\mathrm{sky}} 4\pi^{1/2}} \Gamma\left(\alpha + \frac{5}{2}\right), \tag{6.10}$$

which are named the specific rate of change in galaxy number density at $z = 0$, and the normalization to the source flux counts distribution. If the luminosity function were a static Schechter function in a static Euclidean universe of infinite radius then $\frac{\mathrm{d}N}{\mathrm{d}F\,\mathrm{d}\Omega} = \kappa_\star F^{-5/2}$.

6.3.1 Error Analysis Details

The statistical uncertainty in the binned estimators is assumed to be fundamentally Poisson combined with propagation of errors that assumes all factors other than the number of galaxies in a bin are constants, as described in Chapter 2. For the parametric estimator in Equation 6.4, its complicated form makes performing a second order expansion about the maximum likelihood parameters, as is done in frequentist statistics, to find the uncertainty in those parameters tedious and error prone. Further, when there is any region of the parameter space where the likelihood becomes unusually flat, as happens frequently when selection functions are involved, the Taylor expansion must be carried out to higher order to get an estimate in the parameters' uncertainties. These conditions make the work done here an ideal case for the application of a Bayesian analysis using Markov Chain Monte Carlo (MCMC) to estimate the uncertainties in the parameters. The software tool used to perform this error analysis is the Python package known as `emcee` version 2.1.0[1], described in Foreman-Mackey et al. (2013), an implementation of the stretch-move algorithm proposed in Goodman & Weare (2010).

When doing any MCMC analysis the algorithm needs to run for a number of steps before it starts to provide an accurate and uncorrelated sample of the posterior. This process is called 'burn in.' If the initial point is far from the mode of the posterior, then this first step is dominated by a pseudo-random walk toward that mode, effectively making it an inefficient optimization algorithm. This process is even less computationally efficient for emcee because it uses an entire ensemble of independent walkers. To short circuit this process, we started the walkers in a ball around an extremum found using the optimize package of SciPy. When fitting models as complex as the ones used here, there is the added downside that there are frequently multiple local extrema. This factor causes a tradeoff in the usage of emcee and how spread out the initial positions of the walkers are: if the spread is large then the odds of finding a better minimum than the current guess goes up, but walkers will also get stuck in local minima that are uninteresting outliers; if the spread is small, then all of the walkers

[1] `http://dan.iel.fm/emcee/current/`

are characterizing the minimum of interest, but it takes much longer to find any possible lower minima.

In principle, it would be possible to design an algorithm that was mostly emcee, but that periodically trimmed outliers and started new walkers at large distances to search for possible new minima. In practice, it is easier to break the process up into different steps. In minimum finding mode, the initial spread of the walkers is large, centered on the minimum found by a comparatively efficient algorithm, and it restarts any time a new minimum is found that is lower than the initial one. The software then switches to minimum characterizing mode where the initial spread is small, and after a number of burn in steps that are discarded the final sample is produced. If a new minimum is found during minimum characterizing mode, then the minimum characterizing process begins again from the beginning, but the switch is not made back to minimum finding mode under the assumption that the improvement from doing so is marginal.

With any Bayesian analysis the prior must be described. Table 6.4 contains the explicit descriptions of the ranges of the parameters, and the priors assumed on the parameters, for the LF. In most cases the priors are flat in the given parameter, and the majority of the remainder are flat in the logarithm of the parameters. The exceptions to this are the faint end slopes, α, and the initial luminosity index, n_0. Because $\alpha = -2$ gives an unphysical infinite background radiation, we chose to impose a mildly informative prior with a beta distribution shape that excluded the end points of the allowed interval. With n_0 the buildup of $L_\star$ should neither be discontinuously fast, so $n_0 > 0$, nor should it be much slower than the integral of a linear accretion rate, so $n_0 < 10$. Further, the data used here does not constrain the buildup of $L_\star$ directly, so an informative prior that constrains the value of n_0 is used. Explicitly, it is expected that their initial luminosity is proportional to the gas accretion rate, and should therefore be reasonably near linear, so we impose $n_0 = 1 \pm 0.2$ with a log-normal distribution.

Table 6.4. LF Parameter Priors

Param	Min	Max	Units	Prior	Notes
$\kappa_\star$	10^{-3}	10^{2}	$\mathrm{Jy}^{3/2}\,\mathrm{sr}^{-1}$	$\kappa_\star^{-1}$	a
R_{n0}	-50	50	t_H^{-1}	flat	b
L_0	10^{9}	10^{13}	$L_{2.4\,\mu\mathrm{m}\,\odot}$	L_0^{-1}	c
R_L	-50	50	t_H^{-1}	flat	
α	-2	0	—	$-\alpha(2+\alpha)$	
n_0	10^{-15}	10	—	$n_0^{-1}\,\mathrm{e}^{-25\ln(n_0)^2/2}$	d

Note. — Parameter (Param) ranges (from Min to Max) and priors used in fitting the luminosity function. Priors are given in unnormalized form.

[a] Normalization to the static Euclidean number counts. Its relationship to standard Schechter function parameters can be found in Equation 6.10.

[b] Specific rate of change of the galaxy number density at $z = 0$. Its relationship to standard Schechter function parameters can be found in Equation 6.9.

[c] $L_{2.4\,\mu\mathrm{m}\,\odot} = 33.44\,\mathrm{nJy\,Mpc}^2 \leftrightarrow M_{2.4\,\mu\mathrm{m}\,\odot} = 5.337\,\mathrm{mag}$ AB absolute.

[d] This prior has mean 1 and standard deviation 1/5.

6.4 Luminosity Functions

Running `emcee` produces a sequence of model parameters that are distributed as though they were samples taken from the posterior distribution. The sequence of parameters is, therefore, the result of the analysis from which all other results are derived. The chains will, therefore, be published with the paper based on this chapter and at `www.figshare.com` under the digital object identifier (DOI) `10.6084/m9.figshare.4109625` in gzipped IPAC table format. An few example lines from one of the chains can be found in Table 6.5.

The content of that file set is as follows: there is an individual chain for each individual spectroscopic survey (with file names matching the names of the survey), one for each merged subsample described in Table 6.3 with matching names, and two chains, labeled 'High z Prior' and 'High z Trim Prior', where the High z samples were analyzed with the mean and standard deviation in α from the matching Low z samples used as additional Gaussian priors in the analysis. The reason for only using the faint end slope as a prior is discussed in Section 6.4.1.

Table 6.5. Example Lines from MCMC Chains

`StepNum`	`WalkerNum`	`ln_KappaStar`	`R_n`	`ln_Lstar`	`R_L`	`alpha`	`ln_n0`
—	—	$\ln\left(\mathrm{Jy}^{3/2}\,\mathrm{sr}^{-1}\right)$	Gyr^{-1}	$\ln\left(\mathrm{Jy\,Mpc}^2\right)$	Gyr^{-1}	—	—
0	0	2.0414	−0.056289	8.7190	−0.13463	−1.5071	−0.30514
0	1	1.8404	−0.013686	8.2423	−0.19569	−1.2721	−0.03764
0	2	2.1309	0.224666	7.6358	−0.29812	−0.9931	−0.01672
0	3	2.5518	0.095079	8.6992	−0.22876	−1.4027	0.41558
0	4	1.8430	−0.007250	8.2185	−0.21643	−1.3473	0.03394

Note. — Example lines from one of the chains produced by `emcee` in the tables under DOI `10.6084/m9.figshare.4109625`. Floating point values truncated here for brevity, but not in the downloadable tables. `StepNum` is the zero indexed step number that the ensemble was at in the chain, and `WalkerNum` is the number of the walker which was at the position defined by the row for that step. `ln_KappaStar` is the natural logarithm of $\kappa_\star$ in $\mathrm{Jy}^{3/2}\,\mathrm{sr}^{-1}$ (see Equation 6.10). `R_n` is the specific rate of change of the galaxy number density evaluated at the present time in Gyr^{-1} (see Equation 6.9). `ln_Lstar` is the natural logarithm of $L_\star$ in $\mathrm{Jy\,Mpc}^2$ evaluated at $z = 0$ $\left(M_\star = -\frac{2.5}{\ln 10}\ln\left[\frac{L_\star}{3631\,\mathrm{Jy}\,4\pi 10^{-10}\,\mathrm{Mpc}^2}\right] \approx -1.086\ln\left[\frac{L_\star}{\mathrm{Jy\,Mpc}^2}\right] - 13.352 \text{ for AB absolute mag}\right)$. `R_L` is the long term decay constant in $L_\star$ in Gyr^{-1}. `alpha` is the faint end slope of the luminosity function. `ln_n0` is the natural logarithm of the early time power law index of the evolution of $L_\star$ (see Equation 6.8)

Of all of the analysis chains produced, High z Prior is the canonical one for this work based on a subjective evaluation of statistical accuracy and bias. A comparison of the $N_{\rm obs}/N_{\rm mdl}$ binned estimator using all of the data to the LF with the mean parameters from the High z Prior chain can be found in Figure 6.2. The solid red lines, of varying opacity and brightness, are the result of evaluating the High z Prior LF model at five equally spaced redshifts from 0.01 to 1 (0.01, 0.258, 0.505, 0.743, 1). The three 3.6 μm LFs from Dai et al. (2009), color corrected to 2.4 μm using the mean SED from Chapter 3, are plotted at $z = 0.38$ using black dashed ('all'), red dotted ('early'), and blue dash-dotted ('late') lines.

Two features stick out most prominently in Figure 6.2. First, the parametric estimator places the value of $\phi_\star$ a factor of about 1.7 higher than the binned estimator, though this is within the statistical uncertainty in $\phi_\star$ for Hi z Prior. Second, the falloff at the bright end appears to be better described as a power law than exponential. The former is likely caused by the fact that the data content of Figure 6.2 is drawn from all the samples, without restriction on redshift, while the plotted LF is of the mean parameters from the High z Prior chain. The cause of the latter is uncertain. Averaging the evolving fit LF over different redshifts using the observed redshift distribution did not produce the observed power law shape. Further, limiting the plot to data in the High z sample does not alter this feature significantly, either, so it is unlikely to be an artifact related to photometry of resolved sources. The explanation that, qualitatively, seems most likely to cause the feature is the presence of AGN in the sample, which are observed to have a power law falloff to the LF on the bright end (see Equation 5, and surrounding discussion, in Richards et al., 2006). While this means that the fit LF doesn't match all of the details of the real LF, this was an expected consequence of using a single Shecther function for the LF and not separate LFs for different galaxy types. The global properties of the LF, like predictions of galaxy count and luminosity density, should still correspond with the observable values in the same way that a Gaussian fit to a data set will reproduce the mean and standard deviation, even if the data are not Gaussian distributed.

Detailed analyses of the different posterior chains is done in Subsection 6.4.1, including an examination of the necessity of splitting the combined samples by redshift, and evidence for luminosity uncertainty contributing to the softening of the high luminosity falloff. Comparisons with the results of other measurements of the luminosity function is done in Subsection 6.4.2.

6.4.1 Internal Comparisons

Because the parametric estimator used in this work is new, it is important to analyze multiple data set that all have different selection criteria and compare the results to see if the systematic biases have been correctly managed. The mean parameters from each of the posterior chains can be found in Table 6.6, and parameters derived from those mean parameters are found in Table 6.7.

All of the uncertainties given in the tables are purely statistical uncertainties derived from the Bayesian posterior of the data. They do not include sources of error that are, for the purposes of this work, systematic, including: the accuracy of the cosmological parameters ($\approx 3\%$), the peculiar velocity the Milky Way ($\approx 0.6\%$), the accuracy of the completeness assessments of the different surveys ($\approx 2\%$), selection effects not modeled, cosmic variance (assumed small), the accuracy of the AllWISE W1 photometric zero point (1.5%, Jarrett et al., 2011), and the accuracy of the numerical integration algorithms used ($\approx 2\%$). The combination of these effects implies 5.0% systematic uncertainty in the determination of $L_\star$, 3.4% in $\kappa_\star$, 6.0% in $\phi_\star$, an assumed e-fold per Hubble time in the evolution rate parameters, and an assumed 3% in α.

All of the parameters on a given line in Tables 6.6 and 6.7 are correlated, to greater or lesser degrees. Including tables or plots of the correlation among the parameters would take up a prohibitive amount of room, so this work only contains a single example of the covariance matrix among the primary parameters constructed from the High z Prior chain in Table 6.8. It should be noted that the full correlation among parameters is not necessarily encapsulated by a covariance matrix, particularly the correlation between $\ln n_0$ and R_n. A closer examination of the correlations in the High z chain, and a comparison between how correlated the parameters using different parameterizations are, can be found in Appendix B.

The biggest trend in Table 6.6 is in R_n, with the lower depth surveys consistent with the number density of galaxies currently declining and the higher depth surveys with the opposite. While it is possible that this is a real feature of the data, whether from a turnover in the comoving number density of galaxies or cosmic variance from the Milky way existing in an low density region, selection biases must first be ruled out. A preliminary analysis of the SDSS subset with a W1 flux maximum of 2 mJy (15.65 AB mag) suggested that this effect was being driven by the galaxies with high apparent flux, and not the faint galaxies that dominate number counts for samples with minimum luminosity significantly lower than $L_\star$. Because faint galaxies dominate the number density of galaxies, it is unlikely that a trend driven by the presence of bright objects in the sample is a real phenomenon, neither cosmic trend nor cosmic variance.

As the error bars on R_n show, this parameter is poorly constrained by the data, so a small bias in a correlated parameter, even a weekly correlated one, can drive a big change in R_n. Since bright galaxies are also more likely to be resolved or marginally resolved, we decided to work around the problem by dividing the combined samples at $z = 0.2$ where the number of galaxies with high `w1rchi2` fell to a level low enough to be negligible (see Figure 6.1). The advantage of a redshift split instead of a flux cut is that it does not increase the impact of the systematic uncertainties inherent in the the final estimator used. The only parameter from the low redshift sample that the analysis with lower maximum F_{W1} that is plausibly not affected by a bias affecting resolved sources is the faint end slope. Given the luminosity range covered by the Low z samples makes it the strongest constraint on α available, we use the mean and standard deviation of α from the corresponding Low z samples as Gaussian priors on the High z Prior samples.

In order to estimate the possible systematic impact the Trim samples were constructed. The Trim samples are identical to their corresponding combined samples, but each survey is limited to the region in luminoisty-redshift space where the completeness is at least 98% of its maximum value; the regions enclosed by the faint blue lines in the L-z plots of Chapter 5. This substantially reduces the size and depth of the sample, so it is more vulnerable to cosmic and statistical variance. The Low z and Low z Trim chains agree within the statistical

Table 6.6. Luminosity Function Bayesian Mean Parameters

Survey	$\kappa_\star$	R_n[a]	$L_\star$[a]	R_L	α	n_0
—	$\mathrm{Jy}^{3/2}\,\mathrm{sr}^{-1}$	t_H^{-1}	$10^{10}\,L_{2.4\,\mu\mathrm{m}\,\odot}h^{-2}$	t_H^{-1}	—	—
6dFGS	2.94 ± 0.07	-4.9 ± 0.8	3.15 ± 0.07	-3.4 ± 0.3	-0.91 ± 0.02	0.9 ± 0.2
SDSS	4.06 ± 0.03	-3.55 ± 0.09	3.34 ± 0.03	-2.4 ± 0.2	-0.957 ± 0.005	1.0 ± 0.2
GAMA	4.0 ± 0.1	0.2 ± 0.2	2.67 ± 0.09	-12.7 ± 0.8	-0.95 ± 0.02	8.3 ± 0.6
AGES	5.4 ± 0.3	1.8 ± 0.3	2.2 ± 0.2	-5.0 ± 0.7	-0.57 ± 0.06	1.8 ± 0.4
WISE/DEIMOS	8 ± 2	1 ± 2	5 ± 2	-3 ± 1	-1.1 ± 0.3	1.0 ± 0.2
zCOSMOS	4.4 ± 0.5	1.8 ± 0.8	2.6 ± 0.5	-4.5 ± 0.5	-0.9 ± 0.1	0.9 ± 0.2
Low z	3.11 ± 0.02	-7.47 ± 0.09	3.41 ± 0.02	-1.5 ± 0.2	-1.059 ± 0.004	0.8 ± 0.2
High z	5.0 ± 0.2	0.6 ± 0.2	2.66 ± 0.05	-2.8 ± 0.1	-0.68 ± 0.03	0.56 ± 0.08
High z Prior	5.7 ± 0.2	0.1 ± 0.2	3.12 ± 0.05	-2.6 ± 0.1	-1.050 ± 0.004	0.50 ± 0.07
Low z Trim	3.24 ± 0.03	-7.7 ± 0.2	3.62 ± 0.04	-0.4 ± 0.2	-0.972 ± 0.008	0.9 ± 0.2
High z Trim	9 ± 1	-0.8 ± 0.7	3.9 ± 0.4	-4.8 ± 0.5	-1.93 ± 0.04	1.0 ± 0.2
Hi z Trim Prior	5.0 ± 0.6	1.9 ± 0.7	2.9 ± 0.2	-4.3 ± 0.4	-0.935 ± 0.008	1.0 ± 0.2

Note. — Mean parameters from the Bayesian posterior functions. The top half of the table is broken down by survey, and the bottom half is one of the combined analyses of all data sets. $\kappa_\star$ is the Euclidean flux counts normalization (see Equation 6.10). R_n is the specific rate of change of the numeric density of galaxies (see Equation 6.9). R_L is the long time decay constant in $L_\star$ and n_0 is the initial luminosity index (see Equation 6.8). For $\kappa_\star$, $L_\star$, and n_0 the means are geometric means, in keeping with the values published in the posterior chains.

[a] Parameter evaluated at $z = 0$.

uncertainties, with the exception of $L_\star$. Even though the effects on the High z samples was more dramatic, this is to be expected given the reduced effective depth and loss of low luminosity sources, especially in the AGES and *WISE*/DEIMOS samples. When the power law part of the LF is not directly sampled, where the LF is linear in a log-log plot, the information about α is encoded in the higher order moments of what was observed, increasing sensitivity to statistical and cosmic variance fluctuations.

The numerical comparisons discussed above provide a nice overview of the behavior of the different sets, but no work is complete without graphical comparisons of the fit models to binned estimators for the data. The comparisons of the unbinned ML fits with two binned estimators, $1/V_{\max}$ and $N^{\rm obs}/N^{\rm mdl}$, can be found in Figures 6.3, 6.4, and 6.5. The first notable feature of the grid of plots in Figure 6.3 is that the $N^{\rm obs}/N^{\rm mdl}$ agrees better with the

Table 6.7. Luminosity Function Derived Parameters

Survey	$\phi_\star$ [a]	R_ϕ	$M_\star$ [a] $- 5\log_{10} h$	$z_\star$	$\rho_{L2.4\,\mu\mathrm{m}}$ [a]	R_ρ [a]	z_ρ
—	$10^{-2}h^3\,\mathrm{Mpc}^{-3}$	t_H^{-1}	AB mag	—	$10^8 L_{2.4\,\mu\mathrm{m}\,\odot}\,\mathrm{Mpc}^{-3}$	t_H^{-1}	—
6dFGS	0.86 ± 0.03	-5.2 ± 0.7	-20.91 ± 0.03	1.7 ± 0.3	1.81 ± 0.04	-7.6 ± 0.6	4.1 ± 0.6
SDSS	1.09 ± 0.01	-3.61 ± 0.09	-20.973 ± 0.008	1.0 ± 0.1	2.49 ± 0.01	-4.93 ± 0.07	2.8 ± 0.4
GAMA	1.51 ± 0.07	0.0 ± 0.2	-20.73 ± 0.04	0.43 ± 0.01	2.76 ± 0.05	-4.2 ± 0.2	0.43 ± 0.02
AGES	2.4 ± 0.2	0.4 ± 0.2	-20.53 ± 0.09	1.3 ± 0.2	3.4 ± 0.2	-2.8 ± 0.4	1.1 ± 0.1
WISE/DEIMOS	1.2 ± 0.8	1 ± 2	-21.4 ± 0.5	1.3 ± 0.6	5 ± 1	-1 ± 1	0.5 ± 0.7
zCOSMOS	1.8 ± 0.5	1.5 ± 0.5	-20.7 ± 0.2	2.3 ± 0.3	3.1 ± 0.3	-2.0 ± 0.4	1.5 ± 0.3
Low z	0.814 ± 0.009	-7.43 ± 0.09	-20.994 ± 0.008	0.65 ± 0.09	2.013 ± 0.009	-8.09 ± 0.06	4.8 ± 0.6
High z	1.81 ± 0.08	-0.1 ± 0.2	-20.73 ± 0.02	2.4 ± 0.2	3.0 ± 0.1	-2.4 ± 0.2	2.5 ± 0.3
High z Prior	1.69 ± 0.08	0.2 ± 0.2	-20.90 ± 0.02	2.5 ± 0.3	3.8 ± 0.1	-1.9 ± 0.2	2.3 ± 0.3
Low z Trim	0.77 ± 0.01	-7.7 ± 0.2	-21.06 ± 0.01	-0.7 ± 0.2	1.92 ± 0.02	-7.1 ± 0.2	4.2 ± 0.6
High z Trim	1.1 ± 0.3	3 ± 1	-21.2 ± 0.1	2.4 ± 0.4	50 ± 40	-1.1 ± 0.6	0.8 ± 0.5
Hi z Trim Prior	1.7 ± 0.3	1.7 ± 0.7	-20.80 ± 0.08	2.1 ± 0.3	3.3 ± 0.4	-1.6 ± 0.5	1.2 ± 0.3

Note. — Bayesian mean values related to the luminosity function calculated from the posterior chains separately from the parameters in Table 6.6, with $h = 0.7$. The means of $\phi_\star$ and $\rho_{L2.4\,\mu\mathrm{m}}$ are geometric means. R_ϕ is the specific rate of change of $\phi_\star$ (assumed constant for all redshifts, see Equation 2.31). $z_\star$ is the redshift at which the model predicts $L_\star$ will peak (Equation 2.32). $\rho_{2.4\,\mu\mathrm{m}}$ is the present day $2.4\,\mu$m luminosity density of galaxies (see Equation 2.41), R_ρ is its specific rate of change (Equation 2.42), and z_ρ is the redshift at which the model predicts j to have peaked (Equation 2.45).

[a] Parameter evaluated at $z = 0$.

Table 6.8. Hi z Sample with Low z Prior Luminosity Function Bayesian Parameter Posterior Covariance

Parameter	σ	$\delta \ln \kappa_\star$	$\delta R_n t_H$	$\delta \ln L_\star(0)$	$\delta R_L t_H$	$\delta\alpha$	$\delta \ln n_0$
$\delta \ln \kappa_\star$	0.03029	1.000	0.9023	−0.5915	−0.1510	−0.04423	−0.2330
$\delta R_n t_H$	0.2040	0.9023	1.000	−0.8257	−0.4389	0.06990	−0.02677
$\delta \ln L_\star(0)$	0.01524	−0.5915	−0.8257	1.000	0.7285	−0.1243	−0.2852
$\delta R_L t_H$	0.1210	−0.1510	−0.4389	0.7285	1.000	−0.009374	−0.8508
$\delta\alpha$	0.004266	−0.04423	0.06990	−0.1243	−0.009374	1.000	−0.009308
$\delta \ln n_0$	0.1431	−0.2330	−0.02677	−0.2852	−0.8508	−0.009308	1.0000

Note. — The σ column contains the standard deviation of the parameters, and the remaining rows and columns comprise the matrix of correlation coefficients between the parameters, considered pairwise. All values given to four significant figures.

fit luminosity functions than the $1/V_{\rm max}$ estimator. This is to be expected since $N^{\rm obs}/N^{\rm mdl}$ is closer to a maximum likelihood estimator, and the fits were done using unbinned maximum likelihood. In particular, the $N^{\rm obs}/N^{\rm mdl}$ outperforms $1/V_{\rm max}$ where the approximation that the selection function is constant with redshift is a bad one. The difference is particularly stark for panel **b**, SDSS, where the shallow optical selection makes SED variability particularly relevant. The next obvious feature is the disagreement of the fitted faint end slope with the binned ones in panel **d**, AGES. There is a local minimum in the likelihood with a faint end slope closer to $\alpha = -1$, but it is not a global minimum. There are two reasons this fails to be a global minimum: the low faint end completeness of AGES giving the less luminous galaxy bins bigger error bars, and a fluctuation in the data. These facts are more apparent in an examination of the first row of Figure 6.5, where the apparent disagreement vanishes.

The final feature of note in the luminosity function plots is the upturns at the faint ends of panels **b** (SDSS) and **c** (GAMA). It is likely the same feature that caused Loveday et al. (2012) and Kelvin et al. (2014) to use a double luminosity function to fit the data. While a double LF would provide better agreement to the data, it is unclear without a deeper examination of the data the extent to which the additional LF is modeling a fundamental feature of the universe (for example, the split between red and blue galaxies) or a cosmic variance fluctuation in the data. One example of an even bigger fluctuation can be seen in panel **c** of Figure 5.12 of Chapter 5. There is a significant over-density in the Sloan data near its peak at around $z = 0.75$. The over-density that causes that bump goes by the name the Sloan Great Wall, discovered in Gott et al. (2005), and it is a good example of how large cosmic variance can get.

It is also profitable to compare the observed redshift histograms against the predictions based on the luminosity function and selection function; plots containing such comparisons can be found in Figure 6.6. The power of this comparison is that, unlike the binned/unbinned LF comparisons in the earlier figures, the data in this figure need not be limited to sources with measured *WISE* fluxes. Thus, the comparison between the black histogram and darker lines is not one of a fit with the data it was fit to, but the extrapolation of the LF and selection function with new data. The first noteworthy feature of the plots in Figure 6.6 is that the High z Prior LF (blue dashed lines) provide more accurate extrapolations, overall, than the individual survey fits (solid red lines). That said, the extrapolations over-predict the number of galaxies in the high redshift tails of panels **b** and **c** (SDSS and GAMA), and badly under-predict the high redshift tails of panel **a** (6dFGS). It is impossible to say what combination of the following this is due to: the galaxy types of the samples changing with fainter luminosity limits, the mean SED evolving with redshift, and the functional form of $L_\star$ evolution being wrong. The changing sample content is a direct consequence of the well known fact that the brightest galaxies are red, so the higher the luminosity limit of a survey the redder its galaxy sample will be, thus affecting the mean SED and, through that, the selection function. The mean SED is also certain to evolve with redshift, with galaxies being bluer in the past than they are now, and no such evolution was modeled for this work. The extra sources in the high redshift tail of the 6dFGS graph is, possibly, a result of confusion boosting the flux estimate of sources that would, ideally, have not met the survey's flux limit.

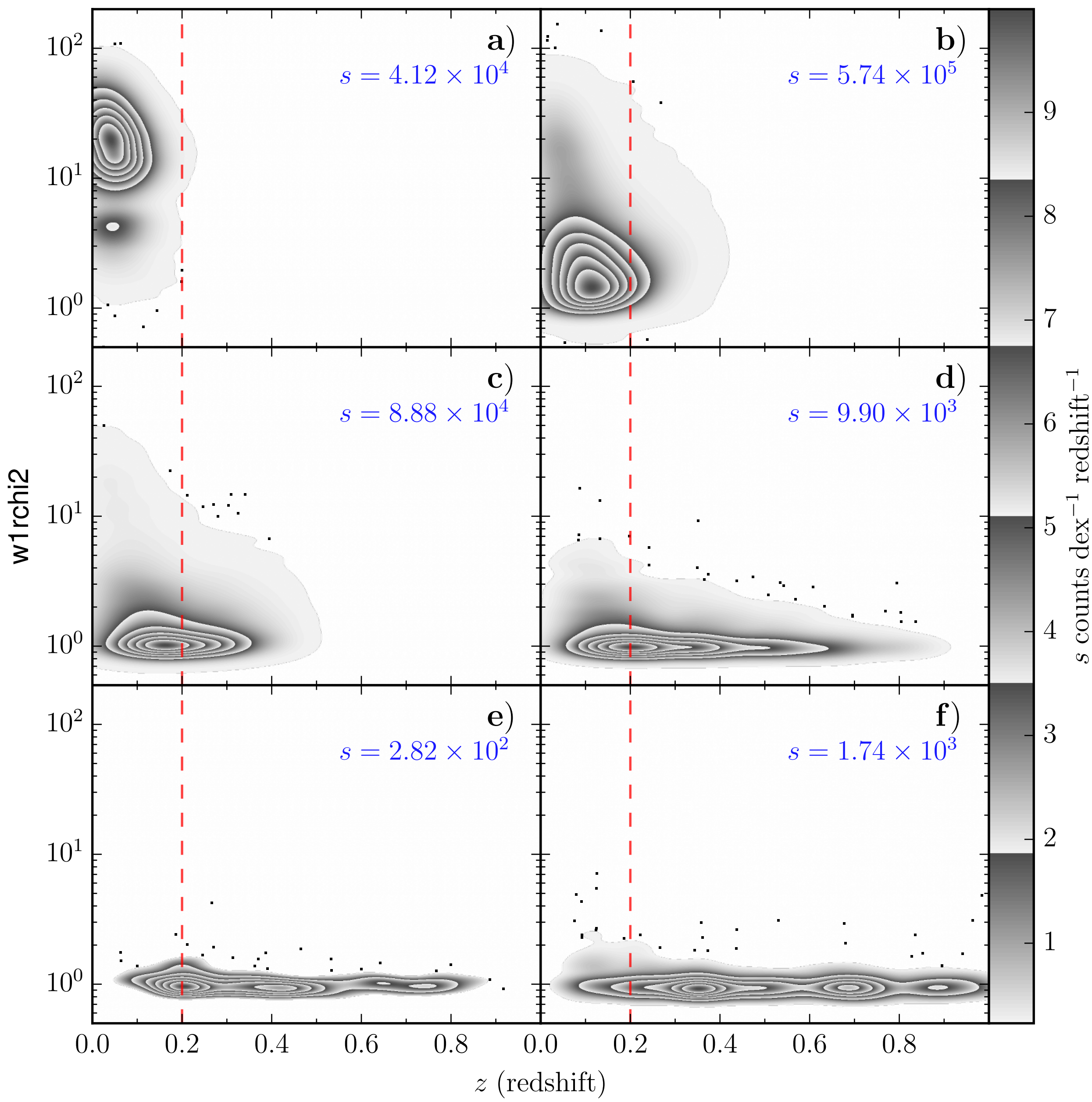

Figure 6.1: Illustration of the trend in `w1rchi2` with redshift. Each graph has its own maximum value for the color bar scale, labeled on the plot as the parameter s. The vertical line at $z = 0.2$ illustrates the dividing line between the low z and high z subsamples. Panel **a** is made using the 6dFGS sample, **b** SDSS, **c** GAMA, **d** AGES, **e** *WISE*/DEIMOS, **f** zCOSMOS.

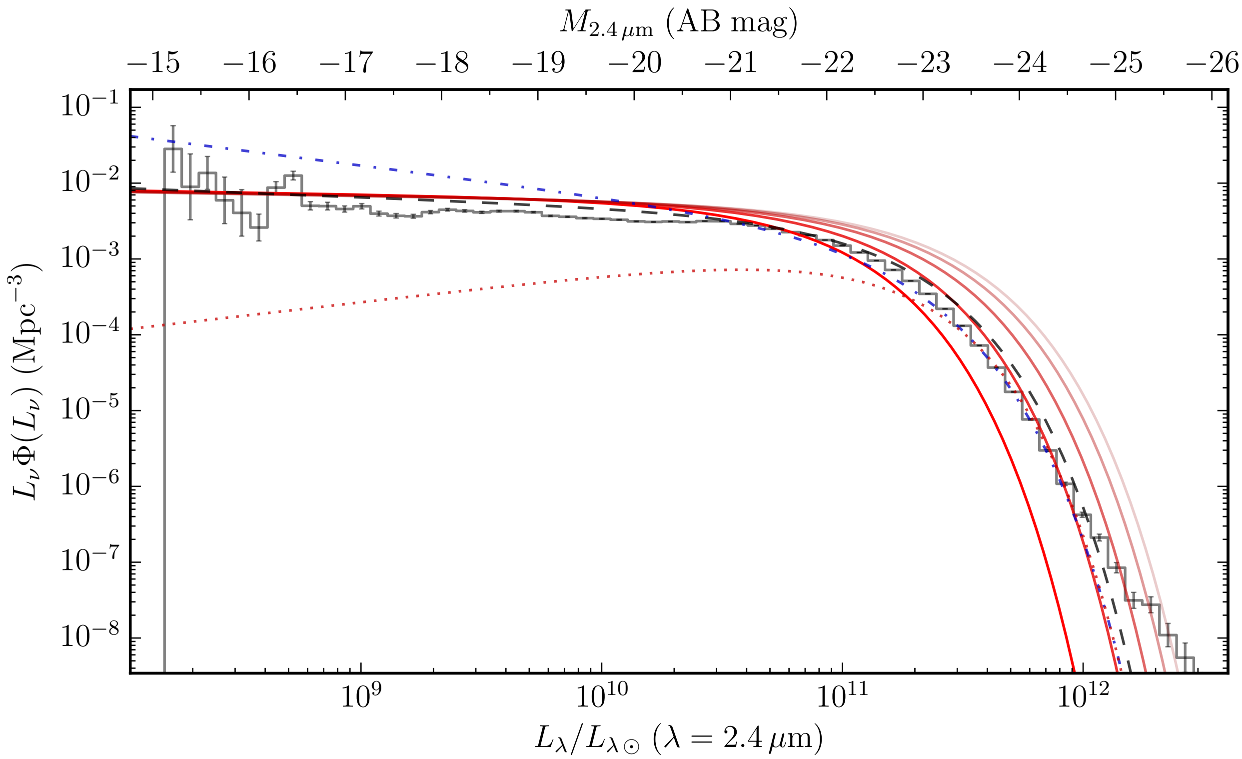

Figure 6.2: Binned $N_{\mathrm{obs}}/N_{\mathrm{mdl}}$ estimate of the LF compared with fit LFs. Broad agreement among the estimators is apparent, with details emerging that the parametric model does not capture. The grey histogram with error bars is the $N_{\mathrm{obs}}/N_{\mathrm{mdl}}$ estimator applied to the combination of all data. The solid red lines of varying opacity and darkness are the LFs from the mean parameters of the High z Prior chain (see Table 6.6) evaluated at equally spaced redshifts between $z = 0.01$ and 1.0 (0.01, 0.258, 0.505, 0.743, 1), inclusively, with the opacity decreasing as z increases. The remaining lines are based on 3.6 μm LF fits from Dai et al. (2009) evaluated at $z = 0.38$ and adapted to 2.4 μm using the mean SED from Chapter 3, with the black dashed line corresponding to their 'all' sample, the red dotted line to their 'early' sample, and the blue dash-dotted line to their 'late' sample.

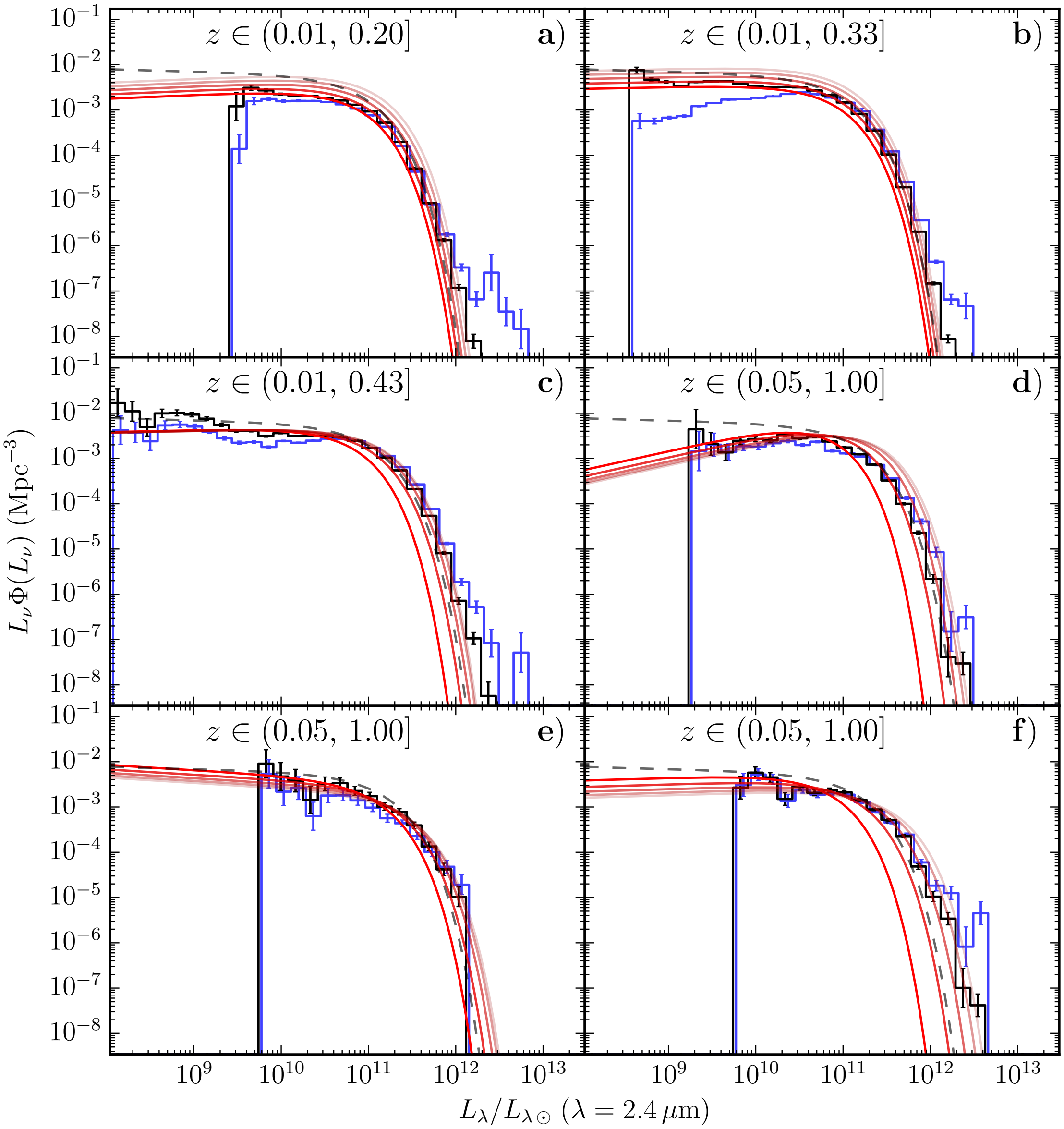

Figure 6.3: Above is a grid of plots comparing luminosity function fits (lines) to binned estimators (steps) for the luminosity function over the entire redshift range noted in the panel. The solid red lines are the LFs fit to the data used to make the panel (not to histograms in the panel), and the dashed line is the mean LF of the High z Prior chain. The combined LFs are evaluated at the middle redshift of the interval in the panel, and the red lines are evaluated at 5 equally spaced redshifts in their panel's redshift interval (inclusive of endpoints). The black histogram is from the $N^{\rm obs}/N^{\rm mdl}$ estimator, and the blue is the $1/V_{\max}$ offset to the right for clarity. Panels **a** through **f** are from the surveys: 6dFGS, SDSS, GAMA, AGES, *WISE*/DEIMOS, and zCOSMOS, respectively.

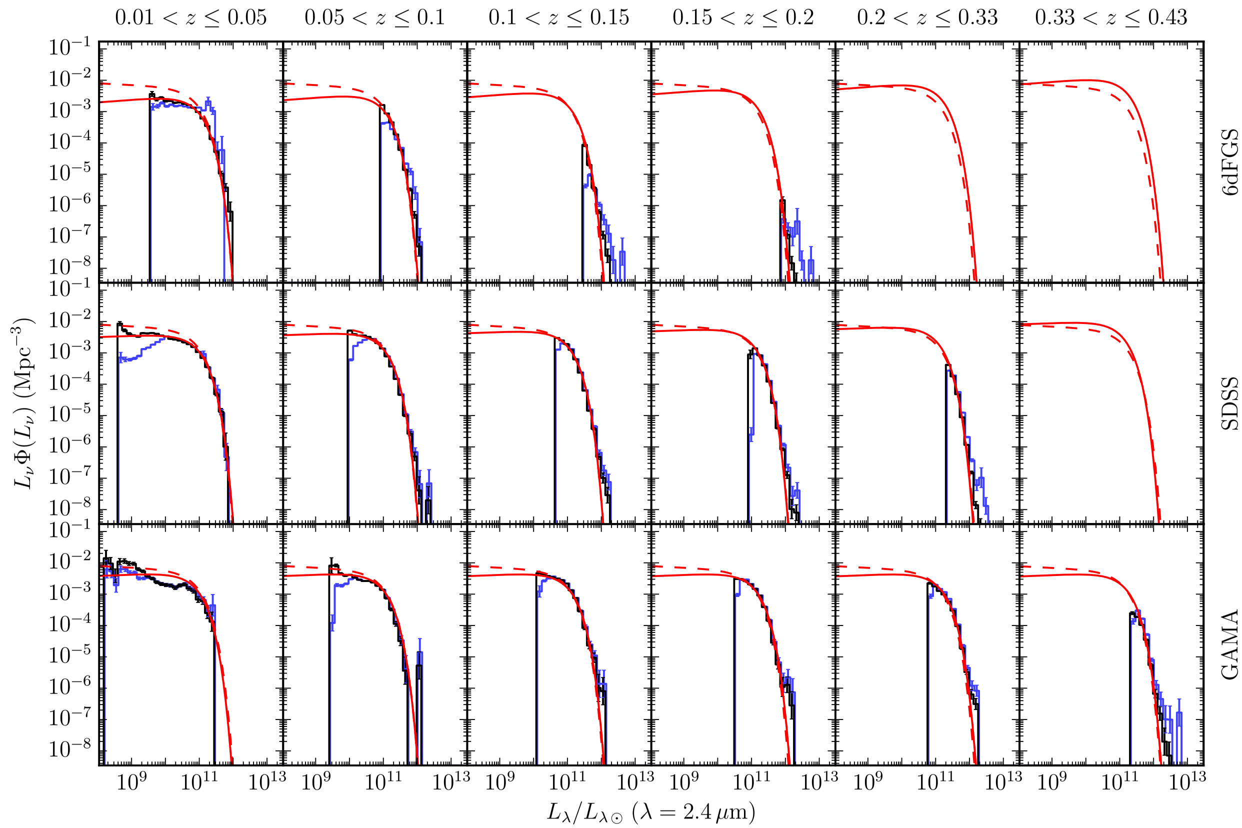

Figure 6.4: Above is a grid of plots comparing luminosity function fits (lines) to binned estimators (steps) for the shallow surveys. Each column represents a different redshift range noted at its top, and each row corresponds to a different shallow survey noted at its right. The solid lines are the LFs fit to the survey in the row (not to histograms in the row), and the dashed line is the mean LF of the High z Prior chain. All LFs are evaluated at the middle redshift of the interval in the column. The black histogram is from the $N^{\mathrm{obs}}/N^{\mathrm{mdl}}$ estimator, and the blue is the $1/V_{\mathrm{max}}$ offset to the right for clarity.

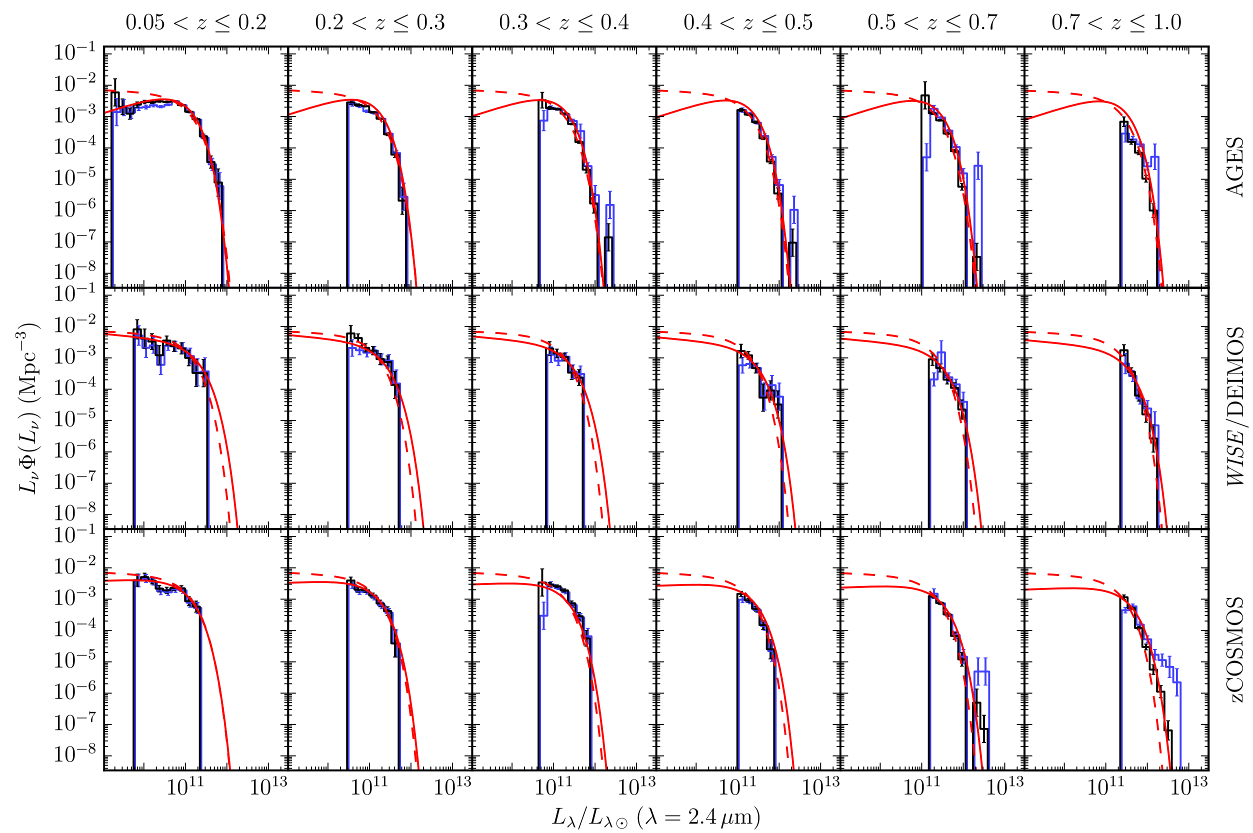

Figure 6.5: Above is a grid of plots comparing luminosity function fits (lines) to binned estimators (steps) for the deep surveys. Each column represents a different redshift range noted at its top, and each row corresponds to a different shallow survey noted at its right. The solid lines are the LFs fit to the survey in the row (not to histograms in the row), and the dashed line is the mean LF of the High z Prior chain. All LFs are evaluated at the middle redshift of the interval in the column. The black histogram is from the $N^{\mathrm{obs}}/N^{\mathrm{mdl}}$ estimator, and the blue is the $1/V_{\max}$ offset to the right for clarity.

6.4.2 External Comparisons

In order to make the Schechter parameters in other papers comparable to the ones measured in this one it was necessary to use the mean SED from this work to color correct their values of $L_\star$ and, wherever possible, use the evolution measured in the other papers to bring them all to redshifts 0, 0.38, and 1.5. The literature parameters can be found in Table 6.9 alongside the mean High z Prior parameters from this work. Further, the external works often have measurements of the LF in multiple filters; when that is the case, the observation filter with wavelength closest to the W1's 3.4 μm was used for the primary parameter comparisons. On the whole, this work's estimate of $L_\star$ is lower than the literature and its estimate for $\phi_\star$ is higher, but not radically so, especially compared to the spread among the literature values. The values for $L_\star$ at high redshift ($z = 1.5$) have a much larger spread, making this epoch ripe for studies based on deeper imaging surveys.

The spread in measured specific evolution rates, shown in Table 6.10, is considerably larger than the primary parameters. The uncertainties are not included in the table, but they're generally more than $0.1\,t_H^{-1}$ and less than $1\,t_H^{-1}$. The most directly comparable values, the ones at ${}^{0.1}z$, [3.6], and 2.4 μm, are all largely consistent. Most importantly, the specific rate of change in the density of galaxies, R_n, should be the same for all the different surveys in all bandpasses. That the spread is so large is likely attributable to a combination of selection effects, the inadequacy of a single Schechter function to describe all types of galaxies in all bandpasses, and the fact that R_n is one of the least well constrained parameters by the data.

The final comparison is a graphical one of the models for the evolution of $L_\star$ and $\rho_{L2.4\,\mu\mathrm{m}}$ from this work to an empirical models from Madau & Dickinson (2014) and Scully et al. (2014) in this work's Figure 6.7. The model from the review in Madau & Dickinson (2014) is for the evolution of the cosmic star formation rate density, ψ (Equation 15 there), and the the model from Scully et al. (2014) is a 1-σ variability band in luminosity density evolution for the K filter ($\lambda \approx 2.2\,\mu$m) scaled using the mean SED ($L_K/L_\nu(2.4\,\mu\mathrm{m}) = 1.199$). The data used to produce the empirical model from Madau & Dickinson (2014) was, essentially, scaled luminosity densities measured in the far ultraviolet and far infrared. Most importantly, the

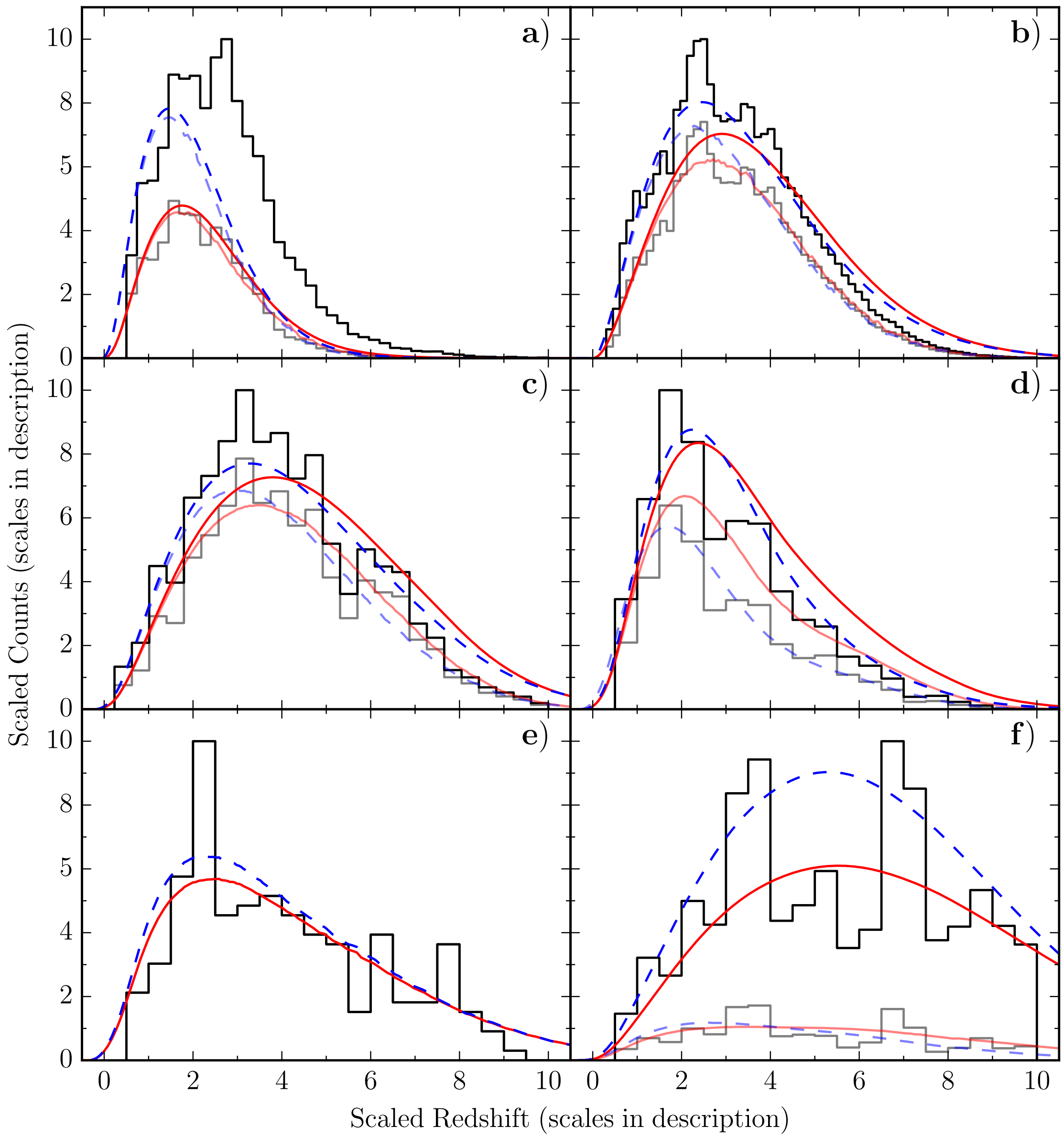

Figure 6.6: Above is a grid of plots comparing simple histograms of observed targets with redshift to the predicted counts from the combination of selection function and LF. The grey histogram is the *WISE* detected subset used in measuring the luminosity functions, and the black contains every high quality source in the survey. The solid red lines are the predicted count density, times bin width, from the LF for the panel's survey, and the dashed blue lines are the combined LF. The light lines are models for the grey histogram, and the dark lines are for the black histogram. The survey, x-axis scale, and y-axis scale for each panel, **a**–**f**, are: 6dFGS, 0.02, 541.3; SDSS, 0.033, 2922.8; GAMA, 0.043, 537.2; AGES, 0.1, 158.8; *WISE*/DEIMOS, 0.1, 3.3; and zCOSMOS, 0.1, 82.1, respectively.

measurements used to produce the empirical model for ψ spans the range of redshifts from 0 to 8, so their estimate would place the peak of the luminosity density somewhere between redshifts 1.3 and 2.5 based on data. The data on ρ_K evolution from Scully et al. (2014) is primarily below redshift 2, and based on statistically interpolating measured values from the literature, and constructing the band from an ensemble of such interpolations. Considering that all of the data used in this work has a redshift below 1, and most of that less than 0.5, the crude evolution model used here does surprisingly well at locating the epoch where $L_\star$ and $\rho_{L2.4\,\mu\mathrm{m}}$ peak. Figure 6.7 also shows that the peaks in $L_\star$ and ρ_L are, possibly, too broad, but this is not surprising given the simplicity of the model and limits of the data used.

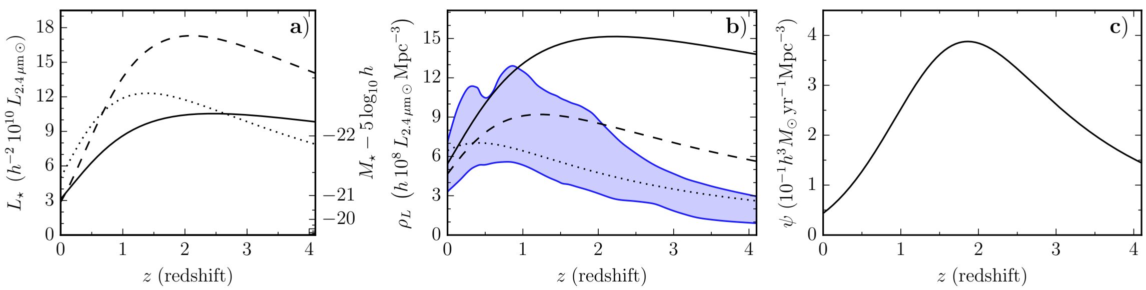

Figure 6.7: Luminosity Evolution

Graphs of empirical models for the evolution of the luminosity of galaxies. Black lines in panels **a** and **b** are a plot of models from this work, the light blue region in panel **b** is a 1-σ confidence band from a meta-analysis in Scully et al. (2014) (K-band scaled with the mean SED, data primarily from Arnouts et al., 2007), and panel **c** is the empirical model for the star formation rate density reviewed in Madau & Dickinson (2014). In panels **a** and **b** the identities of the lines are: the dotted line is the fit to the *WISE*/DEIMOS sample, the dashed line is to the High z Trim Prior sample, and the solid line is to the High z Prior sample.

6.5 Discussion

The consistency of the results in this work with the literature shows that, while the goal of increasing the statistical accuracy of the LF measurements has been met, that increased ac-

Table 6.9. Comparison with Other IR Schechter LF Measurements

Paper	Obs Band	α	$10^{-8}\,\rho_{L2.4\,\mu\mathrm{m}}(0)$	$\phi_\star(0)$	$\phi_\star(0.38)$	$\phi_\star(1.5)$	$L_\star(0)$	$L_\star(0.38)$	$L_\star(1.5)$
—	—	—	$hL_{2.4\,\mu\mathrm{m}\,\odot}\,\mathrm{Mpc}^{-3}$		$10^{-2}h^3\,\mathrm{Mpc}^{-3}$			$10^{10}\,L_{2.4\,\mu\mathrm{m}\,\odot}h^{-2}$	
Loveday (2000)	K	-1.2 ± 0.2	7 ± 6	1.2 ± 0.8	—	—	5 ± 2	—	—
Kochanek et al. (2001)	K_s	-1.09 ± 0.06	7.5 ± 0.9	1.2 ± 0.1	—	—	4.5 ± 0.2	—	—
Pozzetti et al. (2003)[b]	K_s	-1.2 ± 0.1	2 ± 3	0.1 ± 0.1	0.2	0.4	19 ± 9	17	14
Bell et al. (2003)	K_s	-0.86 ± 0.04	16 ± 1	4.2 ± 0.2	—	—	4.1 ± 0.2	—	—
Babbedge et al. (2006)	c1[a]	-0.92 ± 0.04	5 ± 5	1 ± 1	2	2	4.4 ± 0.4	0.28	0.25
Cirasuolo et al. (2007)[b]	K	-0.99 ± 0.04	5.0 ± 0.8	0.65 ± 0.09	0.80	0.63	7.8 ± 0.7	7.8	10.0
Arnouts et al. (2007)[b]	K	-1.1 ± 0.2	12 ± 3	1.5 ± 0.6	1.1	0.64	8 ± 3	8	11
Dai et al. (2009)	c1[a]	-1.12 ± 0.16	3.9 ± 0.9	1.08 ± 0.03	—	—	3.3 ± 0.6	5.1	18
Smith et al. (2009)	K	-0.81 ± 0.04	5.7 ± 0.3	1.66 ± 0.08	—	—	3.7 ± 0.1	5.3	14.9
Loveday et al. (2012)	z	-1.07 ± 0.02	5.1 ± 0.8	1.3 ± 0.2	1.1	0.63	3.9 ± 0.2	7.0	41
Kelvin et al. (2014)	K	-1.16 ± 0.04	7 ± 2	0.7 ± 0.1	—	—	9 ± 2	—	—
This work	W1	-1.050 ± 0.004	5.4 ± 0.2	1.69 ± 0.08	1.6	1.5	3.12 ± 0.05	5.6	9.9

Note. — Paper is the work from which the measurements came, in chronological order. 'Obs Band' is the observation band used to calculate the luminosity function. $\rho_{L2.4\,\mu\mathrm{m}}(0)$ is the $2.4\,\mu$m luminosity density at $z = 0$, $\phi_\star(z)$ is the LF normalization at redshift z, and $L_\star(z)$ is the value of $L_\star$ at redshift z. Uncertainties from this work do not include systematic uncertainties, and so are underestimated. The conversion factors used are: $L_K/L_\nu(2.4\,\mu\mathrm{m}) = 1.199$, $L_{K_s}/L_\nu(2.4\,\mu\mathrm{m}) = 1.234$, $L_{c1}/L_\nu(2.4\,\mu\mathrm{m}) = 0.842$, and $L_z/L_\nu(2.4\,\mu\mathrm{m}) = 0.924$.

[a] *Spitzer*/IRAC channel 1, $\lambda = 3.6\,\mu$m.

[b] Parameters here are based on linear interpolation/extrapolation.

Table 6.10. Evolution Rate Comparisons

Paper	z_0	Band	$\partial \ln L_\star / \partial t$	R_ϕ	R_n	R_ρ
			t_H^{-1}	t_H^{-1}	t_H^{-1}	t_H^{-1}
Blanton et al. (2003b)	0.1	$^{0.1}u$	−3.4	−2.6	−2.3	−5.9
		$^{0.1}g$	−1.6	−0.3	−0.1	−1.9
		$^{0.1}r$	−1.3	−0.1	−0.2	−1.4
		$^{0.1}i$	−1.3	−0.5	−0.5	−1.8
		$^{0.1}z$	−0.6	−1.8	−1.9	−2.4
Dai et al. (2009)	0.25	[3.6]	−0.8	0[a]	−0.1	−0.8
		[4.5]	−0.7	0[a]	0.0	−0.7
Cool et al. (2012)	0.3	$^{0.1}r$	−1.0	0.4	0.4	−0.5
Loveday et al. (2012)	0.13	$^{0.1}u$	−4.8	6.5	6.1	1.8
		$^{0.1}g$	−2.2	1.2	0.9	−1.1
		$^{0.1}r$	−0.5	−1.4	−1.5	−1.9
		$^{0.1}i$	−1.1	0.0	−0.1	−1.2
		$^{0.1}z$	−1.3	0.4	0.3	−0.9
Loveday et al. (2015)	0.2	$^{0.1}r$	−0.7	−0.7	−0.9	−1.4
This work	0.38	$2.4\,\mu$m	−1.8	0.2	0.1	−1.7

Note. — Paper is the work from which the measurements came, in chronological order. z_0 is the mean or median redshift of the data in the work, and is the redshift at which the parameters were evaluated to make this table. Band is the passband in which the luminosity function was measured. $\partial \ln L_\star / \partial t$ is the specific rate of change of $L_\star$, measured in units of inverse Hubble times. R_ϕ is the specific rate of change of $\phi_\star$ (see Equations 2.31), R_n is the specific rate of change in the number density of galaxies (see Equation 2.34), and R_ρ is the specific rate of change in the $2.4\,\mu$m luminosity density (see Equation 2.42)

[a]This parameter was set to this value, not measured.

curacy has not, yet, uncovered any new facets of galaxy evolution. The internal comparisons show that there is still room for improvement in the techniques used here. In particular, closer attention paid to ensuring that the full flux of resolved galaxies is measured without contamination from foreground stars will permit a further large jump in sample size. Improvement in the performance of numerical integration of arbitrary high dimensional Gaussian functions over rectangular regions would make spectro-luminosity functional, Ψ, based techniques able to analyze samples constructed using the sort of complicated color selection done for DEEP2 (Newman et al., 2013), the SDSS luminous red galaxy sample (Eisenstein et al., 2001), and the SDSS quasar sample (Richards et al., 2002).

Improvements in the form of Ψ that could allow it to fit the data more closely need a little more thought to the overall approach of the analysis before implementation. The primary approach used in the measurement of LFs is to classify galaxies into types and measure separate LFs for each type. It is not obvious, but the improvements suggested in Chapter 2, where the total Ψ is written as a sum over components, falls into the classification category. The way that the sum over components with Ψ becomes a classification scheme, effectively, is because the fluxes measured for each source will place it closest to one mean SED. If we define the square distance to the SED as the exponent in $\mathcal{L}_{\mathrm{SED}}$ then the majority of sources will most strongly affect the the LF parameters that correspond to the SED to which they are closest by that distance measure – with a few in a boundary region dividing their influence among the terms. Thus, especially if the mean SEDs are fixed, the model effectively classifies the sources by which term in the total spectro-luminosity functional the source has the greatest impact on. The more fluxes per source brought to bear in the analysis, the sharper that divide between source types is.

The less common approach would be to, instead of classifying galaxies, analyzing their composition. Think of it as the difference between deciding whether a galaxy 'is a' versus how much the galaxy 'has a'. The advantage of the composition approach is that it addresses an ambiguity not dealt with directly by the model for estimating Ψ developed here: how many galaxies does each source represent? We know from images of local galaxies that the moderate to large galaxies have smaller galaxies in their halos (for example: the Large and

Small Magellanic Clouds). As distance increases, the light from any satellite galaxies must, inevitably, be merged into the light from their primaries. The hallmark of a compositional approach is that it does not just assign probabilities to a source being in different classes, it divides the source's luminosity among them. So, for example, it could be possible to talk about dividing the Ψ into massive stars (say O, B, and A), intermediate stars (F and G), light stars (K, M, and lighter), stellar and supernova remnants, nebular emission, and AGN. The primary challenge would be to figure out what form the base luminosity function, Φ, of each of these should take. While it would seem that an increased richness of photometric data would also be required in order to analyze the composition of each galaxy, it isn't necessary to get a detailed analysis of every galaxy to get an accurate picture of the average composition of galaxies that is encoded in Ψ.

One question that is answerable by improving the techniques developed here, and adding data for galaxies in the redshift range of 1 to 3 is: which peaked first, $L_\star$ or ρ_L? The reason this question is of interest is because it encodes information about the comparative rate of star formation versus galaxy mergers; the former boosts both quantities, the latter only boosts $L_\star$. We would, for example, expect $L_\star$ to peak first in a universe where star formation continued in small galaxies after it and collisions slowed down for large ones. The converse would be the case if star formation was a relatively short epoch that cut off in most galaxies and the majority of individual galaxy luminosity growth was through accretion. The data and simple evolution models used here cannot answer this question, though they hint that $L_\star$ peaked first.

Another question that will require even greater care to answer is: when did (or will) the number density of galaxies peak? The question is equivalent to asking when $R_n = 0$. Though that is an equation that can, in principle, be solved using the parameters in this work, the spread in values produced are so large as to make the answer meaningless. It would take an evolutionary model with greater physical fidelity combined with more data to provide an answer worth examining.

6.6 Conclusion

The combination of the six different redshift surveys described in Chapter 5, made possible by the analysis techniques derived in Chapter 2, has produced measurements of the Schechter LF parameters that are comparable to the literature in terms of statistical precision for $\phi_\star$, and a marked improvement for $L_\star$ and α. The parameters describing the evolution of $L_\star$ and $\phi_\star$, R_L and R_ϕ, are less well constrained, but still comparable to the literature. Improving the constraints will require refinements in the process from end to end.

The photometry of bright, resolved and marginally resolved, galaxies requires improvements that bring them in line with the quality of our photometry for point source. In the ideal case, a photometric survey with sufficient sensitivity to resolve the wings of the Airy profile produced by even the largest galaxies, and the software tools needed to remove foreground contamination from stars, would guarantee that close enough to all of the light in the galaxy has been directly observed to measure accurate luminosities and colors for each whole galaxy.

The accuracy of the spectro-luminosity functional, $\Psi[L_\nu](z)$, can be improved in the straightforward way: writing it as a sum of spectro-luminosity functionals, each with its own LF and Gaussian $\mathcal{L}_{\mathrm{SED}}$. It may also be possible to improve the performance of Ψ by a rethinking how the LF is defined – instead of classifying galaxies into mutually exclusive categories, split into constituent parts with their own luminosity. The upside of a such an approach is that it naturally handles cases where multiple unresolved galaxies are contained in the same object.

Perhaps more important than increasing the fidelity of Ψ is adding a model of the effective radius of galaxies so that surface brightness limits on galaxy selection can be modeled. Likewise, re-deriving an approximation of the estimator for the likelihood of observing an entire catalog so that it includes the effect of galaxy environment. Adding the effect of environment, for example using the two point function ($\xi(r)$), in the likelihood of the catalog is the most natural way to introduce cosmic variance to the process.

Finally, measuring fluxes and redshifts for even fainter galaxies using instruments like the

Multi-Object Spectrometer for Infra-Red Exploration (MOSFIRE) on the Keck II telescope, and the James Webb Space Telescope (JWST), will allow for explorations of the evolution of the faint end slope of galaxies, better constrain the evolution of $\phi_\star$ and $L_\star$ with more high redshift data, and even, potentially, find a downturn in the LF at faint luminosity where galaxies and star clusters overlap as gas accreting gravitationally bound systems.

CHAPTER 7

The Extragalactic BackGround Light

The study of the extragalactic background light (EBL) in the optical and near infrared has received a lot of attention in the last decade, especially near a wavelength of $\lambda \approx 3.5\,\mu$m, with remaining tension among different techniques for estimating the background. In this chapter we present a measurement of the contribution of galaxies to the EBL at $3.4\,\mu$m that is based on the measurement of the luminosity function in Chapter 6 and the mean spectral energy distribution of galaxies in Chapter 3. The mean and standard deviation of our most reliable Bayesian posterior chain gives a $3.4\,\mu$m background of $I_\nu = 9.0 \pm 0.5\,\mathrm{kJy\,sr^{-1}}$ ($\nu I_\nu = 8.0 \pm 0.4\,\mathrm{nW\,m^{-2}\,sr^{-1}}$), with systematic uncertainties unlikely to be greater than $2\,\mathrm{kJy\,sr^{-1}}$. This result is higher than most previous efforts to measure the contribution of galaxies to the $3.4\,\mu$m EBL, but is consistent with the upper limits placed by blazars and the most recent direct measurements of the total $3.4\,\mu$m EBL.

7.1 Introduction

The extragalactic background light (EBL) is another name for a fundamental component of the cosmos - the overall spectrum and density of photons in the universe. In terms of both quantity of energy and photons the dominant component of the EBL is the cosmic microwave background (CMB). While the study of the CMB provides a wealth of information about both the universe at the time those photons were emitted and how the evolving universe has modified those photons, there is a lot to be learned from the study of the

[0]This chapter is based on a paper in preparation for submission to The Astrophysical Journal in 2017 by the authors: S. E. Lake, E. L. Wright, R. J. Assef, T. H. Jarrett, S. Petty, S. A. Stanford, D. Stern, and C.-W Tsai.

EBL frequencies that are dominated by photons emitted at different epochs. Studies of the whole of the EBL have revealed that there are, broadly speaking, four peaks in its spectral energy distribution (SED): the CMB in the rough wavelength range 320 μm to 22 mm, a dust emission of galaxies peak from 64 to 700 μm, a stellar photospheric peak from 0.15 μm to 4 μm, and an active galactic nuclei (AGN) and stellar remnant peak in X-rays from 4 to 580 pm. This characterization is based on Figure 1 of the review Cooray (2016).

While the energy content of the radiation field (of which the EBL is a part) has had a sub-dominant impact on the evolution of space-time, itself, since the redshift of matter-radiation equality (around $z = 3000$; Hinshaw et al., 2013), its spectrum encodes useful information about the history of star and structure formation in the universe. With the exception of high energy photons (energy roughly higher than the Lyman-α transition), once the intergalactic medium achieved full reionization the universe became transparent. The primary consequence of this is that once a photon escapes from the dense matter in a galaxy halo it has a low probability of ever scattering again, leaving it to eventually be redshifted into oblivion by cosmic expansion. In the meantime, this means that when we sample the small fraction of the EBL that reaches our detectors, we are sampling an integrated record of all the light the universe has emitted, the accumulated SED of the universe as a whole.

The primary challenge in directly measuring the EBL is removing the large glare of foreground light sources, especially the reflected sunlight from dust in our solar system known as the zodiacal light (studies using this approach include: Gorjian et al., 2000; Wright & Reese, 2000; Wright & Johnson, 2001; Matsumoto et al., 2005; Levenson et al., 2007; Tsumura et al., 2013; Sano et al., 2016). It is for that reason that two other techniques have come to the fore in the attempts to study the EBL in the optical and near-infrared. The first is to study resolved galaxies, directly, and extrapolating to the unresolved galaxies to estimate how much light galaxies have released into the EBL (for example: Fazio et al., 2004; Levenson & Wright, 2008; Domínguez et al., 2011; Helgason et al., 2012; Driver et al., 2016; Stecker et al., 2016). The challenge with this technique lies in the accuracy of the extrapolation technique used. The second is to leverage the fact that low energy photons can pair produce with very high energy photons, providing opacity to them (for example:

Aharonian et al., 2006; Mazin & Raue, 2007). Ideally this means that high energy gamma rays produced by blazars, typically in the TeV range of energy, are sampling the EBL directly in intergalactic space. The catch that limits the accuracy of this technique is the limit of our ability to determine the gamma ray spectrum pre-extinction, including the production mechanisms and location (see, for example, Essey & Kusenko, 2010).

There is a small controversy in this field in the measurement of the background around $3.5\,\mu$m, where direct measures are higher than the upper limits from gamma ray blazars by about a factor of 2, and the lower limits from extrapolating number counts are not definitive. With the goal of providing more information relevant to the discussion, this work is based on the extrapolation technique. Rather than extrapolating the flux histogram, as was done in Fazio et al. (2004); Levenson & Wright (2008); Driver et al. (2016), this work uses an approach based on extrapolating the luminosity function, as was done in Domínguez et al. (2011); Helgason et al. (2012); Stecker et al. (2016). Rather than harvesting luminosity functions from the literature, though, the measurement in this work is based on a measurement of the luminosity function from scratch that leveraged large public spectroscopic redshift databases and the AllWISE photometry database to construct an luminosity function (LF) and mean galaxy SED optimized for measuring the contribution of galaxies to the EBL at $3.4\,\mu$m. The reliance on spectroscopic redshifts reduces the exposure to systematic uncertainties inherent in photometric redshift surveys, and the measurement of a new LF from scratch permits us to feed forward all of the information about the significant correlations among estimated LF parameters into the background estimates.

The structure of this paper is as follows: Section 7.2 covers the equations that relate the LF and mean SED of galaxies to the source flux histogram and integrated background, Section 7.3 contains a short summary of the results from previous chapters used to measure the background and its uncertainty, Section 7.4 presents estimates of the $3.4\,\mu$m background and flux histograms at various wavelengths, and Section 7.5 discusses the relation of this papers results to the existing science.

7.2 Theoretical Tools

Chapter 2 contains a fuller treatment of a mathematical object called the spectro-luminoisty functional, denoted $\Psi[L_\nu](\nu)$. One property of Ψ is that the comoving spectral luminosity density ρ_{L_ν} (L_ν per unit comoving volume, related to the spectral emission coefficient of radiative transfer, j_ν, by a factor of 4π), is the first moment of it:

$$\rho_{L_\nu} = \int [\mathcal{D}L_\nu] L_\nu \Psi[L_\nu](z). \tag{7.1}$$

Splitting $\Psi[L_\nu](z)$ into the traditional luminosity function, $\Phi(L, z)$, and the likelihood of a galaxy having an SED given that a normalization luminosity is fixed (the normalized SED is $\ell_\nu(\nu) \equiv L_\nu(\nu)/L_{2.4\,\mu\mathrm{m}}$ here) gives:

$$\begin{aligned}
\rho_{L_\nu} &= \int \mathrm{d}L_{2.4\,\mu\mathrm{m}} \int [\mathcal{D}\ell_\nu]\, \ell_\nu\, \mathcal{L}_{\mathrm{SED}}[\ell_\nu](\cdot|L_{2.4\,\mu\mathrm{m}}, z)\, L_{2.4\,\mu\mathrm{m}}\Phi(L_{2.4\,\mu\mathrm{m}}, z) \\
&= \int \mathrm{d}L_{2.4\,\mu\mathrm{m}}\, \mu_\nu(L_{2.4\,\mu\mathrm{m}}, z)\, L_{2.4\,\mu\mathrm{m}}\Phi(L_{2.4\,\mu\mathrm{m}}, z),
\end{aligned} \tag{7.2}$$

where $\mathcal{L}_{\mathrm{SED}}[\ell_\nu](.|L_{2.4\,\mu\mathrm{m}}, z)$ is the likelihood that a galaxy at redshift z with $2.4\,\mu$m luminosity $L_{2.4\,\mu\mathrm{m}}$ will have the normalized SED given by ℓ_ν. The dot and vertical pipe character, '|', are there to emphasize that $L_{2.4\,\mu\mathrm{m}}$ and z are treated as non-random variables for $\mathcal{L}_{\mathrm{SED}}$, in the same way the notation is used for conditional probabilities. This is relevant because it affects what units $\mathcal{L}_{\mathrm{SED}}$ has, that is it is a density with respect to the random variables, and not the non-random ones. The second line of Equation 7.2 is an application of the definition of the mean normalized SED, $\mu_\nu \equiv \langle \ell_\nu \rangle$.

The transition from spectral luminosity density to the background is achieved by treating each infinitesimal comoving volume element, $\mathrm{d}V_c$, as a galaxy with SED $L_\nu = \rho_{L_\nu}\,\mathrm{d}V_c$ that subtends a solid angle $\mathrm{d}\Omega$. The relationship between observed flux surface brightness, $\frac{\mathrm{d}F_\nu}{\mathrm{d}\Omega} \equiv I_\nu$, which is the physical quantity that defines the EBL, then follows from the definition of luminosity distance, $D_L(z)$:

$$\begin{aligned}
F_\nu(\nu_{\rm obs})\,\mathrm{d}\nu_{\rm obs} &= \frac{L_\nu(\nu_{\rm rest})\,\mathrm{d}\nu_{\rm rest}}{4\pi D_L^2(z)} \Rightarrow \\
\frac{\mathrm{d}I_\nu(\nu)}{\mathrm{d}z} &= \frac{\rho_{L_\nu}([1+z]\nu)}{4\pi[1+z]D_{\rm cT}^2(z)}\left(\frac{\mathrm{d}V_c}{\mathrm{d}z}\right)\frac{1}{\Omega_{\rm sky}} \\
&= \frac{\rho_{L_\nu}([1+z]\nu)}{\Omega_{\rm sky}[1+z]}\left(\frac{\mathrm{d}D_c}{\mathrm{d}z}\right),
\end{aligned} \tag{7.3}$$

where D_c is the radial comoving distance at redshift z.

Combining Equations 7.2 and 7.3 gives the contribution to the background per unit luminosity per unit redshift:

$$\frac{\mathrm{d}^2 I_\nu}{\mathrm{d}z\,\mathrm{d}L_\nu} = \frac{\mu_\nu([1+z]\nu, L_\nu, z)}{\Omega_{\rm sky}[1+z]}\left(\frac{\mathrm{d}D_c}{\mathrm{d}z}\right) L_\nu \Phi(L_\nu, z). \tag{7.4}$$

Note that the more familiar K-correction can be written in terms of μ_ν as
$K = -2.5\log_{10}([1+z]\cdot\mu_\nu)$. The quantity in Equation 7.4 is useful enough to assign it a symbol of its own, since it is the density of contribution to the background, $\mathcal{B}_\nu(\nu) \equiv \frac{\mathrm{d}^2 I_\nu}{\mathrm{d}z\,\mathrm{d}L}$.

Equation 7.4 can be integrated directly to calculate the predicted background at any frequency, but since the EBL can also be calculated from the integral of the flux times the density of sources per unit flux per unit solid angle,

$$I_\nu = \int_0^\infty \mathrm{d}F_\nu\, F_\nu\, \frac{\mathrm{d}^2 N}{\mathrm{d}F_\nu\,\mathrm{d}\Omega}, \tag{7.5}$$

it is worthwhile to derive an expression for the source counts in order to provide a more detailed check on the LF model in comparison to data not used in the measurement. The number of galaxies per unit observed flux per unit solid angle on the sky is given by:

$$\begin{aligned}
\frac{\mathrm{d}^2 N}{\mathrm{d}F_\nu\,\mathrm{d}\Omega} &= \frac{1}{\Omega_{\rm sky}}\int \mathrm{d}z \int \mathrm{d}L_\nu\, \delta\left(F_\nu - \frac{L_\nu \mu_\nu(\nu[1+z])}{4\pi[1+z]D_{\rm cT}^2(z)}\right)\frac{\mathrm{d}V_c}{\mathrm{d}z}\Phi(L_\nu, z) \\
&= \frac{16\pi^2}{\Omega_{\rm sky}}\int \mathrm{d}z \frac{\mathrm{d}D_c}{\mathrm{d}z}\left(\frac{[1+z]D_{\rm cT}^4(z)}{\mu_\nu(\nu[1+z])}\right)\Phi\left(\frac{F_\nu 4\pi[1+z]D_{\rm cT}^2(z)}{\mu_\nu(\nu[1+z])}, z\right),
\end{aligned} \tag{7.6}$$

where $D_{\rm cT}(z)$ is the comoving distance transverse to the line of sight (also called D_M for 'proper motion' distance).

7.3 Summary of Results Used

As Equation 7.4 shows, the two necessary quantities for calculating the EBL are the mean SED of galaxies and the LF. For the mean SED, this work uses the overall mean from Chapter 3 that was constructed from fitting templates from Assef et al. (2010) to targets in the zCOSMOS survey described in Lilly et al. (2009) and Knobel et al. (2012). The resulting mean SED is shown in Figure 7.1. The plot also contains the 1-σ band of SED variety around the mean SED because where the width of that band compared to the position of the mean SED becomes too great determines where the Gaussian approximation $\mathcal{L}_{\mathrm{SED}}$ begins to break down. The vertical lines are guides to where particular parts of the mean SED contribute to the 3.4 μm EBL.

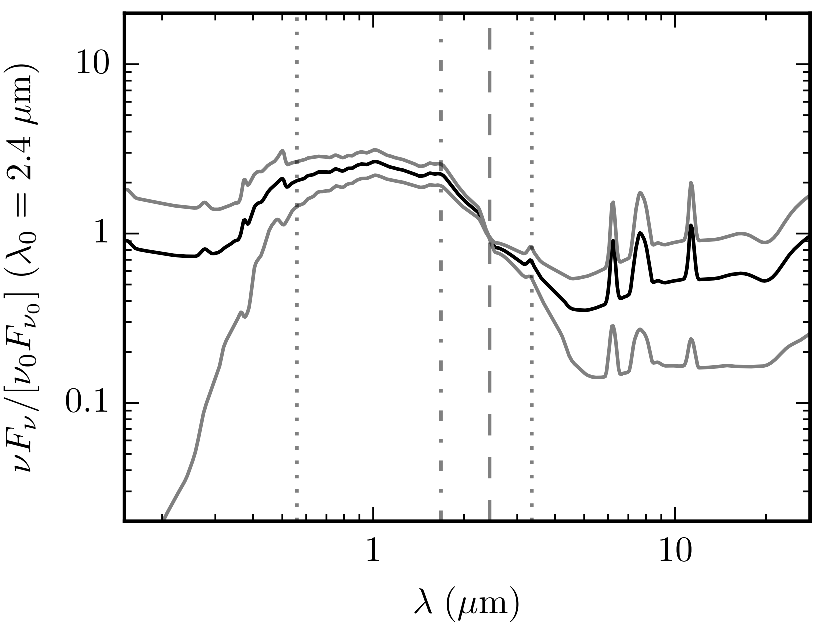

Figure 7.1: The mean SED of galaxies as approximated using fits to the templates in Assef et al. (2010) done in Chapter 3. The grey lines show the band of 1-σ in SED variety, and the accuracy of the Gaussian approximation is limited to regions where that band is sufficiently narrow compared to the mean SED. The vertical lines are guides to the parts of the mean SED that galaxies at particular redshifts contribute to the 3.4 μm background. The vertical dashed line shows the effective rest frame wavelength of W1 for galaxies at $z = 0.38$ ($\lambda \approx 2.4$ μm), the vertical dotted lines shows the same for galaxies at $z = 0$ and $z = 5$, and the vertical dash-dotted line is for galaxies at $z = 1$.

For the LF this chapter uses the set of Markov Chain Monte Carlo (MCMC) chains that sample the posterior probability of LF parameters from Chapter 6 and available under digital object identifier (DOI) 10.6084/m9.figshare.4109625. The measurement that produced the chains is based on a combination of several spectroscopic redshift data sets with public photometric databases, especially the AllWISE data release. The LF that the chains have parameters for is a Schechter LF:

$$\Phi(L, z) = \frac{\phi_\star(z)}{L_\star(z)} \left(\frac{L}{L_\star(z)}\right)^\alpha \mathrm{e}^{-L/L_\star(z)}. \tag{7.7}$$

The evolution models for $\phi_\star$ and $L_\star$ are similar to the commonly used Lin et al. (1999), modifed to use lookback time, $t_L(z)$, instead of redshift and to set $L_\star(t_0) = 0$ at some lookback time t_0. The exact parameterizations are:

$$\phi_\star(t_L) = \phi_0 \mathrm{e}^{-R_\phi t_L}, \text{ and} \tag{7.8}$$

$$L_\star(t_L) = L_0 \mathrm{e}^{-R_L t_L} \left(1 - \frac{t_L}{t_0}\right)^{n_0}, \tag{7.9}$$

where ϕ_0, R_ϕ, L_0, R_L, α, n_0, and t_0 are all constants. The only constant not, in some way, measured is t_0 which is set to the lookback time of recombination, equivalent to the redshift $z_{\mathrm{recomb}} = 1088.16$ according to the WMAP 9 year ΛCDM parameters matrix[1] (giving $t_0 = 0.9828\, t_H = 13.73\,\mathrm{Gyr}$). Full details of how to extract these parameters from the contents of the chain files are given in Chapter 6.

For every set of parameters in the LF chains two backgrounds are calculated: the background from sources with $z \leq 1$ and $z \leq 5$. The first redshift limit is set to match the upper limit on the data used to measure the LFs, and so marks the lower edge of model validity. The upper limit at $z = 5$ is set to capture as much of the background predicted by the model as possible without relying on the parts of the mean SED where the size of the SED covariance makes the Gaussian approximation of $\mathcal{L}_{\mathrm{SED}}$ invalid.

[1] `https://lambda.gsfc.nasa.gov/product/map/current/params/lcdm_wmap9.cfm`

7.4 Backgrounds and Number Counts

The backgrounds that correspond to the posterior MCMC chains from Chapter 6 will be published under DOI:10.6084/m9.figshare.4245443 when the paper based on this chapter is published in a peer reviewed journal. Each posterior LF chain has a corresponding file containing the backgrounds calculated for each element in the LF chain. Examples of histograms constructed using the posterior chains can be found in Figure 7.2. While the shallowest data set plotted, the black lines of Panel **c** are visibly asymmetric, all of the distributions are visually similar to log-normal distributions.

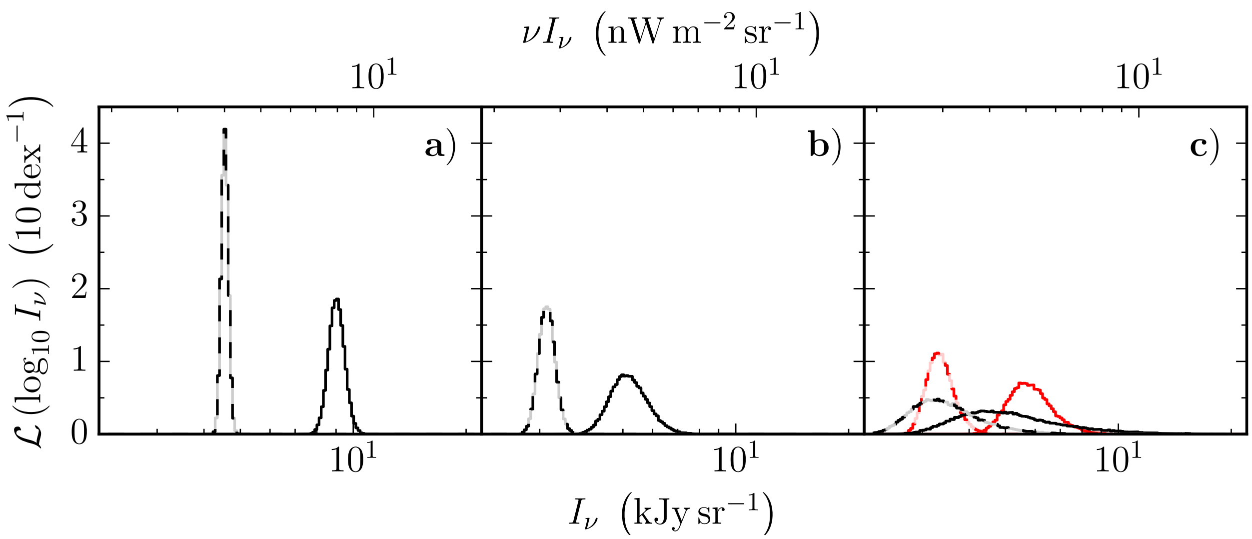

Figure 7.2: Histograms of EBL posteriors that correspond to different LF posteriors from Chapter 6. The dashed lines are histograms of the $z \leq 1$ predictions and the solid lines are of the $z \leq 5$. Panel **a** is based on the High z Prior chain, Panel **b** is based on the High z Trim Prior chain, and Panel **c** uses the survey specific chains from *WISE*/DEIMOS (black) and zCOSMOS (red). Each posterior chain contains a total of $210,000$ samples.

The symmetry of the histograms in log-space makes a description of each result as a log-normal distribution, parameterized by its geometric mean, $\langle \log_{10} I_\nu \rangle$, and logarithm standard deviation, $\left\langle \left(\log_{10} I_\nu - \langle \log_{10} I_\nu \rangle\right)^2 \right\rangle$, a good approximation of the whole distribution. The means and standard deviations for all of the log-background posterior chains can be found in Figure 7.3, with the blue bar highlighting the official result for this chapter, $I_\nu(\lambda =$

$3.4\,\mu\text{m}) = 9.03^{+0.46}_{-0.43}\,\text{kJy}\,\text{sr}^{-1}$ ($7.96^{+0.40}_{-0.38}\,\text{nW}\,\text{m}^{-2}\,\text{sr}^{-1}$). The full details of what defines all of the samples that fix the model parameters can be found in Chapter 6. The survey specific samples (above the dotted line) are sorted in order of increasing depth (defined as median redshift) with shallowest on top. The combined samples (below the dotted line) are Low z when the data is limited to redshift $z \leq 0.2$, High z when $0.2 < z \leq 1.0$, Prior when the faint end slope (α) of the LF is constrained using the mean and standard deviation of the faint and slope of the corresponding Low z sample, and Trim when the contributions of each survey are limited to areas in the luminosity-redshift plane where the survey is more than 98% of its maximum completeness. In sum, the Trim samples sacrifice sample size and depth for reduced systematic uncertainty, and the Prior samples combine the aspect of the Low z samples least affected by a bias of uncertain origin that affects bright sources.

The important features to note in Figure 7.3 are: the samples most affected by the unknown bias identified in Chapter 6 (6dFGS, SDSS, Low z, and Low z Trim) have the expected backgrounds so high they can accurately be described as outliers, and there is an increasing trend in the predicted background with survey depth (GAMA, AGES, *WISE*/DEIMOS, and zCOSMOS, in order). The presence of the High z Trim sample in the category of outliers is a consequence of that chain having a mean faint end slope of $\alpha = -1.93 \pm -0.04$, nearer the point where the LF estimate diverges at $\alpha = -2$ than the other samples which all have α nearer to -1. It is likely that the same fluctuation that makes the α of the High z Trim sample so negative was displaced into a faster comoving number density evolution; one that implies galaxies are presently increasing in comoving number density at 1.9 ± 0.7 e-folds per Hubble time, reducing the estimated background. For all of these reasons, and because it has the greatest statistical precision, the High z Prior is most likely to prove the most accurate when compared with even better, deeper, measurements made in the future.

The priors imposed on the LF parameters in Chapter 6 were chosen to be analytically calculable and minimally informative, with the exception of the parameter that defines the poorly constrained early time behavior of $L_\star$, n_0. These priors induce an implicit prior on the backgrounds calculated here that is, essentially, impossible to calculate analytically due to complexity and reliance on numerically defined SED templates. For that reason, the data

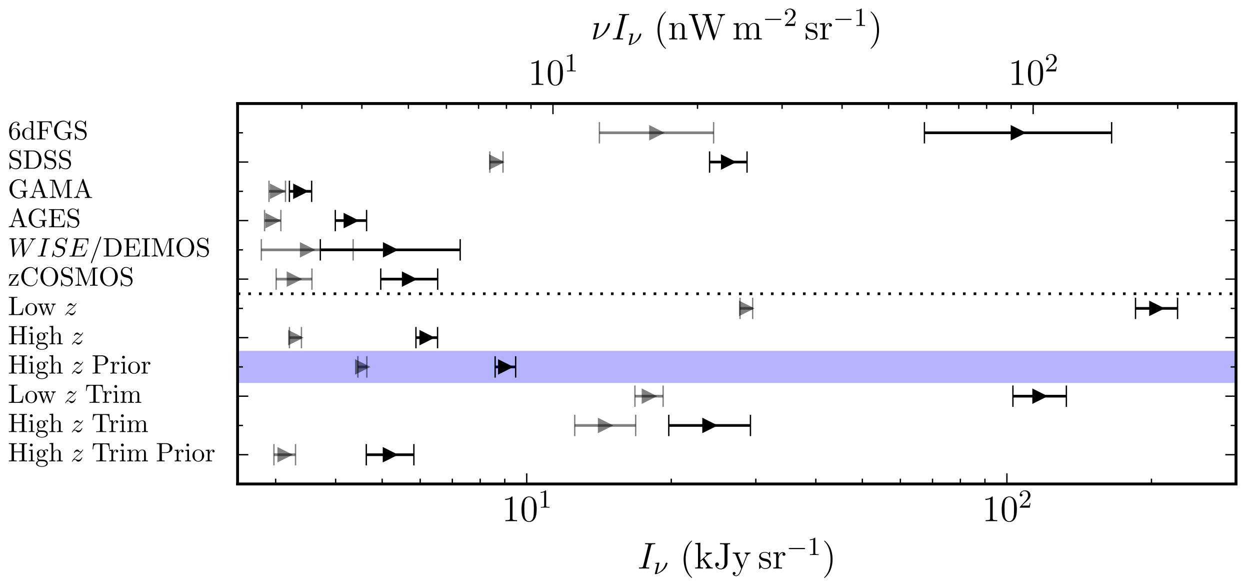

Figure 7.3: All of the 3.4 μm EBL predictions made using the posterior chains from Chapter 6. The grey points are the $z \leq 1$ backgrounds, and the black points are the $z \leq 5$ ones. The dotted lines divides the survey based samples (above) from the combined samples (below). The blue bar highlights background based on the canonical chain from Chapter 6.

set published with this work also includes an MCMC chain describing the background prior. A histogram of that chain can be found in Figure 7.4. The black line is the histogram of the $z \leq 5$ background, and the grey line is of the $z \leq 1$ background, offset to the right by 1%, for clarity. The prior is clearly not flat in either I_ν or $\ln I_\nu$ in the region of interest. It is, in fact, slightly biased to the low side. Given that the response of a log-normal distribution, $f(\ln(x)) \propto \exp(-[\ln x - \mu]^2/[2\sigma^2])$, to a prior that is approximable as x^k (here $k \approx -0.5$ for most of the range of interest) is to shift it by an amount that depends on the width of the distribution, $\delta\mu = k\sigma^2$. Because $|k\sigma| < 1$ for all of the posteriors produced here, the shift will be less than σ in all cases; for the High z Prior result, in particular, the shift in the mean caused by the prior is the same as dividing the mean I_ν by 0.998.

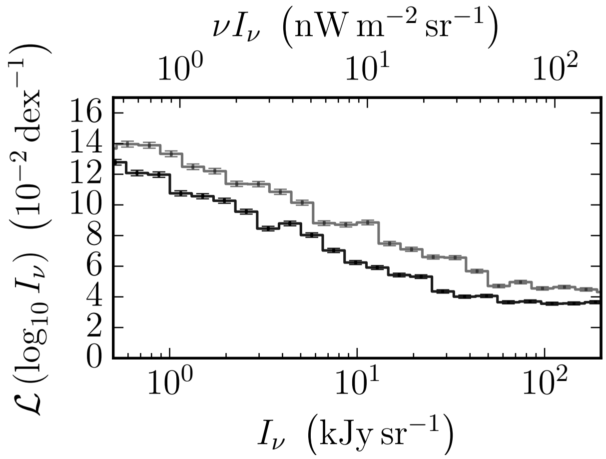

Figure 7.4: Prior induced on the EBL posterior by the priors on the LF parameters in Chapter 6, zoomed in to the range most relevant to the EBL estimate in this work. The black line is the prior for $z \leq 5$ backgrounds, and the grey line is for the $z \leq 1$ backgrounds. The grey line is shifted to the right by 1% of the width of the plot. The chain used to construct this histogram contained 322,560 samples, in total, and the error bars are approximated by assuming Poisson statistics. Note that the black and grey lines are not independent, since they were calculated using the same MCMC LF parameter chains.

7.5 Discussion

The models used to calculate the 3.4 μm EBL in this work have two shortcomings most relevant to the EBL estimate. First, the mean SED did not evolve with luminosity or redshift. Second, the faint end slope of the LF was also a constant. Figure 7.5 contains a plot highlighting where in redshift-luminosity space the 3.4 μm EBL originates. As expected, the model predicts that the EBL is dominated by low to moderate redshift objects with luminosities near $L_\star$. Studies of the high redshift universe consistently show that galaxies in the early universe have optical and ultraviolet spectra dominated by high mass stars, making them, on average, more blue than low redshift galaxies. Bouwens et al. (2009) and Bouwens et al. (2014), for example, found that galaxies exhibited a trend of bluer ultraviolet slope, decreasing $\beta = \frac{\mathrm{d}\ln L_\lambda}{\mathrm{d}\ln\lambda}$, for both increasing redshift and decreasing luminosity. Similarly, studies of the mass function of galaxies show a trend of decreasing α with increasing redshift (see the compilation in Table 1 of Conselice et al., 2016) to a minimum around the -2 predicted by the ΛCDM models in Jenkins et al. (2001).

Both color evolution and faint end slope evolution suggest that the EBL measurements produced here are underestimates. The former would tend to increase size of the high redshift tail of the bottom plot in Figure 7.5, and the latter would increase the low luminosity tail of the left hand plot in the same figure. These factors are counter-balanced by the fact that the model has slower evolution in $L_\star$ at high redshift than would be suggested by comparisons with Figure 9 of Madau & Dickinson (2014), which would narrow the high redshift tail.

It is difficult to predict how these competing factors will work out when more accurate measurements are available. The SED evolution is unlikely to contribute more than a factor of 10 to the thickness of the high redshift tail. Evolution in $L_\star$ is likely to be of a similar size. The interesting challenge is presented by the evolution in α, where measurements with $\alpha \leq -2$ require the explicit addition of a low luminosity cutoff to the LF to produce a finite contribution to the background. This means that fully constraining the contribution of galaxies to the EBL will require measuring galaxies on the faint end slope of the LF to either eliminate $\alpha \leq -2$ or to find the LF's faint end cutoff. Interestingly, the presence of a faint end cutoff, $L_{\min}$, with a steep faint end slope, $\alpha \leq -2$, increases the impact that $L_\star$ evolution has on the predicted EBL because $L_{\min}$ enters into EBL calculations in a ratio with $L_\star$.

Figure 7.6 shows how the primary estimate in this work compares with values from the literature from wavelengths in the range 3.4 to 3.6 μm, adjusted to 3.4 μm assuming I_ν is approximately a constant with wavelength. Points in Figure 7.6 include direct observations of the EBL (Sano et al., 2016; Tsumura et al., 2013; Levenson et al., 2007; Matsumoto et al., 2005; Wright & Johnson, 2001; Wright & Reese, 2000; Gorjian et al., 2000), upper limits based on the examination of the extinction of TeV gamma rays from blazar spectra (Mazin & Raue, 2007; Aharonian et al., 2006), estimates of the contribution of galaxies based on extrapolating galaxy source flux counts (Driver et al., 2016; Levenson & Wright, 2008; Fazio et al., 2004), and other LF based estimates (Stecker et al., 2016; Helgason et al., 2012; Domínguez et al., 2011). What can be seen from the comparisons is that, while the 3.4 μm

EBL measured here is higher than measurements from most comparable works, it is still consistent the blazar limits and the direct measurements. Judging by the relationship to the literature measurements, any modification from the true value caused by the systematic limitations in this work is unlikely be more than about $2\,\mathrm{kJy\,sr^{-1}}$ ($1.8\,\mathrm{nW\,m^{-2}\,sr^{-1}}$) in either direction.

Further confirmation of the basic accuracy of the model used to predict the EBL can be found from comparing observed source flux counts to predicted ones across different wavelengths. Figure 7.7 contains comparisons of the observed source flux histograms (black lines) to the predicted contribution of galaxies based on the mean LF of the posterior chains produced from the High z Prior, High z Trim Prior, and *WISE*/DEIMOS samples (red, blue, and grey dashed lines, respectively). The top row contains comparisons to the AllWISE flux counts for all source with in the northern galactic cap ($b \geq 30°$) with no artifact flags set and a signal to noise ratio (SNR) at least 4 in the plotted band. The plotted flux is the standard point spread function (psf) flux, so it will have inaccuracies at the bright end. Those inaccuracies are unobservable, though, because no effort was made to separate stars from galaxies and the star counts dominate there. No completeness corrections were applied to any of the data, either, so the faint end of the observations is expected to undershoot the predictions.

The next two rows are counts from the Sloan Digital Sky Survey (SDSS) data release 10 database table named `PhotoObj`. The SDSS sources are limited to two circular regions with 3° radius that are antipodes – centered at J2000 right ascension and declination $(163.56309°, 7.27216°)$ and $(343.56309°, -7.27216°)$. A source is excluded if it has any of the following flags, as explained in the SDSS database schema browser[2], set for the band in question (column named `flags_`[band letter]): `EDGE`, `BLENDED`, `NODEBLEND`, `SATURATED`, `TOO_LARGE`, `MOVED`, `MAYBE_CR`, and `MAYBE_EGHOST`. Each source also had to have an SNR ≥ 4, just like the AllWISE sources. The plotted fluxes are the `modelFlux_`[band letter] columns, so they won't describe stars accurately, but that shouldn't matter for the same reason the

[2]`http://skyserver.sdss.org/dr10/en/help/browser/browser.aspx#&&history=enum+PhotoFlags+E`

psf fluxes do not meaningfully affect the AllWISE plots.

What the plots in Figure 7.7 show is that the model used here performs better than expected in predicting the number counts at wavelengths where the Gaussian approximation of $\mathcal{L}_{\rm SED}$ is no longer valid (particularly SDSS g and u). In all wavelengths and for all of the predictions plotted, the flux counts predictions are reasonably close to the observed histograms. The comparison makes clear how, using flux counts alone or using LFs measured at different wavelengths, it would be easy to get an estimate of the $3.4\,\mu$m background to be closer to the $5 \pm 1\,\mathrm{kJy\,sr^{-1}}$ of the High z Trim Prior based estimates, plotted in blue, than the High z Prior based estimate, plotted in red, depending on the how strict the definition of 'galaxy' is and how incompleteness at the faint end is modeled. The comparisons also show that there is still untapped information that can be used to more tightly constrain the full spectro-luminosity functional in future works. The over-prediction at the faint end of the W1 plot is to be expected because of incompleteness from both the limit of photometric sensitivity[3] and confusion[4].

7.6 Conclusion

We showed from analyzing the mean SED of galaxies using more than a thousand galaxies with an average of more than 5 photometric observations of each galaxy, and the $2.4\,\mu$m LF of galaxies using more than half a million galaxies with spectroscopic redshifts, that the contribution of galaxies to EBL at $3.4\,\mu$m is $I_\nu = 9.0 \pm 0.5\,\mathrm{kJy\,sr^{-1}}$ ($\nu I_\nu = 8.0 \pm 0.4\,\mathrm{nW\,m^{-2}\,sr^{-1}}$), with systematic uncertainties unlikely to be greater than $2\,\mathrm{kJy\,sr^{-1}}$. This value is consistent with both direct measures of the background and constraints based on blazar spectra. Recent work on the production of gamma rays by blazar protons relaxes the strength of these constraints (Essey & Kusenko, 2010; Essey et al., 2011; Aharonian et al., 2013), leaving room for contributions from extended galaxy halos (discussed in Cooray et al., 2012) and from a large faint galaxy population implied by the steepening faint end slope of

[3] http://wise2.ipac.caltech.edu/docs/release/allwise/expsup/sec2_4a.html

[4] http://wise2.ipac.caltech.edu/docs/release/allsky/expsup/sec6_2.html#brt_stars

the mass function (compiled in Conselice et al., 2016). Settling the contribution from high z faint galaxies will require deeper redshift surveys, to more firmly establish the steepness of the faint end slope, and work to establish how the faint end of the LF cuts off. Two examples of possible mechanisms that can provide a faint end cutoff to the LF are: an intrinsic lower bound to the halo mass function, and a deviation in the halo mass to light conversion factor (caused, for example, by a lower limit on the halo mass capable of accreting and cooling baryons from the inter-galactic medium into star forming clouds).

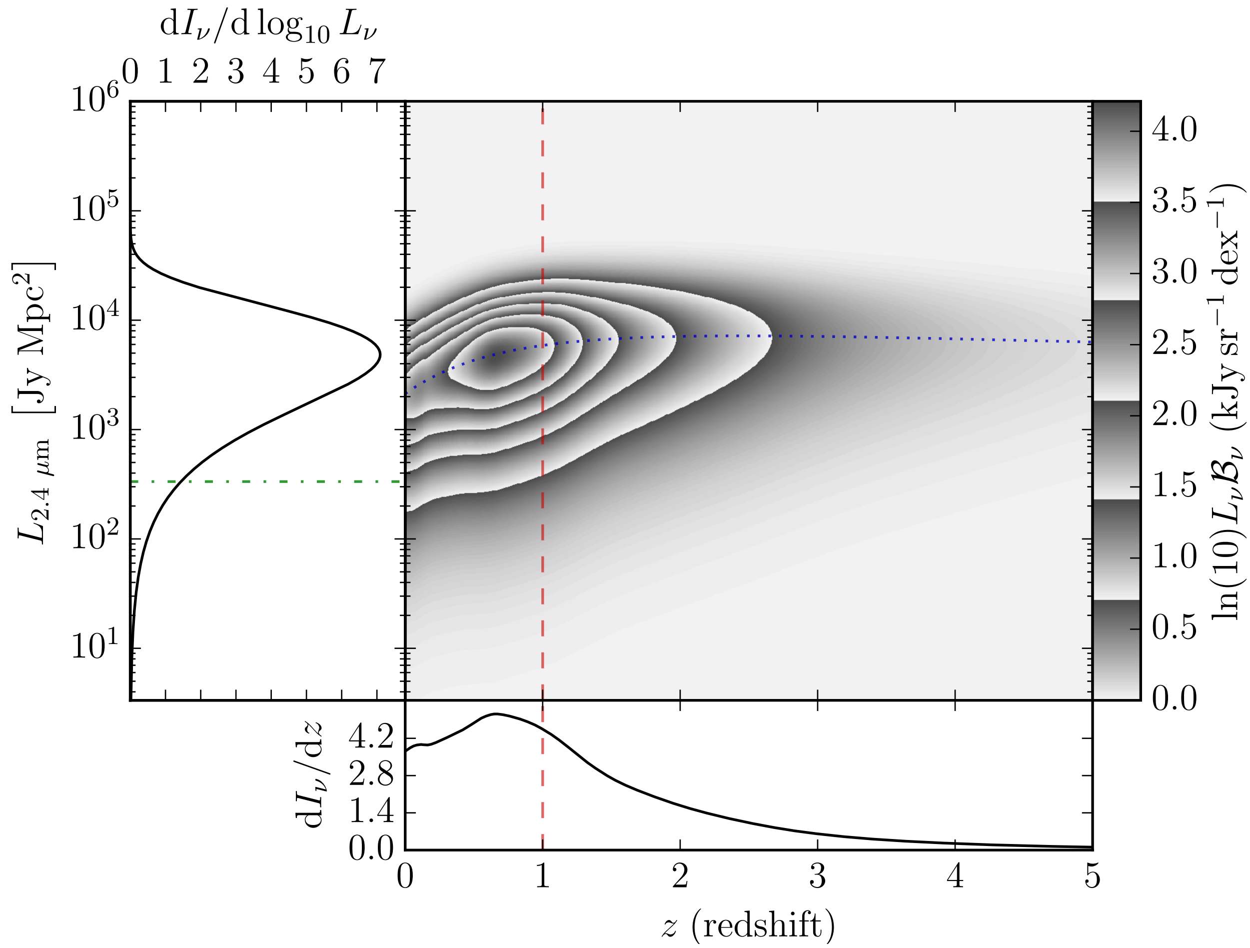

Figure 7.5: Bivariate density of contributions to the $3.4\,\mu$m EBL by galaxies according to the mean model from the High z Prior MCMC posterior chain, with the marginal densities abutting. The blue dotted line on the bivariate density shows the evolution of $L_\star$, the red vertical dashed line highlights the extent of the data the models were fit to, and the green dash-dotted line marks $10^{10}L_{2.4\,\mu\mathrm{m}\odot}$ (where the galaxy's spectral luminosity, L_ν, at wavelength $\lambda = 2.4\,\mu$m is the same as L_ν at the same point in the spectrum as 10^{10} suns). The total $3.4\,\mu$m background in this plot is $9.06\,\mathrm{kJy\,sr^{-1}}$ ($7.99\,\mathrm{nW\,m^{-2}\,sr}$).

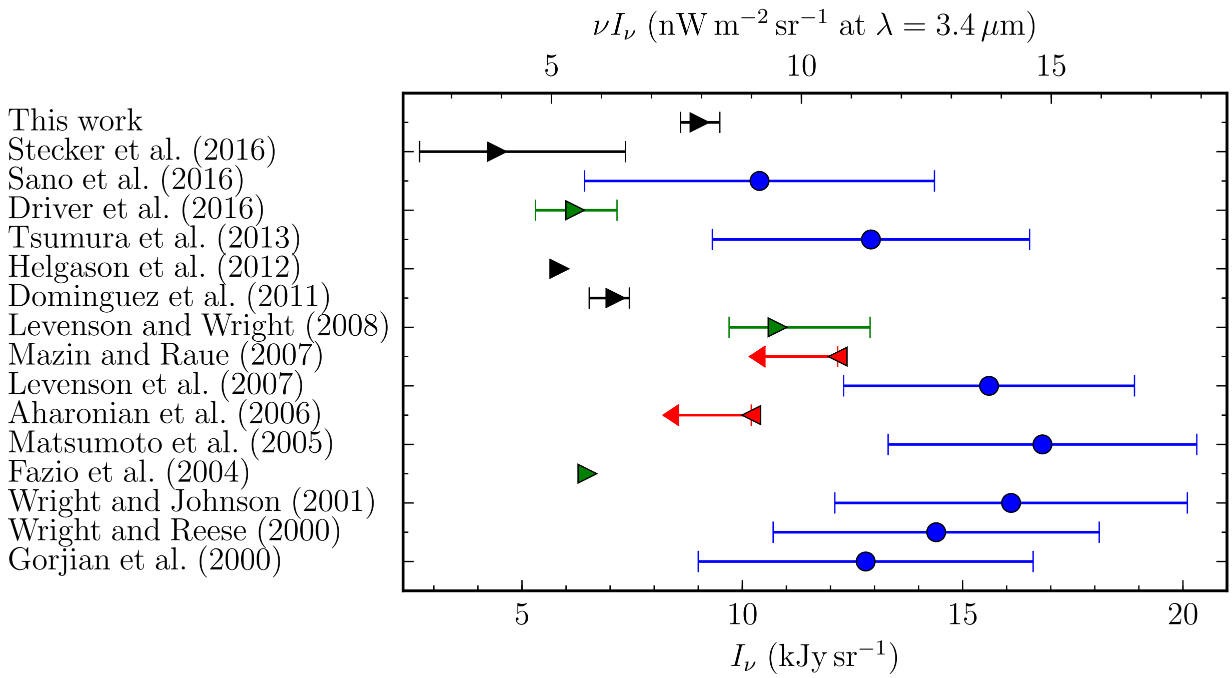

Figure 7.6: Comparison of different values measured for the EBL for wavelengths near $3.4\,\mu$m ordered by year of publication then first author last name. The points plotted as blue circles are direct observations of the EBL, the green triangles are based on integrating extrapolated galaxy flux histograms to 0, the red inverted triangles are upper limits from blazar extinction models, and the black triangles are luminosity function based estimates of what galaxies contribute to the EBL. Points without error bars (Fazio et al., 2004; Helgason et al., 2012) did not include error estimates in the original work.

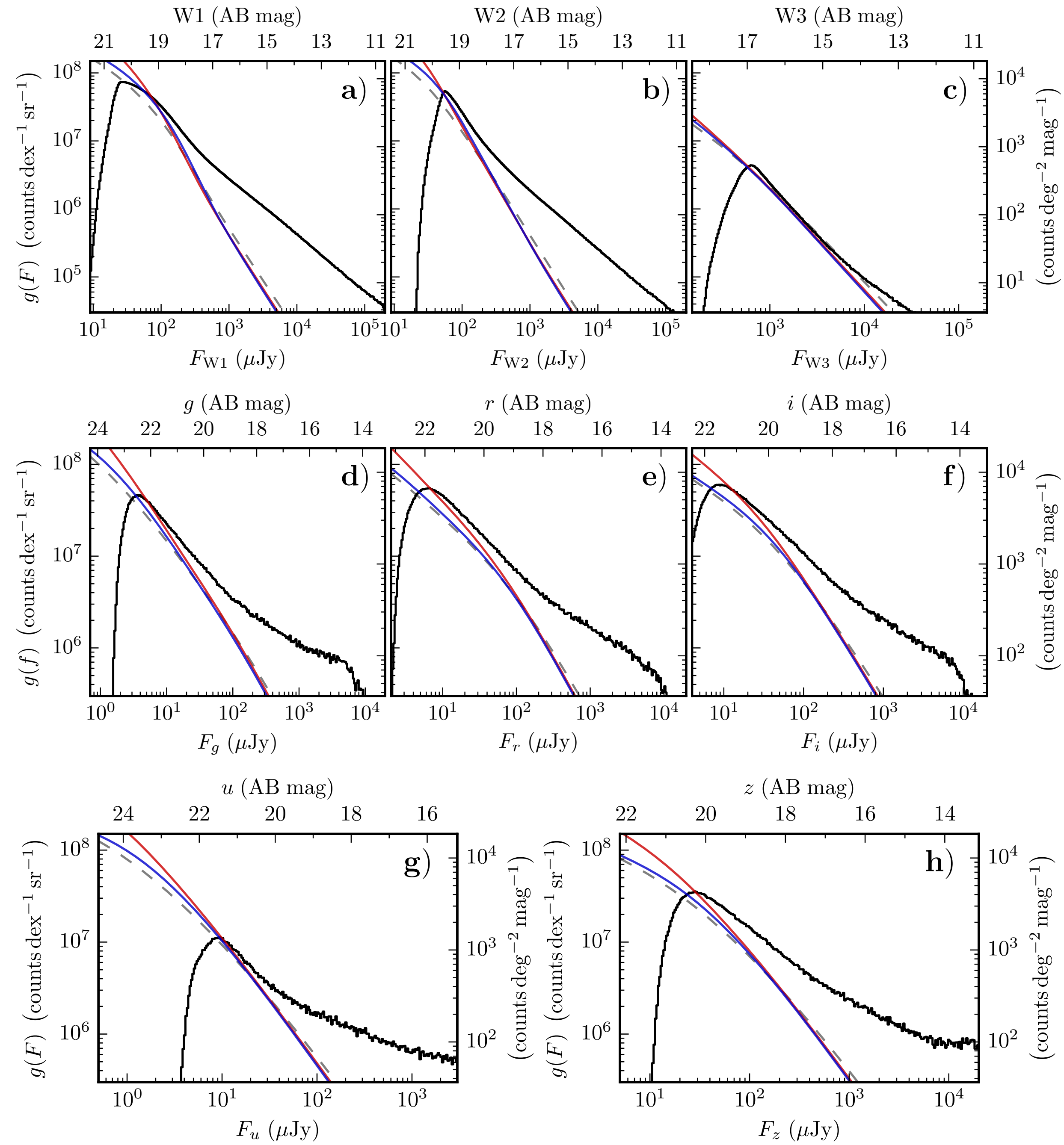

Figure 7.7: Comparisons of the predicted source flux counts, $g(f) = \frac{\mathrm{d}^2 N}{\mathrm{d}\log_{10} F\,\mathrm{d}\Omega}$, from the MCMC chain mean models of Chapter 6 to observed flux counts in AllWISE and SDSS bands. No effort was made to separate stars from galaxies in the observed fluxes, so the observed histograms (black lines) should be greater than the predictions at all fluxes where the survey is complete. The three predictions plotted are based on the mean LFs from the samples Chapter 6 labels as High z Prior (red line), High z Trim Prior (blue line), and *WISE*/DEIMOS (grey dashed line).

CHAPTER 8

Conclusions

This project began with the goal of measuring the $3.4\,\mu$m EBL through measuring the LF of galaxies using several public redshift surveys, and one small one carried out to ensure that we had proper control of the observational biases, combined with the all sky survey carried out by the *WISE* satellite and team. In the process, we discovered that the mathematical tools developed to measure the LF to that point were not adequate to analyzing a sample of galaxies that had a smoothly varying selection function in the redshift-luminosity plane. Such a smoothly varying selection function is an inevitable consequence of measuring luminosities either with a fixed rest frame definition or on galaxies that have multiple observer frame flux limits imposed.

To remedy the limitations, we explored the concept of a spectro-luminosity functional, $\Psi[L_\nu](z)$, a mathematical structure from which it is possible to construct every color-color plot, color-manitude diagram, and luminosity function possible. This exploration yielded fruit in terms of a Gaussian approximation to the uncertainty added to a measurement when a K-correction, or any other filter transformation, is applied to a flux measurement, a new way to estimate a galaxy's selection function in redshift-luminosity space, and a new unbinned likelihood for estimating the parameters of the ordinary luminosity function, $\Phi(L, z)$.

The effort in developing $\Psi[L_\nu](z)$ based estimators payed off, mostly, with estimates for the faint end slope, $\alpha = -1.050 \pm [0.004_{\rm stat},\ 0.03_{\rm sys}]$, and the characteristic luminosity, $L_\star(z=0) = 6.4 \pm [0.1_{\rm stat},\ 0.3_{\rm sys}] \times 10^{10} L_{2.4\,\mu{\rm m}\,\odot}$
($M_\star = -21.67 \pm [0.02_{\rm stat},\ 0.05_{\rm sys}]\,{\rm AB\,mag}$), that have improved statistical precision over the literature in this wavelength range, and comparable precision for the characteristic

number density, $\phi_\star(z = 0) = 5.8 \pm [0.3_{\mathrm{stat}},\ 0.3_{\mathrm{sys}}] \times 10^{-3}\,\mathrm{Mpc}^{-3}$, and the evolution parameters for $\phi_\star$, $R_\phi = 1 \pm [1_{\mathrm{stat}},\ 7_{\mathrm{sys}}] \times 10^{-2}$ e-folds Gyr^{-1}, and $L_\star$, $\frac{\partial L_\star}{\partial t}\Big|_{z=0} = -0.147 \pm [0.005_{\mathrm{stat}},\ 0.07_{\mathrm{sys}}]$ e-folds Gyr^{-1}. The primary feature of the data that prevented the techniques from reaching their full potential is a bias of unknown origin that affected bright, low redshift galaxies. Possible origins for this bias include flaws in the photometry of resolved and marginally resolved sources, and the position of the Milky Way in a relatively underdense region of the large scale structure of galaxies (cosmic variance), though the former is more likely than the latter.

We then used the MCMC parameter chains of the LF posterior to calculate the $3.4\,\mu$m EBL, I_ν, they implied. The resulting estimate for the contribution of galaxies closer than $z = 5$ is $I_\nu = 9.0 \pm 0.5\,\mathrm{kJy\,sr^{-1}}$ ($\nu I_\nu = 8.0 \pm 0.4\,\mathrm{nW\,m^{-2}\,sr^{-1}}$). This value is higher than most estimates of the contribution of galaxies to the $3.4\,\mu$m EBL, and lower than both direct measures and the constraints from inferred extinction of TeV blazar spectra. There is outside evidence to suggest that the model that lead to our EBL result is an overestimate ($L_\star$ too high at high z) and that it is an underestimate (α too high and SED color too red at high z).

There is still a lot of room for improvement in the results produced here, and the remainder of this chapter is spent discussing the improvements to the theoretical tools and the experimental data

8.1 Theoretical Improvements

The easiest improvement that can be implemented would be a change in how the LF parameters evolve with time. The parameterization used here was chosen to be similar to a common parameterization used in the literature, and not for any fidelity to the physical processes galaxies undergo. Galaxies are observed to undergo two processes relevant to the evolution of the luminosity function: merging in collisions, and accretion of gas to fuel quasars and form stars. It is not obvious how these processes should affect $L_\star$ and $\phi_\star$. Luminosity density and number density, however, should be unchanged by mergers and gas accretion, respectively, so it may be more accurate to model their evolution and calculate the corresponding values of $L_\star$ and $\phi_\star$. Another approach that could be interesting to explore would be to model the halo mass function and couple that to an empirical model for a halo's ability to accrete and cool gas at a given redshift in order to produce an evolving minimum luminosity and faint end slope of the LF.

The next improvements to implement would be ones that improve the fidelity of $\Psi[L_\nu](z)$ to observed statistics of galaxies. One improvement that would be an obvious extension of the work done in the text would be to break up Ψ into a sum of spectro-luminosity functionals, with one for each class of galaxy (usually: red sequence, blue cloud, and AGN). The mathematics of that process makes it equivalent to classifying the galaxies by whichever SED they're closest to, with the exception of edge cases, especially if more observed fluxes than the selection fluxes are fed into the fitting process. In contrast to an 'is a' (classification) approach, it may be possible to break down galaxies into component parts, a 'has a' (composition) approach. The primary difference between the approaches is that under a classification system all of the luminosity is, effectively, assigned to the selected class, while under a composition approach the luminosity gets split among the component parts. Either approach can handle the evolution of the SED shape with magnitude in a natural way, since galaxies with different SEDs will have different LFs, but the evolution with cosmological time is a topic that would require more careful thought.

Another obvious extension would be to increase the number of template spectra, including the possibility of modifying their types. Care must be exercised in balancing fidelity with computational load, though, because the covariance matrix among the templates grows in size as the square of the number of templates. Even so, increasing the number of templates may, ultimately, be the most computationally tractable way to address dust extinction and emission. Another way that may work would be to produce a vector of parameters that fix the entire SED (for example: metallicity Z, mean stellar age, effective radius, and halo mass), call them $\vec{p}$, and add their distribution, $f(\vec{p})$, to the model by multiplying it by Ψ. In that case, $\mathcal{L}_{\mathrm{SED}}$ would be a delta functional, though smoothing it to a finite width distribution would be a possibly useful option. Adding radius in this way would have the added benefit of bringing surface brightness cuts into the scope of the model.

Perhaps the most important improvement would be to find a way to add considerations based on galaxy environment to the model. This improvement may also prove to be the most difficult to implement correctly, because it requires both a rethinking of the physics (how environment affects galaxy SED), and a reworking of the statistical approach that constructs the likelihood of the entire catalog of galaxies in a galaxy by galaxy fashion.

From a purely computational perspective, the model is presently constrained by the lack of algorithms that integrate an arbitrary Gaussian function in more than two dimensions over a rectangular region in a deterministic fashion, quickly. Without the deterministic requirement, the current state of the art in Gaussian integration is to use a Monte Carlo algorithm in order to avoid the 'curse of dimensionality'. The requirement for a deterministic algorithm comes from the fact that most function optimization routines available in libraries assume that the function returns deterministic results. Using a Monte Carlo integrator would, therefore, require adapting at least one optimization routine to handle non-deterministic behavior in the likelihood function. It may be possible, though, to exploit the fact that the integrand is separable with a change of variables that alters the rectangular integration region into a parallelotope (high dimensional parallelogram). Doing that reduces the number of expensive function calls to scale proportional to d, the number of dimensions, instead of exponentially, with the large number of multiplications and sums remaining in the integral amenable to parallelization on a computer graphics card.

8.2 Experimental Improvements

The least expensive improvement to the data would be to produce a proper extended source catalog for the AllWISE image atlas. Doing so would, hopefully, address the bright source bias that reduced the statistical precision of the results in the work presented here. Even better would be to advance the process of measuring the total flux of extended objects. Doing so would improve the longevity of old photometric surveys, reducing the need for aperture matching, or forced position reanalyses when new data sets become available.

Beyond new techniques, the standard astronomer's answer applies: more observations. More photometric surveys, with higher resolution, and greater depth are always helpful, but the key improvement for constraining the contribution of galaxies to the EBL will be to obtain more spectroscopic redshifts that meet the following criteria: widely spaced on the sky to minimize cosmic variance, selection criteria that are simple to model, luminosities fainter than local $L_\star$ by at least a factor of 10, a large number ($N \gtrsim 10^4$), and, most importantly, in the redshift range 1 to 3. All of these requirements are ideally achieved with a space telescope in the 2-plus meter range that isn't limited to the near infrared atmospheric windows ground telescopes are, and that is capable of measuring the redshifts of many galaxies at once. It should be possible, though, to constrain the background adequately using The James Webb Space Telescope (JWST) in concert with ground based instruments like the Multi-Object Spectrograph for Infra-Red Exploration (MOSFIRE) on the Keck I telescope[1], and the next generation of thirty meter class ground-based telescopes.

8.3 Acknowledgements to Public Data Sets

In this section we include the acknowledgements requested by the teams whose hard work to produce and maintain various public data sets made this work possible.

8.3.1 *WISE* Project

This publication makes use of data products from the Wide-field Infrared Survey Explorer, which is a joint project of the University of California, Los Angeles, and the Jet Propulsion Laboratory/California Institute of Technology, and NEOWISE, which is a project of the Jet Propulsion Laboratory/California Institute of Technology. WISE and NEOWISE are funded by the National Aeronautics and Space Administration.

[1]`http://www2.keck.hawaii.edu/inst/mosfire/`

8.3.2 SDSS Project

Funding for SDSS-III has been provided by the Alfred P. Sloan Foundation, the Participating Institutions, the National Science Foundation, and the U.S. Department of Energy Office of Science. The SDSS-III web site is http://www.sdss3.org/.

SDSS-III is managed by the Astrophysical Research Consortium for the Participating Institutions of the SDSS-III Collaboration including the University of Arizona, the Brazilian Participation Group, Brookhaven National Laboratory, Carnegie Mellon University, University of Florida, the French Participation Group, the German Participation Group, Harvard University, the Instituto de Astrofisica de Canarias, the Michigan State/Notre Dame/JINA Participation Group, Johns Hopkins University, Lawrence Berkeley National Laboratory, Max Planck Institute for Astrophysics, Max Planck Institute for Extraterrestrial Physics, New Mexico State University, New York University, Ohio State University, Pennsylvania State University, University of Portsmouth, Princeton University, the Spanish Participation Group, University of Tokyo, University of Utah, Vanderbilt University, University of Virginia, University of Washington, and Yale University.

8.3.3 GAMA Project

GAMA is a joint European-Australasian project based around a spectroscopic campaign using the Anglo-Australian Telescope. The GAMA input catalogue is based on data taken from the Sloan Digital Sky Survey and the UKIRT Infrared Deep Sky Survey. Complementary imaging of the GAMA regions is being obtained by a number of independent survey programs including GALEX MIS, VST KiDS, VISTA VIKING, WISE, Herschel-ATLAS, GMRT and ASKAP providing UV to radio coverage. GAMA is funded by the STFC (UK), the ARC (Australia), the AAO, and the participating institutions. The GAMA website is http://www.gama-survey.org/ .

Based on observations made with ESO Telescopes at the La Silla or Paranal Observatories under programme ID 175.A-0839.

8.3.4 2MASS Project

This publication makes use of data products from the Two Micron All Sky Survey, which is a joint project of the University of Massachusetts and the Infrared Processing and Analysis Center/California Institute of Technology, funded by the National Aeronautics and Space Administration and the National Science Foundation.

8.3.5 MAST Project

Some/all of the data presented in this paper were obtained from the Mikulski Archive for Space Telescopes (MAST). STScI is operated by the Association of Universities for Research in Astronomy, Inc., under NASA contract NAS5-26555. Support for MAST for non-HST data is provided by the NASA Office of Space Science via grant NNX13AC07G and by other grants and contracts.

8.3.6 NDWFS Project

This work made use of images and/or data products provided by the NOAO Deep Wide-Field Survey (Jannuzi and Dey 1999; Jannuzi et al. 2005; Dey et al. 2005), which is supported by the National Optical Astronomy Observatory (NOAO). NOAO is operated by AURA, Inc., under a cooperative agreement with the National Science Foundation.

8.3.7 IPAC Team

This research has made use of the NASA/ IPAC Infrared Science Archive, which is operated by the Jet Propulsion Laboratory, California Institute of Technology, under contract with the National Aeronautics and Space Administration.

8.3.8 GALEX Team

Based on observations made with the NASA Galaxy Evolution Explorer. GALEX is operated for NASA by the California Institute of Technology under NASA contract NAS5-98034.

And thank you to the teams behind: **6dFGS**, **AGES**, **zCOSMOS**, **SDWFS**, and **COSMOS**.

APPENDIX A

Mathematical Derivations

This chapter contains more detailed derivations of some important mathematical identities, especially from Chapter 2.

A.1 Marginalization of Gaussian Functionals

A.1.1 Theorem:

If $\{|w_i\rangle\}$ is a set of N linearly independent non-Euclidean normalized weighting functions (eg bandpass filters), and Σ is an invertible linear Hermitian operator on function space then:

$$\begin{aligned}\Phi(L_i) \equiv \int [\mathcal{D}f] \; & \left[\left(\prod_{i=1}^{N} \delta\left(L_i - \langle w_i|f\rangle\right) \right) \right. \\ & \left. \frac{\mathcal{N}}{\sqrt{\mathrm{Det}(\Sigma)}} \; \exp\left(-\frac{1}{2} \left[\langle f| - \langle f_0|\right] \Sigma^{-1} \left[|f\rangle - |f_0\rangle\right] \right) \right] \\ = & \frac{1}{(2\pi)^{N/2} \sqrt{\det([\langle w_i|\Sigma|w_j\rangle])}} \\ & \cdot \exp\left(-\frac{1}{2} \sum_{i,j} \left[L_i - \langle f_0|w_i\rangle\right] \left[\langle w_k|\Sigma|w_l\rangle\right]^{-1}_{i,j} \left[L_j - \langle w_j|f_0\rangle\right] \right) \end{aligned} \tag{A.1}$$

A.1.2 Proof:

Let $\delta(x) \to \lim_{\sigma\to 0} \frac{1}{\sigma\sqrt{2\pi}} \exp\left(-|x|^2\sigma^{-2}/2\right)$, then:

$$\begin{aligned}
\Phi(L_i,\sigma) = \int [\mathcal{D}f]\ \frac{\mathcal{N}}{\sigma^N (2\pi)^{N/2}\sqrt{\mathrm{Det}(\Sigma)}}\ \exp\Bigg(&-\frac{1}{2}\left[\langle f| - \langle f_0|\right]\Sigma^{-1}\left[|f\rangle - |f_0\rangle\right] \\
&-\frac{1}{2\sigma^2}\sum_{i=1}^{N} |L_i - \langle w_i|f\rangle|^2\Bigg) \\
= \ldots \exp\Bigg(-\frac{1}{2}\Big[&\langle f|\Sigma^{-1}|f\rangle - \langle f_0|\Sigma^{-1}|f\rangle - \langle f|\Sigma^{-1}|f_0\rangle + \langle f_0|\Sigma^{-1}|f_0\rangle \\
&+\frac{1}{\sigma^2}\sum_i \langle f|w_i\rangle\langle w_i|f\rangle - L_i\langle w_i|f\rangle - L_i\langle f|w_i\rangle + L_i^2\Big]\Bigg).
\end{aligned} \tag{A.2}$$

Letting $|v\rangle \equiv \sum_{i=1}^N L_i|w_i\rangle$, $W \equiv \sum_{i-1}^N |w_i\rangle\langle w_i|$, and $|v'\rangle \equiv (\kappa + W\sigma^{-2})^{-1}(\sigma^{-2}|v\rangle + \kappa|f_0\rangle)$ produces:

$$\begin{aligned}
\Phi = \ldots \exp\Bigg(-\frac{1}{2}\Bigg[&\langle f|\left(\Sigma^{-1} + \frac{1}{\sigma^2}W\right)|f\rangle - \left(\langle f_0|\Sigma^{-1} + \frac{1}{\sigma^2}\langle v|\right)|f\rangle \\
&-\langle f|\left(\Sigma^{-1}|f_0\rangle + \frac{1}{\sigma^2}|v\rangle\right) + \langle f_0|\Sigma^{-1}|f_0\rangle + \sum_i \frac{L_i^2}{\sigma^2}\Bigg]\Bigg) \\
= \ldots \exp\Bigg(-\frac{1}{2}\Bigg[&(\langle f| + \langle v'|)\left(\Sigma^{-1} + W\frac{1}{\sigma^2}\right)(|f\rangle + |v'\rangle) \\
&-\langle v'|\left(\Sigma^{-1} + \frac{1}{\sigma^2}W\right)|v'\rangle + \langle f_0|\Sigma^{-1}|f_0\rangle + \sum_i \frac{L_i^2}{\sigma^2}\Bigg]\Bigg) \\
= \frac{1}{\sigma^N(2\pi)^{N/2}}\ &\exp\left(-\frac{1}{2}\left[-\langle v'|\left(\Sigma^{-1} + \frac{1}{\sigma^2}W\right)|v'\rangle + \langle f_0|\Sigma^{-1}|f_0\rangle + \sum_i \frac{L_i^2}{\sigma^2}\right]\right) \\
\cdot \mathcal{N}\sqrt{\mathrm{Det}(\kappa)} &\int [\mathcal{D}f]\exp\left(-\frac{1}{2}(\langle f| + \langle v'|)\left(\Sigma^{-1} + \frac{1}{\sigma^2}W\right)(|f\rangle + |v'\rangle)\right) \\
= \frac{1}{\sigma^N(2\pi)^{N/2}}\ &\exp\Bigg(-\frac{1}{2}\Bigg[-\left(\langle f_0|\Sigma^{-1} + \frac{1}{\sigma^2}\langle v|\right)\left(\Sigma^{-1} + \frac{1}{\sigma^2}W\right)^{-1} \\
&\left(\Sigma^{-1}|f_0\rangle + \frac{1}{\sigma^2}|v\rangle\right) + \langle f_0|\Sigma^{-1}|f_0\rangle + \sum_i \frac{L_i^2}{\sigma^2}\Bigg]\Bigg) \\
\cdot &\sqrt{\mathrm{Det}\left(\Sigma^{-1}\left[\Sigma^{-1} + \frac{1}{\sigma^2}W\right]^{-1}\right)}
\end{aligned} \tag{A.3}$$

Now let Π be the projection operator that projects function space onto the space spanned by $\{|w_i\rangle\}$, and let $\Pi_\perp$ project onto it's orthogonal compliment in function space, implying

$\Pi + \Pi_\perp = \mathrm{Id}$, $\Pi^2 = \Pi$, $\Pi_\perp^2 = \Pi_\perp$, $W\Pi = W$, and $W\Pi_\perp = 0$. Thus:

$$\begin{aligned}
\mathrm{Id} + \Sigma W \sigma^{-2} &= (\Pi + \Pi_\perp)(\mathrm{Id} + \Sigma W \sigma^{-2})(\Pi + \Pi_\perp) \\
&= \Pi(\mathrm{Id} + \Sigma W \sigma^{-2})\Pi + \Pi_\perp(\Sigma W \sigma^2)\Pi + \Pi_\perp \Pi_\perp \Rightarrow \\
\mathrm{Det}(\mathrm{Id} + \Sigma W \sigma^{-2}) &= \mathrm{Det}_\perp(\Pi_\perp) \cdot \det(\mathrm{Id} + \Pi \Sigma W \sigma^{-2}),
\end{aligned} \tag{A.4}$$

where det is an ordinary determinant on an $N \times N$ matrix and $\mathrm{Det}_\perp(\Pi_\perp) = 1$.

Using an ordinary inverse for $(\Sigma^{-1} + W\sigma^{-2})^{-1}$ is not possible because W is singular. The calculation is possible to carry out using a pseudo-inverse, however, which can be done using a similar breakdown to what was used above. Thus:

$$\begin{aligned}
(\Sigma^{-1} + W\sigma^{-2}) &= (\Pi + \Pi_\perp)(\Sigma^{-1} + W\sigma^{-2})(\Pi + \Pi_\perp) \\
&= \Pi(\Sigma^{-1} + W\sigma^{-2})\Pi + \Pi\Sigma^{-1}\Pi_\perp + \Pi_\perp\Sigma^{-1}\Pi + \Pi_\perp\Sigma^{-1}\Pi_\perp.
\end{aligned} \tag{A.5}$$

Equation A.5 is a block-wise decomposition of $(\Sigma^{-1} + W\sigma^{-2})$, permitting application of a block-wise matrix inversion algorithm:

$$\begin{bmatrix} A & B \\ C & D \end{bmatrix}^{-1} = \begin{bmatrix} (A - BD^{-1}C)^{-1} & -(A - BD^{-1}C)^{-1}BD^{-1} \\ -D^{-1}C(A - BD^{-1}C)^{-1} & D^{-1} + D^{-1}C(A - BD^{-1}C)^{-1}BD^{-1} \end{bmatrix} \tag{A.6}$$

Applying Equation A.6 and assuming $WW^{-1} = \Pi$ then performing an expansion in σ to minimum needed order:

$$\begin{aligned}
\Pi(\Sigma^{-1} + W\sigma^{-2})^{-1}\Pi &= (\Pi[\Sigma^{-1} + W\sigma^{-2}]\Pi - \Pi\Sigma^{-1}[\Pi_\perp\Sigma^{-1}\Pi_\perp]^{-1}\Sigma^{-1}\Pi)^{-1} \\
&= \sigma^2 W^{-1}(\Pi + \Pi[\Sigma^{-1} + \Sigma^{-1}(\Pi_\perp\Sigma^{-1}\Pi_\perp)^{-1}\Sigma^{-1}]\Pi W^{-1}\sigma^2)^{-1} \\
&\approx \sigma^2 W^{-1}(\mathrm{Id} - [\Sigma^{-1} + \Sigma^{-1}(\Pi_\perp\Sigma^{-1}\Pi_\perp)^{-1}\Sigma^{-1}]W^{-1}\sigma^2) \\
&\quad + \mathcal{O}(\sigma^6) \\
\Pi(\Sigma^{-1} + W\sigma^{-2})^{-1}\Pi_\perp &= -\sigma^2 W^{-1}\Sigma^{-1}(\Pi_\perp\Sigma^{-1}\Pi_\perp)^{-1} + \mathcal{O}(\sigma^4) \\
\Pi_\perp(\Sigma^{-1} + W\sigma^{-2})^{-1}\Pi &= -\sigma^2(\Pi_\perp\Sigma^{-1}\Pi_\perp)^{-1}\kappa W^{-1} + \mathcal{O}(\sigma^4) \\
\Pi_\perp(\Sigma^{-1} + W\sigma^{-2})^{-1}\Pi_\perp &= (\Pi_\perp\Sigma^{-1}\Pi_\perp)^{-1} + \mathcal{O}(\sigma^2).
\end{aligned} \tag{A.7}$$

It is now possible to calculate the exponent from Equation A.3 to zeroth order in σ, keeping in mind that $\Pi_\perp|v\rangle = 0$:

$$\begin{aligned}
E &= -\left(\langle f_0|\Sigma^{-1} + \frac{1}{\sigma^2}\langle v|\right)\left(\Sigma^{-1} + \frac{1}{\sigma^2}W\right)^{-1}\left(\Sigma^{-1}|f_0\rangle + \frac{1}{\sigma^2}|v\rangle\right) \\
&\quad + \langle f_0|\Sigma^{-1}|f_0\rangle + \sum_i \frac{L_i^2}{\sigma^2} \\
&\approx \langle f_0|[\Sigma^{-1} - \Sigma^{-1}(\Pi_\perp\Sigma^{-1}\Pi_\perp)^{-1}\Sigma^{-1}]|f_0\rangle \\
&\quad - \langle v|W^{-1}[\Sigma^{-1} - \Sigma^{-1}(\Pi_\perp\Sigma^{-1}\Pi_\perp)^{-1}\Sigma^{-1}]|f_0\rangle \\
&\quad - \langle f_0|[\Sigma^{-1} - \Sigma^{-1}(\Pi_\perp\Sigma^{-1}\Pi_\perp)^{-1}\Sigma^{-1}]W^{-1}|v\rangle \\
&\quad + \langle v|W^{-1}[\Sigma^{-1} - \Sigma^{-1}(\Pi_\perp\Sigma^{-1}\Pi_\perp)^{-1}\Sigma^{-1}]W^{-1}|v\rangle \\
&\quad - \frac{1}{\sigma^2}\langle v|W^{-1}|v\rangle + \frac{1}{\sigma^2}\sum_i L_i^2 + \mathcal{O}(\sigma^2)
\end{aligned} \tag{A.8}$$

Two quick lemmas are needed to complete the proof.

A.1.2.1 Lemma: Block-wise Decomposition of $\Sigma^{-1} - \Sigma^{-1}(\Pi_\perp\Sigma^{-1}\Pi_\perp)^{-1}\Sigma^{-1}$

$$\begin{aligned}
[\Sigma^{-1} - \Sigma^{-1}(\Pi_\perp\Sigma^{-1}\Pi_\perp)^{-1}\Sigma^{-1}]\Pi_\perp &= \Sigma^{-1}\Pi_\perp - \Sigma^{-1}(\Pi_\perp\Sigma^{-1}\Pi_\perp)^{-1}\Pi_\perp\Sigma^{-1}\Pi_\perp \\
&= \Sigma^{-1}\Pi_\perp - \Sigma^{-1}\Pi_\perp = 0 \\
\Pi_\perp[\Sigma^{-1} - \Sigma^{-1}(\Pi_\perp\Sigma^{-1}\Pi_\perp)^{-1}\Sigma^{-1}] &= \Pi_\perp\Sigma^{-1} - \Pi_\perp\Sigma^{-1}\Pi_\perp(\Pi_\perp\Sigma^{-1}\Pi_\perp)^{-1}\Sigma^{-1} \\
&= \Pi_\perp\Sigma^{-1} - \Pi_\perp\Sigma^{-1} = 0 \Rightarrow \\
\Sigma^{-1} - \Sigma^{-1}(\Pi_\perp\Sigma^{-1}\Pi_\perp)^{-1}\Sigma^{-1} &= \Pi[\Sigma^{-1} - \Sigma^{-1}(\Pi_\perp\Sigma^{-1}\Pi_\perp)^{-1}\Sigma^{-1}]\Pi
\end{aligned} \tag{A.9}$$

Equation A.9 and Equation A.6 combined imply:

$$\begin{aligned}
\Sigma^{-1} - \Sigma^{-1}(\Pi_\perp\Sigma^{-1}\Pi_\perp)^{-1}\Sigma^{-1} &= \left(\left[\Sigma^{-1} - \Sigma^{-1}(\Pi_\perp\Sigma^{-1}\Pi_\perp)^{-1}\Sigma^{-1}\right]^{-1}\right)^{-1} \\
&= [\Pi\Sigma\Pi]^{-1}
\end{aligned} \tag{A.10}$$

A.1.2.2 Lemma: $W = V^\dagger V$, V Invertible

Let $\{|w_i'\rangle\}$ be an orthonormal basis of span($\{|w_i\rangle\}$), perhaps requiring a regularization of some of the $|w_i\rangle$ (eg $w(\nu) = 1 = \lim_{b\to\infty} 1 - \Theta(\nu - b)$, with $\Theta(x)$ the Heaviside function, for a bolometric luminosity). Then $\Pi = \sum_i |w_i'\rangle\langle w_i'|$ and:

$$
\begin{aligned}
W &= \sum_i |w_i\rangle\langle w_i| \\
&= \sum_{i,j} |w_i\rangle\langle w_i'|w_j'\rangle\langle w_j| \\
&= \left(\sum_i |w_i\rangle\langle w_i'|\right)\left(\sum_j |w_j'\rangle\langle w_j|\right) \\
&\equiv V^\dagger V. \qquad \text{(A.11)}
\end{aligned}
$$

The invertability of V follows immediately from the linear independence of $\{|w_i'\rangle\}$.

Combining Equations A.3, A.7, and A.8 with the preceding lemmas gives:

$$
\begin{aligned}
\Phi(L_i,\sigma) &= \frac{1}{(2\pi)^{N/2}}\left[\det\left(\sigma^2 \mathrm{Id} + \Pi\Sigma W\right)\right]^{-1/2} \\
&\quad \cdot \exp\left(-\frac{1}{2}\left[\langle f_0|(\Pi\Sigma\Pi)^{-1}|f_0\rangle - \langle v|W^{-1}(\Pi\Sigma\Pi)^{-1}|f_0\rangle\right.\right. \\
&\qquad \left.\left. -\langle f_0|(\Pi\Sigma\Pi)^{-1}W^{-1}|v\rangle + \langle v|W^{-1}(\Pi\Sigma\Pi)^{-1}W^{-1}|v\rangle\right]\right) \\
&\quad \cdot \exp(\mathcal{O}(\sigma^2)) \Rightarrow \\
\Phi(L_i) &\equiv \lim_{\sigma\to 0}\Phi(L_i,\sigma) \\
&= \frac{1}{(2\pi)^{N/2}}\left[\det\left(\Pi\Sigma W\right)\right]^{-1/2} \\
&\quad \cdot \exp\left(-\frac{1}{2}\left[(\langle v| - \langle f_0|W)(W\Sigma W)^{-1}(|v\rangle - W|f_0\rangle)\right]\right). \qquad \text{(A.12)}
\end{aligned}
$$

To complete the proof, we let $|L\rangle \equiv \sum_i L_i|w_i'\rangle \Rightarrow |v\rangle = V^\dagger|L\rangle$ to get:

$$
\begin{aligned}
\Phi(L_i) &= \frac{1}{(2\pi)^{N/2}}\left[\det\left(\Pi\Sigma V^\dagger V\right)\right]^{-1/2} \\
&\quad \cdot \exp\left(-\frac{1}{2}\left[(\langle L|V - \langle f_0|V^\dagger V)(V^\dagger V\Sigma V^\dagger V)^{-1}(V^\dagger|L\rangle - V^\dagger V|f_0\rangle)\right]\right) \\
&= \frac{1}{(2\pi)^{N/2}}\left[\det\left(V\Sigma V^\dagger\right)\right]^{-1/2} \\
&\quad \cdot \exp\left(-\frac{1}{2}\left[(\langle L| - \langle f_0|V^\dagger)(V\Sigma V^\dagger)^{-1}(|L\rangle - V|f_0\rangle)\right]\right) \\
&= \frac{1}{(2\pi)^{N/2}}\left[\det\left([\langle w_i|\Sigma|w_j\rangle]\right)\right]^{-1/2} \\
&\quad \cdot \exp\left(-\frac{1}{2}\sum_{i,j}\left[(L_i - \langle f_0|w_i\rangle)[\langle w_l|\Sigma|w_m\rangle]^{-1}_{i,j}(L_j - \langle w_j|f_0\rangle)\right]\right), \qquad \text{(A.13)}
\end{aligned}
$$

q.e.d.

APPENDIX B

Example Covariances from Posterior Chains

One of the primary reasons given for using $\kappa_\star$ and R_n in measuring the luminosity function (LF) is that the parameters have a lower correlation in the resulting posterior. The actual amounts of inter-parameter correlation depends on the depth of the survey, at least partly because of the choice of standard redshift, $z_{\rm std} = 0.38$ for this work. It is possible for the prior in α imposed on the chains labeled with the term "Prior" to affect the level of apparent correlations, so this chapter presents a comparison of the correlations in the High z chain in the standard parameterization presented in this work, using $\kappa_\star$ and R_n, with the correlations using the more standard $\phi_\star$ and R_ϕ. The relationships between the parameters are given in Equations 2.46 and 2.37 of Chapter 2, and recreated here for convenience:

$$\kappa_\star = \frac{\phi_\star(z=0)[L_\star(z=0)]^{3/2}}{\Omega_{\rm sky}4\pi^{1/2}}\Gamma\left(\alpha+\frac{5}{2}\right)$$
$$R_n = R_\phi - \min(1+\alpha, 0)\left[R_L + \frac{n_0}{t_0 - t_L}\right].$$

Figure B.1 contains a table of plots that show how the density of the parameters in the High z chain, considered pairwise; the relevant plots are in the first two columns. Table B.1 contains the covariance matrix of the same set of parameters, which is both more precise about the covariance of the parameters, and less informative for the parameters that have non-Gaussian covariance (primarily the $\ln n_0$-R_L correlation). Figure B.2 and Table B.2 contains the same information about the same chain where the $\ln\kappa_\star$ and R_n parameters have been replaced with $\ln\phi_\star$ and R_ϕ. One example where the correlation is particularly reduced is between $\ln L_\star$ and $\ln\kappa_\star$ ($\rho = -0.2308$) versus $\ln L_\star$ and $\ln\phi_\star$ ($\rho = -0.6605$).

One global measure of how correlated the variables are, as an ensemble, is the mutual

Table B.1. Hi z Sample Luminosity Function Bayesian Base Parameter Posterior Covariance

Parameter	σ	$\delta \ln \kappa_\star$	$\delta R_n t_H$	$\delta \ln L_\star(0)$	$\delta R_L t_H$	$\delta\alpha$	$\delta \ln n_0$
$\delta \ln \kappa_\star$	0.03060	1.000	0.8073	−0.2308	−0.01338	−0.2757	−0.2725
$\delta R_n t_H$	0.2001	0.8073	1.000	−0.7170	−0.4081	0.1424	0.004816
$\delta \ln L_\star(0)$	0.01896	−0.2308	−0.7170	1.000	0.6566	−0.6221	−0.3179
$\delta R_L t_H$	0.1351	−0.01338	−0.4081	0.6566	1.000	−0.1427	−0.8863
$\delta\alpha$	0.02980	−0.2757	0.1424	−0.6221	−0.1427	1.000	0.06147
$\delta \ln n_0$	0.1457	−0.2725	0.004816	−0.3179	−0.8863	0.06147	1.000

Note. — The σ column contains the standard deviation of the parameters, and the remaining rows and columns comprise the matrix of correlation coefficients between the parameters, considered pairwise. All values given to four significant figures.

information. For a multivariate Gaussian distribution, this is:

$$I(\mathbf{x}) = -\frac{1}{2} \ln |\rho|, \tag{B.1}$$

where $|\rho|$ is the absolute value of the determinant of the correlation matrix of the random variables, $\mathbf{x}$, and the result here is in "nats" (for bits, substitute $\ln \to \log_2$). In the special case where $\mathbf{x}$ is two-dimensional with a single correlation coefficient, ρ_0, $I = -\ln(1-\rho_0^2)/2$. The closer to 0 the mutual information is, the more statistically independent the variables are. For the chain with $\kappa_\star$ and R_n the mutual information is 4.7 nats (5.8 bits), and for the chain with $\phi_\star$ and R_ϕ it is 5.0 nats (7.3 bits).

The plots in figures B.1 and B.2 were produced using the Python module `corner.py` version 1.0.2.

Table B.2. Hi z Sample Luminosity Function Bayesian Schechter Parameter Posterior Covariance

Parameter	σ	$\delta \ln \phi_\star(0)$	$\delta R_\phi t_H$	$\delta \ln L_\star(0)$	$\delta R_L t_H$	$\delta\alpha$	$\delta \ln n_0$
$\delta \ln \phi_\star$	0.04541	1.000	0.9185	−0.6605	−0.3925	0.008575	0.003534
$\delta R_\phi t_H$	0.1913	0.9185	1.000	−0.3765	−0.1510	−0.2465	−0.2155
$\delta \ln L_\star(0)$	0.01896	−0.6605	−0.3765	1.000	0.6566	−0.6221	−0.3179
$\delta R_L t_H$	0.1351	−0.3925	−0.1510	0.6566	1.000	−0.1427	−0.8863
$\delta\alpha$	0.02980	0.008575	−0.2465	−0.6221	−0.1427	1.000	0.06147
$\delta \ln n_0$	0.1457	0.003534	−0.2155	−0.3179	−0.8863	0.06147	1.000

Note. — The σ column contains the standard deviation of the parameters, and the remaining rows and columns comprise the matrix of correlation coefficients between the parameters, considered pairwise. All values given to four significant figures.

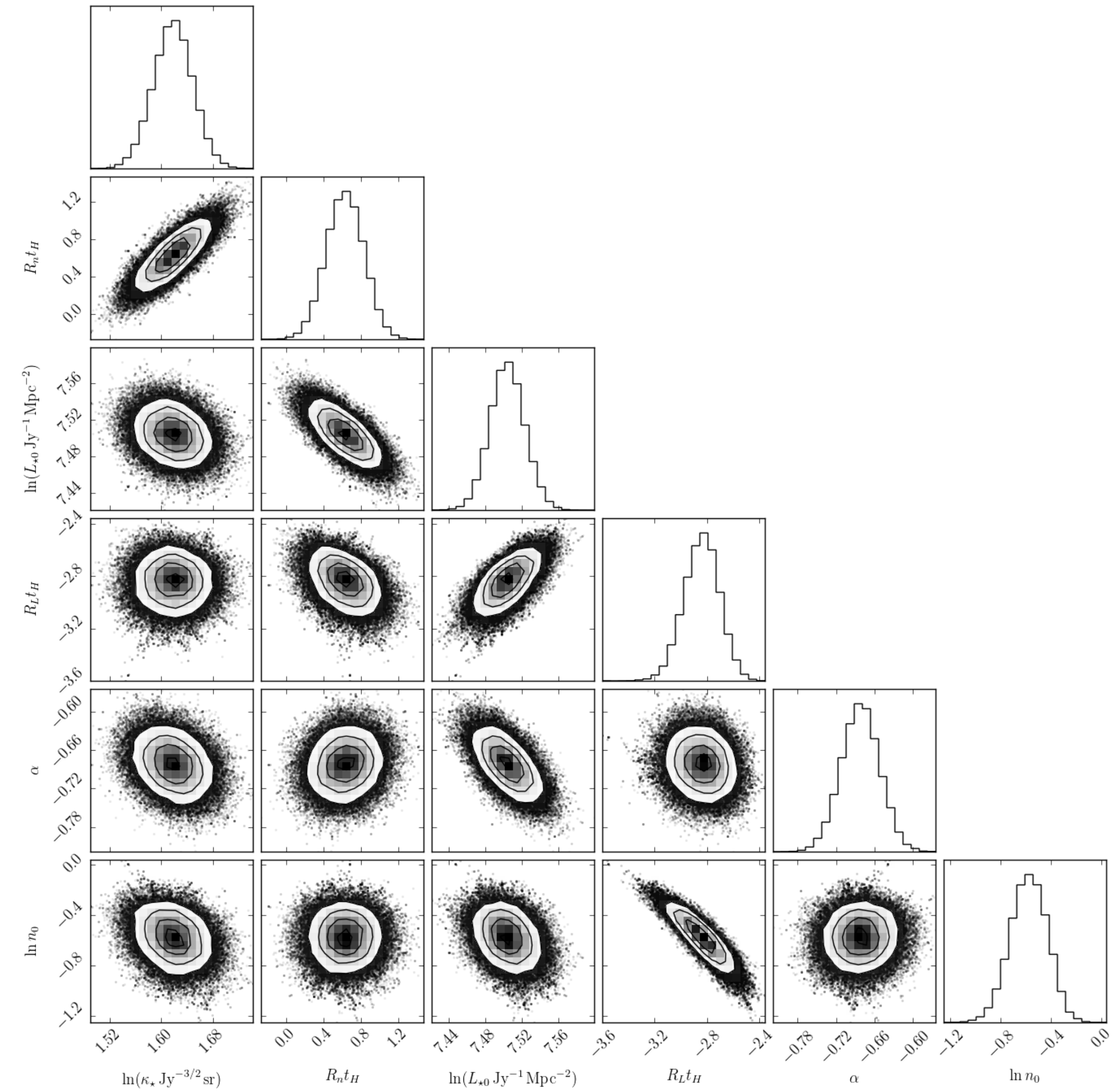

Figure B.1: Corner plot of pairwise distributions for parameters in the High z posterior chain. The parameters are: $\ln \kappa_\star$ where $\kappa_\star$ is the normalization of the $z = 0$ Euclidean flux counts $\left(\frac{\mathrm{d}N}{\mathrm{d}F\,\mathrm{d}\Omega} = \kappa_\star F^{-5/2}\right)$ in $\mathrm{Jy}^{3/2}\,\mathrm{sr}^{-1}$, R_n is the specific rate of change in the number density of galaxies at $z = 0$, $L_\star$ is the $2.4\,\mu$m luminosity scale in the Schechter function at $z = 0$ in $\mathrm{Jy\,Mpc}^2$, R_L is the long time exponential decay constant in $L_\star$, α is the faint end slope of the LF, and n_0 is the early time power law exponent of $L_\star$ buildup.

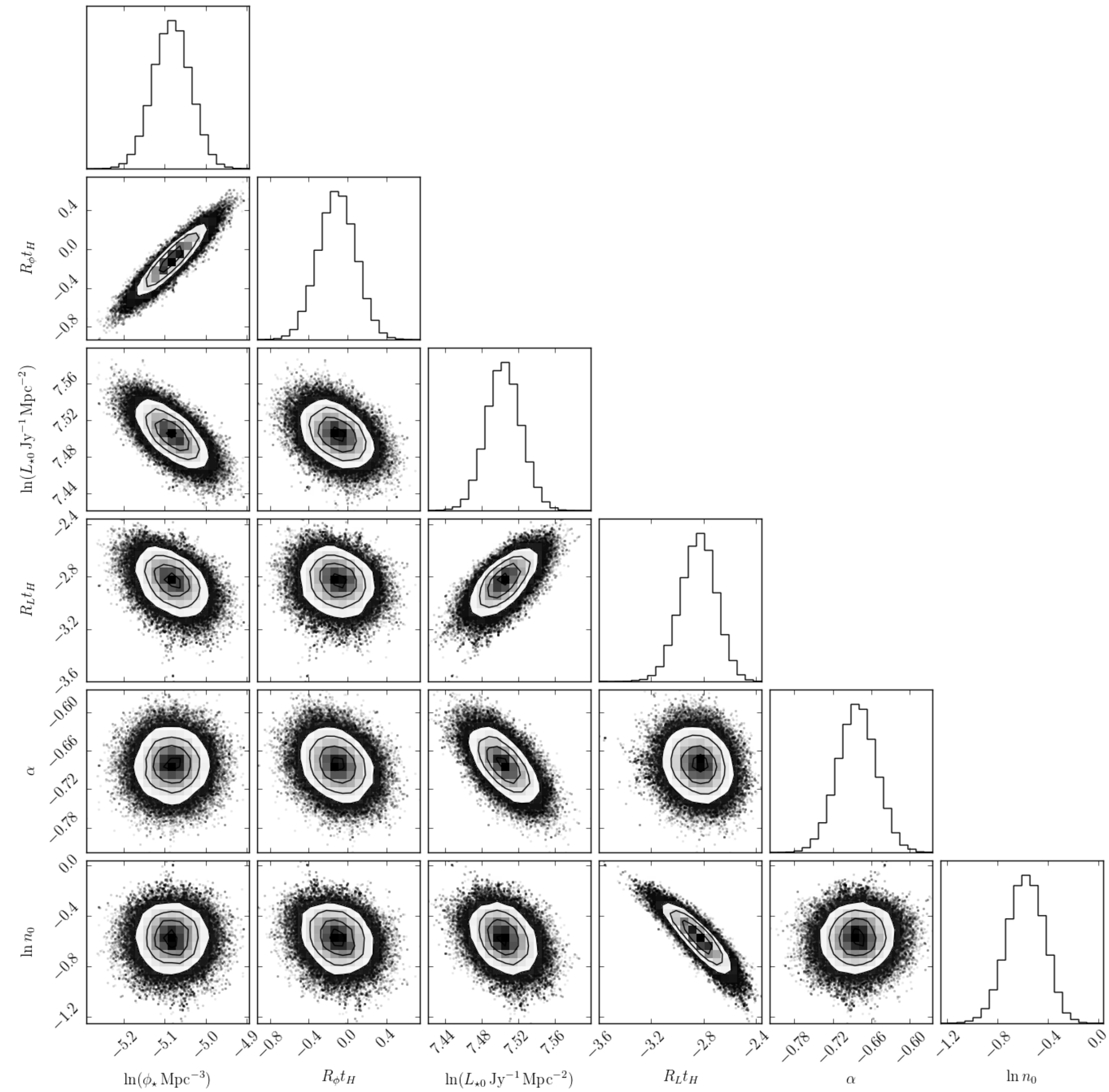

Figure B.2: Corner plot of pairwise distributions for parameters in the High z posterior chain, modified to use default Schechter parameters. The parameters are: $\ln \phi_\star$ where $\phi_\star$ is the value of the LF evaluated at $L_\star$ times $L_\star$ ($\phi_\star \equiv L_\star \Phi(L_\star)$), R_ϕ is the specific rate of change in $\phi_\star$ at $z = 0$, $L_\star$ is the $2.4\,\mu$m luminosity scale in the Schechter function at $z = 0$ in $\mathrm{Jy\,Mpc}^2$, R_L is the long time exponential decay constant in $L_\star$, α is the faint end slope of the LF, and n_0 is the early time power law exponent of $L_\star$ buildup.

Bibliography

Abazajian, K. N., Adelman-McCarthy, J. K., Agüeros, M. A., et al. 2009, ApJS, 182, 543

Aharonian, F., Essey, W., Kusenko, A., & Prosekin, A. 2013, Phys Rev D, 87, 063002

Aharonian, F., Akhperjanian, A. G., Bazer-Bachi, A. R., et al. 2006, Nature, 440, 1018

Ahn, C. P., Alexandroff, R., Allende Prieto, C., et al. 2014a, ApJS, 211, 17

—. 2014b, ApJS, 211, 17

Aihara, H., Allende Prieto, C., An, D., et al. 2011, ApJS, 193, 29

Albeverio, S., & Mazzucchi, S. 2011, Scholarpedia, 6, 8832, revision #137047

Arnouts, S., Walcher, C. J., Le Fèvre, O., et al. 2007, A&A, 476, 137

Ashby, M. L. N., Stern, D., Brodwin, M., et al. 2009, ApJ, 701, 428

Assef, R. J., Kochanek, C. S., Brodwin, M., et al. 2010, The Astrophysical Journal, astro-ph.CO, 970

Assef, R. J., Stern, D., Kochanek, C. S., et al. 2013, ApJ, 772, 26

Avni, Y., & Bahcall, J. N. 1980, ApJ, 235, 694

Babbedge, T. S. R., Rowan-Robinson, M., Vaccari, M., et al. 2006, MNRAS, 370, 1159

Baldry, I. K., Robotham, A. S. G., Hill, D. T., et al. 2010, MNRAS, 404, 86

Bell, E. F., McIntosh, D. H., Katz, N., & Weinberg, M. D. 2003, ApJS, 149, 289

Binggeli, B., Sandage, A., & Tammann, G. A. 1988, ARA&A, 26, 509

Blanton, M. R., Brinkmann, J., Csabai, I., et al. 2003a, AJ, 125, 2348

Blanton, M. R., Hogg, D. W., Bahcall, N. A., et al. 2003b, ApJ, 592, 819

Bouwens, R. J., Illingworth, G. D., Franx, M., et al. 2009, ApJ, 705, 936

Bouwens, R. J., Illingworth, G. D., Oesch, P. A., et al. 2014, ApJ, 793, 115

Bruzual, G., & Charlot, S. 2003, MNRAS, 344, 1000

Capak, P., Aussel, H., Ajiki, M., et al. 2007, ApJS, 172, 99

Cardelli, J. A., Clayton, G. C., & Mathis, J. S. 1989, ApJ, 345, 245

Cartier, P., & DeWitt-Morette, C. 2000, Journal of Mathematical Physics, 41, 4154

Cirasuolo, M., McLure, R. J., Dunlop, J. S., et al. 2007, MNRAS, 380, 585

Cole, S., Norberg, P., Baugh, C. M., et al. 2001, MNRAS, 326, 255

Colless, M., Peterson, B. A., Jackson, C., et al. 2003, arXiv:astro-ph/0306581v1, arXiv:astro-ph/0306581v1

Conselice, C. J., Wilkinson, A., Duncan, K., & Mortlock, A. 2016, ApJ, 830, 83

Cool, R. J., Eisenstein, D. J., Kochanek, C. S., et al. 2012, ApJ, 748, 10

Cooper, M. C., Newman, J. A., Davis, M., Finkbeiner, D. P., & Gerke, B. F. 2012, spec2d: DEEP2 DEIMOS Spectral Pipeline, Astrophysics Source Code Library, ascl:1203.003

Cooray, A. 2016, Royal Society Open Science, 3, 150555

Cooray, A., Smidt, J., De Bernardis, F., et al. 2012, Nature, 490, 514

Cutri, R. M., Wright, E. L., Conrow, T., et al. 2013, Explanatory Supplement to the AllWISE Data Release Products, Tech. rep., Infrared Processing and Analysis Center (IPAC)

Dai, X., Assef, R. J., Kochanek, C. S., et al. 2009, ApJ, 697, 506

Domínguez, A., Primack, J. R., Rosario, D. J., et al. 2011, MNRAS, 410, 2556

Drinkwater, M. J., Jurek, R. J., Blake, C., et al. 2010, MNRAS, 401, 1429

Driver, S. P., Andrews, S. K., Davies, L. J., et al. 2016, ApJ, 827, 108

Efstathiou, G., Ellis, R. S., & Peterson, B. A. 1988a, MNRAS, 232, 431

—. 1988b, MNRAS, 232, 431

Eisenhardt, P. R. M., Wu, J., Tsai, C.-W., et al. 2012, ApJ, 755, 173

Eisenstein, D. J., Annis, J., Gunn, J. E., et al. 2001, AJ, 122, 2267

Essey, W., Kalashev, O., Kusenko, A., & Beacom, J. F. 2011, ApJ, 731, 51

Essey, W., & Kusenko, A. 2010, Astroparticle Physics, 33, 81

Faber, S. M., Phillips, A. C., Kibrick, R. I., et al. 2003, in Society of Photo-Optical Instrumentation Engineers (SPIE) Conference Series, Vol. 4841, Instrument Design and Performance for Optical/Infrared Ground-based Telescopes, ed. M. Iye & A. F. M. Moorwood, 1657–1669

Fazio, G. G., Ashby, M. L. N., Barmby, P., et al. 2004, ApJS, 154, 39

Feldman, G. J., & Cousins, R. D. 1998, Physical Review D, 57, 3873

Foreman-Mackey, D., Hogg, D. W., Lang, D., & Goodman, J. 2013, PASP, 125, 306

Goodman, J., & Weare, J. 2010, Communications in Applied Mathematics and Computational Science, 5, 65

Gorjian, V., Wright, E. L., & Chary, R. R. 2000, ApJ, 536, 550

Gott, III, J. R., Jurić, M., Schlegel, D., et al. 2005, ApJ, 624, 463

Helgason, K., Ricotti, M., & Kashlinsky, A. 2012, ApJ, 752, 113

Hinshaw, G., Larson, D., Komatsu, E., et al. 2013, ApJS, 208, 19

Hogg, D. W., Baldry, I. K., Blanton, M. R., & Eisenstein, D. J. 2002, ArXiv Astrophysics e-prints, astro-ph/0210394

Humason, M. L., Mayall, N. U., & Sandage, A. R. 1956, AJ, 61, 97

Ilbert, O., Tresse, L., Arnouts, S., et al. 2004, Monthly Notices of the Royal Astronomical Society, 351, 541

Jannuzi, B. T., & Dey, A. 1999, in Astronomical Society of the Pacific Conference Series, Vol. 193, The Hy-Redshift Universe: Galaxy Formation and Evolution at High Redshift, ed. A. J. Bunker & W. J. M. van Breugel, 258

Jarrett, T. H., Dickman, R. L., & Herbst, W. 1994, ApJ, 424, 852

Jarrett, T. H., Cohen, M., Masci, F., et al. 2011, ApJ, 735, 112

Jenkins, A., Frenk, C. S., White, S. D. M., et al. 2001, MNRAS, 321, 372

Johnston, R. 2011, A&A Rv, 19, 41

Jones, D. H., Peterson, B. A., Colless, M., & Saunders, W. 2006, MNRAS, 369, 25

Jones, D. H., Saunders, W., Colless, M., et al. 2004, MNRAS, 355, 747

Jones, D. H., Read, M. A., Saunders, W., et al. 2009, MNRAS, 399, 683

Kelvin, L. S., Driver, S. P., Robotham, A. S. G., et al. 2014, MNRAS, 439, 1245

Knobel, C., Lilly, S. J., Iovino, A., et al. 2012, ApJ, 753, 121

Kochanek, C. S., Pahre, M. A., Falco, E. E., et al. 2001, ApJ, 560, 566

Kochanek, C. S., Eisenstein, D. J., Cool, R. J., et al. 2012, ApJS, 200, 8

Lake, S. E., Wright, E. L., Petty, S., et al. 2012, AJ, 143, 7

Lang, D., Hogg, D. W., & Schlegel, D. J. 2014, ArXiv e-prints, arXiv:1410.7397

Lawrence, A., Warren, S. J., Almaini, O., et al. 2007, MNRAS, 379, 1599

Lee, S.-K., Ferguson, H. C., Somerville, R. S., Wiklind, T., & Giavalisco, M. 2010, ApJ, 725, 1644

Levenson, L. R., & Wright, E. L. 2008, ApJ, 683, 585

Levenson, L. R., Wright, E. L., & Johnson, B. D. 2007, ApJ, 666, 34

Lilly, S. J., Le Brun, V., Maier, C., et al. 2009, ApJS, 184, 218

Lin, H., Yee, H. K. C., Carlberg, R. G., et al. 1999, ApJ, 518, 533

Liske, J., Baldry, I. K., Driver, S. P., et al. 2015, MNRAS, 452, 2087

Liu, F., Cutri, R., Greanias, G., et al. 2008, in SPIE Conference Series, Vol. 7017

Loveday, J. 2000, MNRAS, 312, 557

Loveday, J., Norberg, P., Baldry, I. K., et al. 2012, MNRAS, 420, 1239

—. 2015, MNRAS, 451, 1540

Lynden-Bell, D. 1971, MNRAS, 155, 95

Madau, P., & Dickinson, M. 2014, ARA&A, 52, 415

Mancone, C. L., & Gonzalez, A. H. 2012, PASP, 124, 606

Maraston, C. 2005, MNRAS, 362, 799

Marshall, H. L., Tananbaum, H., Avni, Y., & Zamorani, G. 1983, ApJ, 269, 35

Martin, D. C., Fanson, J., Schiminovich, D., et al. 2005, ApJ, 619, L1

Masters, D., & Capak, P. 2011, PASP, 123, 638

Matsumoto, T., Matsuura, S., Murakami, H., et al. 2005, ApJ, 626, 31

Mazin, D., & Raue, M. 2007, A&A, 471, 439

Miyaji, T., Hasinger, G., & Schmidt, M. 2001, A&A, 369, 49

Montero-Dorta, A. D., & Prada, F. 2009, MNRAS, 399, 1106

Nakahara, M. 2003, Geometry, Topology and Physics, 2nd edn. (Taylor & Francis Group), 19–26

Newman, J. A., Cooper, M. C., Davis, M., et al. 2013, ApJS, 208, 5

Oke, J. B., Cohen, J. G., Carr, M., et al. 1995, PASP, 107, 375

Page, M. J., & Carrera, F. J. 2000, MNRAS, 311, 433

Peskin, M. E., & Schroeder, D. V. 2007, An Introduction to Quantum Field Theory (Perseus Press)

Polletta, M., Tajer, M., Maraschi, L., et al. 2007, ApJ, 663, 81

Pozzetti, L., Cimatti, A., Zamorani, G., et al. 2003, A&A, 402, 837

Press, W. H., & Schechter, P. 1974, ApJ, 187, 425

Richards, G. T., Fan, X., Newberg, H. J., et al. 2002, AJ, 123, 2945

Richards, G. T., Strauss, M. A., Fan, X., et al. 2006, AJ, 131, 2766

Rieke, G. H., Alonso-Herrero, A., Weiner, B. J., et al. 2009, ApJ, 692, 556

Sandage, A., Tammann, G. A., & Yahil, A. 1979, The Astrophysical Journal, 232, 352

Sanders, D. B., Salvato, M., Aussel, H., et al. 2007, ApJS, 172, 86

Sano, K., Kawara, K., Matsuura, S., et al. 2016, ApJ, 818, 72

Schechter, P. 1976, ApJ, 203, 297

Schlegel, D. J., Finkbeiner, D. P., & Davis, M. 1998, ApJ, 500, 525

Schmidt, M. 1968, ApJ, 151, 393

Scoville, N., Aussel, H., Brusa, M., et al. 2007, ApJS, 172, 1

Scully, S. T., Malkan, M. A., & Stecker, F. W. 2014, ApJ, 784, 138

Silva, L., Granato, G. L., Bressan, A., & Danese, L. 1998, ApJ, 509, 103

Simha, V., Weinberg, D. H., Conroy, C., et al. 2014, ArXiv e-prints, arXiv:1404.0402

Skrutskie, M. F., Cutri, R. M., Stiening, R., et al. 2006, AJ, 131, 1163

Smith, A. J., Loveday, J., & Cross, N. J. G. 2009, MNRAS, 397, 868

Stecker, F. W., Scully, S. T., & Malkan, M. A. 2016, ApJ, 827, 6

Stern, D., Eisenhardt, P., Gorjian, V., et al. 2005, ApJ, 631, 163

Strauss, M. A., Weinberg, D. H., Lupton, R. H., et al. 2002, AJ, 124, 1810

Takeuchi, T. T., Yoshikawa, K., & Ishii, T. T. 2000, ApJS, 129, 1

Tsumura, K., Matsumoto, T., Matsuura, S., Sakon, I., & Wada, T. 2013, PASJ, 65, arXiv:1307.6740

Willmer, C. N. A. 1997, AJ, 114, 898

Wolf, S., & Hillenbrand, L. A. 2003, ApJ, 596, 603

Wright, E. L., & Johnson, B. D. 2001, ArXiv Astrophysics e-prints, astro-ph/0107205

Wright, E. L., & Reese, E. D. 2000, ApJ, 545, 43

Wright, E. L., Eisenhardt, P. R. M., Mainzer, A. K., et al. 2010, AJ, 140, 1868

Zacharias, N., Monet, D. G., Levine, S. E., et al. 2004, in Bulletin of the American Astronomical Society, Vol. 36, American Astronomical Society Meeting Abstracts, 1418

Zehavi, I., Zheng, Z., Weinberg, D. H., et al. 2005, ApJ, 630, 1

Zinn-Justin, J. 2009, Scholarpedia, 4, 8674, revision #147600